Superconducting Microwave Resonators for Hybrid Quantum Systems in Extreme Conditions

Dissertation
der Mathematisch-Naturwissenschaftlichen Fakultät
der Eberhard Karls Universität Tübingen
zur Erlangung des Grades eines
Doktors der Naturwissenschaften
(Dr. rer. nat.)

vorgelegt von
Benedikt Wilde
aus Göttingen

Tübingen
2025

Gedruckt mit Genehmigung der Mathematisch-Naturwissenschaftlichen Fakultät der Eberhard Karls Universität Tübingen.

Tag der mündlichen Qualifikation	12. Februar 2026
Dekan	Prof. Dr. Thilo Stehle
1. Berichterstatter	Prof. Dr. Reinhold Kleiner
2. Berichterstatter	Prof. Dr. Ioan Pop

Abstract

Hybrid quantum systems play an essential role in efforts towards the advancements of quantum information technology and quantum sensing by bridging distinct technological platforms. In particular, hybrid systems comprising superconducting microwave circuits are being pursued intensely in light of existing achievements in superconducting qubits and precise quantum control in microwave circuits. Their realization relies on the design of superconducting resonators capable of coupling to an oscillatory mode of a second quantum system, facilitating the probing and manipulation of one via the other. In order to accommodate the coupled system, its particular constraints and requirements must be respected, which may be quite extreme from the perspective of established superconducting circuit design and operation. Overcoming this challenge has proved to be a substantial obstacle for the attainment of strongly coupled hybrid systems, despite spectacular advances in superconducting microwave circuits individually. In this work, we examine two approaches tackling this issue for different hybrid quantum systems, focusing on the optimization and characterization of the superconducting circuits. The first device aims at a superconductor-atom hybrid system through the coupling to Rydberg-Rydberg transitions in ultra-cold ^{87}Rb atoms trapped near the superconducting chip. Using simulations in conjunction with theoretical considerations, we demonstrate a comprehensive geometry parameter optimization procedure for maximum coupling rate. Presenting an experimental implementation of the resulting circuit, we validate its suitability for use under the intended operation conditions, including the option of tuning the electronic transition frequencies using a dc voltage. Secondly, we investigate a device designed for applications in large magnetic in-plane fields used to mediate coupling to integrated micromechanical oscillators; more specifically it is a flux-tunable SQUID resonator comprising Josephson nano-constrictions as nonlinear inductive components. Performing a thorough characterization of its frequency and Kerr anharmonicity tuning behavior at fields up to several hundred mT, we discover a pronounced asymmetry in its flux response at large fields. We show this asymmetry to be caused by the nano-constrictions turning into Josephson diodes, develop an intuitive macroscopic model for its field-induced emergence and reconstruct the diode current-phase relation from the flux tuning data. Several figures of merit informing the suitability of the SQUID resonators for optomechanical systems as well as other applications are improved by the diode effect, highlighting the potential of Josephson diodes in superconducting microwave circuits. Our results provide a promising stepping stone for the advancement of hybrid systems involving superconducting microwave circuits, putting new and exciting operation and coupling regimes within reach.

Abriss

Hybride Quantensysteme spielen als Bindeglied zwischen verschiedenen Technologien eine zentrale Rolle in Quanteninformatik und -sensorik. Besonders Varianten mit supraleitenden Mikrowellenschaltungen werden angesichts bestehender Erfolge mit supraleitenden Qubits sowie präziser Manipulierbarkeit intensiv verfolgt. Ihre Umsetzung beruht auf der Entwicklung eines supraleitenden Resonators, der an eine Schwingungsmode eines zweiten Quantensystems koppeln kann und so die Untersuchung und Steuerung eines Systems durch das andere ermöglicht. Hierfür müssen die speziellen Anforderungen und Einschränkungen des jeweiligen gekoppelten Systems berücksichtigt werden, die aus Sicht der etablierten Praxis für Konzeption und Betrieb supraleitender Schaltungen durchaus extrem sein können. Dieser Umstand hat sich als beachtliches Hindernis für die Verwirklichung stark gekoppelter hybrider Systeme erwiesen, obgleich mit supraleitenden Mikrowellenschaltungen allein spektakuläre Fortschritte erzielt wurden. In dieser Arbeit betrachten wir zwei Ansätze für verschiedene hybride Quantensysteme, diese Hürde zu überwinden, wobei wir uns auf die Optimierung und Charakterisierung der supraleitenden Schaltungen konzentrieren. Der erste Resonator zielt auf die Kopplung an Rydberg-Rydberg-Übergänge von nahe des Chips gefangenen kalten ^{87}Rb-Atomen. Mithilfe von Simulationen sowie theoretischen Erwägungen optimieren wir die Resonator-Abmessungen für möglichst hohe Kopplung, präsentieren eine experimentelle Umsetzung der resultierenden Struktur und bestätigen ihre Eignung für die vorgesehenen Betriebsbedingungen, die eine Verstimmung der elektronischen Übergänge durch das Anlegen von Gleichspannung einschließen. Als Zweites untersuchen wir einen Chip für Anwendungen mit großen Magnetfeldern in der Leiterebene, die eine Kopplung mit in die Schaltung integrierten mikromechanischen Resonatoren ermöglichen; genauer geht es um einen Fluss-verstimmbaren SQUID-Resonator mit Josephson-Einschnürungskontakten als nichtlineare Induktivitäten. Indem wir die Frequenz- und Kerr-Nichtlinearitäts-Verstimmung in Feldern von bis zu mehreren hundert mT charakterisieren, stellen wir eine deutliche Asymmetrie im Fluss-Verhalten bei hohen Feldern fest. Als Ursache eruieren wir einen Josephson-Dioden-Effekt in den Einschnürungs-Kontakten, entwickeln ein intuitives makroskopisches Modell für sein feldabhängiges Auftreten und ermitteln mithilfe des Verstimmungsverhaltens der Dioden ihre Strom-Phasen-Beziehung. Der Effekt verbessert mehrere Kenngrößen von SQUID-Resonatoren für Anwendungen wie optomechanische Systeme, was das Potential von Dioden für supraleitende Mikrowellenschaltungen unterstreicht. Unsere Ergebnisse stellen einen vielversprechenden Ausgangspunkt für die Weiterentwicklung hybrider Systeme dar und rücken neue, aussichtsreiche Betriebs- und Kopplungsbereiche in greifbare Nähe.

Contents

1 Introduction

Resonance is one of the most pervasive fundamental concepts in physics today. In particular, the harmonically driven, linearly damped harmonic oscillator is a model which is discussed in any introductory physics lecture and that finds application in fields ranging from mechanical engineering to particle physics. The equation of motion of the basic one-dimensional case can be written as

$$\ddot{x} + \kappa\dot{x} + \omega_0^2 x = A_\mathrm{d} \mathrm{e}^{\mathrm{i}\omega_\mathrm{d} t}, \tag{1.1}$$

where $x(t)$ is the oscillating quantity, κ quantifies the damping, ω_0 is the (angular) resonance frequency, which is also its oscillation frequency in the absence of damping and driving, and the right-hand side of the equation is some harmonic driving excitation with amplitude A_d and frequency ω_d. (For real-valued quantities we follow the established convention of interpreting only the real part of x as physically relevant.) The well-known solution to this equation of motion takes the form (except for the special case of the un-damped oscillator driven at resonance)

$$x(t) = X_\mathrm{s} \mathrm{e}^{\mathrm{i}\omega_\mathrm{d} t} + X_\mathrm{f} \mathrm{e}^{(\mathrm{i}\omega_\kappa - \kappa/2)t} \tag{1.2}$$

with the (complex) amplitudes X_s of the stationary, forced oscillation and X_f of a freely decaying oscillation, whose frequency is given by $\omega_\kappa^2 = \omega_0^2 - \kappa^2/4$ and which may or may not be present depending on the initial conditions. The stationary amplitude is given by

$$X_\mathrm{s}(\omega_\mathrm{d}) = \frac{A_\mathrm{d}}{\omega_0^2 - \omega_\mathrm{d}^2 + \mathrm{i}\kappa\omega_\mathrm{d}}, \tag{1.3}$$

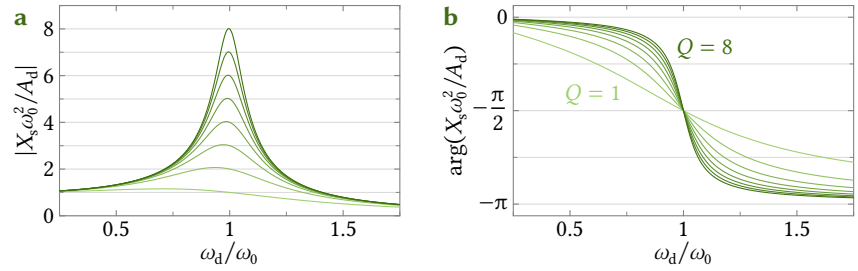

Figure 1.1: Stationary amplitude of the driven harmonic oscillator. We show both **a** the magnitude of the stationary oscillation amplitude and **b** its phase relative to the driving force as given by (1.3) for different quality factors $Q = \omega_0/\kappa \in \{1, 2, 3, 4, 5, 6, 7, 8\}$ (light to dark). The driving frequency ω_d is normalized to the resonance frequency ω_0 and the stationary amplitude X_s is normalized to the static displacement A_d/ω_0^2.

revealing the essence of resonant behavior: If the oscillator is only slightly damped $\kappa \ll \omega_0$ and is excited at frequencies close to ω_0, the resulting amplitude can grow very large, much larger than the excitation amplitude might otherwise suggest. At $\omega_d = \omega_0$, it is larger than the corresponding static displacement ($\omega_d = 0$) by the quality factor $Q = \omega_0/\kappa$. Somewhat surprisingly, the maximum amplitude is reached not when driving at ω_0 or ω_κ but when $\omega_d^2 = \omega_0^2 - \kappa^2/2$, though the oscillator contains maximum energy at $\omega_d = \omega_0$. For high-quality resonators $Q \gg 1$, however, this is an insignificant distinction and thus it is usually neglected. Some examples of the distinctive resonance curves representing the magnitude as well as the phase of $X_s(\omega_d)$ are shown in Figure 1.1.

While the ubiquitous applicability of this concept in the physical sciences may surprise anyone not familiar with the subject matter, its significance for mechanical systems seems obvious. Even in prehistoric times, it must have been known that, for example, sitting on a branch, using small but well-timed movements, one may induce great oscillations in the branch, possibly to the point where one can no longer hold on to it or where the branch breaks from its tree. Given such an overt presence in our natural environment as well as the apparent simplicity of the equation of motion (1.1), one might expect resonance phenomena to belong to the earliest ones explored in modern science and their theoretical description to have been among the first ones tackled by the pioneers of calculus and by students of physics ever since. However, the true history of the subject is much messier and far more interesting [1]. Let us indulge ourselves by tracing this history and appreciating our own place in it.

Though not the first [2], an influential early description of resonance was given by Galilei in 1638 [3]. While the word *resonance* was born from acoustics – in the sense that a musical instrument can be made to sound by playing a tone of matching

pitch nearby –, and it should remain exclusive to this domain for another two and a half centuries, Galilei recognized that the ringing of a heavy bell by a rope followed the same principles. On the other hand, he asserted that a resonator would only ever oscillate at its natural frequency no matter the driving force, an error that may have contributed to the correct behavior being overlooked or forgotten for many generations to come. One might expect Newton to have been the first one to write down and solve the equation of motion (1.1), but he did not; instead, it was Euler who undertook this a century after Galilei, albeit without the damping term [4]. He obtained the correct solutions, remarking on the two resulting oscillation frequencies and discussing the special case of resonant driving, where, in the absence of damping, the amplitude grows without limits. While Euler certainly appreciated the mathematical advances made in the process, he completely failed to recognize the physical significance of his result, deeming it a mere curiosity, and no one else took notice of it either. Thus, the dynamics of forced oscillations were completely forgotten, only to be independently re-discovered and overlooked multiple times throughout the nineteenth century: By Young studying tides [5, 6], by Seebeck studying acoustics [7] and again by Redtenbacher studying engines [8]. This last case is particularly peculiar, as Redtenbacher was not merely ignored but actively refuted by his colleagues, who were arguing that the dangerous regime of resonant engine speeds he predicted could not possibly exist [9], a confusion that was partly born from the absence of damping in Redtenbacher's treatment of the matter, though both Young and Seebeck had included it.

Only during the second half of the century did the phenomenon of forced mechanical oscillations begin to find notable appreciation among physicists. In 1863 Helmholtz included the relevant theory in a textbook on acoustics [10] – without citing any previous authors – and this, at last, was not completely disregarded. Rayleigh notes Helmholtz' results in his own 1877 acoustics textbook [11] and remarks on their relevance for applications outside of acoustics. While the slow recognition of the significance of mechanical resonance in physics was thus finally underway, the disciplines that could have most obviously benefited from the associated insights, namely structural and mechanical engineering, remained reluctant to adopt them; despite various disasters like bridges collapsing under the stress of resonant excitation all throughout the nineteenth century. Even after the turn of the century, multiple authors were lamenting the lack of consideration of resonance in technical applications and working on remedying this state [12, 13], and it should take the better part of the new century until this task was completed [1].

A notable contrast to this slow recognition of the significance of mechanical resonance – and possibly an important factor in resolving that deficit – is the much shorter history of electromagnetic resonance. It was first observed in 1853 by Thomson (the later Lord Kelvin) in the discharge of a capacitor through an inductive wire [14]; what we would now call an LC resonator. Shortly after Oberbeck pointed

out the parallel to mechanical resonance in 1885 [15], Hertz was able to use the phenomenon to create and detect electromagnetic waves [16], an accomplishment that should quickly facilitate a revolution in communications technology.

Given this historical backdrop, it was maybe in the spirit of the times that, when Planck attempted to develop a model explaining the spectrum of black body radiation at the end of the nineteenth century, he employed a collection of harmonic oscillators to do so, prompting him to introduce his famous constant and to thus usher in the era of quantum physics [17, 18]. In subsequent years, this approach was successfully applied to multiple other problems, e.g. in explaining the photoelectric effect [19] and the temperature-dependence of specific heat in a solid [20], and when the first theory of quantum mechanics emerged in 1925, it too did so in the form of an infinite series of harmonic oscillators [21, 22]. By now, the harmonic oscillator was firmly established as a model system for quantum mechanical energy transfer and thus it was not long before it was applied to radiation in the so-called second quantization [23, 24], a development that also gave us the creation and annihilation operator formalism that is most conveniently used to describe the quantum harmonic oscillator to this day.

Charmingly, the substantial role oscillations in electrical circuits and their technical applicability had played in the development of the subject of classical resonance should be echoed by their significance for the field of quantum oscillations a century later; as attested by the most recent Nobel Prize in Physics [25]. The key to this potential for the field is the fact that, despite its macroscopic dimensions, a superconducting LC circuit behaves like a quantum harmonic oscillator, i.e. like a quantum mechanical single particle system. Unlike the microscopic world of atoms and elementary particles this description is normally applied to, the properties of circuits and the interactions between them can be specially designed and controlled for the intended application. For example, including nonlinear elements into an LC circuit can modify its eigenenergy structure from the equidistant states characterizing the harmonic oscillator to one with varying transition energies, resembling the energy spectrum of electronic orbitals in atoms, which is why those circuits are sometimes called artificial atoms. Furthermore, when the lower-most transition is sufficiently detuned from higher ones, the corresponding states can be operated as an effective two-level system, implementing a superconducting qubit. As these simple examples illustrate, superconducting resonant circuits offer a plethora of possibilities to investigate and exploit quantum effects like light-matter interaction or quantum information processing, and the associated field of circuit quantum electrodynamics (QED) is presently a rich and active area of research [26].

Of particular interest within this maturing field are so-called hybrid quantum systems, where two or more different kinds of quantum oscillators are coupled to each other [27–29]. The superconducting circuits may be made to interact with quantum systems such as trapped atoms, electronic and nuclear spins, optical cavi-

ties and mechanical resonators. Besides a fundamental desire to investigate and advance our understanding of quantum mechanical coupling, a core motivation for tackling the challenging task of combining such distinct physical systems is the desire to evade the disadvantages of one system by combining it with another that exhibits complementary strengths; this is especially intriguing for quantum computing applications, where large coherence times, fast and controllable interactions as well as scalability are all desired features of a qubit but can usually not be simultaneously realized within a single physical implementation. Another prominent goal is to experimentally access and control a system which cannot easily be manipulated directly via a coupled oscillator for which a mature, comprehensive interface is available; as is the case for superconducting microwave resonators.

In addition to direct, coherent energy transfer between the resonators, where one oscillator drives the other analogously to (1.1), the coupling can be specially engineered in order to achieve a number of distinct behaviors, e.g. by introducing nonlinear elements. One important variation is the so-called parametric coupling, where one oscillator modifies some parameter characterizing the other, rather than directly driving its excitation amplitude. This approach facilitates the coupling of resonators with vastly different resonance frequencies by inputting an additional strong pump tone at a frequency matching the difference (or sum) between them, enabling the transduction of a quantum state from a low-frequency to a high-frequency system and vice versa. Most commonly, this is realized using so-called *dispersive coupling*, where the displacement of the low-frequency resonator from its equilibrium state changes the resonance frequency of the high-frequency resonator. More recently, though, so-called *dissipative coupling*, where the low-frequency displacement instead changes the decay rate of the high-frequency resonator, has begun to be experimentally investigated in circuit QED, too [30]. As with many other experiments, these effects were first realized in the related field of cavity QED [31, 32], working with atoms and lasers rather than superconducting circuits and microwave signals, before being pursued anew in circuit QED, taking advantage of its greater flexibility and control regarding system parameters. It was within this pioneering field of cavity QED that detection and manipulation of single quanta was first achieved, an accomplishment that earned the Nobel Prize in Physics 2012 [33, 34], and that optomechanical coupling was first investigated, typically working with a Fabry–Perot-type optical cavity consisting of two mirrors that couples to the movement of one of the mirrors.

Besides the implementation of a suitable coupling interface between the distinct quantum systems, a particular challenge with regard to their realization comes from the boundary conditions associated with their fabrication and experimental operation. Often, these individual demands cannot be simultaneously satisfied without compromise and finding an appropriate solution requires exploring novel and unusual approaches and designs. In this work, we shall examine two instances

of such exploration, in each case describing a superconducting microwave resonator that was designed with the extreme conditions associated with a particular hybrid system in mind, and testing and characterizing it in those conditions; the coupling itself is left to future investigations. By *extreme conditions* here we are referring to environments that are onerous and demanding from the perspective of the resonator design. To illustrate this perspective, let us recapitulate the principles and conventions usually followed in order to achieve a high-quality superconducting microwave resonator.

Most obviously, low temperatures are required for the superconducting state to form, necessitating more or less sophisticated cooling technology depending on the materials used; the critical temperatures T_c for Al and Nb, two superconductors typically employed in circuit QED devices, are 1.18 K and 9.25 K, respectively [35]. However, whenever ground state operation of a resonator is desired – as is always the case for qubit operation –, the temperature has to be lowered sufficiently to suppress thermal excitation of the resonator. In order to reach the mK temperatures necessary for ground-state operation of a microwave resonator (for reference, $h \cdot 10\,\mathrm{GHz} = k_B \cdot 480\,\mathrm{mK}$ with Planck's constant h and Boltzmann's constant k_B), a dilution refrigerator is needed. In this case, the critical temperature of the chosen material is not as relevant, though a device that is also operational in a simpler setup at higher temperatures might still be advantageous for testing during the development phase.

Another factor that may disrupt the superconducting state is the magnetic field the sample is exposed to, which will decrease the Cooper pair density, increase quasiparticle losses (as well as kinetic inductance) and induce Shubnikov vortices detrimental to microwave measurements even at field values well below the critical field* B_c. General, concrete values for B_c as a hard limit are difficult to give for thin films, as the critical field is dependent on the field direction as well as on the film thickness. For a typical Al film of ~100 nm thickness the in-plane critical field is larger than the bulk value by a factor ~10 [36, 37], but with a zero-temperature bulk value of ~10 mT [35] this still only results in values of around (10 – 100) mT at measurement conditions. When magnetic fields are not required for operation, this restriction can be addressed relatively easily by shielding the sample from external magnetic fields. On the other hand, when large fields are needed in the targeted hybrid system, one can alleviate its impact by choosing a more tolerant material; Nb has a critical field exceeding that of Al by a factor of 20 [35].

*As attested by the presence of vortices, these thin films are normally Type II superconductors (even if the bulk material is Type I), so two critical fields B_{c1} and B_{c2} exist, with superconductivity ceasing only at the larger value B_{c2}. Further complicating matters, field-focusing effects can cause vortices to enter the film at applied (average) fields far below even B_{c1}, depending on the device geometry. For the present, cursory discussion, however, we allow ourselves to glance past these complications.

One more aspect to consider in the pursuit of high-quality superconducting microwave circuits regards the coupling of a resonator to its environment, or rather the prevention of this interaction. Apart from a well-defined coupling to the input-output lines, any transfer of energy between the sample circuits and the environment is usually undesired and appears as a loss and noise channel in the experiment, with losses being the dominant consideration in the already necessary cryogenic environment. Some loss channels, like dielectric losses in the substrate, cannot be completely eliminated, though the choice of appropriate materials can greatly reduce them. The possibility of electromagnetic radiation into free space, however, is suppressed in an effective manner by enclosing the circuit in a small conductive box. The key is to choose the dimensions of the box sufficiently small for all its electromagnetic oscillation modes to be at frequencies far from the circuit resonance frequency, making radiation into the box cavity impossible.

Besides these points there exist a multitude of considerations regarding design and fabrication that apply to simple circuit-QED devices as well as to complex ones, where some trade-off between simplicity and enhanced functionality has to be contemplated. While the available options may be restricted by the intended use in a hybrid system, these aspects will greatly depend on the particulars of the specific circuit, so they need to be discussed on an individual basis. As the targeted hybrid systems of the resonators treated in this work are quite distinct, we shall postpone a detailed description of their design and fabrication as well as a more complete introduction to the corresponding chapters, only providing a concise overview here.

In Chapter 3 we examine a resonator intended for hybrid systems with optically trapped Rydberg atoms. Electronic states in cold atoms can be used as qubits with coherence times several orders of magnitudes larger than those of superconducting qubits, while the latter are superior in speed and scalability [27]. A natural combination of the two technologies is thus to use superconducting qubits for processing and trapped atoms as quantum memory; Rydberg atoms with their large electric transition dipole moments are ideal for the necessary coupling to a microwave resonator.* Besides the storage of quantum information, its transmission to a remote location is an additional challenge associated with superconducting qubits, as the microwave frequencies they operate at are not suitable for communication over long distances. Signals at the aptly named telecom wavelengths in the optical regime are much better suited for this task and so transduction of quantum information between the two regimes is being actively researched, with several approaches involving Rydberg atoms having been demonstrated [38–40].

*The long-lived electronic states desirable as quantum memory reside in the hyperfine ground state manifold, not in the Rydberg manifold. Luckily, transferring states between the two manifolds is less challenging than the resonator coupling, for which Rydberg states are a major asset [38].

For either application, cold atoms need to be trapped in close vicinity to a superconducting resonator in order to facilitate coupling between the two systems. Besides requiring an ultra-high vacuum environment with means to prepare and cool a suitable cloud of atoms, the resonator itself needs to expose an interaction region where the coupling can take place. In particular, this means that it cannot be housed in a tight metal housing as usual, but needs to provide access both for the atoms to approach and for laser beams used to manipulate and probe those atoms. The coupling scheme chosen for our experiment relies on optically trapped Rydberg atoms, taking advantage of their extremely large electric transition dipole moments to facilitate large coupling rates. Thus, the interaction region must be one where oscillations in the resonator create large electric field strengths that should at the same time be as homogeneous as possible so that all atoms in the cloud experience the same field and thus the same coupling. Naturally, for a thin-film resonator, the fields are strongest close to the chip surface, but the atoms cannot be moved arbitrarily close to it, as the focused laser beam trapping them would then strike substrate and film, with detrimental consequences for the superconducting state. A final challenge is to match the resonator frequency to a suitable Rydberg transition such that the two systems become resonant and can exchange energy, a point that is conveniently addressed by designing the resonator with the option of applying an electric dc field to the interaction region that can be used to tune the Rydberg transitions into resonance exploiting their Stark shift.

Using numerical simulations both for the Rydberg transitions and for the field distribution in the vicinity of a resonator geometry designed to provide the necessary access as well as the possibility of applying a dc voltage to its capacitance, we develop a device capable of realizing coupling rates approaching the strong coupling regime. We characterize its microwave properties in a setup suited for the envisioned hybrid experiment and discuss limitations as well as possible improvements of the design, paving the way for the achievement of strong coupling in superconductor-atom hybrid systems.

Following this, in Chapter 4, we discuss a different resonator design, one comprising magnetically induced Josephson nano-diodes, that is intended for use in large magnetic in-plane fields. The Josephson junctions form a superconducting quantum interference device (SQUID) that acts as a flux-tunable inductance forming part of the LC resonator, thus allowing its resonance frequency to be tuned. Both the SQUID and the large magnetic fields are required for an envisioned hybrid system where a micromechanical oscillator is coupled to the microwave resonator via its displacement modulating the flux coupled into the SQUID, known as an optomechanical interaction. Similar systems have been realized before [41], but have thus far been limited by their use of Al as superconductor, prohibiting the application of strong magnetic fields. In an effort to push this boundary, we investigate the use of Nb as resonator material, with a particular focus on the field-response

of nano-constriction Josephson junctions milled into the superconducting film using a focused neon-ion-beam (Ne-FIB). As before, we leave the implementation of the full hybrid system to future efforts, focusing only on the performance of the microwave resonator.

Surprisingly, we find that the magnetic field induces an asymmetry in the flux tuning behavior of the resonator, that is, the field turns the nano-constrictions into Josephson diodes. Superconducting diodes have recently generated wide-spread interest, as they promise exciting possibilities in several fields not necessarily related to hybrid systems [42]. The prospect of compact Josephson-diodes for operation in large magnetic fields is thus an exciting development in and of itself. Here, their presence in a SQUID resonator provides us with the capability to probe their current-phase relation (CPR) [43], rather than just measuring their critical current as is common in dc experiments. Given this possibility, we are able to develop a macroscopic Josephson diode model explaining the field-induced emergence of the observed asymmetry, reconstructing the field-dependent diode CPR.

We characterize several such SQIUD resonators in magnetic in-plane fields of up to 300 mT, analyzing their flux-tuning behavior and extracting their CPRs. To additionally verify the intrinsicality of the induced asymmetry to the nano-constrictions, we demonstrate that not only the resonance frequency but also the resonator Kerr anharmonicity shows a bimodal response at large fields. The chapter also includes detailed descriptions of all relevant experimental and analytical elements, including the procedure of aligning the applied field with the chip surface and a comprehensive discussion of the new Josephson diode model.

Finally, in Chapter 5 we summarize the results from the preceding chapters, briefly reflecting on potential next steps and perspectives for future research.

Before turning to these concrete circuits, however, Chapter 2 provides a short overview of the theory describing the coupling those circuit designs are destined for. The goal of this chapter is not to cover all the details involved in the specific instances discussed in the later chapters; the relevant theory for each particular case will be treated in the corresponding chapter as necessary. Rather, the intent is to remind the reader of the basics of describing coupled quantum mechanical oscillators and to point out some important concepts emerging from it.

References

[1] J. Bleck-Neuhaus, *Mechanical resonance: 300 years from discovery to the full understanding of its importance*, arXiv:1811.08353 [physics.hist-ph] (2018).

[2] C. Truesdell, *Outline of the history of flexible or elastic bodies to 1788*, The Journal of the Acoustical Society of America **32**, 1647–1656 (1960).

[3] G. Galilei, *Dialogues concerning two new sciences*, trans. from the Italian and from the Latin by H. Crew and A. de Salvio, with an intro. by A. Favaro (Macmillan, 1914), originally published as *Discorsi e dimostrazioni matematiche intorno a due nuove scienze*, (Elzevir, 1638).

[4] L. Euler, *On a new class of oscillations*, trans. from the Latin by S. R. Bistafa, Euleriana **2**, 11–26 (2022),
originally published as *De novo genere oscillationum* Commentarii academiae scientiarum Petropolitanae **11**, 128–149 (1750), written in 1739.

[5] T. Young, *A theory of the tides, including the consideration of resistance*, Journal of Natural Philosophy, Chemistry, and the Arts **35**, 145–159 (1813).

[6] T. Young, *Tides*, in *Supplement to the encyclopaedia britannica*, Vol. 6 (1824), pp. 658–675.

[7] A. Seebeck, *Ueber Schwingungen unter der Einwirkung veränderlicher Kräfte*, Annalen der Physik **138**, 289–306 (1844).

[8] F. Redtenbacher, *Die Gesetze des Lokomotiv-Baues* (Bassermann, 1855).

[9] P. Zech, *Die Schwingungsbewegungen der Lokomotiven*, in *Jahres-Bericht der Königlich Polytechnischen Schule zu Stuttgart, für das Studienjahr 1866/67* (Metzler, 1867).

[10] H. Helmholtz, *Die Lehre von den Tomepfindungen als physiologische Grundlage für die Theorie der Musik* (Vieweg, 1963).

[11] J. W. S. Baron Rayleigh, *Theory of sound*, Vol. 1 (Macmillan, 1877).

[12] A. Sommerfeld, *Beiträge zum dynamischen Ausbau der Festigkeitslehre*, Physikalische Zeitschrift **3**, 266–272, 286–291 (1902).

[13] M. Radaković, *Über die Bewegung eines Motors unter Berücksichtigung der Elastizität seines Fundamentes*,
Zeitschrift für Mathematik und Physik **48**, 28–39 (1903).

[14] W. Thomson, *On transient electric currents*, The London, Edinburgh, and Dublin Philosophical Magazine and Journal of Science **5**, 393–405 (1853).

[15] A. Oberbeck,
Ueber eine der Resonanz ähnliche Erscheinung bei electrischen Schwingungen, Annalen der Physik **262**, 245–253 (1885).

[16] H. Hertz, *Ueber sehr schnelle electrische Schwingungen*,
Annalen der Physik **267**, 421–448 (1887).

[17] M. Planck, *Über irreversible Strahlungsvorgänge*, *Fünfte Mittheilung (Schluss)*, in Sitzungsberichte der Königlich Preußischen Akademie der Wissenschaften zu Berlin (1899), pp. 440–480.

[18] M. Planck,
Zur Theorie des Gesetzes der Energieverteilung im Normalspectrum,
in Verhandlungen der Deutschen Physikalischen Gesellschaft im Jahre 1900 (1900), pp. 237–245.

[19] A. Einstein, *Über einen die Erzeugung und Verwandlung des Lichtes betreffenden heuristischen Gesichtspunkt*,
Annalen der Physik **322**, 132–148 (1905).

[20] P. Debye, *Zur Theorie der spezifischen Wärmen*,
Annalen der Physik **344**, 789–839 (1912).

[21] W. Heisenberg, *Über quantentheoretische Umdeutung kinematischer und mechanischer Beziehungen*, Zeitschrift für Physik **33**, 879–893 (1925).

[22] M. Born and P. Jordan, *Zur Quantenmechanik*,
Zeitschrift für Physik **34**, 858–888 (1925).

[23] P. A. M. Dirac,
The quantum theory of the emission and absorption of radiation,
Proceedings of the Royal Society A **114**, 243–265 (1927).

[24] V. Fock, *Konfigurationsraum und zweite Quantelung*,
Zeitschrift für Physik **75**, 622–647 (1932).

[25] The Nobel Committee for Physics, *Scientific background to the Nobel prize in physics 2025, for the discovery of macroscopic quantum mechanical tunnelling and energy quantisation in an electric circuit*, (2025)
https://www.nobelprize.org/prizes/physics/2025/advanced-information/.

[26] A. Blais, A. L. Grimsmo, S. M. Girvin, and A. Wallraff,
Circuit quantum electrodynamics,
Reviews of Modern Physics **93**, 025005 (2021).

[27] Z.-L. Xiang, S. Ashhab, J. Q. You, and F. Nori, *Hybrid quantum circuits: Superconducting circuits interacting with other quantum systems*,
Reviews of Modern Physics **85**, 623–653 (2013).

[28] G. Kurizki, P. Bertet, Y. Kubo, K. Mølmer, D. Petrosyan, P. Rabl, and J. Schmiedmayer, *Quantum technologies with hybrid systems*,
Proceedings of the National Academy of Sciences **112**, 3866–3873 (2015).

[29] A. A. Clerk, K. W. Lehnert, P. Bertet, J. R. Petta, and Y. Nakamura,
Hybrid quantum systems with circuit quantum electrodynamics,
Nature Physics **16**, 257–267 (2020).

[30] M. Kazouini, J. Peter, Z. E. Guo, B. Wilde, K. Uhl, D. Koelle, R. Kleiner, and D. Bothner, *Tunable and nonlinearity-enhanced dispersive-plus-dissipative coupling in photon-pressure circuits*, arXiv:2511.22571 [quant-ph] (2025).

[31] H. J. Kimble, *Strong interactions of single atoms and photons in cavity QED*, Physica Scripta **1998**, 127–137 (1998).

[32] M. Aspelmeyer, T. J. Kippenberg, and F. Marquardt, *Cavity optomechanics*, Reviews of Modern Physics **86**, 1391–1452 (2014).

[33] S. Haroche, *Nobel lecture: Controlling photons in a box and exploring the quantum to classical boundary*, Reviews of Modern Physics **85**, 1083–1102 (2013).

[34] D. J. Wineland, *Nobel lecture: Superposition, entanglement, and raising Schrödinger's cat*, Reviews of Modern Physics **85**, 1103–1114 (2013).

[35] R. Kleiner and D. Koelle, *Basic properties of superconductivity*, in *The SQUID handbook, Fundamentals and technology of SQUIDs and SQUID systems*, Vol. 1, edited by J. Clarke and A. I. Braginski (Wiley VCH, 2004) Appendix 1, pp. 357–366.

[36] A. M. Toxen, *Critical fields of thin superconducting films. I. Thickness effects*, Physical Review **127**, 382–386 (1962).

[37] R. Meservey and P. M. Tedrow, *Properties of very thin aluminum films*, Journal of Applied Physics **42**, 51–53 (1971).

[38] N. Lauk, N. Sinclair, S. Barzanjeh, J. P. Covey, M. Saffman, M. Spiropulu, and C. Simon, *Perspectives on quantum transduction*, Quantum Science and Technology **5**, 020501 (2020).

[39] N. J. Lambert, A. Rueda, F. Sedlmeir, and H. G. L. Schwefel, *Coherent conversion between microwave and optical photons—An overview of physical implementations*, Advanced Quantum Technologies **3**, 1900077 (2020).

[40] A. Kumar, A. Suleymanzade, M. Stone, L. Taneja, A. Anferov, D. I. Schuster, and J. Simon, *Quantum-enabled millimetre wave to optical transduction using neutral atoms*, Nature **615**, 614–619 (2023).

[41] I. C. Rodrigues, D. Bothner, and G. A. Steele, *Coupling microwave photons to a mechanical resonator using quantum interference*, Nature Communications **10**, 5359 (2019).

[42] M. Nadeem, M. S. Fuhrer, and X. Wang, *The superconducting diode effect*, Nature Reviews Physics **5**, 558–577 (2023).

[43] K. Uhl, D. Hackenbeck, D. Koelle, R. Kleiner, and D. Bothner, *Extracting the current-phase relation of a monolithic three-dimensional nanoconstriction using a dc-current-tunable superconducting microwave cavity*, Physical Review Applied **22**, 064052 (2024).

2 Fundamentals of coupled resonators

Before delving into the details of concrete circuits for hybrid quantum systems, let us recapitulate the basics of how such systems are described theoretically. We will not go into an exhaustive description of everything one might want to consider, but rather give a concise overview of relevant concepts and approaches related to the systems discussed in the following chapters. While the basic theory treated in the initial sections can be found in any textbook on quantum mechanics, no standard reference covering all of the formalism and couplings discussed toward the end of the chapter exists. The interested reader may turn to a number of excellent recent review articles covering the subject matter for further details [1–6].

2.1 The harmonic oscillator

The quantum mechanical harmonic oscillator is most conveniently described using ladder operators, i.e. using a Hamiltonian of the form

$$H = \hbar\omega_a \left(a^\dagger a + \frac{1}{2}\right) \tag{2.1}$$

with the resonance frequency ω_a, the creation operator $a^\dagger$ and the annihilation operator a, which obey the commutation relation

$$[a, a^\dagger] = 1. \tag{2.2}$$

The energy eigenstates $|n\rangle$ of the Hamiltonian with $n \in \mathbb{N}$, when operated on by the ladder operators, obey

$$a\,|n\rangle = \sqrt{n}\,|n-1\rangle \tag{2.3}$$

$$a^\dagger|n\rangle = \sqrt{n+1}\,|n+1\rangle \tag{2.4}$$

$$a^\dagger a\,|n\rangle = n\,|n\rangle. \tag{2.5}$$

We call $|0\rangle$ the ground state, or vacuum state, of the resonator and can obtain all other eigenstates by repeated application of the ladder operators, saying that $a^\dagger$ adds one excitation to the resonator and a removes one. The eigenstates are thus characterized only by the number of excitations in the resonator, which is why they are also called number states and $a^\dagger a$ is called the number operator. From the equations above we easily obtain the commutation relations

$$a^\dagger a\, a = a\,(a^\dagger a - 1) \qquad [a^\dagger a, a] = -a \tag{2.6}$$

$$a^\dagger a\, a^\dagger = a^\dagger(a^\dagger a + 1) \qquad [a^\dagger a, a^\dagger] = a^\dagger. \tag{2.7}$$

The ground state energy $\hbar\omega_a/2$ does not contribute to the dynamics of the system, which is why the corresponding term in the Hamiltonian is often omitted, a practice that we shall also employ from here on.

2.2 Two-level systems

The simplest non-trivial quantum system is one having only two energy eigenstates, a ground state $|0\rangle$ and an excited state $|1\rangle$. Such systems are of particular interest as atoms of quantum information, analogously to the bit in classical information technology, and are called qubits in this context. We can describe the two involved states like the first two number states of a harmonic oscillator, i.e. using the same formalism as before but truncating the Fock space, removing states with more than one excitation. To that end, we replace $a^\dagger$ with the raising operator $\sigma^+ = |1\rangle\langle 0|$ and a with the lowering operator $\sigma^- = |0\rangle\langle 1|$ that obey

$$\sigma^+|0\rangle = |1\rangle \qquad \sigma^+|1\rangle = 0 \tag{2.8}$$

$$\sigma^-|0\rangle = 0 \qquad \sigma^-|1\rangle = |0\rangle. \tag{2.9}$$

Any result obtained for harmonic oscillators can easily be applied to two-level systems by performing this substitution, keeping the truncated state space in mind. Thus, we will constrain our description in the following sections to coupled harmonic oscillators and refrain from repeatedly noting the parallel results for two-level systems explicitly.

In practice, a true two-level system is often not necessary, as any two states from a more complex quantum system can act as an approximate two-level system as long as interaction with other states is sufficiently suppressed – though realistically corrections for the impact of those states are often necessary. On one hand, this requires decays to potentially present lower-energy states to be weak enough that they occur much slower than the total duration of the target experiment. On the other hand, transitions to all other states must be detuned from the target transition; unlike in the harmonic oscillator, where all states are equidistant in energy. In fact, one way to realize a qubit is to explicitly implement this condition by modifying a superconducting LC circuit (i.e. a harmonic oscillator) via the introduction of a nonlinear inductance – thus making it anharmonic and detuning its energy transitions – and to then use the lowest two resulting states as qubit-states.

2.3 A note on conventions and notation

Calculating the Heisenberg equation of motion for the harmonic oscillator from its Hamiltonian (2.1) we find

$$\dot{a} = \mathrm{i}[H/\hbar, a] = -\mathrm{i}\omega_a a, \tag{2.10}$$

which, given some initial value a_0, is easily solved by

$$a = \mathrm{e}^{-\mathrm{i}\omega_a t}\, a_0. \tag{2.11}$$

While perfectly reasonable in principle, the sign in the exponent (and thus in the derivative) is at odds with conventions from classical theory, making an identification of the operator a with classical quantities less convenient. One option for restoring the correspondence would be to instead consider the equation of motion for $a^\dagger$, which does have the desired sign. However, this is not a common approach in the literature and what is instead done sometimes is that the sign is simply dropped. While this breaks the correspondence of the equation of motion with the Hamiltonian, it does not change the predicted system dynamics at all, yielding identical results except for the rotation orientation of all solutions. In this chapter, we will consistently follow the usual definition of the Heisenberg picture, keeping the sign in the equations above. We mention the fact as an aid for reconciling differing signs when comparing the expressions with equivalent ones elsewhere, e.g. in later chapters, most notably in Section 4.15 where we use classical fields rather than quantum mechanical operators.

A related convention regards the sign of the exponential in the Fourier transform, which is usually negative when transforming from time to frequency domain and

positive when transforming back. In order not to have to refer to a in (2.11) as having negative frequency, we invert that convention for this chapter, writing

$$\hat{a}(\omega) = \frac{1}{\sqrt{2\pi}} \int_{\mathbb{R}} \mathrm{e}^{\mathrm{i}\omega t}\, a(t)\, \mathrm{d}t \tag{2.12}$$

for the Fourier transform $\hat{a}$ of a. Note that this implies that the Fourier transform of $\dot{a}(t)$ is $-\mathrm{i}\omega\hat{a}(\omega)$, with an additional sign compared to the usual convention, which is precisely what we want here.

We emphasize that the accent on $\hat{a}$ denotes that the object was Fourier transformed to frequency space, not that it is an operator, as is often done in the context of quantum mechanics.

2.4 Resonators in direct contact

In general, the Hamiltonian describing two coupled resonators takes the form

$$H = H_0 + H_{\mathrm{int}} \tag{2.13}$$

where H_0 describes the two independent harmonic oscillators

$$H_0/\hbar = \omega_a a^\dagger a + \omega_b b^\dagger b \tag{2.14}$$

and H_{int} describes their interaction. The simplest form this interaction can take is that of coherent transfer of excitations between the two resonators

$$H_{\mathrm{int}}/\hbar = g\,(ab^\dagger + a^\dagger b), \tag{2.15}$$

where g is a frequency quantifying the coupling strength. This is known as a *beam-splitter interaction* in the quantum optical domain.

At resonance $\omega_a = \omega_b =: \omega_0$, we can diagonalize this Hamiltonian by introducing the normal mode operators $c_+ = (a+b)/\sqrt{2}$ and $c_- = (a-b)/\sqrt{2}$, resulting in

$$H = (\omega_0 + g)\, c_+^\dagger c_+ + (\omega_0 - g)\, c_-^\dagger c_-. \tag{2.16}$$

It is easily verified that $c_\pm$ and $c_\pm^\dagger$ fulfill the commutation relations of two independent harmonic oscillators, i.e. the modes hybridize and behave like two un-coupled resonators with frequencies $\omega_0 \pm g$. Using the hybridized modes, we obtain the Heisenberg time evolution

$$c_+(t) = \mathrm{e}^{-\mathrm{i}(\omega_0+g)t}\, c_+(0) \qquad c_-(t) = \mathrm{e}^{-\mathrm{i}(\omega_0-g)t}\, c_-(0) \tag{2.17}$$

and from this the solutions for the original operators

$$a(t) = \frac{1}{\sqrt{2}}\left(c_+(t) + c_-(t)\right) = \mathrm{e}^{-\mathrm{i}\omega_0 t}\left(\cos(gt)\, a(0) - \mathrm{i}\sin(gt)\, b(0)\right) \tag{2.18}$$

$$b(t) = \frac{1}{\sqrt{2}}\left(c_+(t) - c_-(t)\right) = \mathrm{e}^{-\mathrm{i}\omega_0 t}\left(\cos(gt)\, b(0) - \mathrm{i}\sin(gt)\, a(0)\right) \tag{2.19}$$

revealing the well-known Rabi oscillations of excitation amplitude between the two resonators, moving from one to the other and back again at the frequency $2g$.

2.5 Coupling to the environment

Up to now, we have not considered any loss mechanisms or input channels adding excitations to the resonators, finding that any energy in the system stays there indefinitely. In reality, any resonator experiences some losses and we require input and output channels to access the resonator experimentally. Both of these mechanisms can be summarized as interaction with the environment and are modeled as a bath of harmonic oscillators coupled to the system as described in the previous section. Let us consider the simple case of a single harmonic oscillator coupled to the environment

$$H/\hbar = \omega_a a^\dagger a + H_{\mathrm{bath}}/\hbar. \tag{2.20}$$

The bath Hamiltonian H_{bath} takes the shape of an infinite collection of harmonic oscillators, either as a discrete sum or, as we do here, as an integral

$$H_{\mathrm{bath}}/\hbar = \int_{\mathbb{R}} \omega\, q^\dagger(\omega) q(\omega) + \mathrm{i}\sqrt{\kappa/2\pi}\left(a q^\dagger(\omega) - a^\dagger q(\omega)\right) \mathrm{d}\omega \tag{2.21}$$

where κ is the coupling strength and $q(\omega)$ and $q^\dagger(\omega)$ follow the continuous version of the usual commutation relation

$$\left[q(\omega), q^\dagger(\omega')\right] = \delta(\omega - \omega'). \tag{2.22}$$

Note that we assume κ to be constant over the relevant frequency range here, which is usually a good approximation.

In order to better understand the effect of this coupling, let us calculate the Heisenberg equations of motion and follow the calculations from [7]

$$\dot{a} = -\mathrm{i}\omega_a a - \sqrt{\frac{\kappa}{2\pi}} \int_{\mathbb{R}} q(\omega)\, \mathrm{d}\omega \tag{2.23}$$

$$\dot{q}(\omega) = -\mathrm{i}\omega q(\omega) + \sqrt{\frac{\kappa}{2\pi}}\, a. \tag{2.24}$$

The second equation is solved by

$$q(\omega) = \mathrm{e}^{-\mathrm{i}\omega(t-t_0)}\, q_0(\omega) + \sqrt{\frac{\kappa}{2\pi}} \int_{t_0}^{t} \mathrm{e}^{-\mathrm{i}\omega(t-t')}\, a(t')\, \mathrm{d}t' \tag{2.25}$$

where $q_0(\omega)$ is the value of $q(\omega)$ at $t = t_0$. Plugging this into (2.23) we obtain

$$\dot{a} = -\mathrm{i}\omega_a a - \sqrt{\frac{\kappa}{2\pi}} \int_{\mathbb{R}} \left(\mathrm{e}^{-\mathrm{i}\omega(t-t_0)}\, q_0(\omega) + \sqrt{\frac{\kappa}{2\pi}} \int_{t_0}^{t} \mathrm{e}^{-\mathrm{i}\omega(t-t')}\, a(t')\, \mathrm{d}t' \right) \mathrm{d}\omega. \tag{2.26}$$

Next, we note

$$\int_{\mathbb{R}} \mathrm{e}^{-\mathrm{i}\omega(t-t')}\, \mathrm{d}\omega = 2\pi\, \delta(t-t') \tag{2.27}$$

$$\int_{t_0}^{t} a(t')\, \delta(t-t')\, \mathrm{d}t' = \frac{a(t)}{2} \tag{2.28}$$

and we define the input field operator a_{in} as the (inverse) Fourier transform of $q_0(\omega)$

$$\mathrm{i}a_{\mathrm{in}} = \frac{1}{\sqrt{2\pi}} \int_{\mathbb{R}} \mathrm{e}^{-\mathrm{i}\omega(t-t_0)} q_0(\omega)\, \mathrm{d}\omega, \tag{2.29}$$

which follows the usual commutation relation $[a_{\mathrm{in}}, a_{\mathrm{in}}^\dagger] = 1$. For the motivation behind the i on the left-hand side, see the end of this section. With all this, we finally find the so-called quantum Langevin equation

$$\dot{a} = -\mathrm{i}\omega_a a - \mathrm{i}\sqrt{\kappa}\, a_{\mathrm{in}} - \frac{\kappa}{2}\, a. \tag{2.30}$$

This form is the common starting point for analysis using the input-output formalism described in the next section.

As we already alluded to above, we can separate the resonator losses into purposefully designed interactions with some input-output channel, termed *external* losses, and the remaining, often undesirable interactions, termed *internal* losses. Formally, we model this using two separate bath Hamiltonians with separate loss rates κ_{ext} and κ_{int}

$$\dot{a} = -(\mathrm{i}\omega_a + \kappa/2)\, a - \mathrm{i}\sqrt{\kappa_{\mathrm{int}}}\, a_{\mathrm{int,in}} - \mathrm{i}\sqrt{\kappa_{\mathrm{ext}}}\, a_{\mathrm{ext,in}}, \tag{2.31}$$

where κ is now the total loss rate $\kappa = \kappa_{\mathrm{int}} + \kappa_{\mathrm{ext}}$.

In the presence of a strong input tone, the noise input terms do not contribute relevantly to the dynamics and can be dropped, i.e. we can use $a_{\mathrm{int,in}} = 0$ and have $a_{\mathrm{ext,in}} =: a_{\mathrm{in}}$ represent just the coherent input drive

$$\dot{a} = -(\mathrm{i}\omega_a + \kappa/2)\, a - \mathrm{i}\sqrt{\kappa_{\mathrm{ext}}}\, a_{\mathrm{in}}. \tag{2.32}$$

Note that introducing the i in the definition of a_{in} (2.29) is somewhat arbitrary and not at all universal in the literature. Arguably, it is rather unnecessary, but it makes (2.32) and similar equations of motion somewhat more intuitive, as all driving components feature a $-\mathrm{i}$ while the damping rate $\kappa/2$ does not. We will see in Section 2.8 that a coupled resonator results in a similar driving term with an imaginary coefficient. We follow this convention mostly for consistency with other publications from our group (cf. theory sections in the following chapters).

2.6 Input-output theory

The so-called input-output theory is a formalism useful for analyzing the frequency response predicted by a quantum system Hamiltonian, as it relates the expected output field to the input field and the solution of the Langevin equation*

$$a_{\text{out}} = a_{\text{in}} - \mathrm{i}\sqrt{\kappa_{\text{ext}}}\, a. \tag{2.33}$$

Experimentally, microwave circuits are commonly characterized using a vector network analyzer (VNA) that scans the frequency response by inputting a probe tone $a_{\text{in}} = \alpha_{\text{s}} \exp(-\mathrm{i}\omega_{\text{s}} t)$ with some frequency ω_{s} and amplitude α_{s} into the input line, detecting the output signal returned from the device at the same frequency ω_{s} and outputting the complex ratio S_{11} of the two. According to (2.33), the result is

$$S_{11}(\omega_{\text{s}}) = \frac{\langle \hat{a}_{\text{out}}(\omega_{\text{s}}) \rangle}{\langle \hat{a}_{\text{in}}(\omega_{\text{s}}) \rangle} = 1 - \mathrm{i}\sqrt{\kappa_{\text{ext}}}\, \frac{\langle \hat{a}(\omega_{\text{s}}) \rangle}{\langle \hat{a}_{\text{in}}(\omega_{\text{s}}) \rangle}. \tag{2.34}$$

Let us examine this using the example of a simple harmonic oscillator as described by (2.32). After a Fourier transform we find

$$\hat{a} = \frac{\mathrm{i}\sqrt{\kappa_{\text{ext}}}}{\mathrm{i}(\omega - \omega_a) - \kappa/2}\, \hat{a}_{\text{in}} = \mathrm{i}\sqrt{\kappa_{\text{ext}}}\, \chi_{\text{s}}\, \hat{a}_{\text{in}} \tag{2.35}$$

where we introduced the susceptibility

$$\chi_{\text{s}} = \frac{1}{\mathrm{i}(\omega - \omega_a) - \kappa/2}. \tag{2.36}$$

The reflection coefficient is now given by

$$S_{11}(\omega_{\text{s}}) = 1 + \kappa_{\text{ext}} \chi_{\text{s}}(\omega_{\text{s}}), \tag{2.37}$$

*Note that the $-\mathrm{i}$ here is a consequence of introducing the i in the definition of a_{in} (2.29).

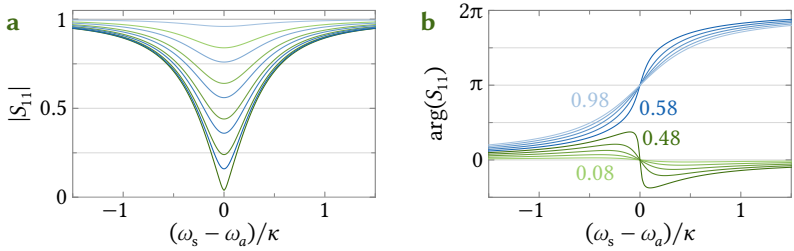

Figure 2.1: Reflection response of a simple harmonic oscillator. We show both **a** the magnitude and **b** the phase of the reflection coefficient S_{11} given by (2.37) with respect to the probe detuning $\omega_s - \omega_a$ normalized to the linewidth κ. Colors indicate different external linewidths $\kappa_{ext}/\kappa \in \{0.08, 0.18, 0.28, 0.38, 0.48, 0.58, 0.68, 0.78, 0.88, 0.98\}$ (light green to light blue) with green lines corresponding to an undercoupled ($\kappa_{ext} < \kappa/2$) and blue lines corresponding to an overcoupled resonator ($\kappa_{ext} > \kappa/2$); labels in the phase plot denote the κ_{ext}/κ values for some lines.

showing the familiar Lorentzian profile, which is depicted in Figure 2.1 for a selection of external linewidths. We also obtain the explicit solution for the stationary resonator field in the presence of the scanning tone

$$a(t) = \mathrm{i}\sqrt{\kappa_{ext}}\,\chi_s(\omega_s)\,\alpha_s \mathrm{e}^{-\mathrm{i}\omega_s t}, \tag{2.38}$$

though that is of less interest in the context of microwave measurements.

2.7 Single-port vs two-port coupling

It is important to note that some details of the expressions (2.32) and (2.33) forming the starting point of the input-output formalism depend on how exactly the coupling to the input-output signal lines is implemented. In the previous sections we implicitly assumed a reflection-type measurement of a resonator coupled to the end of a single input-output transmission line, where all of the energy leaving the resonator via the κ_{ext}-coupling goes towards the VNA. A second common configuration is that of a circuit side-coupled to a transmission line, for which the transmission spectrum S_{21} is measured. In this case the resonator couples equally to either propagation direction of the adjacent transmission line, both of which act as a loss channel while only one of them acts as an input port and the other as an output port; thus the only necessary modification to the Langevin equation (2.32) and the input-output relation (2.33) is to replace κ_{ext} with $\kappa_{ext}/2$. Note that the term with $\kappa = \kappa_{int} + \kappa_{ext}$ characterizing the total losses remains unchanged.

We will see this difference in the following chapters: In Chapter 3 we have an end-coupled resonator, and accordingly (3.32) on page 68 gives an expression

for S_{11} that is equivalent* to (2.37). By contrast, Chapter 4 explores a side-coupled resonator design, and thus (4.15) on page 105 gives an S_{21}-expression which differs from the former by the κ_{ext}-contribution being only half as large.

2.8 Probe response of resonators in direct contact

Let us consider the case of two harmonic oscillators in direct contact introduced in Section 2.4 once more, this time including the environment and analyzing the system using input-output theory. The full Hamiltonian is

$$H/\hbar = \omega_a a^\dagger a + \omega_b b^\dagger b + g\,(ab^\dagger + a^\dagger b) + H_{\text{bath}}/\hbar, \tag{2.39}$$

where H_{bath} contains terms modeling the coupling of both resonators to the environment as outlined in Section 2.5. We imagine a system where only resonator a has an input-output line and is probed using a VNA, i.e. $\kappa_{b,\text{ext}} = 0$. For brevity, we write $\kappa_{\text{ext}} := \kappa_{a,\text{ext}}$. This results in the coupled equations of motion

$$\dot{a} = -(\mathrm{i}\omega_a + \kappa_a/2)\,a - \mathrm{i}g b - \mathrm{i}\sqrt{\kappa_{\text{ext}}}\,a_{\text{in}} \tag{2.40}$$

$$\dot{b} = -(\mathrm{i}\omega_b + \kappa_b/2)\,b - \mathrm{i}g a. \tag{2.41}$$

The second equation can easily be solved by Fourier transform, yielding

$$\hat{b} = \frac{\mathrm{i}g}{\mathrm{i}(\omega - \omega_b) - \kappa_b/2}\,\hat{a} = \mathrm{i}g\chi_b\hat{a}, \tag{2.42}$$

where we introduced

$$\chi_b = \frac{1}{\mathrm{i}(\omega - \omega_b) - \kappa_b/2}. \tag{2.43}$$

Plugging this result into the Fourier transform of (2.40) we find

$$\hat{a} = \frac{\mathrm{i}\sqrt{\kappa_{\text{ext}}}}{\mathrm{i}(\omega - \omega_a) - \kappa_a/2 + g^2\chi_b}\,\hat{a}_{\text{in}} = \mathrm{i}\sqrt{\kappa_{\text{ext}}}\,\chi_{\text{s}}\hat{a}_{\text{in}} \tag{2.44}$$

with the probe susceptibility

$$\chi_{\text{s}} = \frac{1}{\mathrm{i}(\omega - \omega_a) - \kappa_a/2 + g^2\chi_b}. \tag{2.45}$$

Thus, the probe response $S_{11} = 1 + \kappa_{\text{ext}}\chi_{\text{s}}$ takes the usual Lorentzian shape (2.37) of a single harmonic resonator when the coupling g is small, but is modified near ω_b when the coupling is not negligible.

*As noted in Section 2.3, the frequencies in the equations of motion carry opposite signs in later chapters, which is also reflected in these expressions.

2.9 The cooperativity of coupled resonators

We can interpret the effective susceptibility (2.45) of the coupled resonators as resonator b shifting the resonance frequency and the linewidth of resonator a by comparing it with the expression (2.36) for an individual resonator. That is, the coupled system reacts to the probe tone just like a simple resonator with resonance frequency $\omega_a + \Delta\omega_a$ and linewidth $\kappa_a + \Delta\kappa_a$, where the frequency dependent shifts are given by

$$\Delta\omega_a(\omega) = -\operatorname{Im}(g^2\chi_b) = \frac{g^2(\omega-\omega_b)}{(\omega-\omega_b)^2+\kappa_b^2/4} \tag{2.46}$$

$$\Delta\kappa_a(\omega) = -2\operatorname{Re}(g^2\chi_b) = \frac{g^2\kappa_b}{(\omega-\omega_b)^2+\kappa_b^2/4}. \tag{2.47}$$

This perspective is particularly useful when the coupled resonator has a much larger linewidth than the probed one $\kappa_b \gg \kappa_a$, since the impact $g^2\chi_b$ of the coupled resonator on the probe response will then vary very little over the range of the probed resonance. Thus, the apparent shifts of resonance frequency and linewidth can be well approximated by their values at ω_a, i.e. we can use the probe-frequency-independent values $\Delta\omega_a \approx \Delta\omega_a(\omega_a)$ and $\Delta\kappa_a \approx \Delta\kappa_a(\omega_a)$. Some exemplary resonance spectra illustrating these points are presented in Figure 2.2.

In order to quantify the strength of the interaction, the maxima of these shifts relative to the un-shifted linewidth are useful quantities. For $\Delta\kappa_a$, this maximum is reached when the two oscillators are resonant $\omega_a = \omega_b$, whereas $\Delta\omega_a$ is largest when they are detuned by half the linewidth of the coupled resonator $\omega_a = \omega_b \pm \kappa_b/2$. The corresponding maximum shifts are

$$\Delta\kappa_a^{\max} = \frac{4g^2}{\kappa_b} = \mathcal{C}\kappa_a \tag{2.48}$$

$$\Delta\omega_a^{\max} = \pm\frac{g^2}{\kappa_b} = \pm\mathcal{C}\kappa_a/4 \tag{2.49}$$

where we introduced the cooperativity

$$\mathcal{C} = \frac{4g^2}{\kappa_a\kappa_b} \tag{2.50}$$

as a measure for the coupling. A large cooperativity $\mathcal{C} \gg 1$ indicates that excitations in resonator a decay primarily into resonator b, rather than through channels intrinsic to resonator a.

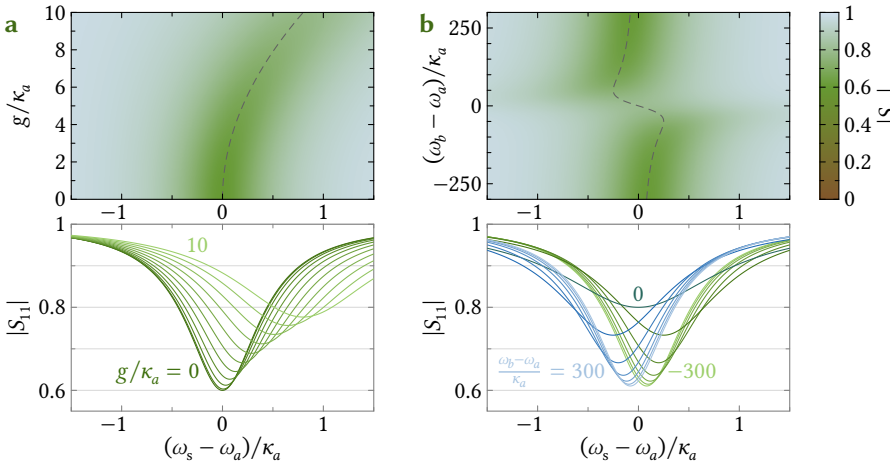

Figure 2.2: A coupled resonator shifts and broadens the resonance response. We show exemplary $|S_{11}|$-spectra for a resonator a coupled to a second resonator b with a much larger linewidth $\kappa_b/\kappa_a = 100$ for different **a** coupling rates g (with $(\omega_b-\omega_a)/\kappa_a = -100$) and **b** resonance frequency detunings $\omega_b-\omega_a$ (with $g/\kappa_a = 5$, corresponding to unit cooperativity $\mathcal{C} = 1$). The lines in the bottom plots correspond to horizontal cuts through the top plots at the tick positions; for reference some lines are labeled with the appropriate value. Dashed gray lines in the top plots mark the apparent resonance frequency shift $\Delta\omega_a(\omega_a)/\kappa_a$ as given by (2.46). All plots are for an undercoupled input-output line $\kappa_{ext}/\kappa_a = 0.2$. Note that frequency splitting would require a considerably larger $g/\kappa_a > 25$ than shown here, and strong coupling a still larger $g/\kappa_a > 50$, cf. Section 2.10.

2.10 The strong coupling regime

The case where the two coupled oscillators are resonant $\omega_a = \omega_b$ is of particular relevance. In this scenario, we can write $\Delta := \omega - \omega_a = \omega - \omega_b$ for the probe tone detuning from the common resonance frequency and find the resonance condition for the coupled system by setting the denominator in (2.45) equal to 0, obtaining

$$\Delta^{\pm} = -\mathrm{i}\,\frac{\kappa_a+\kappa_b}{4} \pm \sqrt{g^2 - \left(\frac{\kappa_a-\kappa_b}{4}\right)^2}. \tag{2.51}$$

In analogy with the simple harmonic oscillator (2.36), the real part of each complex solution $\Delta^{\pm}$ represents its resonance frequency while the imaginary part represents half its negative decay rate. Thus, (2.51) reveals that the coupled resonators hybridize, forming two normal modes. For weak coupling, they differ in linewidth while showing the same resonance frequency $\Delta = 0$ as the individual resonators, whereas for sufficiently large coupling rates $|g| > |\kappa_a - \kappa_b|/4$, they are

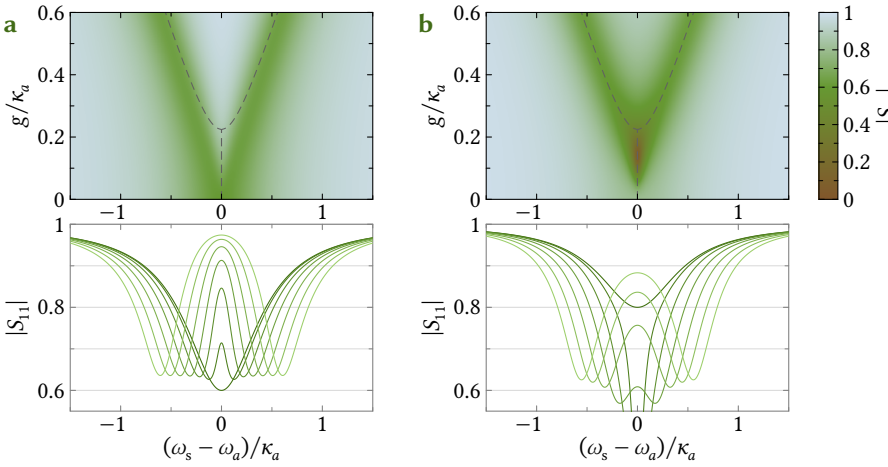

Figure 2.3: Two resonantly coupled resonators form hybridized modes. We show exemplary $|S_{11}|$-spectra for **a** an undercoupled ($\kappa_{ext}/\kappa_a = 0.2$) as well as **b** an overcoupled ($\kappa_{ext}/\kappa_a = 0.9$) resonator a that is resonantly coupled to a second resonator b ($\omega_b = \omega_a$) for different coupling strengths g. The lines in the bottom plots correspond to horizontal cuts through the top plots at the tick positions; from $g/\kappa_a = 0$ for the darkest to $g/\kappa_a = 0.6$ for the lightest line. Dashed gray lines in the top plots mark the normal mode frequencies as given by (2.51). We use $\kappa_b/\kappa_a = 0.1$ for all plots, so a g/κ_a value of 0.16 is needed for unit cooperativity, at least 0.23 for normal mode frequency splitting, 0.36 for its resolvability and 0.55 for strong coupling.

located on either side of the individual resonance frequency, each with an identical linewidth $(\kappa_a + \kappa_b)/2$. Deep in the split-frequency regime $|g| \gg |\kappa_a - \kappa_b|/4$, the two normal mode resonance frequencies are separated by the Rabi frequency $2g$, but for weaker coupling rates $|g| \gtrsim |\kappa_a - \kappa_b|/4$, they may not be resolvable in the S_{11} spectrum. As a rule of thumb, two modes are considered to be resolvable when their separation is larger than their linewidths, and demanding this for the normal modes $|\mathrm{Re}(\Delta^\pm)| > |\mathrm{Im}(\Delta^\pm)|$ yields

$$|2g| > \sqrt{\frac{\kappa_a^2 + \kappa_b^2}{2}} \tag{2.52}$$

as a condition for normal mode resolvability. Some exemplary resonance spectra illustrating the normal mode splitting are presented in Figure 2.3.

Now, the *strong coupling regime* refers to coupling rates that are large enough to overwhelm dissipative effects, meaning that the Rabi frequency is larger than the total decay rate

$$|2g| > \kappa_a + \kappa_b. \tag{2.53}$$

Naturally, this threshold is not a sharp one and often the somewhat simpler condition $|2g| > \kappa_a, \kappa_b$ or the stricter $|g| > \kappa_a, \kappa_b$ are stated. The importance of the strong coupling regime derives from the fact that only here coherent state transfer between two resonators is possible, as this requires the transfer of states to be performed more quickly than their decay. This is an essential prerequisite for applications relying on the control of individual quanta, such as quantum computing and quantum sensing. Accordingly, much of the work in the development of hybrid systems, including this one, is focused on reaching the strong coupling regime.

Note that $p + q > \max(p, q) \geq \sqrt{(p^2 + q^2)/2} \geq \sqrt{pq}$ for any two positive real numbers p, q (with the equalities holding for $p = q$). Thus, strong coupling always implies resolvable normal mode splitting on resonance, which in turn is a stricter condition than a large cooperativity $\mathcal{C} > 1$, especially so when the coupled resonators differ greatly in linewidth.

2.11 The rotating frame approximation

One common type of coupling is one that is proportional to the displacement operators $x_a = a + a^\dagger$ and $x_b = b + b^\dagger$ of the coupled resonators

$$H_{\text{int}}/\hbar = g x_a x_b = g(a + a^\dagger)(b + b^\dagger), \tag{2.54}$$

sometimes called dipole coupling. To better understand which of the four coupling terms dominate the system dynamics, it is useful to perform a transformation into the interaction picture

$$\begin{aligned} \tilde{H}_{\text{int}}/\hbar &= \mathrm{e}^{\mathrm{i}H_0 t/\hbar} \cdot H_{\text{int}}/\hbar \cdot \mathrm{e}^{-\mathrm{i}H_0 t/\hbar} \\ &= g\left(\mathrm{e}^{-\mathrm{i}(\omega_a+\omega_b)t}\, ab + \mathrm{e}^{\mathrm{i}(\omega_b-\omega_a)t}\, ab^\dagger + \mathrm{e}^{-\mathrm{i}(\omega_b-\omega_a)t}\, a^\dagger b + \mathrm{e}^{\mathrm{i}(\omega_a+\omega_b)t}\, a^\dagger b^\dagger\right). \end{aligned} \tag{2.55}$$

In the usual case of the two resonance frequencies being close $|\omega_b - \omega_a| \ll \omega_a + \omega_b$, we may neglect the quickly rotating first and last terms, as their contribution will average out over any relevant time, and keep only the mixed terms*

$$\tilde{H}_{\text{int}}/\hbar \approx g\left(\mathrm{e}^{\mathrm{i}(\omega_b-\omega_a)t}\, ab^\dagger + \mathrm{e}^{-\mathrm{i}(\omega_b-\omega_a)t}\, a^\dagger b\right), \tag{2.56}$$

which is known as the *rotating frame approximation*. Transformed back from the interaction picture, we have

$$H_{\text{int}}/\hbar \approx g\,(ab^\dagger + a^\dagger b), \tag{2.57}$$

*This approximation also requires $g \ll \omega_a, \omega_b$; the converse case is known as the *ultra-strong coupling regime*. However, as this work focuses on efforts aimed at reaching the much weaker strong coupling regime, we can safely ignore this extreme case and assume the rotating wave approximation to hold.

obtaining the familiar expression (2.15) of the interaction Hamiltonian for directly coupled resonators. When one of the resonators is replaced by a two-level system, this corresponds to the interaction of an atom (or a qubit) with an optical cavity, leading to the *Jaynes–Cummings model*.

2.12 The optomechanical coupling

In an optomechanical system, the resonators are typically coupled in such a way that the resonance frequency ω_a of the optical cavity depends on the position x_b of the mechanical cavity, which is oscillating at a much slower rate $\omega_b \ll \omega_a$,

$$\omega_a(x_b) = \omega_a(0) + \frac{\partial \omega_a}{\partial x_b}\, x_b + \mathcal{O}(x_b^2). \tag{2.58}$$

Usually, considering this first order dependence is sufficient. The displacement of the mechanical resonator can be written as

$$x_b = x_b^{\mathrm{zpf}}\,(b + b^\dagger) \tag{2.59}$$

with the zero-point fluctuation x_b^{zpf} of the resonator position. Introducing the singe-photon coupling strength

$$g_0 = -\frac{\partial \omega_a}{\partial x_b}\, x_b^{\mathrm{zpf}} \tag{2.60}$$

and writing $\omega_a := \omega_a(0)$ for brevity, we obtain the optomechanical Hamiltonian

$$H/\hbar = \omega_a(x_b)\, a^\dagger a + \omega_b b^\dagger b = \omega_a a^\dagger a + \omega_b b^\dagger b - g_0\, a^\dagger a\,(b + b^\dagger). \tag{2.61}$$

The negative sign of the coupling term is chosen because in the canonical case of a Fabry–Perot optical cavity with one of its mirrors acting as the mechanical resonator, a positive displacement of the mirror (i.e. an increase of the cavity length) leads to a decreased resonance frequency, i.e. $\partial\omega_a/\partial x_b < 0$ and thus $g_0 > 0$ with this definition.

We note that this interaction is not exclusive to optomechanical systems; for example it may also be realized using two microwave cavities, in which case it is referred to as a photon pressure interaction. Nonetheless, we shall continue to call it an optomechanical interaction here, allowing us to conveniently refer to the high-frequency resonator a as its optical and the low-frequency resonator b as its mechanical component.

Unlike the Hamiltonians we considered above, (2.61) is nonlinear, in the sense that the resulting equations of motion are nonlinear, due to the interaction term

containing a product of more than two ladder operators. While linear coupling allows for the transfer of states between two oscillators, many other applications such as frequency transduction, amplification or quantum state preparation require nonlinear dynamics. Unfortunately, g_0 is typically very small, making the single-photon strong coupling regime and thus the exploitation of this nonlinear coupling for single-quantum manipulation unattainable in practice up to now. Rather, optomechanical systems are operated in a linearized regime, enabled by a strong pump tone driving the optical cavity which, as we will see in the next section, boosts the effective coupling rate at the expense of losing the nonlinearity in the effective Hamiltonian.

The work presented in Chapter 4 is part of the effort to alleviate this situation by increasing g_0. Specifically, the approach is based on a SQUID resonator whose resonance frequency can be tuned via the application of a magnetic flux Φ_b; concepts that are explained in detail there and that we shall not further concern ourselves with at this point. What is essential here is that a mechanical resonator can be integrated into the SQUID loop such that $\Phi_\mathrm{b}^\mathrm{zpf} \propto B_\parallel x_b^\mathrm{zpf}$ with a magnetic in-plane field $B_\parallel$. Together with the flux responsivity $\mathcal{F} = \partial\omega_a/\partial\Phi_\mathrm{b}$, a design parameter of the SQUID resonator, the single-photon coupling rate is thus $g_0 \propto \mathcal{F} B_\parallel x_b^\mathrm{zpf}$. Given this hybrid platform, we may thus advance towards the single-photon strong coupling regime by designing resonators with large $\mathcal{F}$ that can be operated in strong magnetic in-plane fields $B_\parallel$.

2.13 Linearization of the optomechanical coupling

Let us conclude this theoretical prelude by tracing the linearization of the optomechanical Hamiltonian that we alluded to above, though we will not use it in the following chapters. It relies on the introduction of a strong pump tone driving the optical cavity $a_\mathrm{p} = \alpha_\mathrm{p} \exp(-\mathrm{i}\omega_\mathrm{p} t)$, which we can model by adding the term*

$$H_\mathrm{p}/\hbar = \sqrt{\kappa_\mathrm{ext}}\,(a a_\mathrm{p}^\dagger + a^\dagger a_\mathrm{p}) \tag{2.62}$$

to the Hamiltonian, where we write $\kappa_\mathrm{ext} = \kappa_{a,\mathrm{ext}}$ as before. We can now transform the Hamiltonian into a rotating frame $H' = UHU^\dagger - \mathrm{i}\hbar U \partial U^\dagger/\partial t$ using the transformation $U = \exp(\mathrm{i}\omega_\mathrm{p} t a^\dagger a)$. Noting that the pump terms are time-independent in that frame

$$U \cdot H_\mathrm{p}/\hbar \cdot U^\dagger = \sqrt{\kappa_\mathrm{ext}}\,(\alpha_\mathrm{p}^* a + \alpha_\mathrm{p} a^\dagger), \tag{2.63}$$

*Note that a_p is not a ladder operator here, it is just the multiplication with a complex number, so in particular $a_\mathrm{p}^\dagger = a_\mathrm{p}^*$. The new term H_p is constructed in such a way that the equation of motion for a has the form given by (2.32), it does not describe the quantum mechanical dynamics of the pump field.

and that $U\partial U^\dagger/\partial t = -\mathrm{i}\omega_\mathrm{p}\, a^\dagger a$, we obtain

$$H'/\hbar = -\Delta a^\dagger a + \omega_b b^\dagger b - g_0\, a^\dagger a\,(b + b^\dagger) + \sqrt{\kappa_\mathrm{ext}}\,(\alpha_\mathrm{p}^* a + \alpha_\mathrm{p} a^\dagger) \tag{2.64}$$

with $\Delta = \omega_\mathrm{p} - \omega_a$ the pump detuning from the optical resonance frequency.

For the linearization, we make the ansatz that the optical cavity state differs only slightly from a coherent state induced by the strong pump tone, i.e. $a = \alpha + c$ in the rotating frame, with some large amplitude α, that we choose to be real without loss of generality, and a small fluctuating term c. The Hamiltonian becomes, after some rearrangements,

$$\begin{aligned} H'/\hbar = &-\Delta c^\dagger c + \omega_b b^\dagger b - \alpha g_0\,(c + c^\dagger)(b + b^\dagger) - g_0 c^\dagger c (b + b^\dagger) \\ &- \alpha\Delta\,(c + c^\dagger) + \sqrt{\kappa_\mathrm{ext}}\,(\alpha_\mathrm{p}^* c + \alpha_\mathrm{p} c^\dagger) - \alpha^2 g_0\,(b + b^\dagger) \\ &- \alpha^2\Delta + \sqrt{\kappa_\mathrm{ext}}\,(\alpha_\mathrm{p} + \alpha_\mathrm{p}^*). \end{aligned} \tag{2.65}$$

We can now perform the linearization by dropping the last term in the first line, which is much smaller than the preceding term due to not containing the large factor α. The terms in the second line correspond to average radiation pressure forces on the resonators and may be omitted after shifting the displacement coordinate system appropriately. Finally, the terms in the last line are numerical constants with no effect on system dynamics and can be dropped, leaving us with the approximated Hamiltonian

$$H'/\hbar \approx -\Delta c^\dagger c + \omega_b b^\dagger b - \alpha g_0\,(c + c^\dagger)(b + b^\dagger). \tag{2.66}$$

It is identical to (2.54) with an effective coupling constant $g = -\alpha g_0$, where the fluctuation oscillations c act as an oscillator with the, possibly negative, effective resonance frequency $-\Delta$.

Going to the interaction picture, analogously to (2.55), we find

$$\tilde{H}'_\mathrm{int}/\hbar = -\alpha g_0 \left(\mathrm{e}^{\mathrm{i}(\Delta-\omega_b)t}\, cb + \mathrm{e}^{\mathrm{i}(\Delta+\omega_b)t}\, cb^\dagger + \mathrm{e}^{-\mathrm{i}(\Delta+\omega_b)t}\, c^\dagger b + \mathrm{e}^{-\mathrm{i}(\Delta-\omega_b)t}\, c^\dagger b^\dagger\right) \tag{2.67}$$

and can again perform the rotating wave approximation, depending on the value of Δ. If the pump is near the red sideband of the optical cavity $\Delta \approx -\omega_b$, we obtain the beam-splitter interaction of two coupled harmonic oscillators of nearly identical frequency, as before

$$H'_\mathrm{int,rsb}/\hbar \approx -\alpha g_0\,(cb^\dagger + c^\dagger b). \tag{2.68}$$

Using this mode, the mechanical resonator can be cooled by scattering phonons into the optical cavity, mediated by the red-detuned driving tone. If we instead pump on the blue sideband $\Delta \approx \omega_b$, we must keep the other two terms in the rotating wave approximation

$$H'_\mathrm{int,bsb}/\hbar \approx -\alpha g_0\,(cb + c^\dagger b^\dagger), \tag{2.69}$$

obtaining a so-called *two-mode squeezing interaction* where one pump photon excites both the optical and the mechanical resonators, useful for applications in entanglement of the two modes or amplification of mechanical excitations.

A third notable regime is that of pumping directly on resonance $\Delta = 0$. In this case, no rotating wave approximation is possible, but instead the $c^\dagger c$ term drops out of the Hamiltonian

$$H'_{\mathrm{or}}/\hbar = \omega_b b^\dagger b - \alpha g_0 \,(c + c^\dagger)(b + b^\dagger). \tag{2.70}$$

Here, the mechanical displacement $b + b^\dagger$ results in a phase shift of the optical mode, which in turn can be used for displacement detection.

References

[1] Z.-L. Xiang, S. Ashhab, J. Q. You, and F. Nori, *Hybrid quantum circuits: Superconducting circuits interacting with other quantum systems*, Reviews of Modern Physics **85**, 623–653 (2013).

[2] M. Aspelmeyer, T. J. Kippenberg, and F. Marquardt, *Cavity optomechanics*, Reviews of Modern Physics **86**, 1391–1452 (2014).

[3] P. Krantz, M. Kjaergaard, F. Yan, T. P. Orlando, S. Gustavsson, and W. D. Oliver, *A quantum engineer's guide to superconducting qubits*, Applied Physics Reviews **6**, 021318 (2019).

[4] A. A. Clerk, K. W. Lehnert, P. Bertet, J. R. Petta, and Y. Nakamura, *Hybrid quantum systems with circuit quantum electrodynamics*, Nature Physics **16**, 257–267 (2020).

[5] A. Blais, A. L. Grimsmo, S. M. Girvin, and A. Wallraff, *Circuit quantum electrodynamics*, Reviews of Modern Physics **93**, 025005 (2021).

[6] S. Barzanjeh, A. Xuereb, S. Gröblacher, M. Paternostro, C. A. Regal, and E. M. Weig, *Optomechanics for quantum technologies*, Nature Physics **18**, 15–24 (2022).

[7] C. W. Gardiner and M. J. Collett, *Input and output in damped quantum systems: Quantum stochastic differential equations and the master equation*, Physical Review A **31**, 3761–3774 (1985).

The following chapter is derived from a manuscript with co-authors.

author contributions

B. W. designed and fabricated the superconducting device as well as its sample holder and adjustable setup mount, performed the resonator simulations, the measurements, the data analysis, contributed to concept and theory, prepared the figures and wrote the first draft of the manuscript. M. K. performed the numerical simulations of the Rydberg level structure and its Stark shift, and contributed to theory. M. R. contributed to setup enhancements and to theory. A. G. contributed to theory and to supervision. D. K. contributed to project funding and participated in scientific discussions. J. F. acquired the project funding and contributed to supervision and scientific discussions. R. K. acquired the project funding, contributed to the concept, and was responsible for global project supervision. D. B. supervised all aspects regarding the superconducting resonator, contributed to theory and figure layout, and wrote the first draft of the manuscript. All authors discussed the results and conclusions, and contributed to manuscript revisions.

acknowledgments

The authors gratefully acknowledge technical support by Markus Turad, Ronny Löffler (instrument scientists at the core facility LISA$^+$), Christoph Back and Florian Jessen. Furthermore, we thank Benedikt Ferdinand, Reinhardt Maier and Conny Glaser for helpful discussions. This research was supported with funding from the Deutsche Forschungsgemeinschaft (DFG) via grant numbers 421077991 (KL 930/16-1), 490939971 (BO 6068/1-1) and 465199066 (FOR 5413/1), as well as from the EU QuantERA project MOCA with the DFG grant number 491986552 (FO 740/5-1 and KL 930/18-1). We also acknowledge support by the COST actions NANOCOHYBRI (CA16218) as well as SUPERQUMAP (CA21144).

data availability

All data presented in this chapter, including raw data, as well as the corresponding processing scripts are publicly available on the repository Zenodo with the identifier 10.5281/zenodo.14009235.

3 Tunable hybrid systems with optically trapped Rydberg atoms

The content of this chapter was published as

Superconducting on-chip microwave cavity for tunable hybrid systems with optically trapped Rydberg atoms

Benedikt Wilde, Manuel Kaiser, Malte Reinschmidt, Andreas Günther, Dieter Koelle, Józef Fortágh, Reinhold Kleiner and Daniel Bothner

Physical Review Applied **23**, 064016 (2025)

Hybrid quantum systems are highly promising platforms for addressing important challenges of quantum information science and quantum sensing. Their implementation, however, is technologically non-trivial, since each component typically has unique experimental requirements. Here, we work towards a hybrid system consisting of a superconducting on-chip microwave circuit in a dilution refrigerator and optically trapped ultra-cold atoms. Specifically, we focus on the design optimization of a suitable superconducting chip and on the corresponding challenges and limitations. We unfold detailed microwave-cavity engineering strategies for maximized and tunable coupling rates to atomic Rydberg-Rydberg transitions in ^{87}Rb atoms while respecting the boundary conditions due to the presence of a laser beam near the surface of the chip. Finally, we present an experimental implementation of the superconducting microwave chip and discuss the cavity characteristics as a function of temperature and applied dc voltage. Our results illuminate the required consideration aspects for a flexible, tunable superconductor-atom hybrid system, and lay the groundwork for realizing this exciting platform in a dilution refrigerator with vacuum Rabi frequencies approaching the strong-coupling regime.

3.1 Introduction

Coupling superconducting microwave circuits to other physical platforms such as spins, phonons, quantum dots or atoms has the potential to enable a large variety of groundbreaking hybrid quantum technologies [1–3]. Hybrid architectures are particularly promising for compensating intrinsic weaknesses of specific quantum systems by the strengths of the other components. A prominent example are hybrid systems with superconducting qubits [3–5] – the circuits provide fast and reliable quantum processors, but suffer from short coherence times and from a lack of technologies to reliably transmit microwave-photonic quantum states over long distances. Both challenges could be solved by coupling the superconducting circuits to e.g. mechanical oscillators or to atoms, which in principle can both serve as quantum memories [6–11] and microwave-to-optical transducers [12–15]. However, combining different platforms in a single device and with sufficiently large coupling rates to facilitate coherent state transfer between them is typically a highly non-trivial experimental task. In this chapter, we focus on the specific aspect of interfacing neutral atoms with a superconducting on-chip microwave resonator; in particular on the design of a suitable and optimized superconducting chip for the coupling to ultracold Rydberg atoms.

Different possibilities to couple superconducting cavities to atoms have been explored in the past. The most famous is probably the method of coupling individual flying Rydberg atoms to a three-dimensional superconducting microwave cavity, an ultra-low-loss photon-box, which allowed for groundbreaking and unprecedented control over photonic quantum states [16]. Rydberg atoms are ideal for achieving large coupling rates to microwave photons since they possess large electric transition dipole moments [17–20]. Similar experimental settings with propagating atom beams are lately being investigated using on-chip microwave cavities, although with much higher cavity losses and lower coupling rates [21–24]. A second approach is interfacing on-chip microwave circuits with atomic ensembles trapped nearby [25–28], which has the advantage of atomic (quasi-)stationarity and a potentially large collective enhancement of otherwise small interaction rates [6, 7, 29]. The atom-trapping can be achieved either magnetically on (microwave) atom-chips [25, 30] or with optical tweezers [31–33], i.e. a strongly focused laser beam which is red-detuned from a suitable atomic resonance. Magnetic trapping with superconductors is accompanied by complications in microwave-chip design [26, 34] due to the necessity for on-chip trap-current leads and Meissner distortion of external magnetic fields [35]. Optical trapping close to the chip surface does not come with these constraints and has been discussed in various proposals [32, 36], but has yet to be demonstrated. It does, however, imply various technological challenges related to combining lasers with a mK system and superconductors, that need to be considered with care. Independent of the trapping method, one

of the most critical aspects of a potentially useful superconductor-atom hybrid system is the single-photon coupling rate – the vacuum Rabi frequency – which in all existing on-chip implementations has been orders of magnitude below the strong-coupling regime [22, 27, 28].

Here, we report the development of an on-chip superconducting microwave cavity which has been optimized for the electric dipole-coupling to Rydberg transitions in optically trapped ultra-cold atomic ensembles. The chosen resonance frequency is around 11 GHz, which is directly compatible with state-of-the art superconducting qubits. In addition to the microwave field, our resonator design enables the application of a dc electric field for tuning the Rydberg transitions into and out of resonance as well as compensating stray electric fields from the chip surface, e.g. due to adsorbates [28, 37–39]. We discuss the geometric boundary conditions that allow the chips to be approached by a high-intensity focused laser beam and devise the layout of the circuit based on the expected profile of the resulting atom-trap. As a next step, we demonstrate how to optimize the geometric details of the superconducting resonator for achieving large vacuum Rabi frequencies and reveal that even with conservative parameter estimates the strong-coupling regime is within reach. Finally, we present an implementation of the optimized microwave chip and show experimental results of its characterization in a cold-atom dilution refrigerator. We discuss in particular the dependence of cavity properties on temperature and applied dc voltage. Our device and results pave the way for a new generation of tunable superconductor-atom hybrid systems in a mK environment and in the strong-coupling regime.

3.2 Preliminary considerations

We begin by visualizing our experimental concepts and by defining the boundary conditions as well as the chosen parameter space for the envisioned superconductor-atom hybrid system, cf. Figure 3.1. Our final objective is to implement the system in a dilution refrigerator, since only then the microwave circuits will be in their quantum ground state. The specific cold-atom dilution refrigerator under consideration has been presented in [40], and throughout the present chapter we will respect the restrictions given by this cryogenic system. These include the size of the windows for optical access to the mK plate and the presence of a magnetic conveyor belt to transfer the atoms from the position of the magneto-optical trap (MOT) at 6 K to the mixing chamber plate, where the superconducting chip is mounted.

The target hybrid system provides a variety of exciting perspectives, such as enabling novel on-chip quantum experiments with Rydberg atoms [41–44], advances in quantum frequency-conversion [13–15, 33, 45, 46], hybrid quantum gates and the realization of atomic quantum memories [19, 42], atom number counting [47, 48],

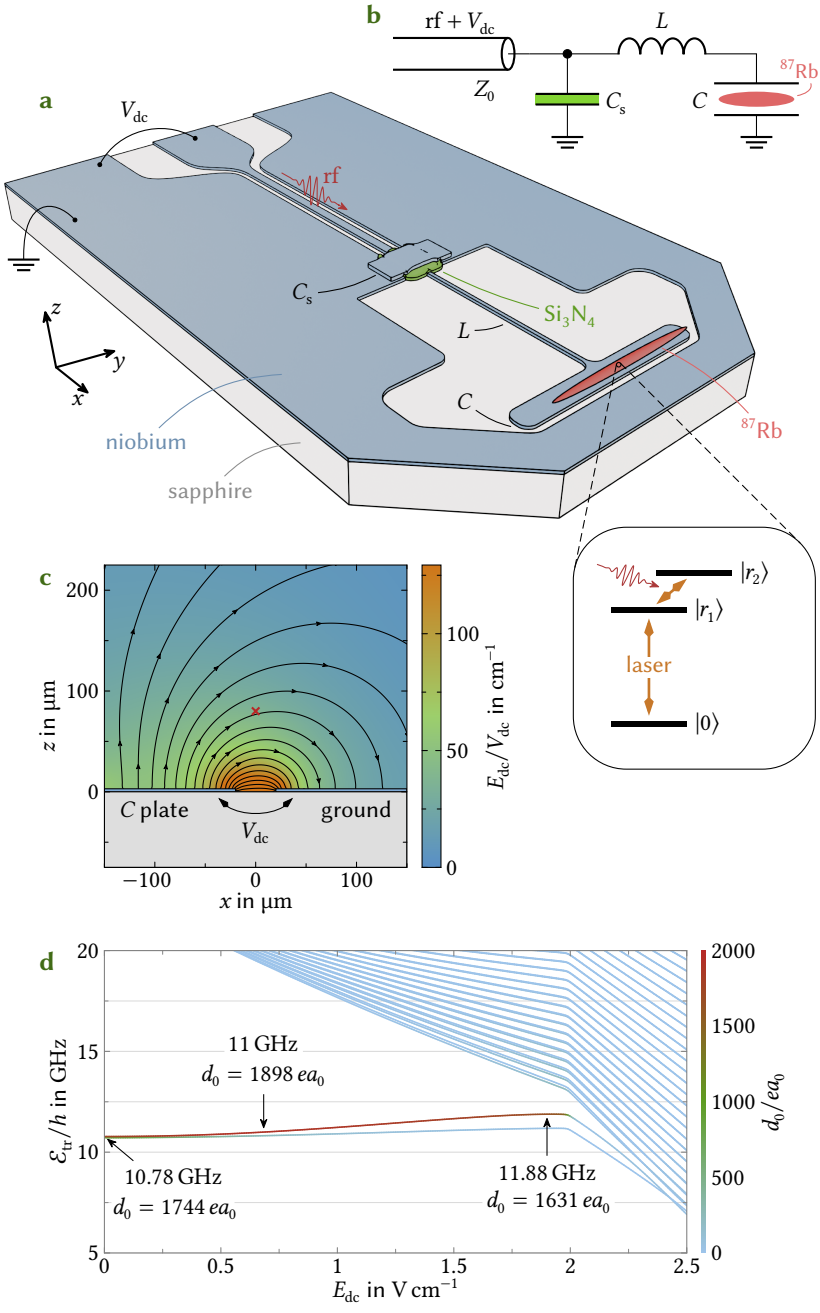
a
b
c
d
rf + V_{dc}
Z_0
L
C_s
C
^{87}Rb
V_{dc}
rf
Si_3N_4
niobium
sapphire
$|r_2\rangle$
$|r_1\rangle$
laser
$|0\rangle$
z in µm
x in µm
C plate
ground
E_{dc}/V_{dc} in cm^{-1}
$\mathcal{E}_{tr}/h$ in GHz
E_{dc} in V cm^{-1}
d_0/ea_0
11 GHz
$d_0 = 1898\, ea_0$
10.78 GHz
$d_0 = 1744\, ea_0$
11.88 GHz
$d_0 = 1631\, ea_0$

cavity cooling [44], and electric field sensing [21, 24, 49]. Since essentially all of these will considerably benefit from a high microwave-cavity–Rydberg interaction strength, high gate speed and gate fidelity as well as from protocol simplicity, we focus on a system with a 2D microwave circuit coupled to a pair of Rydberg states with an easily preparable ground state and large transition dipole moment. Particularly interesting would be the single-atom–single-photon strong coupling regime, which enables e.g. quantum-coherent single-excitation state transfer between the microwave cavity and a single Rydberg atom, and could enable the hybridization of superconducting qubits and Rydberg atoms using the cavity as a quantum bus in the next step [19, 50, 51]. Compared to their 3D counterparts, 2D microwave circuits can provide orders of magnitude larger zero-point microwave fields due to their compact mode volume, but at the expense of a much lower quality factor (assuming

Figure 3.1: A superconducting on-chip microwave cavity with dc voltage access for coupling to optically trapped Rydberg atoms. **a** Schematic of the envisioned hybrid system. On top of a sapphire substrate (light gray), a superconducting microwave resonator is patterned from a thin layer of niobium (Nb, blue). The resonant LC circuit comprises an inductance L and a capacitance C. At one of its ends, the circuit is coupled to a coplanar waveguide (CPW) feedline by a trilayer shunt capacitor C_s, and at its other end to an ensemble of ultra-cold rubidium ^{87}Rb atoms. The atoms (red cigar) are levitating $\sim 80\,\mu$m above the capacitor gap of the circuit, confined in an optical dipole trap. The center of the capacitor gap at the substrate surface is at $\boldsymbol{r} = (x, y, z) = (0, 0, 0)$. **b** Equivalent circuit of the microwave resonator with a resonance frequency $\omega_0 = 1/\sqrt{LC_{\mathrm{tot}}}$, where $C_{\mathrm{tot}}^{-1} = C^{-1} + C_s^{-1}$. The CPW feedline has a characteristic impedance $Z_0 \approx 50\,\Omega$. Due to the shunt-coupling to the feedline, it is possible to apply a dc bias voltage V_{dc} to the circuit capacitance C in which the atomic ensemble is placed. Using a laser (not shown), the atoms can be excited from their electronic ground-state $|0\rangle$ to the Rydberg manifold $|r_i\rangle$, where Rydberg-Rydberg transitions with large electric dipole moments and frequencies in the GHz regime can couple to the superconducting resonator. Here, we focus on a transition with a transition frequency $(\mathcal{E}_2 - \mathcal{E}_1)/h \approx 11\,\mathrm{GHz}$, where h is Planck's constant and $\mathcal{E}_i = \mathcal{E}(|r_i\rangle)$. **c** Cross-sectional schematic in the vicinity of the position of the atomic ensemble with $y = 0$ and the numerically simulated ratio of dc electric field strength E_{dc} to applied voltage V_{dc} versus x-z-position; electric field lines are indicated. Values close to the gap edges that exceed the scale of the colorbar are drawn in the orange of the maximum. The resulting field at the location of the atomic ensemble (marked ×) is $E_{\mathrm{dc}} = V_{\mathrm{dc}} \cdot 37\,\mathrm{cm}^{-1}$. **d** Differential Stark map showing transition frequencies $\mathcal{E}_{\mathrm{tr}}/h = (\mathcal{E} - \mathcal{E}_1)/h$ within the rubidium Rydberg manifold in the vicinity of the zero-field transition $|59\mathrm{P}_{3/2}, m_j = \frac{3}{2}\rangle \rightarrow |58\mathrm{D}_{5/2}, m_j = \frac{3}{2}\rangle$. The corresponding transition dipole moments d_0 in units of ea_0 (e is the elementary charge, a_0 is the Bohr radius) are indicated by color. The red line marks the high-d_0 target transition $|r_1\rangle \rightarrow |r_2\rangle$. At $E_{\mathrm{dc}} = 0.68\,\mathrm{V\,cm}^{-1}$, which corresponds to $V_{\mathrm{dc}} = 18.7\,\mathrm{mV}$, it has a transition frequency of 11 GHz and $d_0 = 1898\,ea_0$.

the same material), which explains the necessity for the use of a superconductor. Speed and simplicity are furthermore important since the system already has a high experimental complexity by default and it contains various low-frequency noise and decoherence sources such as atom motion, atom losses, voltage noise, laser phase noise and position vibrations of the chip / the laser beam, induced e.g. by the dilution refrigerator pulse tube. Further advantages of a chip-based implementation are easy access to the microwave cavity for the dipole trap, low photon absorption probability on the mK components, small Meissner-distortion of the magnetic trapping fields during atom preparation, and compactness of the complete microwave-part, which (at least in our system) has to fit into the center of a split-coil at the end of a magnetic conveyor belt (cf. Section 3.16 as well as [40]). Finally, our chosen approach will leave sufficient space and access to potentially add components for a single-atom detector [28] in a later experimental stage.

We start by considering the most important requirements of our envisioned hybrid system. First and foremost, the superconducting chip and in particular its packaging need to allow optical access at the location of the atoms. Secondly, the atoms should be trapped as close to the chip surface as possible to maximize the interaction with the superconducting cavity. The atoms should also be confined to a small region to minimize interaction inhomogeneities across the ensemble [27, 28]. Direct interaction of trapping-laser photons with the superconducting chip, however, should be avoided, since this would lead to Cooper pair breaking or even to heating of the entire mixing chamber to which the chip is anchored. We conclude that a system like the one shown in Figure 3.1a provides the best balance in addressing these initial requirements: An optical dipole trap (laser not shown) is used to levitate an atomic cloud ~80 µm above the chip surface* and close to the edge of a tip-tapered superconducting chip. The result is similar to the approach in [36], albeit completely planar and devoid of normal metal elements. Our design also takes the elongated ensemble distribution in a fridge-compatible dipole trap into account. The details of the exact shape and size of the chip, the shape of the atomic cloud and the chip-atom distance are discussed in Sections 3.3 and 3.4.

The ellipsoidal shape of the atomic ensemble in combination with the objective of maximized vacuum Rabi frequencies dictate some of the requirements for the layout details of the superconducting resonator. Firstly, all the ensemble atoms should be able to participate in the interaction with equal coupling strength; this reduces inhomogeneous broadening and increases the collective coupling [52, 53].

*The distance of 80 µm seems to come out of nowhere here, but it follows from the (setup-restrained) laser focus width, the length of the atomic cloud (defined by the dipole trap profile and the cloud temperature) and the optimal width of the superconducting chip in combination with a maximum value for how many laser photons we allow to shine on the chip. Additionally, we take a small safety margin of ~20 µm into account. The details of each of these aspects (except for the margin) are discussed in Section 3.3 (dipole trap and cloud temperature), in Section 3.4 (capacitor and chip layout/size), as well as in Section 3.12 (calculation of laser light hitting the chip).

It is therefore essential that the resonator and microwave fields are translationally invariant along the longitudinal axis of the ensemble. Secondly, since we target an electric dipole interaction, all the electric microwave fields should ideally be concentrated in the region of the atoms. Hence, the optimal layout is a lumped-element LC circuit with the capacitance C directly below the position of the atoms and a minimal amount of stray capacitances. Based on these factors, we devised the T-shaped microwave cavity shown in Figure 3.1a: A single straight inductance L is connected to a coplanar capacitance C to ground; to minimize the stray capacitance, the ground plane has a large distance to the circuit elements except in the interaction region with the atoms. At this point it also becomes clear why coplanar waveguide cavities – as often used in theoretical proposals and in other experimental approaches [7, 18, 22–24, 26–28, 34, 36, 42, 46] – are not ideal for maximized coupling and field homogeneity. By their very nature as distributed element circuits, they come with significantly distributed (i.e. stray) capacitances and spatially varying microwave electric fields along the transmission line.

As a third design aspect, it would be highly beneficial to be able to apply a dc electric field E_{dc} to the atomic ensemble. This can not only be used to tune the Rydberg transition into and out of resonance with the cavity, but also to (partially) compensate for static parasitic adsorbate fields. To allow for this option, we couple the microwave cavity to its coplanar waveguide (CPW) feedline by means of a parallel-plate shunt capacitor C_{s} to ground [54]. In this coupling scheme the CPW center conductor remains uninterrupted and galvanically connected to L and C, so a dc electric field above the chip can be realized simply by applying a dc voltage V_{dc} to the feedline center conductor, cf. Figure 3.1c. If necessary, the direction of the dc field can be adjusted from x- to z-direction by moving the dipole trap with the atoms along x. Generating the dc electric field via the cavity itself has the elegant side-effect of obtaining (nearly) identical dc and microwave field configurations, which could be used to pre-select a slice of resonant atoms in the cloud which then all couple with identical Rabi frequency to the cavity photons [28].

Finally, we need to design the cavity for a specific resonance frequency matching a chosen Rydberg-Rydberg transition in ^{87}Rb atoms. For frequency-compatibility with the most common superconducting quantum circuits and common microwave equipment we decided to operate in the frequency range $\sim 10\,\mathrm{GHz} - 12\,\mathrm{GHz}$. In addition to a matching transition frequency, a suitable Rydberg-Rydberg transition needs to have a large electric dipole transition matrix element and be sufficiently distant from other such transitions. We choose the transition $|59\mathrm{P}_{3/2}, m_j = \frac{3}{2}\rangle \rightarrow |58\mathrm{D}_{5/2}, m_j = \frac{3}{2}\rangle$ with a transition frequency $\mathcal{E}_{\mathrm{tr}}/h \approx 11\,\mathrm{GHz}$ and a transition dipole moment of $d_0 \approx 1800\, e a_0$, the exact values being dependent on the dc electric field. A differential Stark map around the corresponding transition is shown in Figure 3.1d, illustrating that it possesses the required properties. It has been numerically calculated using the methods described in [28, 55], cf. Section 3.10.

3.3 Of lasers and atoms

Since it defines the further layout of the chip and the resonator, we calculate the shapes of the focused laser beam and of the atomic ensemble trapped by it before considering aspects of the chip design on a more quantitative level. Several critical length scales are competing with each other here and a satisfying compromise between the beam waist at the focus, the angle of divergence and the distance from the chip surface has to be found, cf. Figure 3.2a. As laser wavelength for the dipole trap we choose $\lambda_{\mathrm{dp}} \approx 800\,\mathrm{nm}$, which is red-detuned from the rubidium D_1 ($|5S_{1/2}\rangle \rightarrow |5P_{1/2}\rangle$) and D_2 ($|5S_{1/2}\rangle \rightarrow |5P_{3/2}\rangle$) transitions at 795 nm and 780 nm, respectively. For a given laser intensity $I_{\mathrm{dp}}(\boldsymbol{r})$, which is a function of position $\boldsymbol{r}$, the trapping potential can be calculated by [31]

$$U_{\mathrm{dp}}(\boldsymbol{r}) = \left(-\frac{\pi c_0^2}{2\omega_1^3}\left(\frac{\Gamma_1}{\omega_1-\omega_{\mathrm{dp}}}+\frac{\Gamma_1}{\omega_1+\omega_{\mathrm{dp}}}\right) - \frac{\pi c_0^2}{\omega_2^3}\left(\frac{\Gamma_2}{\omega_2-\omega_{\mathrm{dp}}}+\frac{\Gamma_2}{\omega_2+\omega_{\mathrm{dp}}}\right)\right) I_{\mathrm{dp}}(\boldsymbol{r}), \tag{3.1}$$

with the vacuum speed of light c_0, the laser frequency ω_{dp} and the frequencies $\omega_1 = 2\pi\cdot 377\,\mathrm{THz}$ and $\omega_2 = 2\pi\cdot 384\,\mathrm{THz}$ as well as the linewidths $\Gamma_1 = 2\pi\cdot 5.75\,\mathrm{MHz}$ and $\Gamma_2 = 2\pi\cdot 6.07\,\mathrm{MHz}$ of the atomic transitions D_1 and D_2, respectively [56].

The intensity distribution of a focused Gaussian laser beam propagating in y-direction and focused in the $y = 0$ plane is given by

$$I_{\mathrm{dp}}(\boldsymbol{r}) = \frac{2P_{\mathrm{dp}}}{\pi w^2(y)}\,\exp\!\left(-\frac{2r^2}{w^2(y)}\right) \tag{3.2}$$

Figure 3.2: Position and trapping characteristics of the atoms near the superconducting microwave chip. a Schematic of the chip tip in front view, viewing direction is $-x$ with a small elevation angle, cf. Figure 3.1. Above the chip surface, at a distance z_0, the ensemble of atoms is trapped by a focused laser beam (dipole trap). The beam waist ($1/e^2$ radius) in the focus plane is denoted as w_{dp} and the Rayleigh length of the beam focus as l_{R}. For a chip width underneath the laser axis $l_{\mathrm{ch}} = 1.6\,\mathrm{mm}$ we choose $z_0 = 80\,\mu\mathrm{m}$ and $w_{\mathrm{dp}} = 15\,\mu\mathrm{m}$, which corresponds to $l_{\mathrm{R}} = 0.88\,\mathrm{mm}$. In **b** and **c** we show the resulting trapping potential $U_{\mathrm{dp}}/k_{\mathrm{B}}$ for ground-state rubidium atoms in z- and y-direction, respectively, using a laser with wavelength $\lambda_{\mathrm{dp}} = 800\,\mathrm{nm}$ and power $P_{\mathrm{dp}} = 50\,\mathrm{mW}$. More details on the calculation and the parameters used can be found in the main text. For a realistic assumption of an atomic ensemble temperature $T_{\mathrm{Rb}} \sim 1\,\mu\mathrm{K}$, we get the Gaussian single-atom density profiles ρ_{sp} (red lines and shaded areas) overlaid to the potentials in panels b and c. The width of the atomic cloud is $d_{\mathrm{Rb}} = 2.3\,\mu\mathrm{m}$ in z-direction (as well as in x-direction) and $l_{\mathrm{Rb}} = 0.19\,\mathrm{mm}$ in y-direction (we define the size of the distribution as six standard deviations).

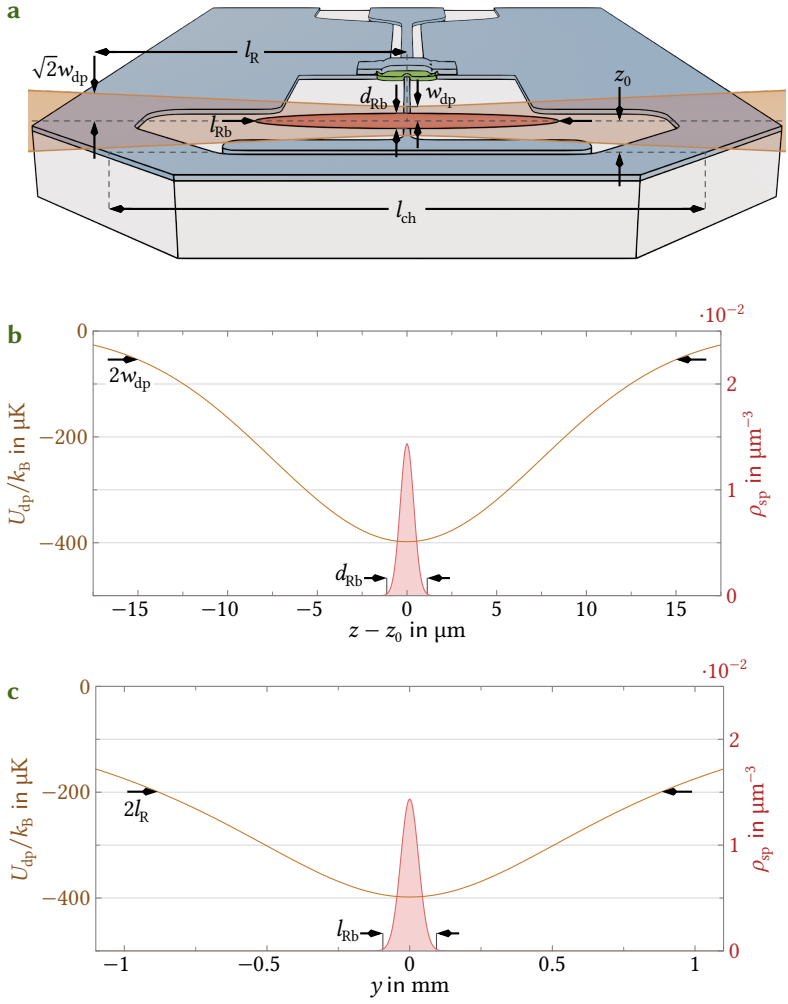
a
l_R
$\sqrt{2}w_{dp}$
z_0
d_{Rb}
w_{dp}
l_{Rb}
l_{ch}
b
$\cdot 10^{-2}$
$2w_{dp}$
d_{Rb}
U_{dp}/k_B in µK
ρ_{sp} in µm^{-3}
$z - z_0$ in µm
c
$\cdot 10^{-2}$
$2l_R$
l_{Rb}
U_{dp}/k_B in µK
ρ_{sp} in µm^{-3}
y in mm

with $r = \sqrt{x^2 + \tilde{z}^2}$ the radial distance from the focus center in the x-z-plane. Here $\tilde{z} := z - z_0$ is the z-distance from that focus center, which is positioned at a distance z_0 from the chip surface. Thus, the overall shape of the trapping potential is that of a Gaussian in x- and z-direction and that of a Lorentzian in y-direction: The $1/e^2$ radius of the beam $w(y)$ is given by

$$w(y) = w_{\mathrm{dp}} \sqrt{1 + \frac{y^2}{l_{\mathrm{R}}^2}} \tag{3.3}$$

with the beam waist in the focus plane w_{dp}. The Rayleigh length l_{R} appearing here is not independent of the beam waist, but given by

$$l_{\mathrm{R}} = \frac{\pi w_{\mathrm{dp}}^2}{\lambda_{\mathrm{dp}}}. \tag{3.4}$$

It defines the length in propagation direction on which the beam radius increases by a factor of $\sqrt{2}$ from w_{dp} at $y = 0$. Considering the dimensions of the cryogenic setup and the windows for optical access, we can comfortably work with $w_{\mathrm{dp}} = 15\,\mu\mathrm{m}$, which corresponds to $l_{\mathrm{R}} = 0.88\,\mathrm{mm}$. Together with the width of the superconducting chip underneath the laser beam axis, these values provide a limit for how close to the surface the atoms can be trapped while ensuring that only minor amounts of laser radiation reach the chip.

The next question for designing cavity and chip is how large the atom cloud in that trap will be. The two main parameters defining the size are the ensemble temperature T_{Rb}, which we expect to be on the order of $\sim 1\,\mu\mathrm{K}$, and the laser power P_{dp}. With $P_{\mathrm{dp}} = 50\,\mathrm{mW}$ we find a maximum trap depth of $T_{\mathrm{dp}} = |U_{\mathrm{dp}}|/k_{\mathrm{B}} \approx 400\,\mu\mathrm{K}$, cf. Figure 3.2, and for the much colder atoms the trap shape constitutes in good approximation a harmonic oscillator potential in all three dimensions. The atomic distribution in a 3D harmonic potential is a 3D Gaussian [57], and the single-particle density profile is described by

$$\rho_{\mathrm{sp}}(r, y) = \frac{1}{\sqrt{2\pi}^3 \sigma_r^2 \sigma_y} \exp\Big(-\frac{r^2}{2\sigma_r^2} - \frac{y^2}{2\sigma_y^2}\Big). \tag{3.5}$$

The radial and longitudinal variances σ_r^2 and σ_y^2 are

$$\sigma_q^2 = \frac{k_{\mathrm{B}} T_{\mathrm{Rb}}}{m_{\mathrm{Rb}} \omega_q^2}, \quad q \in \{r, y\} \tag{3.6}$$

with m_{Rb} the mass of a rubidium atom, k_{B} Boltzmann's constant, and ω_r (ω_y) the radial (longitudinal) harmonic oscillation frequency, cf. Section 3.11. From the

shape of our beam we finally obtain a cloud extension of $d_{\mathrm{Rb}} := 6\sigma_r = 2.3\,\mu\mathrm{m}$ in radial direction and $l_{\mathrm{Rb}} := 6\sigma_y = 0.19\,\mathrm{mm}$ in longitudinal direction, cf. also Figure 3.2. To be on the safe side and have sufficient margin even for elevated cloud temperatures of up to $T_{\mathrm{Rb}} \sim 5\,\mu\mathrm{K}$ we set the length of the capacitor plate along the laser axis to be fixed at $l = 1\,\mathrm{mm}$.

Two remaining, mutually dependent values that we need to determine are the width l_{ch} of the chip underneath the laser axis and the distance z_0 of the atoms from the chip surface. It is intuitively clear from Figure 3.2 that a wider chip requires a larger atom-chip distance, at least if we want to avoid the tail of the Gaussian laser beam to shine on the superconductor. As a satisfying compromise including some margin for error we find a chip width of $l_{\mathrm{ch}} = 1.6\,\mathrm{mm}$ and a chip-atom distance of $z_0 = 80\,\mu\mathrm{m}$. These values guarantee completely negligible direct interaction between the laser photons and the superconductor, cf. Section 3.12, while still providing enough space for capacitor, gap and ground plane as discussed above. Since on the other hand a chip with a constant width of 1.6 mm is not convenient for mounting and wire bonding, and does not provide much space for minimizing stray capacitances, we have opted as an ideal solution for a tapered-tip design. Regarding the atom-chip distance, we will experimentally explore the possibility to reduce it further in the future, although there might be additional aspects to consider, such as parasitic stray fields that can get very strong close to the surface [28, 37–39].

We note at this point that due to the large parameter space to consider and various experimental options (laser wavelength, laser intensity, beam profile, ensemble temperature) there might exist even more ideal configurations to be discovered. Our considerations, however, describe an instructive way for how to engineer a satisfying compromise based on specific boundary conditions and experimental and technological choices. That being said and the atom position being fixed, we are ready to optimize the details of the superconducting microwave resonator for maximized interaction rates in the next section.

3.4 Maximizing the coupling rate

The optimization of the resonator layout for large interaction rates can be condensed into the maximization of the electric microwave field per photon at the atom position $z_0 = 80\,\mu\mathrm{m}$ above the capacitor gap. The strength of the interaction on the single-quantum level is encoded in the single-photon coupling rate g, which enters the interaction Hamiltonian of the Rabi model as

$$\hat{H}_{\mathrm{int}}/\hbar = g(\hat{a} + \hat{a}^\dagger)(\hat{\sigma}_+ + \hat{\sigma}_-). \tag{3.7}$$

Here, $\hat{a}$ and $\hat{a}^\dagger$ are the annihilation and creation operators of the microwave field mode, respectively, and $\hat{\sigma}_+ = |r_2\rangle\langle r_1|$ and $\hat{\sigma}_- = |r_1\rangle\langle r_2|$ are the raising and lowering

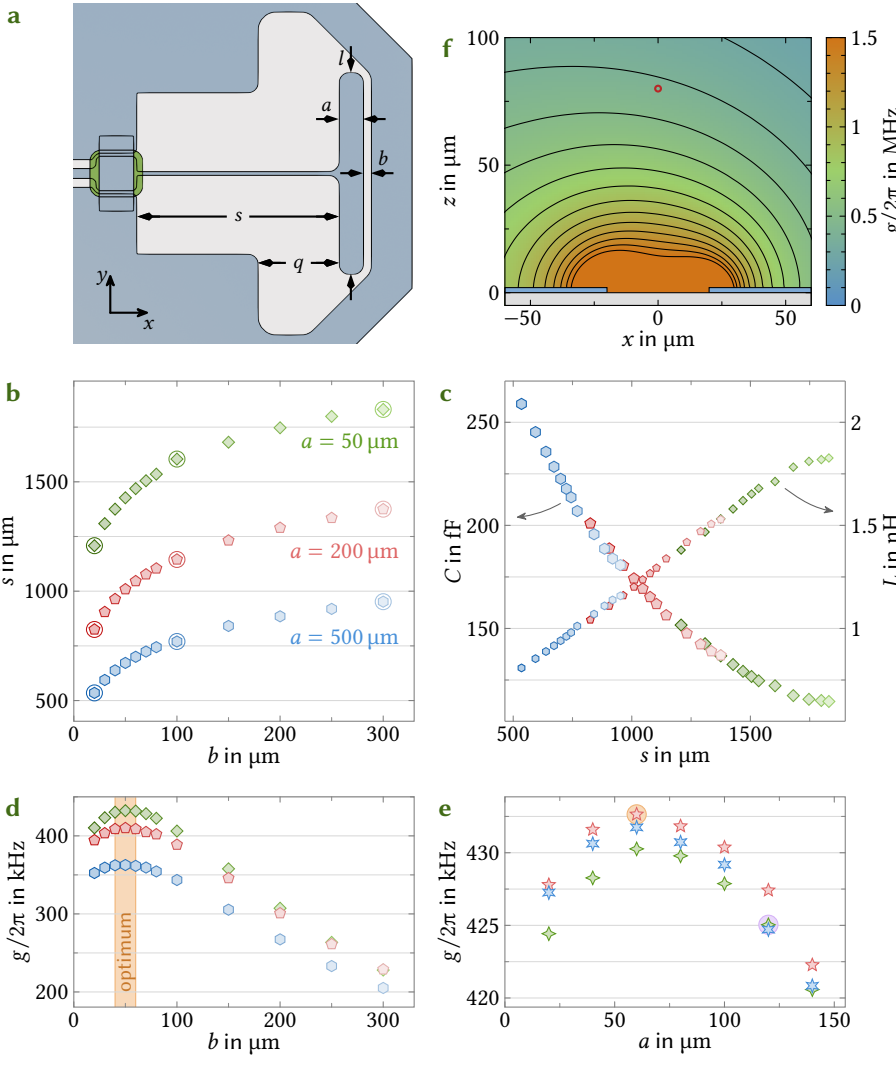
a
l
a
b
s
q
y
x
f
z in µm
x in µm
g/2π in MHz
b
s in µm
b in µm
a = 50 µm
a = 200 µm
a = 500 µm
c
C in fF
L in nH
s in µm
d
g/2π in kHz
b in µm
optimum
e
g/2π in kHz
a in µm

Figure 3.3: Optimizing the geometry parameters of the superconducting cavity for maximized coupling strength. **a** Schematic of the chip in top view with definition of all relevant resonator parameters used in the optimization. The length of the inductance wire is s, the width of the capacitor plate is a, and the gap width between plate and ground-plane at the far end is b. The length of the capacitor plate $l = 1\,\mathrm{mm}$ is a fixed parameter chosen to accommodate atomic cloud lengths of up to $\sim 0.8\,\mathrm{mm}$ (cf. Figure 3.2). Also, the general shape of the ground plane cutout including the parameter $q = 400\,\mu\mathrm{m}$ is kept unchanged during the optimization process. If we change either a or b to optimize the coupling rate to the atoms, the capacitance C changes accordingly and we need to adjust s to keep $\omega_0 = 2\pi \cdot 11\,\mathrm{GHz}$. In **b** we present the resulting s for $a \in \{$◇ $50\,\mu\mathrm{m}$, ⬠ $200\,\mu\mathrm{m}$, ⬡ $500\,\mu\mathrm{m}\}$ and various b. The value of b is additionally indicated by a color intensity gradient, which is also applied to the corresponding data in panels c and d. The values for s are obtained by an iterative simulation procedure using *Sonnet* for the circled values and by interpolation for the other values (see main text). **c** shows the corresponding C and $L = 1/\omega_0^2 C$ (the inductance values having smaller marks for better differentiation) for each parameter set (a, b, s) from panel b. The values for C are obtained from *Comsol Multiphysics* simulations which simultaneously provide the electric field strength at the position of the atomic ensemble center $(x, y, z) = (0, 0, 80)\,\mu\mathrm{m}$ for a given voltage across the capacitor. This field strength in turn can be used to calculate the coupling rate $g = E_{\mathrm{zpf}} d_0/\hbar$, where d_0 is the transition dipole matrix element and $E_{\mathrm{zpf}} = |\boldsymbol{E}_{\mathrm{zpf}}|$ is the root-mean-square field amplitude of the resonator quantum ground state. **d**, **e** Coupling rate g at the center of the atom cloud for various a and b (with $d_0 = 1898 e a_0$). In d we use the same values for a as before, in e we focus on $b \in \{$✧ $40\,\mu\mathrm{m}$, ☆ $50\,\mu\mathrm{m}$, ✲ $60\,\mu\mathrm{m}\}$, since that is the region of strongest coupling as indicated by the orange interval in d. The maximum value $g_{\mathrm{max}} = 2\pi \cdot 433\,\mathrm{kHz}$ is obtained for $a = 60\,\mu\mathrm{m}$ and $b = 50\,\mu\mathrm{m}$ (orange highlighted data point). The device presented in this chapter was fabricated with $a = 120\,\mu\mathrm{m}$ and $b = 40\,\mu\mathrm{m}$ (violet highlighted data point), corresponding to $g = 2\pi \cdot 425\,\mathrm{kHz} = 0.98 g_{\mathrm{max}}$. **f** g as a function of position $(x, y = 0, z)$ near the capacitor gap at the end of a resonator with $a = 120\,\mu\mathrm{m}$, $b = 40\,\mu\mathrm{m}$ and $s = 1.1\,\mathrm{mm}$. Contour lines mark curves of equal coupling strength at the values indicated by ticks in the colorbar. Values close to the gap edges that exceed the scale of the colorbar are drawn in the orange of the maximum. The position of the atomic ensemble is marked by a red circle with to-scale diameter d_{Rb} (cf. Figure 3.2).

operators of the Rydberg state pair. The coupling rate g is closely related to the vacuum Rabi frequency $\Omega_0 = 2g$ (for zero detuning between atom and photon) and describes the rate of energy exchange between the two systems. In terms of practical variables, g can be expressed as

$$g = \frac{E_{\mathrm{zpf}}\, d_0}{\hbar} \tag{3.8}$$

with the zero-point fluctuation amplitude of the electric microwave field at the position of the atom E_{zpf} and the transition dipole moment of the Rydberg state pair d_0, cf. again Figure 3.1d.

Since the atoms are located considerably above the chip surface, it is not sufficient to maximize the zero-point voltage $V_{\mathrm{zpf}} = \sqrt{\hbar\omega_0/2C}$ of the microwave circuit as it is often the case in planar circuit QED [58, 59]. If that were the case we would just have to minimize the capacitance C while keeping the resonance frequency at 11 GHz. Instead, we need to numerically scan a large parameter space of circuit parameters in order to find the optimum regime. An overview of the relevant variables and an illustration of the optimization procedure are presented in Figure 3.3. Since we have fixed the length of the capacitor plate to $l = 1$ mm, the remaining parameters are the width of the plate a, the size of the capacitor gap to ground b and the length of the inductance s. This last parameter is mainly a control knob to keep the resonance frequency at $\omega_0 = 2\pi \cdot 11\,\mathrm{GHz}$ for all combinations of a and b, but it also contributes to unwanted stray capacitances.

The procedure to determine E_{zpf} for each set of parameters (a, b) is as follows: First, we need to determine the value s that results in the desired resonance frequency. Initially, we use an iterative procedure of simulating the circuit with the software package *Sonnet* for different values of s until the resulting resonance frequency is 11 GHz. Once the function $(a, b) \mapsto s$ is known for a few parameter sets, we can estimate its value at further points by interpolation and in this way quickly scan a large parameter space. Results of this process can be seen in Figure 3.3b. Next, we determine the capacitance C for each parameter set (a, b, s) by numerical simulation with the software package *Comsol Multiphysics* in combination with an analytical correction which takes the mode shape of the microwave fields into account. For completeness, we calculate the corresponding inductance $L = 1/\omega_0^2 C$, cf. Figure 3.3c. Details regarding the simulations and the capacitance correction can be found in Sections 3.13 and 3.14.

From the capacitance simulations with *Comsol Multiphysics*, we furthermore extract the spatial field distribution $\boldsymbol{E}_{\mathrm{dc}}(\boldsymbol{r})$ for $V_{\mathrm{dc}} = 1\,\mathrm{V}$, cf. Figure 3.1c, which we translate into the microwave zero-point field amplitude by

$$E_{\mathrm{zpf}}(\boldsymbol{r}) = \sqrt{\frac{\hbar\omega_0}{2C}}\, \frac{|\boldsymbol{E}_{\mathrm{dc}}(\boldsymbol{r})|}{V_{\mathrm{dc}}}. \tag{3.9}$$

We now need to find the optimal range for a and b which maximizes $g \propto E_{\mathrm{zpf}}$ at $\boldsymbol{r} = (0, 0, z_0)$. Luckily, we find in these simulations that the optimum range of b is only slightly dependent on a and vice versa, and that a in general has not a very strong impact on g in a broad interval of reasonable widths, since the electric field will be concentrated near the gap to ground anyways. The optimum ranges for both variables are comfortably large, with deviations in either of them as large as 50 % reducing the coupling rate only slightly, cf. Figures 3.3d and e. This relaxes the requirements for the exact design values and the fabrication precision. We find $(a, b, s) = (60, 50, 1390)\,\mu\mathrm{m}$ to be the optimal parameters, resulting in $C = 136\,\mathrm{fF}$, $L = 1.53\,\mathrm{nH}$ and a coupling strength $g_{\max} = 2\pi \cdot 433\,\mathrm{kHz}$, cf. Figure 3.3e, orders of magnitude larger than in any previous chip-based implementation [27, 28].

Such a large value of g is highly promising for achieving the strong-coupling regime, which is defined by $2g > \kappa, \gamma_{\mathrm{Ry}}$, where κ is the total linewidth of the superconducting circuit and $\gamma_{\mathrm{Ry}}/2\pi \sim (1 - 10)\,\mathrm{kHz}$ is the atom decay rate of the Rydberg state pair under consideration here. Optimized superconducting coplanar waveguide cavities have been demonstrated to allow for single-photon quality factors $Q_{\mathrm{int}} > 10^6$ [60], which translates to $\kappa_{\mathrm{int}} < 2\pi \cdot 11\,\mathrm{kHz}$ and hence to $2g/\kappa \sim 80$ for our ω_0. In our setting, however, the cavity layout is highly specialized and not an ideal coplanar waveguide, the chip is not packaged compactly in a radiation-tight housing and there will always be some infrared or optical stray light hitting the superconducting film. It is therefore important to characterize as a next step a physical implementation of a typical device.

3.5 Experimental device and setup

We have fabricated and characterized a superconducting cavity chip with parameters very close to the optimal ones determined in the previous section. As geometrical parameters we chose an inductance wire length $s = 1000\,\mu\mathrm{m}$, capacitor dimensions $a = 120\,\mu\mathrm{m}$ and $b = 40\,\mu\mathrm{m}$, and as plate length we stick to the fixed value $l = 1000\,\mu\mathrm{m}$. This results in a design frequency $\omega_0 = 2\pi \cdot 11.6\,\mathrm{GHz}$ ($C = 160\,\mathrm{fF}$, $L = 1.18\,\mathrm{nH}$), i.e. a slightly higher resonance frequency than the previously discussed 11 GHz which is a precaution for the case that we cannot compensate for all parasitic dc fields with V_{dc} and are therefore restricted to the upper range of possible electric fields $E_{\mathrm{dc}} \gtrsim 1\,\mathrm{V\,cm^{-1}}$, cf. Figure 3.1d and [28]. The higher resonance frequency results in an expected coupling rate $g = 2\pi \cdot 438\,\mathrm{kHz}$, slightly larger than the value in Figure 3.3.

The circuit consists of three micro-patterned thin-film layers on top of a tip-tapered sapphire substrate. The first layer is superconducting niobium with a thickness of 80 nm and defines all superconducting structures except for the top-plate of the shunt capacitor. The second layer is 70 nm thick Si_3N_4 as dielectric for

the shunt capacitor and the third layer is again superconducting niobium of 120 nm thickness to finish the parallel-plate capacitor C_s. The shunt capacitance $C_s \approx 20\,\mathrm{pF}$ is designed for a high external quality factor $Q_{\mathrm{ext}} = \omega_0 Z_0 C_s (C + C_s)/C \sim 10^5$ and in contrast to similar earlier implementations [54, 61, 62] the top plate of the capacitor is galvanically connected to the ground planes in order to minimize the impact of a potential shunt inductance. More details regarding chip fabrication can be found in Section 3.15.

For its characterization, the 10 mm × 3.5 mm large superconducting chip is mounted in a cold-atom-compatible manner into a suitable dilution refrigerator, cf. Figure 3.4. The tapered tip of the chip including the complete cavity protrudes over the edge of its microwave housing by 2 mm. Inside the gold-plated copper housing, the chip is wire-bonded directly to the housing along the two long chip edges for grounding and to a Rogers microwave printed circuit board (PCB) at the remaining short edge with the CPW feedline launcher, cf. Section 3.15. The PCB connects the chip to a surface-mounted SMP connector by means of another CPW transmission line. Then, the complete package is inserted through the circular bore of a small superconducting magnet coil which is part of a magnetic quadrupole trap for cold atoms. By design and careful mounting, everything is aligned in a way that the microwave capacitor C on the chip is located close to the center of the quadrupole coils, where the atoms arrive from their 6 K preparation stage and where they are transferred from the magnetic into the optical dipole trap. Simultaneously, the magnet-center is positioned directly on the axis of optical access and the chip surface is oriented parallel to that axis.

The microwave input and output lines in the fridge are equipped with multiple high-frequency components which are typical for the characterization of superconducting quantum circuits at mK temperatures, cf. Figure 3.4 and Section 3.16. A minor difference to common mK setups is that all the temperature stages in our cold-atom fridge have somewhat elevated temperatures compared to standard systems [40], and so the lowest temperature we can (currently) achieve is $T_{\mathrm{min}} \gtrsim 200\,\mathrm{mK}$. On the input line, we have mounted several discrete attenuators and highly attenuating stainless steel coaxial cables (total input attenuation ~70 dB at 11 GHz) to suppress the noise level of the incoming signals to an equivalent temperature close to T_{min}. On the mixing chamber and just before the signals reach the superconducting chip, we have installed a cryogenic circulator and a bias-tee to enable a reflection measurement in combination with the application of a dc voltage. The reflected microwave signal is routed with partially superconducting coaxial cables (up to the $T = 0.5\,\mathrm{K}$ plate) through the circulator towards a cryogenic high-electron-mobility-transistor (HEMT) amplifier in the output line. To additionally shield the device from thermal noise emitted by the HEMT, a cryogenic isolator is inserted at $T = 1.5\,\mathrm{K}$ in between the circulator and the amplifier.

3.6 Measured cavity parameters vs T

The spectroscopic cavity characterization is performed by means of a vector network analyzer (VNA), and we track the reflection response S_{11} around the circuit resonance frequency during the device cooldown to mK. This way we are able to cover a large temperature span up to $T > 4\,\mathrm{K}$, which could not be achieved as easily by the heater on the mK plate alone. A separate temperature sensor is attached directly to the chip mounting-bracket to guarantee a minimal temperature-difference between sensor and sample. The measured absorption resonances, cf. Figure 3.4c for a small selection of temperatures, are analyzed by a data fitting procedure from which we obtain the resonance frequency ω_0 and the internal and external quality factors Q_{int} and Q_{ext}, cf. Section 3.17. At the lowest available temperature $T_{\mathrm{min}} = 224\,\mathrm{mK}$, we find $\omega_0 = 2\pi \cdot 11.708\,\mathrm{GHz}$, $Q_{\mathrm{int}} = 5.2 \cdot 10^3$ and $Q_{\mathrm{ext}} = 18.3 \cdot 10^3$, indicating that the resonator is in the undercoupled regime. Up to $\sim 2.5\,\mathrm{K}$ the cavity properties remain nearly constant, and start to decrease for further increasing temperatures. A decrease of ω_0 and Q_{int} with increasing temperature can be attributed to thermal quasiparticles in the superconductor and a corresponding increase of kinetic inductance. The slight decrease of Q_{ext} with increasing T on the other hand could either be related to a frequency-dependent impedance of the microwave circuitry connected to the chip (cable resonances) or to a non-negligible contribution of Q_{int} to Q_{ext} based on interferences (e.g. in the circulator) and incorrectly attributed losses during the fitting procedure [63]. These factors might also be responsible for the discontinuity of Q_{ext} at $T \sim 1.7\,\mathrm{K}$ which occurs approximately when the aluminum coaxial cables and wire bonds in the setup become superconducting.

Overall, the cavity shows very promising characteristics for the envisioned hybrid system. The resonance frequency is close to its design value and in an ideal range for the targeted Rydberg transition. The external quality factor is smaller than expected, but in principle allows $\kappa = \omega_0/Q \sim 2\pi \cdot 600\,\mathrm{kHz}$ and can be adjusted in future implementations, e.g. by an increased plate area of C_s, a thinner layer of Si_3N_4 or a material with a higher ϵ_r such as amorphous silicon. For the present device and first hybrid experiments, however, Q_{ext} is well-suited, since it does not dominate the total linewidth while still allowing for a comfortable cavity characterization by a considerable resonance-dip depth of 5 dB. The internal quality factor $Q_{\mathrm{int}} = 5.2 \cdot 10^3$ finally is lower than in many other implementations of superconducting circuits, and currently we are not certain why. Possible reasons include stray (infrared) light reaching the superconductor through the cryostat windows, dipole-radiation losses due to a lack of metal housing, as well as surface, interface and dielectric losses on the chip itself. The latter seems improbable because we can achieve $Q_{\mathrm{int}} > 10^5$ at mK temperatures with our fabrication recipe using different cavity layouts and proper microwave-packaging. From our estimates of the radiation losses, we would

also expect an at least tenfold higher Q_{int}. However, if radiation turns out to be the culprit, a careful design of the free-space density of states around the chip tip, e.g. by metal plates that do not impede the optical path, is likely to suppress it to a satisfactorily low level. Optical and infrared stray light could be minimized by suitable filter-shielding of the windows for optical access.

We plan to investigate the exact nature of the loss mechanisms of our cavity in dedicated experiments in the future and we are optimistic that we will be able to improve the quality factor by at least one order of magnitude doing so. Nevertheless, the cavity does already now facilitate getting close to the strong-coupling regime with $\Omega_0 \approx \kappa/3$ which would exceed all previous on-chip realizations by orders of magnitude [27, 28]. Since our setup does not only involve a single Rydberg atom but potentially many of them simultaneously (in an ensemble of $10^4 - 10^6$ atoms), we also expect to observe a transition from the weak-coupling regime to the strong-coupling regime with increasing number of Rydberg atoms. The Dicke model predicts a scaling of the collectively enhanced vacuum Rabi frequency with the root of the number of Rydberg atoms $\sqrt{N_{\text{Ry}}}$ [29], which can in turn be chosen through

Figure 3.4: Cavity characterization in a cold-atom dilution refrigerator. a Schematic of the microwave-part of the dilution fridge setup. A cascade of attenuators (boxes) is mounted to the input line (little arrows at the top indicate the microwave signal direction) to reduce the thermal-noise level of the incoming microwave signal to sub-kelvin levels. The signal is then routed to the device under test (DUT, cf. Figure 3.1) via a cryogenic circulator and through a bias-tee. The bias-tee combines the microwave signal with an applied dc voltage directly in front of the cavity, but none is applied during the measurements presented in this figure. The reflected signal is amplified by ~40 dB using a cryogenic HEMT amplifier on the 6 K stage. A cryogenic isolator on the 1.5 K plate is used to shield the superconducting resonator from thermal noise emitted by the amplifier. **b** Photograph of the mounted resonator. The chip-tip is uncovered in order to allow access for lasers and atoms. Above and below the resonator two superconducting coils can be seen that make up the magnetic quadrupole trap used to load the atoms into the optical tweezers (coils not used here). **c** Reflection $|S_{11}|$ of the microwave resonator at different temperatures between 224 mK and 5 K. Colored dots are experimental data, gray lines are corresponding fit curves, cf. Section 3.17. The curves for $T \leq 2$ K lie on top of each other. From the fit lines, we extract the cavity resonance frequency ω_0 as well as the internal and external quality factors $Q_{\text{int}} = \omega_0/\kappa_{\text{int}}$ and $Q_{\text{ext}} = \omega_0/\kappa_{\text{ext}}$. **d**, **e**, **f** Key fit parameters versus temperature T. We show the resonance frequency shift $\Delta\omega_0 = \omega_0(T) - \omega_0(T_{\text{min}} = 0.2\,\text{K})$ as well as the internal and external quality factors Q_{int} and Q_{ext}. All parameters show a nearly constant value for $T \lesssim 2.5$ K, and a considerable decrease with increasing temperature for larger T. We attribute the discontinuity in Q_{ext} at around 1.7 K to aluminum coaxial cables and/or aluminum wire-bonds becoming superconducting. The decrease of ω_0 and Q_{int} with increasing T can be explained by thermal quasiparticles.

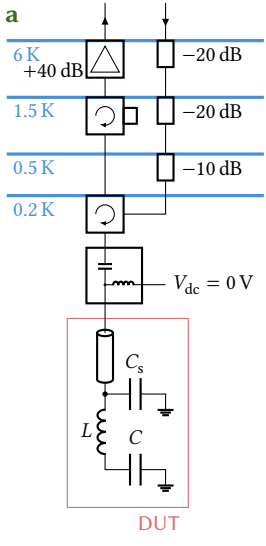
a
6 K
+40 dB
−20 dB
1.5 K
−20 dB
0.5 K
−10 dB
0.2 K
V_{dc} = 0 V
C_s
L
C
DUT

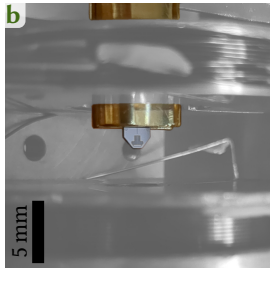
b
5 mm

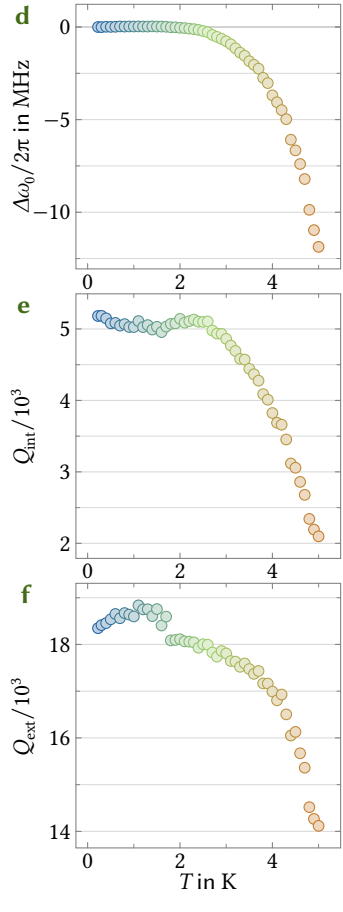
d
$\Delta\omega_0/2\pi$ in MHz
0
−5
−10
0
2
4
e
$Q_{int}/10^3$
5
4
3
2
f
$Q_{ext}/10^3$
18
16
14
T in K

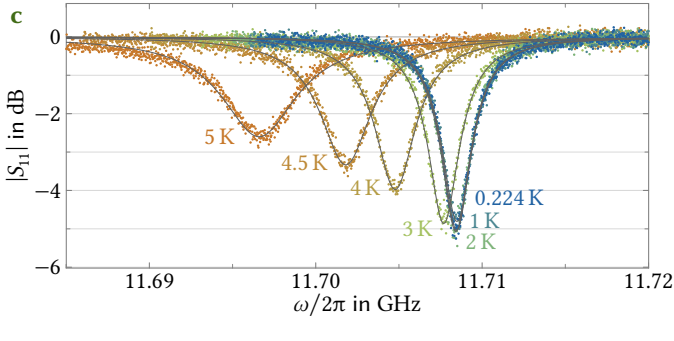
c
$|S_{11}|$ in dB
0
−2
−4
−6
5 K
4.5 K
4 K
3 K
0.224 K
1 K
2 K
11.69
11.70
11.71
11.72
$\omega/2\pi$ in GHz

the intensity of the laser pulses exciting the atoms to the Rydberg manifold from the electronic ground state, cf. Figure 3.1. In order to achieve $\Omega_N = \sqrt{N_{\mathrm{Ry}}}\,\Omega_0 > \kappa$, we need $N_{\mathrm{Ry}} \gtrsim 10$, which is a feasible value for us considering a realistic Rydberg blockade radius on the order of 10 µm [64, 65]. Further optimization strategies for considerably enhanced vacuum Rabi frequencies of coupling to a single atom are discussed in Section 3.9.

3.7 Measured cavity parameters vs V_{dc}

As a second important device characterization we apply a dc voltage V_{dc} to the superconducting resonator, which will later be important to compensate for parasitic dc electric fields from e.g. surface adsorbates and to tune the Rydberg transition frequency into (and out of) resonance with the cavity. Hence, we apply a variable V_{dc} to the dc line of the bias-tee, monitor a possible leakage current I_{dc} and measure the cavity reflection S_{11} for each static value of V_{dc}. The corresponding results are summarized in Figure 3.5. For voltages up to $V_{\mathrm{dc}} = 10\,\mathrm{V}$, the cavity lineshape and resonance frequency remain unmodified to the naked eye. We observe, however, a small leakage current of up to ~500 pA which corresponds to a resistance of 20 GΩ. This value is consistent with earlier observations in analogous systems with trilayer parallel-plate capacitors made with Si_3N_4 [54], but we also cannot exclude a contribution from leakage currents through the bias-tee or the dc wires and connectors.

From fits to the cavity resonance, we find a small shift of the resonance frequency with increasing voltage, cf. Figure 3.5c, and constant values of Q_{int} and Q_{ext} (not shown). However, due to the smallness of the frequency shift, which is comparable to the uncertainty of its absolute value, it is not completely clear whether it is an actual change of the resonance frequency or an artifact e.g. due to changed properties of the bias-tee. On one hand, a red-shift would for instance be compatible with an electrostatic compression of the dielectric in the shunt capacitor; on the other hand, this should also lead to a change of Q_{ext}. A future cavity with a much higher Q could provide more insight into this effect. In essence though, the cavity is very robust with respect to an applied dc voltage up to at least 10 V, which we expect to be more than sufficient considering that this corresponds to an dc electric field of $E_{\mathrm{dc}} \approx 370\,\mathrm{V\,cm^{-1}}$ at the position of the atoms. Typical adsorbate fields are on the order of $10\,\mathrm{V\,cm^{-1}}$ [28, 37, 39] and the Rydberg transition is optimally tuned into resonance at $\lesssim 2\,\mathrm{V\,cm^{-1}}$, cf. Figure 3.1. We finally note that we have applied even higher voltages to other chips at 4.2 K which revealed that the breakdown voltage of the shunt capacitor seems to be around $V_{\mathrm{dc}} \approx 40\,\mathrm{V}$.

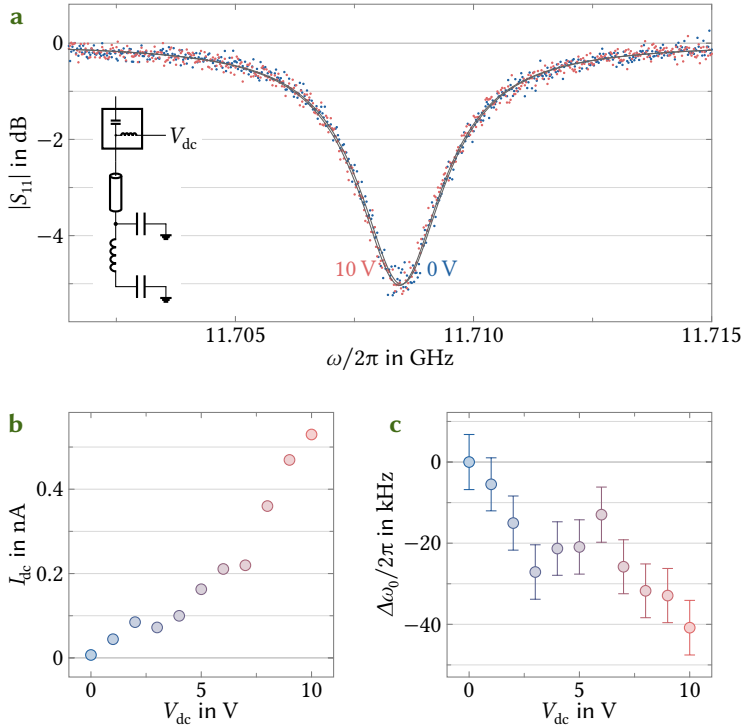

Figure 3.5: Cavity characterization with applied bias-voltage V_{dc}. **a** Reflection $|S_{11}|$ of the microwave resonator at $T = 0.2\,\mathrm{K}$ with $V_{dc} = 0\,\mathrm{V}$ and $V_{dc} = 10\,\mathrm{V}$ in direct comparison. Dots are experimental data and gray lines are overlayed fit curves. No significant shift or widening of the resonance dip is discernible, indicating the robustness of the cavity against dc voltages up to at least 10 V. **b** Leakage current I_{dc} recorded during measurements with different V_{dc}. The observed resistance of $\sim 20\,\mathrm{G\Omega}$ is in the range expected for leakage through the Si_3N_4 shunt capacitor [54]. **c** Resonance frequency shift $\Delta\omega_0$ versus applied dc voltage. Error bars indicate the estimated standard errors as given by the fit routine.

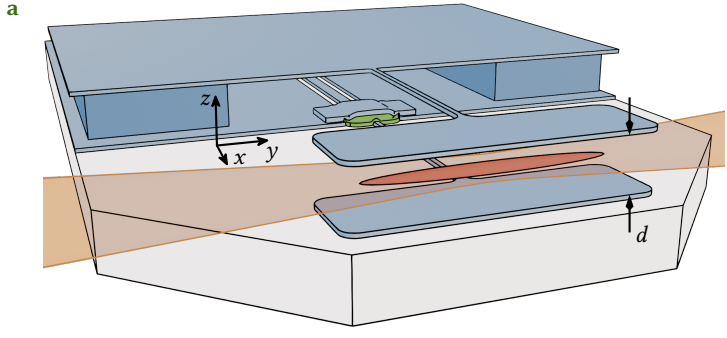
a
z
x
y
d

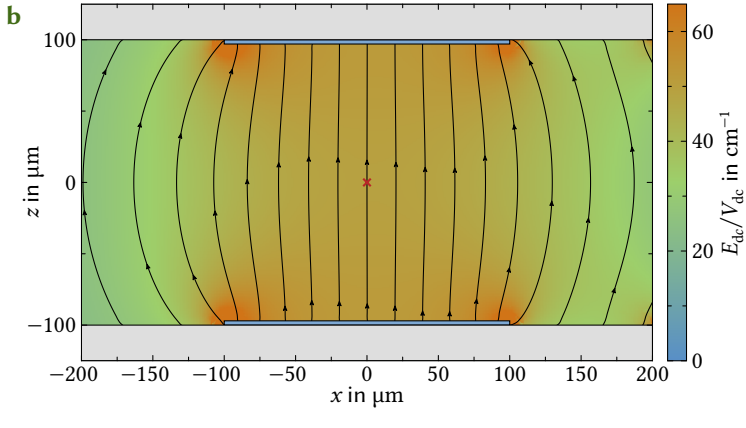
b
100
0
−100
z in µm
−200
−150
−100
−50
0
50
100
150
200
x in µm
60
40
20
0
E_{dc}/V_{dc} in cm^{-1}

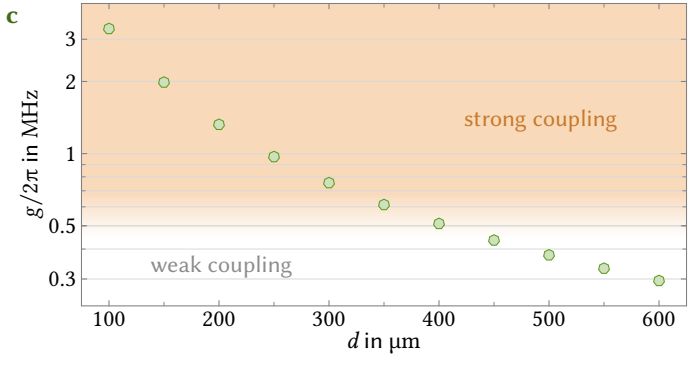
c
3
2
1
0.5
0.3
$g/2\pi$ in MHz
strong coupling
weak coupling
100
200
300
400
500
600
d in µm

3.8 A concept for maximal field homogeneity

Before we conclude our report, we will present a modified concept for the superconducting cavity as a perspective possibility which comes with considerable advantages, but at the expense of a higher complexity. The basic idea is presented in Figure 3.6a and is not based on a single superconducting chip but on two nearly identical chips facing each other with a distance d in a flip-chip assembly. Each of the two chips contains an inductive wire and one half of a (vacuum) parallel plate capacitor, inside of which the dipole trap with the cold atoms will be located. As a spacer between the chips, a superconducting foil, low-loss dielectric patches or indium bump bonds might be suitable choices. The bottom chip furthermore contains the microwave feedline and the shunt capacitor as did the 2D implementation discussed above. The major advantages of this approach lie in the symmetry and in the spatial homogeneity of the electric dc and microwave fields.

For a completely symmetric set of chips, the adsorbate fields from the two chips might either cancel in the center of the capacitor or combine to a homogeneous field as well, which can then easily be compensated by an applied field E_{dc}. Even if the parasitic fields remain inhomogeneous or are accompanied by a considerable gradient, it will be possible to relocate the atoms in the capacitor volume to a more favorable position by shifting the laser axis, affecting only the adsorbate fields with the shift. The property of position-invariance is also very advantageous in case there are any vibrations of the superconducting chips with respect to the dipole trap, e.g. induced by the refrigerator pulse-tube. In principle, vibrations could

Figure 3.6: Modified cavity layout for improved field homogeneity and coupling strength. a Schematic of an alternative design consisting of two chips flipped on top of each other. The bottom chip is similar to the design presented in Figure 3.1, except that there is no ground plane close to the capacitance plate. The top chip (substrate not shown for clarity) features an identical capacitance plate which is connected by a mirror-inductance to a large ground plane. Two cuboid pieces of niobium control the distance d between the two chips while simultaneously acting as superconducting vias connecting the ground planes (other materials are also under consideration). **b** Cross-sectional schematic at the position of the atomic ensemble and the numerically simulated ratio of dc electric field strength E_{dc} over applied voltage V_{dc} versus position for $d = 200\,\mu\mathrm{m}$, $a = 200\,\mu\mathrm{m}$ and $l = 400\,\mu\mathrm{m}$; electric field lines are indicated. Values close to the plate edges that exceed the scale of the colorbar are drawn in the orange of the maximum. Thanks to the parallel plate capacitor geometry, the field around the atomic ensemble position (marked ×) is very homogeneous. **c** Expected coupling strength g for different chip distances d (other parameters are scaled with d, see main text) and a resonance frequency of $\omega_0 = 2\pi \cdot 11\,\mathrm{GHz}$. Assuming a resonator quality factor around 10 000, we reach the strong coupling regime for plate distances below 350 µm, and for the smallest investigated distance $d_{\mathrm{min}} = 100\,\mu\mathrm{m}$ we get $2g_{\mathrm{max}} = 2\pi \cdot 6.6\,\mathrm{MHz} = 6\kappa$.

be compensated by a real-time feedback to the dipole-trap position, however the experiment would be much simpler, and most likely more stable, if vibrations did not matter at all, just as it is the case for homogeneous capacitor fields. Finally, homogeneous fields will minimize any inhomogeneous broadening, making coherent state transfer between the superconducting circuit and the atoms much easier.

Beyond the aspect of increased homogeneity, the 3D approach may also lead to higher vacuum Rabi frequencies than the planar version. To demonstrate the possibility to reach the strong-coupling regime without a strict parameter optimization, we assume that the total circuit capacitance is defined by the two parallel plates and calculate the corresponding dc capacitance C_{3D} including the two substrates by means of *Comsol Multiphysics*. Just as in the 2D case, we also extract the field $\boldsymbol{E}_{\mathrm{dc}}(\boldsymbol{r})$ for an applied voltage $V_{\mathrm{dc}} = 1\,\mathrm{V}$ and calculate g for a resonance frequency $\omega_0 = 2\pi \cdot 11\,\mathrm{GHz}$ as before.

In order to achieve maximum coupling strength, the capacitor dimensions should be chosen just large enough to ensure field homogeneity in the region of the atom cloud. To that end, we choose $a = d$ and $l = \min(2d, 250\,\mu\mathrm{m})$ for a given chip distance d. The smallest chip distance ensuring only a negligible amount of laser power directly reaching the two chips is $\sim 100\,\mu\mathrm{m}$. Since such a small laser-chip distance might not be practically feasible, we also consider chip distances up to 600 µm in our simulations. See Section 3.18 for a more detailed discussion of these parameter considerations.

The resulting simulated coupling rates are plotted in Figure 3.6c. Notably, the transition to the strong coupling regime $2g > \kappa$ is observed for distances $d \lesssim 350\,\mu\mathrm{m}$ if we assume a realistic cavity quality factor $Q \sim 10\,000$. For the smallest possible distance $d_{\min} = 100\,\mu\mathrm{m}$ we even get $g_{\max} = 2\pi \cdot 3.3\,\mathrm{MHz}$, which corresponds to $2g = 6\kappa$ in the case of $Q = 10\,000$ or $2g = \kappa$ in the case $Q = 1656$.

An intuitive measure for the field homogeneity, taking the atom distribution into account, is the weighted standard deviation of the relative difference from the field strength E_0 in the center of the cloud

$$\eta = \sqrt{\int_{\mathbb{R}^3} \rho_{\mathrm{sp}}(\boldsymbol{r}) \left(\frac{E(\boldsymbol{r})}{E_0} - 1\right)^2 \mathrm{d}\boldsymbol{r}}. \tag{3.10}$$

Since contributions outside the cloud region defined by d_{Rb} and l_{Rb} are suppressed by ρ_{sp}, it is sufficient to consider the integral in that region. Evaluating the expression numerically using the field strength $E = |\boldsymbol{E}_{\mathrm{dc}}|$ from the *Comsol Multiphysics* simulations, we obtain $\eta_{2D} = 0.5\,\%$ for the 2D implementation discussed above. The 3D layout with $d = 450\,\mu\mathrm{m}$ has a comparable coupling strength and for this we find $\eta_{3D,450} = 0.02\,\%$, an improvement by a factor of 25. While it increases the coupling strength, scaling the layout to smaller values of d also causes the homogeneous region to shrink and thus increases the inhomogeneity across the atom cloud. For

$d = 200\,\mu\text{m}$ we find $\eta_{3\text{D},200} = 0.2\,\%$, a somewhat less impressive improvement over the 2D implementation, but with a threefold higher coupling rate. This value can be further improved by optimizing the capacitor shape, but this may not be necessary in the end, as inhomogeneities become less relevant further into the strong coupling regime [66].

We note that both chips in the flip-chip assembly could be supplemented with a ground plane surrounding the capacitor plates in a sufficiently large distance such that the dc and microwave electric fields are still concentrated in the space between the two rectangular plates on the two chips. We omitted this potential ground plane here for the sake of simplicity. If included, we expect it to somewhat reduce the field homogeneity and the vacuum Rabi frequency, but at the same time lead to a suppression of potential dipole-radiation losses into free space by counter-charges. The optimal configuration remains to be investigated in the future.

3.9 Discussion

In this chapter we have presented the engineering and optimization of a superconducting microwave chip for the tunable coupling to optically trapped ultra-cold Rydberg atoms in a dilution refrigerator. We focused on a suitable chip outline, an optimized laser-chip distance and on the ideal circuit parameter-set for maximized interaction rates. Despite conservative estimates of various parameters such as the atomic ensemble temperature and a moderate cavity quality factor in the experimental implementation of the superconducting resonator of $Q_{\text{int}} \sim 5200$, our device allows for a single-atom vacuum Rabi frequency in proximity to the strong-coupling regime with $\Omega_0 \sim \kappa/3$. Since we intend to couple to an atomic ensemble, however, we expect a single-photon coupling-enhancement by the root of the number of atoms the laser excited to the Rydberg manifold $\sqrt{N_{\text{Ry}}}$. Thus, we reach the strong coupling region for $N_{\text{Ry}} > 10$. For future devices we furthermore believe to be able to increase Q_{int} by at least one order of magnitude. Finally, we have presented a perspective flip-chip cavity layout which could lead to enhanced field homogeneity and potentially larger coupling rates.

Even the planar implementation could be re-designed in the future to allow for further increased vacuum Rabi frequencies if it turns out that the atom characteristics permit it. If the atomic ensemble in the dipole trap really can be cooled to $T \lesssim 1\,\mu\text{K}$ and if the surface adsorbate fields can be compensated sufficiently well with the applied dc voltage, the entire circuit and chip could be implemented in a much smaller version. The capacitance length could be reduced by a factor of five, and so could the chip width by a corresponding amount. As a consequence, the laser could be focused to $w_{\text{dp}} = 10\,\mu\text{m}$ and the trap-center could approach the chip to $\sim 40\,\mu\text{m}$, which in turn allows for a smaller capacitor plate width and a smaller

gap to ground. Overall, these reductions alone would lead to an increase in E_{zpf} by a factor of ~ 5. More sophisticated possibilities would include deep etching of the substrate to minimize the stray capacitance through the substrate or the use of a substrate material with much smaller ϵ_{r}. To compensate for the strongly reduced C by all these techniques, we could increase the inductance by using a spiral inductor or a very thin film with high kinetic inductance.

Our work uncovered an extensive overview over most of the critical aspects when interfacing superconducting microwave chips with optically trapped atoms and demonstrates a way to deal with the corresponding challenges in order to find a satisfying best-balance compromise. The laid out strategies have the potential to bring dc-tunable and realistic superconductor-atom hybrid systems in the strong-coupling regime into experimental reality. Once implemented, those systems can serve as foundations for novel quantum gates on superconducting microwave chips and towards unexplored regimes of light-matter interaction. On the technological side it is promising for advances in quantum frequency conversion and for the implementation of atomic quantum memories on superconducting chips.

To complete our deliberations, the remaining sections of this chapter contain additional details on some of the points discussed above, including comprehensive descriptions of relevant calculations and simulations as well as information on device fabrication and mounting.

3.10 Stark map of the relevant Rydberg states

The (non-differential) Stark map of Rydberg state energies (calculated as described in [28, 55]) in the vicinity of the states $|r_1\rangle$ and $|r_2\rangle$ making up the target transition is shown in Figure 3.7. The differential Stark map in Figure 3.1d results from this after subtracting $\mathcal{E}_1$ from all lines.

We note that we omit all the possible transitions to negative relative frequencies in Figure 3.1, although they will also couple to the microwave cavity once they are resonant with it. Their dipole transition matrix elements and corresponding coupling rates are several orders of magnitude smaller than that of the target transition, so they are negligible to first order, and their inclusion in Figure 3.1d would lead to an overcrowded image with considerably reduced clarity.

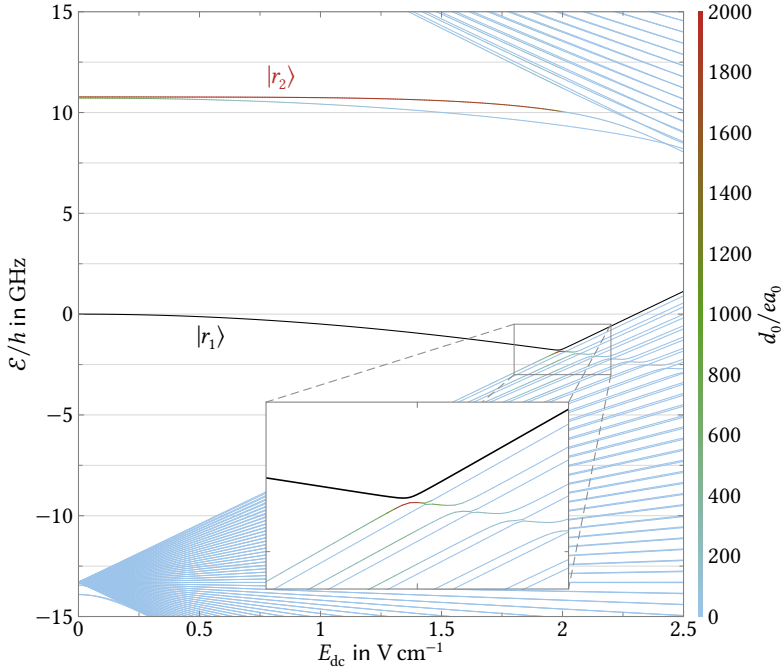

Figure 3.7: Simulated Rydberg state energies in the vicinity of the target transition. The black line marks the initial state of the targeted high-d_0 transition $|r_1\rangle \rightarrow |r_2\rangle$, which at zero field corresponds to $|59\mathrm{P}_{3/2}, m_j = \frac{3}{2}\rangle \rightarrow |58\mathrm{D}_{5/2}, m_j = \frac{3}{2}\rangle$. The energy zero point is chosen to be $\mathcal{E}_1$ at $E_{\mathrm{dc}} = 0$. For all states besides $|r_1\rangle$, the color indicates the transition dipole moment d_0 of the transition from $|r_1\rangle$ to that state, cf. Figure 3.1d, with $|r_2\rangle$ appearing red due to the high associated transition dipole moment. At $E_{\mathrm{dc}} \approx 2\,\mathrm{V\,cm^{-1}}$, the energy of $|r_1\rangle$ bends upwards due to an avoided crossing with a lower energy state, shown magnified in the inset. This results in all transition frequencies $\mathcal{E}_{tr} = \mathcal{E} - \mathcal{E}_1$ shown in Figure 3.1d bending down at that field strength.

3.11 Atom oscillation frequencies in a dipole trap

The radial and longitudinal (axial) oscillation frequencies in the dipole trap ω_r and ω_y, respectively, determine the extension of the atomic cloud as described by (3.5). We find the oscillation frequencies by revisiting the second-order Taylor expansion of a symmetric potential $U(x) = U(-x)$ around its minimum

$$U(x) = U(0) + \frac{1}{2}\partial_x^2 U(0) \cdot x^2 + \mathcal{O}(x^4) \tag{3.11}$$

and the differential equation of a particle with mass m in this potential (we neglect damping and external forces for the sake of simplicity)

$$m\ddot{x} + \partial_x^2 U(0) \cdot x = 0. \tag{3.12}$$

The solution of (3.12) is a harmonic oscillation with (angular) frequency

$$\omega_x = \sqrt{\frac{\partial_x^2 U(0)}{m}}. \tag{3.13}$$

To find the frequencies for rubidium atoms in the dipole trap, we therefore need to calculate

$$\omega_r = \sqrt{\frac{\partial_r^2 U_{\mathrm{dp}}(\mathbf{0})}{m_{\mathrm{Rb}}}} \tag{3.14}$$

$$\omega_y = \sqrt{\frac{\partial_y^2 U_{\mathrm{dp}}(\mathbf{0})}{m_{\mathrm{Rb}}}}. \tag{3.15}$$

The second partial derivatives of the Gaussian (radial) and the Lorentzian (axial) profile of the trap potential around their corresponding extrema are

$$\partial_r^2 \exp\left(-\frac{2r^2}{w_{\mathrm{dp}}^2}\right)\Big|_{r=0} = -\frac{4}{w_{\mathrm{dp}}^2} \tag{3.16}$$

$$\partial_y^2 \left(1 + \frac{y^2}{l_{\mathrm{R}}^2}\right)^{-1}\Big|_{y=0} = -\frac{2}{l_{\mathrm{R}}^2}. \tag{3.17}$$

Combining everything and plugging in all relevant numbers, we find

$$\omega_r = 2\pi \cdot 4.1\,\mathrm{kHz} \tag{3.18}$$

$$\omega_y = 2\pi \cdot 50\,\mathrm{Hz} \tag{3.19}$$

and with $m_{\mathrm{Rb}} = 86.9\,\mathrm{Da}$ we arrive at the values for σ_r and σ_y discussed in the context of Figure 3.2.

3.12 Estimating the laser power reaching the chip

Since optical photons can break Cooper pairs, destroy superconductivity and heat the mixing chamber of a dilution refrigerator, we estimate an upper threshold for the total optical power reaching the superconducting structures in our setup and adjust the laser-chip distance and the laser profile accordingly. We consider two contributions and find that both are sufficiently small to be neglected when the parameters are chosen as discussed in the context of Figure 3.2.

The first way a photon from the dipole-trap laser can reach the chip is by directly hitting the superconductor in the Gaussian tail of the beam profile. At the chip edge, i.e. $y = l_{\mathrm{ch}}/2 = 0.8\,\mathrm{mm}$, the beam radius is $w_{\mathrm{e}} \approx 20\,\mu\mathrm{m}$, meaning that the center of the beam is located at $z_0 = 80\,\mu\mathrm{m} \approx 4w_{\mathrm{e}}$ above the chip surface. We therefore calculate the total power reaching the chip on or below its surface line and find

$$\begin{aligned} P_{\mathrm{dir}} &= \sqrt{\frac{2}{\pi}}\frac{P_{\mathrm{dp}}}{w_{\mathrm{e}}}\int_{z_0}^{\infty}\exp\Big(-\frac{2\tilde{z}^2}{w_{\mathrm{e}}^2}\Big)\,\mathrm{d}\tilde{z} \\ &= \frac{P_{\mathrm{dp}}}{2}\Big(1-\mathrm{erf}\Big(\sqrt{2}\frac{z_0}{w_{\mathrm{e}}}\Big)\Big) = 66\,\mathrm{aW} \end{aligned} \tag{3.20}$$

for $P_{\mathrm{dp}} = 50\,\mathrm{mW}$, which is clearly negligible [67, 68]. Note that if the chip were not tapered but kept its full 3.5 mm width at the position of the laser beam, while also maintaining $z_0 = 80\,\mu\mathrm{m}$ and $w_{\mathrm{dp}} = 15\,\mu\mathrm{m}$, the power incident on the superconductor would increase to $\sim 38\,\mathrm{nW}$.

The second path a photon from the dipole laser can take is being off-resonantly scattered by the atoms in the trap. The scattering rate of an atom at position $\boldsymbol{r}$ in units of scattered photons per atom per second is given by [31]

$$\begin{aligned} \Gamma_{\mathrm{sc}}(\boldsymbol{r}) = \Bigg(&\frac{\pi c_0^2}{2\hbar\omega_1^3}\Big(\frac{\omega_{\mathrm{dp}}}{\omega_1}\Big)^3\Big(\frac{\Gamma_1}{\omega_1-\omega_{\mathrm{dp}}}+\frac{\Gamma_1}{\omega_1+\omega_{\mathrm{dp}}}\Big)^2 \\ &+\frac{\pi c_0^2}{\hbar\omega_2^3}\Big(\frac{\omega_{\mathrm{dp}}}{\omega_2}\Big)^3\Big(\frac{\Gamma_2}{\omega_2-\omega_{\mathrm{dp}}}+\frac{\Gamma_2}{\omega_2+\omega_{\mathrm{dp}}}\Big)^2\Bigg) I_{\mathrm{dp}}(\boldsymbol{r}). \end{aligned} \tag{3.21}$$

For a nearly constant intensity at the center of the trap $I_{\mathrm{dp}} = 2P_{\mathrm{dp}}/\pi w_{\mathrm{dp}}^2$ we find $\Gamma_{\mathrm{sc}} = 2\pi\cdot 15\,\mathrm{s}^{-1}$. Assuming a total atom number of $N_{\mathrm{at}} = 10^6$ in the trap (though 10^4 is more realistic), we obtain as total scattered power

$$P_{\mathrm{sc}} = \hbar\omega_{\mathrm{dp}}\Gamma_{\mathrm{sc}}N_{\mathrm{at}} \approx 23\,\mathrm{pW}. \tag{3.22}$$

This is again negligibly small – even if we assume that all of it is absorbed by the superconductor.

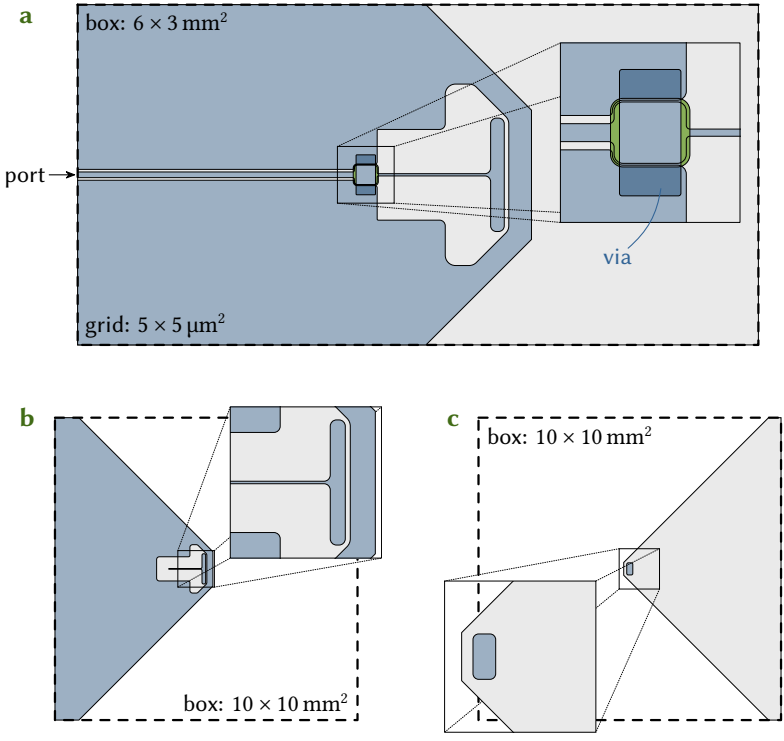

Figure 3.8: Layouts used for rf and dc simulations. Layout for **a** microwave simulation using *Sonnet* and **b** for dc simulations using *Comsol Multiphysics*. **c** Analogous layout for the perspective 3D design. The colors indicate the material, as in previous figures: Gray for sapphire, blue for niobium and green for silicon nitride. In addition, the vias allowing current flow between the bottom and the top layer of the shunt capacitor in *Sonnet* simulations are indicated by a darker blue. The simulation boxes are indicated as thick dashed lines and their dimensions are noted in the drawings. Insets show enlarged regions with small structures. The dimensions of the 2D resonator shown in b correspond to the fields shown in Figures 3.1c and 3.3f, the ones of the 3D resonator in c to those shown in Figure 3.6b.

3.13 Details of simulations with *Sonnet* and *Comsol Multiphysics*

Sonnet simulations were performed using a 6 mm × 3 mm × 2 mm simulation box with the niobium film placed in its center, atop a 330 µm thick sapphire substrate ($\epsilon_r = 10$). We choose the box somewhat smaller than the real device in order to keep simulation time manageable. Due to a software limitation, the substrate fills the entire profile of the simulation box, i.e. it does not follow the taper of the niobium layer. The two niobium layers are modeled with a typical surface inductance value of $L_\square = 0.13\,\mathrm{pH/\square}$.* They are separated by a 100 nm thick silicon nitride brick ($\epsilon_r = 7.5$) in the center and connected by lossles vias on either side. A schematic of such a layout is shown in Figure 3.8a. Since the smallest structure (the inductive wire) has a width of 20 µm, a grid size of 5 µm × 5 µm is sufficient.

For the dc field simulations using *Comsol Multiphysics* we only consider the components that determine the resonator capacitance. That is, we omit the shunt capacitor, which affects the effective capacitance in principle but only with a small contribution, as well as the feedline. We include the inductive wire and add additional spacing to ground around its back end, as shown in Figure 3.8b. In order to minimize distortions of the field in the region of interest (boundary condition: no charges on the simulation box), we choose a large box of 10 mm × 10 mm × 10 mm, with the niobium film placed in its center on top of a sapphire substrate, like in the *Sonnet* layout. The chip is positioned in such a way that the capacitor gap, above which the atom cloud will be positioned, is located in the exact center of the box. Since the total width of the chip was not determined yet and should not affect the relevant fields much, the chip taper is extended all the way to the box edges. We triangulate the simulation mesh very finely (down to 1 µm) in the region of the capacitor and the atom cloud, and more loosely (up to 500 µm) far away from the capacitor, where field gradients are low.

The layout for the dc simulations for the perspective 3D design is essentially the same, except that the ground plane and the inductive wire are omitted, leaving only the capacitor plate, and a second, identical chip is placed above, facing the first. One such chip layout can be seen in Figure 3.8c. The center between the two plates, where the atom cloud will be positioned, is located in the center of the simulation box, with the two chips symmetrically below and above it.

*This value for the surface impedance is obtained by $L_\square = \mu_0 \lambda_L$ with a typical value for sputtered niobium films $\lambda_L \approx 100$ nm. Since our actual λ_L is usually closer to $\lambda_L^* \approx 130$ nm and our bottom-layer (top-layer) film thickness t_{Nb} is 80 nm (120 nm), a more accurate value would be $L_\square^* = \mu_0 \lambda_{eff}^* = \mu_0 \lambda_L^* \coth(t_{Nb}/\lambda_L^*) = 0.30\,\mathrm{pH/\square}$ for the bottom layer and $L_\square^* = 0.22\,\mathrm{pH/\square}$ for the top layer [69, 70]. However, this adjustment would only change the resonance frequencies by ~0.1 %, which is below the accuracy of the simulation and the chip fabrication; therefore it has no significant impact on the current analysis. It should however be kept in mind for e.g. devices fabricated from even thinner or more disordered films.

3.14 Standing-wave correction of the circuit capacitance

The dimensions of the circuit, in particular the inductive wire length s of the resonator, are not sufficiently small to neglect the finite microwave wavelength at 11 GHz when analyzing its resonance properties. In other words, the wire cannot be treated as a simple lumped element inductance, but – in combination with the ground planes – shall be modeled as a distributed element coplanar waveguide of length $\tilde{s} = s - q$ in series with a short, purely inductive wire of length q, cf. Figure 3.9. We neglect any capacitance contribution from the wire part with length q, since it is the farthest from the ground planes.

Given the CPW and substrate dimensions (inductive wire width 20 µm, distance to ground plane 390 µm, substrate thickness 330 µm, average dielectric constant of sapphire $\epsilon_r = 10$), we find the CPW capacitance per unit length $C' = 56\,\mathrm{pF\,m^{-1}}$ with an effective permittivity of $\epsilon_{\mathrm{eff}} = 5.06$ [71]. This yields the phase velocity $v_\phi = c_0/\sqrt{\epsilon_{\mathrm{eff}}} = 1.33 \cdot 10^8\,\mathrm{m\,s^{-1}}$, corresponding to a resonance wavelength $\lambda_0 = 2\pi v_\phi/\omega_0 = 12.1\,\mathrm{mm}$ for $\omega_0 = 2\pi \cdot 11\,\mathrm{GHz}$. Thus, a corresponding quarter-wave standing-wave cavity would have a length of $\lambda_0/4 = 3.0\,\mathrm{mm}$, only about $2.2 \cdot \tilde{s}_{\mathrm{max}}$ with $\tilde{s}_{\mathrm{max}} = 1.4\,\mathrm{mm}$ being the largest considered length, confirming that modeling it as a lumped element inductance is not appropriate.

For the characteristic impedance of the CPW segment with length $\tilde{s}$, we find $Z_1 = 1/v_\phi C' = 135\,\Omega$ (the kinetic inductance contribution can be neglected for our film thickness [72]; it would only change Z_1 by $<1\,\%$, impacting the coupling strength g by $<0.2\,\%$). Seen from the side of the remaining cavity, the short-ended CPW has the input impedance

$$Z_{\mathrm{in}} = \mathrm{i}Z_1 \tan\left(2\pi\frac{\tilde{s}}{\lambda}\right) \tag{3.23}$$

with $\lambda = 2\pi v_\phi/\omega$. We omit the effect of the shunt capacitance C_s on the boundary condition or the effective total capacitance as well as any dissipative contributions, since they are small. The resonance condition can be written as

$$\mathrm{i}Z_1 \tan\left(2\pi\frac{\tilde{s}}{\lambda_0}\right) = -\left(\mathrm{i}\omega_0 L_0 + \frac{1}{\mathrm{i}\omega_0 C_0}\right) \tag{3.24}$$

where C_0 is the capacitance of the plate only and L_0 is the inductance of the circuit without the CPW part (cf. Figure 3.9).

Now assume that at some moment we have the microwave voltage V_0 at the plate capacitance C_0. The voltage V_1 at the input of the transmission line at that moment can be obtained from considering everything connected to the capacitance

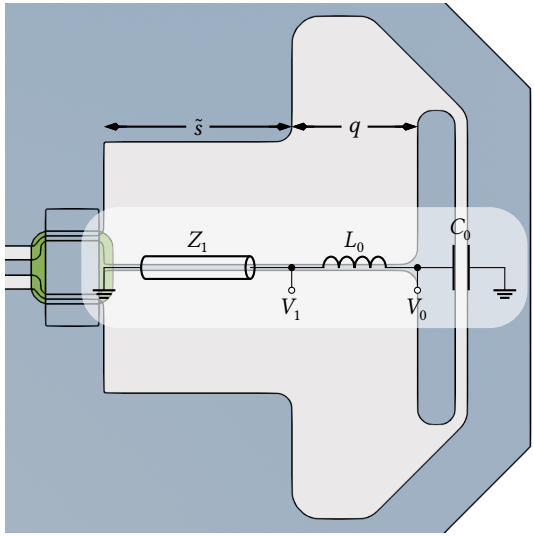

Figure 3.9: Model for the standing-wave correction of the circuit capacitance. We model the leftmost inductive wire section with length $\tilde{s} = s - q$ as a CPW with characteristic impedance Z_1 and the remaining part of length q as a lumped-element inductor L_0. With the capacitance contribution C_0 of the gap between the capacitor plate and ground as well as the voltage V_0 across that gap we can then calculate the voltage V_1 across the CPW. This allows us to determine the energy E_{CPW} stored in the CPW fields and finally the contribution $C_{\mathrm{CPW}}(\tilde{s})$ of the CPW to the effective resonator capacitance C. See main text for the detailed calculation.

to be a voltage divider with

$$V_1 = V_0 \frac{Z_1 \tan(2\pi\tilde{s}/\lambda_0)}{\omega_0 L_0 + Z_1 \tan(2\pi\tilde{s}/\lambda_0)} \tag{3.25}$$

$$= V_0 \omega_0 C_0 Z_1 \tan\left(2\pi\frac{\tilde{s}}{\lambda_0}\right) \tag{3.26}$$

where in the last step we used (3.24).

A final ingredient is the capacitive energy on the CPW, which is given by

$$E_{\mathrm{CPW}} = \frac{1}{2} C' V_\lambda^2 \int_0^{\tilde{s}} \sin^2\left(2\pi\frac{x}{\lambda_0}\right) \mathrm{d}x \tag{3.27}$$

with V_λ the hypothetical maximum voltage at $x = \lambda_0/4$ and the boundary condition

$$V_1 = V_\lambda \sin\left(2\pi\frac{\tilde{s}}{\lambda_0}\right). \tag{3.28}$$

After integration and some algebra we get

$$E_{\mathrm{CPW}} = V_0^2(\omega_0 C_0 Z_1)^2 C' \frac{\tilde{s} - \lambda_0/4\pi \cdot \sin(4\pi\tilde{s}/\lambda_0)}{4\cos^2(2\pi\tilde{s}/\lambda_0)} \tag{3.29}$$

from which we conclude the effective capacitance contribution of the CPW to be

$$C_{\mathrm{CPW}}(\tilde{s}) = (\omega_0 C_0 Z_1)^2 C' \frac{\tilde{s} - \lambda_0/4\pi \cdot \sin(4\pi\tilde{s}/\lambda_0)}{2\cos^2(2\pi\tilde{s}/\lambda_0)}. \tag{3.30}$$

With *Comsol Multiphysics*, we simulated the dc capacitance C_{dc} including the inductive wire, for the effective total capacitance C of our cavity we thus calculate

$$C = C_0 + C_{\mathrm{CPW}}(\tilde{s}) = C_{\mathrm{dc}} - C'\tilde{s} + C_{\mathrm{CPW}}(\tilde{s}), \tag{3.31}$$

the result of which is plotted in Figure 3.3c. Note that from our data there we can also extrapolate the inductance L_0 as the value of the nearly linear $L(s)$ for $s = q = 400\,\mu\mathrm{m}$, which we find to be $L_0 \approx 0.7\,\mathrm{nH}$.

3.15 Device fabrication

The device fabrication of the trilayer chip is executed in four steps. These steps are individually described below. Optical microscopy images of a typical device are shown in Figure 3.10.

Step 1: Microwave cavity patterning. The fabrication starts with dc-magnetron sputtering of 80 nm thick niobium on top of a two-inch r-cut and single-side-polished sapphire wafer. The nominal thickness of the wafer is 330 µm. For optical lithography, the entire wafer is covered with ma-P 1215 photoresist by spin-coating (resist thickness ~1.5 µm) and loaded into a system for maskless optical lithography ($\lambda_{\mathrm{litho}} = 365\,\mathrm{nm}$). After exposure, the resist is developed in ma-D 331/S for 35 s, followed by dry-etching of the pattern into the Nb film using reactive ion etching with SF_6. For cleaning and removal of the remaining resist, the wafer gets rinsed in multiple subsequent baths of acetone, isopropanol and ultra-pure water.

Figure 3.10: Optical microscopy images of a typical device. a A fully fabricated chip mounted in a sample holder. Wire bonds to the PCB at the top as well as to the sample holder body on the sides serve both as electric contacts and as mechanical fasteners holding the chip. The niobium appears black due to the lighting conditions, the transparent sapphire shows the color of the sample holder gold plating at the top and that of the microscope table at the bottom. Red rectangles mark the position of the shunt and the resonator capacitor shown in **b** and **c**, respectively, rotated by 90°. The structures have been colored according to their material: Blue for niobium, green for silicon nitride and gray for sapphire. Chipping caused by the dicing step at the end of fabrication can be seen at the right edge of c.

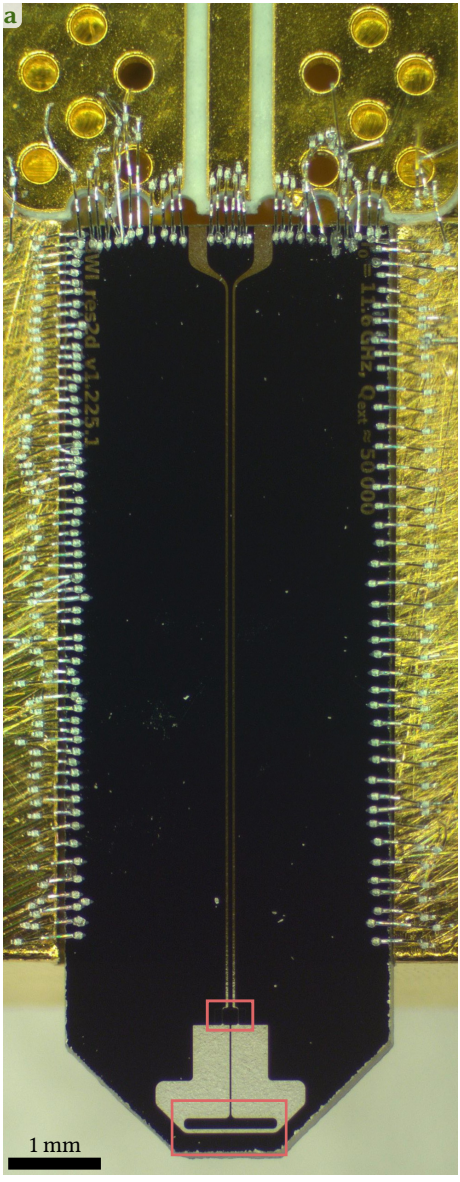
a
1 mm

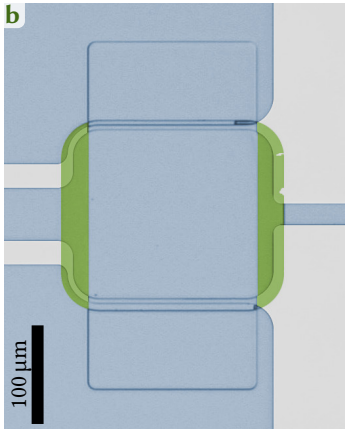
b
100 µm

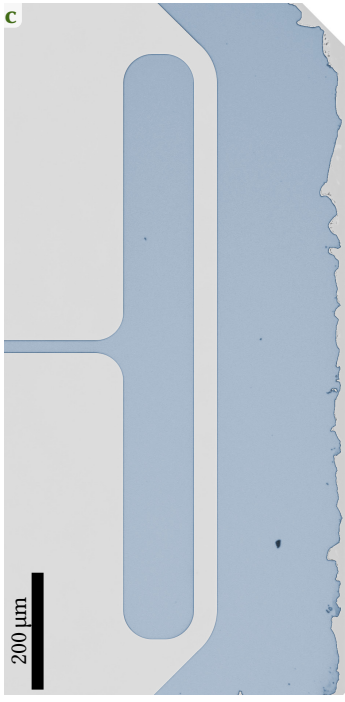
c
200 µm

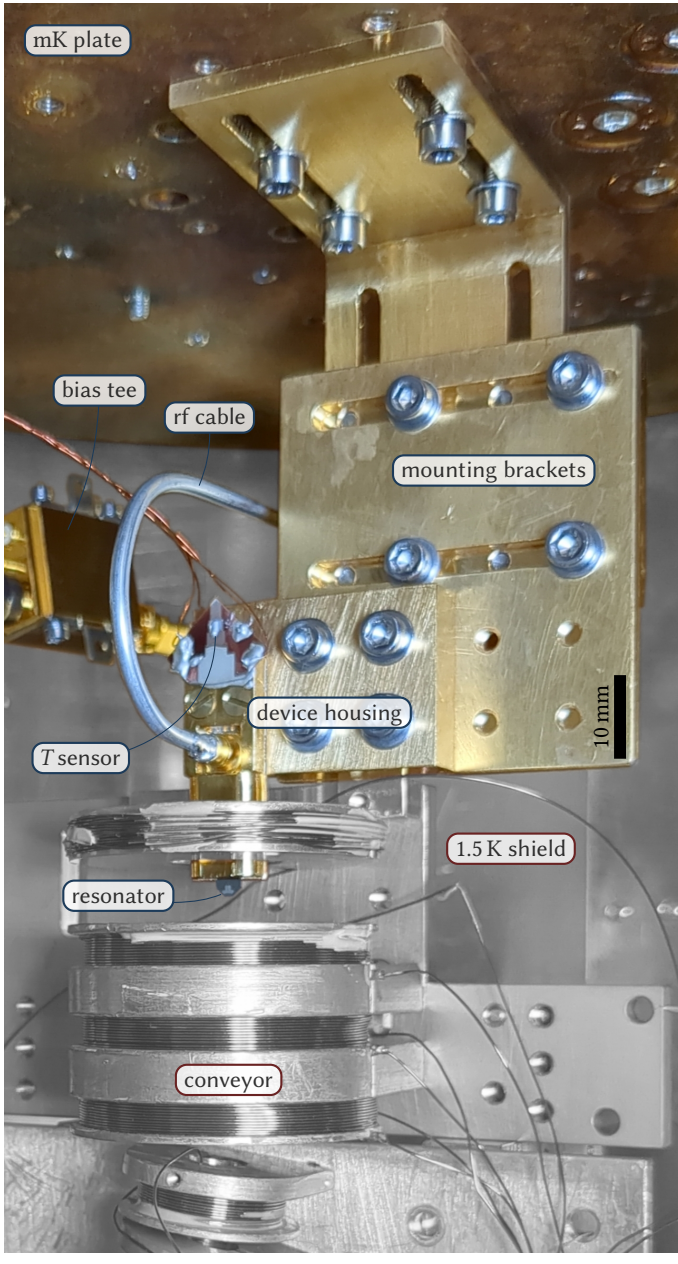
mK plate
bias tee
rf cable
mounting brackets
device housing
T sensor
10 mm
1.5 K shield
resonator
conveyor

Step 2: Dielectric patch for the shunt capacitor. As a second step, we again perform maskless photo-lithography to define the areas on the wafer which will be covered with Si_3N_4 for the parallel-plate shunt capacitor. After resist development identical to step 1, the wafer with the patterned resist structures is placed inside the vacuum chamber of a plasma-enhanced chemical vapor deposition (PECVD) system and is covered with 100 nm of Si_3N_4. Afterwards, an ultrasound-assisted lift-off procedure is performed in acetone which removes the resist and all the Si_3N_4 except at the locations of the later shunt capacitors. Finally, the wafer is rinsed in multiple baths of acetone, isopropanol and ultra-pure water again.

Step 3: Top plate for the shunt capacitor. The third step is almost identical to step 2, but instead of PECVD-grown Si_3N_4, a 120 nm thick layer of niobium is deposited by magnetron sputtering. To guarantee good galvanic contact between the top and bottom Nb layers on the ground planes, a short dry-etching step with SF_6 is performed in-situ before the sputtering process. From our etch rates, we expect a Nb etch depth of 10 nm and a Si_3N_4 etch depth of 30 nm, which reduces the final thickness of the dielectric in the shunt capacitor to ~70 nm. After liftoff in acetone, the wafer is once more cleaned in multiple baths of acetone, isopropanol and ultra-pure water.

Step 4: Dicing and mounting. At the end of the trilayer cavity fabrication, the wafer gets diced into individual, rectangular 10 mm × 3.5 mm chips. In a second dicing step, the corners on the atom-side of each chip are removed, forming the tapered tip. Then, one chip at a time is mounted adjacent to a Rogers printed circuit board (PCB) into a gold-plated copper housing, where it is wire-bonded to microwave feedlines and to ground, cf. Figure 3.10a. The PCB contains a coplanar waveguide feedline leading to an SMP connector, where a microwave cable is attached during measurement. After mounting into the measurement setup, the device characterization is performed.

Figure 3.11: Mounting the device in the dilution refrigerator. The axis of optical access passes through the center of the quadrupole coils at the top of the conveyor transporting the atoms up from their preparation stage. Thus, the resonator must be placed close to that center, such that the atoms can be loaded into the dipole trap and placed in its interaction region. We attach the sample holder to the mK plate using a cascade of mounting brackets allowing three-axis movement for precise alignment of the device position. The conveyor coils as well as the inner-most heat shield are at 1.5 K and depicted in grayscale, all colored parts are at mK. A T sensor is placed directly on the copper housing of the device for precise readout of its temperature. On the left, the bias tee can be seen as well as the aluminum rf cable connecting it to the device (cf. Figure 3.4a).

3.16 Experimental setup

The experimental setup in which we have characterized the superconducting cavity and in which we envision to implement the discussed hybrid system is an Oxford Triton dilution refrigerator with optical access and a second 6 K plate at the bottom for the preparation of ultra-cold atomic ensembles within a magneto-optical trap [40]. Due to the additional cold-atom-specific components in this cryogenic prototype system and the currently large thermal load, the temperature of the plates is somewhat higher than in standard dilution refrigerators. One consequence is that in our current experiment the lowest mixing chamber temperature is $T_{\mathrm{min}} \approx 0.2\,\mathrm{K}$, and the usual 3 K plate has a temperature of 6 K. In previous cooldowns with much less thermal load, the mK plate in the system reached down to $T_{\mathrm{pr}} < 50\,\mathrm{mK}$ and in the future we will try to reach those temperatures again by optimized thermal engineering and radiation isolation measures.

From the top down to the mK plate, however, the fridge looks nearly identical to standard dilution refrigerators and we have equipped the various temperature stages with the usual microwave components for quantum circuits, cf. Figure 3.4a. The (20, 20, 10) dB attenuator cascade on the input line, the stainless-steel coaxial cables, the circulator and the bias-tee together provide a total input attenuation of roughly −70 dB and equilibrate the incoming noise to nearly the base temperature of the system. Hence, the microwave cavity at 11.7 GHz is close to its quantum ground state with $n_{\mathrm{th}} \sim 0.2$. For the rf connections between the different components on the mK stage we use coaxial cables made of superconducting aluminum.

To mount the chip into the center of the magnetic coils, as shown in Figure 3.4b, a mounting-bracket cascade of gold-plated copper allowing three-axis movement is attached to the mK plate, with the microwave box mounted at its end, cf. Figure 3.11. This way, the chip position can be adjusted for optimal height and alignment with the optical axis while avoiding mechanical contact between the device housing at mK and the coils at 1.5 K. Note that, in addition to the thermal load mentioned above, thermal radiation emitted by the coils may contribute to the chip not reaching the lowest possible temperature. To track the chip temperature as precisely as possible, a temperature sensor is mounted directly on the copper housing.

3.17 Fitting and background-correction of resonance data

The ideal reflection-response function of a high-Q series RLC circuit coupled to a feedline with characteristic impedance Z_0 by a shunt capacitor C_{s} is given by

$$S_{11}^{\mathrm{ideal}} = -1 + \frac{2\kappa_{\mathrm{ext}}}{\kappa + 2\mathrm{i}(\omega - \omega_0)} \tag{3.32}$$

with the angular excitation frequency ω and the resonance frequency $\omega_0 = 1/\sqrt{LC_{\text{tot}}}$. The total capacitance is given by $C_{\text{tot}}^{-1} = C^{-1} + C_{\text{s}}^{-1}$, L and C are the inductance and capacitance of the uncoupled circuit, respectively. The internal and external decay rates (linewidths) κ_{int} and κ_{ext}, are given by

$$\kappa_{\text{int}} = \omega_0^2 R C_{\text{tot}} \tag{3.33}$$

$$\kappa_{\text{ext}} = \frac{C_{\text{tot}}}{Z_0 C_{\text{s}}^2} \tag{3.34}$$

and the total decay rate by $\kappa = \kappa_{\text{int}} + \kappa_{\text{ext}}$. The effective resistance R accounts for all internal losses of the circuit, such as resistive, dielectric or radiative losses.

Due to the cabling and all the microwave components in between the vector network analyzer and the circuit, the ideal reflection is not what we measure, though. To take frequency-dependent attenuation, the electrical cable length and possible interferences (e.g. parasitic reflections or imperfect isolation in the circulator) into account, we model the actual measurement signal as

$$S_{11}^{\text{real}} = (a_0 + a_1\omega + a_2\omega^2)\mathrm{e}^{\mathrm{i}(\phi_0+\phi_1\omega)}\Big(1 - \frac{2\kappa_{\text{ext}}\mathrm{e}^{\mathrm{i}\theta}}{\kappa + 2\mathrm{i}(\omega - \omega_0)}\Big). \tag{3.35}$$

Here, we absorbed the minus sign of the ideal response (3.32) into the prefactors, and a_0, a_1, a_2, ϕ_0, ϕ_1 and θ are real-valued fit parameters. During our automated data fitting routine we first remove the absorption resonance from the dataset (leaving a gap in the S_{11}-dataset) and fit the remaining S_{11}-response in a narrow frequency window (typically five to ten times κ) with the background function

$$S_{11}^{\text{bg}} = (a_0 + a_1\omega + a_2\omega^2)\mathrm{e}^{\mathrm{i}(\phi_0+\phi_1\omega)}. \tag{3.36}$$

As a result, we obtain preliminary values for a_0, a_1, a_2, ϕ_0 and ϕ_1. Then, we calculate $S_{11}^{\text{real}}/S_{11}^{\text{bg}}$ for the complete dataset and fit the resulting data with

$$S_{11}^{\theta} = 1 - \frac{2\kappa_{\text{ext}}\mathrm{e}^{\mathrm{i}\theta}}{\kappa + 2\mathrm{i}(\omega - \omega_0)} \tag{3.37}$$

from which we obtain a preliminary set of values for ω_0, κ, κ_{ext} and θ. Finally, we use all the preliminary values for a_0, a_1, a_2, ϕ_1, ϕ_2, ω_0, κ, κ_{ext} and θ as starting parameters to re-fit the original dataset using (3.35). The values thus obtained for ω_0, κ_{int} and κ_{ext} or correspondingly for the quality factors $Q_{\text{int}} = \omega_0/\kappa_{\text{int}}$ and $Q_{\text{ext}} = \omega_0/\kappa_{\text{ext}}$ are the ones presented throughout this chapter, more specifically the ones in Figures 3.4 and 3.5. All the S_{11}-datasets shown in these figures and the corresponding fit curves have been completely background-corrected by dividing the original dataset by S_{11}^{bg} with the background parameters obtained from the final fit. Additionally, we have removed the interference angle θ.

3.18 Plate and distance parameters for the 3D flip-chip architecture

To obtain a series of reasonable capacitor plate geometries for the numerical simulation of the perspective 3D architecture discussed in Figure 3.6, let us start with what we are keeping constant and fixed. Firstly, we keep the beam waist in the focus plane at $w_{dp} = 15\,\mu m$ as well as the laser parameters $\lambda_{dp} = 800\,nm$ and $P_{dp} = 50\,mW$. As a consequence, the Rayleigh length remains $l_R = 0.88\,mm$. Secondly, in order to keep the advantage of high field homogeneity in the center of the capacitor plates, we choose the width of the plates to always be equal to their mutual distance $a = d$. Furthermore, we want the plate length to always be $l \geq l_{min} = 250\,\mu m$, such that a cloud with $T_{Rb} \sim 1\,\mu K$ is comfortably accommodated in a nearly homogeneous field over the complete cloud length. In order to maintain this field homogeneity also for large a, d we choose $l = 2a$, given that this is larger than l_{min}. Finally, we want to keep the laser power reaching the two chips directly in the Gaussian beam tails small. While giving a precise limit is impossible without careful study of the actual device, we can assume $P_{dir} \lesssim 0.1\,nW$ to be a reasonable limit [67, 68]. By inverting (3.20) numerically, we find the ratio $r_e = z_0/w_e = d/2w_e$ that results in $P_{dir} = 0.1\,nW$ to be $r_e = 3.0$, which limits us to $d \gtrsim 2r_e w_{dp} = 90\,\mu m$ even with vanishing chip width. In our simulations, we thus use $d \geq 100\,\mu m$ as a practical limit.

Table 3.1: Capacitor and chip parameters for the eleven simulation points discussed in Figure 3.6. The laser parameters, including the beam waist $w_{dp} = 15\,\mu m$, the wavelength $\lambda_{dp} = 800\,nm$, the resulting Rayleigh length $l_R = 0.88\,mm$ and the power $P_{dp} = 50\,mW$, are kept constant for all parameter sets.

d in µm	a in µm	l in µm	l_{ch} in mm	l_{ch}^{crit} in mm
100	100	250	0.60	0.86
150	150	300	0.70	2.36
200	200	400	0.85	3.51
250	250	500	1.00	4.58
300	300	600	1.15	5.62
350	350	700	1.30	6.64
400	400	800	1.45	7.66
450	450	900	1.60	8.66
500	500	1000	1.75	9.66
550	550	1100	1.90	10.66
600	600	1200	2.05	11.65

Given these preliminary considerations, we simulate the perspective geometry for plate distances d ranging from 100 µm to 600 µm in steps of 50 µm and calculate all other lengths from this. For the chip width l_{ch} at the position where the laser crosses it, we assume a 45° tapered chip profile with 100 µm of padding between the capacitor plate and the chip edge, effectively giving $l_{\mathrm{ch}} = l + a + 250\,\mu\mathrm{m}$. Table 3.1 summarizes the resulting eleven parameter sets used to obtain the coupling rates shown in Figure 3.6c as well as the maximum possible chip width below the laser axis $l_{\mathrm{ch}}^{\mathrm{crit}} = l_{\mathrm{R}}\sqrt{(d/2r_{\mathrm{e}}w_{\mathrm{dp}})^2 - 1}$ that would lead to $P_{\mathrm{dir}} = 0.1\,\mathrm{nW}$ according to (3.20) in each case. These maximum values turn out to be comfortably large for all but the smallest value of d, revealing that further modifications to the design, e.g. additional grounding structures around the capacitor plates, are possible without significant spacial restrictions.

References

[1] Z.-L. Xiang, S. Ashhab, J. Q. You, and F. Nori, *Hybrid quantum circuits: Superconducting circuits interacting with other quantum systems*, Reviews of Modern Physics **85**, 623–653 (2013).

[2] G. Kurizki, P. Bertet, Y. Kubo, K. Mølmer, D. Petrosyan, P. Rabl, and J. Schmiedmayer, *Quantum technologies with hybrid systems*, Proceedings of the National Academy of Sciences **112**, 3866–3873 (2015).

[3] A. A. Clerk, K. W. Lehnert, P. Bertet, J. R. Petta, and Y. Nakamura, *Hybrid quantum systems with circuit quantum electrodynamics*, Nature Physics **16**, 257–267 (2020).

[4] J. Clarke and F. Wilhelm, *Superconducting quantum bits*, Nature **453**, 1031–1042 (2008).

[5] A. Blais, A. L. Grimsmo, S. M. Girvin, and A. Wallraff, *Circuit quantum electrodynamics*, Reviews of Modern Physics **93**, 025005 (2021).

[6] P. Rabl, D. DeMille, J. M. Doyle, M. D. Lukin, R. J. Schoelkopf, and P. Zoller, *Hybrid quantum processors: Molecular ensembles as quantum memory for solid state circuits*, Physical Review Letters **97**, 033003 (2006).

[7] J. Verdú, H. Zoubi, C. Koller, J. Majer, H. Ritsch, and J. Schmiedmayer, *Strong magnetic coupling of an ultracold gas to a superconducting waveguide cavity*, Physical Review Letters **103**, 043603 (2009).

[8] B. Zhao, Y.-A. Chen, X.-H. Bao, T. Strassel, C.-S. Chuu, X.-M. Jin, J. Schmiedmayer, Z.-S. Yuan, S. Chen, and J.-W. Pan, *A millisecond quantum memory for scalable quantum networks*, Nature Physics **5**, 95–99 (2009).

[9] L. Li and A. Kuzmich, *Quantum memory with strong and controllable Rydberg-level interactions*, Nature Communications **7**, 13618 (2016).

[10] A. Wallucks, I. Marinković, B. Hensen, R. Stockill, and S. Gröblacher, *A quantum memory at telecom wavelengths*, Nature Physics **16**, 772–777 (2020).

[11] Y. Liu, Q. Liu, H. Sun, M. Chen, S. Wang, and T. Li, *Coherent memory for microwave photons based on long-lived mechanical excitations*, npj Quantum Information **9**, 80 (2023).

[12] R. W. Andrews, R. W. Peterson, T. P. Purdy, K. Cicak, R. W. Simmonds, C. A. Regal, and K. W. Lehnert, *Bidirectional and efficient conversion between microwave and optical light*, Nature Physics **10**, 321–326 (2014).

[13] J. Han, T. Vogt, C. Gross, D. Jaksch, M. Kiffner, and W. Li, *Coherent microwave-to-optical conversion via six-wave mixing in Rydberg atoms*, Physical Review Letters **120**, 093201 (2018).

[14] D. Petrosyan, K. Mølmer, J. Fortágh, and M. Saffman, *Microwave to optical conversion with atoms on a superconducting chip*, New Journal of Physics **21**, 073033 (2019).

[15] A. Kumar, A. Suleymanzade, M. Stone, L. Taneja, A. Anferov, D. I. Schuster, and J. Simon, *Quantum-enabled millimetre wave to optical transduction using neutral atoms*, Nature **615**, 614–619 (2023).

[16] S. Haroche, *Nobel lecture: Controlling photons in a box and exploring the quantum to classical boundary*, Reviews of Modern Physics **85**, 1083–1102 (2013).

[17] A. S. Sørensen, C. H. van der Wal, L. I. Childress, and M. D. Lukin, *Capacitive coupling of atomic systems to mesoscopic conductors*, Physical Review Letters **92**, 063601 (2004).

[18] D. Petrosyan and M. Fleischhauer, *Quantum information processing with single photons and atomic ensembles in microwave coplanar waveguide resonators*, Physical Review Letters **100**, 170501 (2008).

[19] D. Petrosyan, G. Bensky, G. Kurizki, I. Mazets, J. Majer, and J. Schmiedmayer, *Reversible state transfer between superconducting qubits and atomic ensembles*, Physical Review A **79**, 040304 (2009).

[20] S. D. Hogan, J. A. Agner, F. Merkt, T. Thiele, S. Filipp, and A. Wallraff, *Driving Rydberg-Rydberg transitions from a coplanar microwave waveguide*, Physical Review Letters **108**, 063004 (2012).

[21] T. Thiele, J. Deiglmayr, M. Stammeier, J.-A. Agner, H. Schmutz, F. Merkt, and A. Wallraff, *Imaging electric fields in the vicinity of cryogenic surfaces using Rydberg atoms*, Physical Review A **92**, 063425 (2015).

[22] A. A. Morgan and S. D. Hogan, *Coupling Rydberg atoms to microwave fields in a superconducting coplanar waveguide resonator*, Physical Review Letters **124**, 193604 (2020).

[23] D. M. Walker, A. A. Morgan, and S. D. Hogan, *Cavity-enhanced Ramsey spectroscopy at a Rydberg-atom–superconducting-circuit interface*, Applied Physics Letters **117**, 204001 (2020).

[24] D. M. Walker, L. L. Brown, and S. D. Hogan, *Electrometry of a single resonator mode at a Rydberg-atom–superconducting-circuit interface*, Physical Review A **105**, 022626 (2022).

[25] P. Böhi, M. F. Riedel, J. Hoffrogge, J. Reichel, T. W. Hänsch, and P. Treutlein, *Coherent manipulation of Bose–Einstein condensates with state-dependent microwave potentials on an atom chip*, Nature Physics **5**, 592–597 (2009).

[26] S. Bernon, H. Hattermann, D. Bothner, M. Knufinke, P. Weiss, F. Jessen, D. Cano, M. Kemmler, R. Kleiner, D. Koelle, and J. Fortágh, *Manipulation and coherence of ultra-cold atoms on a superconducting atom chip*, Nature Communications **4**, 2380 (2013).

[27] H. Hattermann, D. Bothner, L. Y. Ley, B. Ferdinand, D. Wiedmaier, L. Sárkány, R. Kleiner, D. Koelle, and J. Fortágh, *Coupling ultracold atoms to a superconducting coplanar waveguide resonator*, Nature Communications **8**, 2254 (2017).

[28] M. Kaiser, C. Glaser, L. Y. Ley, J. Grimmel, H. Hattermann, D. Bothner, D. Koelle, R. Kleiner, D. Petrosyan, A. Günther, and J. Fortágh, *Cavity-driven Rabi oscillations between Rydberg states of atoms trapped on a superconducting atom chip*, Physical Review Research **4**, 013207 (2022).

[29] R. H. Dicke, *Coherence in spontaneous radiation processes*, Physical Review **93**, 99–110 (1954).

[30] J. Fortágh and C. Zimmermann, *Magnetic microtraps for ultracold atoms*, Reviews of Modern Physics **79**, 235–289 (2007).

[31] R. Grimm, M. Weidemüller, and Y. B. Ovchinnikov, *Optical dipole traps for neutral atoms*, in *Advances in atomic, molecular, and optical physics*, Vol. 42 (Academic Press, 2000), pp. 95–170.

[32] B. T. Gard, K. Jacobs, R. McDermott, and M. Saffman, *Microwave-to-optical frequency conversion using a cesium atom coupled to a superconducting resonator*, Physical Review A **96**, 013833 (2017).

[33] J. P. Covey, A. Sipahigil, and M. Saffman, *Microwave-to-optical conversion via four-wave mixing in a cold ytterbium ensemble*, Physical Review A **100**, 012307 (2019).

[34] D. Bothner, M. Knufinke, H. Hattermann, R. Wölbing, B. Ferdinand, P. Weiss, S. Bernon, J. Fortágh, D. Koelle, and R. Kleiner, *Inductively coupled superconducting half wavelength resonators as persistent current traps for ultracold atoms*, New Journal of Physics **15**, 093024 (2013).

[35] D. Cano, B. Kasch, H. Hattermann, R. Kleiner, C. Zimmermann, D. Koelle, and J. Fortágh, *Meissner effect in superconducting microtraps*, Physical Review Letters **101**, 183006 (2008).

[36] M. A. Beck, J. A. Isaacs, D. Booth, J. D. Pritchard, M. Saffman, and R. McDermott, *Optimized coplanar waveguide resonators for a superconductor–atom interface*, Applied Physics Letters **109**, 092602 (2016).

[37] H. Hattermann, M. Mack, F. Karlewski, F. Jessen, D. Cano, and J. Fortágh, *Detrimental adsorbate fields in experiments with cold Rydberg gases near surfaces*, Physical Review A **86**, 022511 (2012).

[38] K. S. Chan, M. Siercke, C. Hufnagel, and R. Dumke, *Adsorbate electric fields on a cryogenic atom chip*, Physical Review Letters **112**, 026101 (2014).

[39] P. L. Ocola, I. Dimitrova, B. Grinkemeyer, E. Guardado-Sanchez, T. Đorđević, P. Samutpraphoot, V. Vuletić, and M. D. Lukin, *Control and entanglement of individual Rydberg atoms near a nanoscale device*, Physical Review Letters **132**, 113601 (2024).

[40] F. Jessen, M. Knufinke, S. C. Bell, P. Vergien, H. Hattermann, P. Weiss, M. Rudolph, M. Reinschmidt, K. Meyer, T. Gaber, D. Cano, A. Günther, S. Bernon, D. Koelle, R. Kleiner, and J. Fortágh, *Trapping of ultracold atoms in a ^{3}He/^{4}He dilution refrigerator*, Applied Physics B **116**, 665–671 (2014).

[41] K. R. Patton and U. R. Fischer, *Ultrafast quantum random access memory utilizing single Rydberg atoms in a Bose–Einstein condensate*, Physical Review Letters **111**, 240504 (2013).

[42] J. D. Pritchard, J. A. Isaacs, M. A. Beck, R. McDermott, and M. Saffman, *Hybrid atom-photon quantum gate in a superconducting microwave resonator*, Physical Review A **89**, 010301 (2014).

[43] L. Sárkány, J. Fortágh, and D. Petrosyan, *Long-range quantum gate via Rydberg states of atoms in a thermal microwave cavity*, Physical Review A **92**, 030303 (2015).

[44] L. Sárkány, J. Fortágh, and D. Petrosyan, *Faithful state transfer between two-level systems via an actively cooled finite-temperature cavity*, Physical Review A **97**, 032341 (2018).

[45] N. Lauk, N. Sinclair, S. Barzanjeh, J. P. Covey, M. Saffman, M. Spiropulu, and C. Simon, *Perspectives on quantum transduction*, Quantum Science and Technology **5**, 020501 (2020).

[46] D. Petrosyan, J. Fortágh, and G. Kurizki, *Coherent interface between optical and microwave photons on an integrated superconducting atom chip*, EPJ Quantum Technology **11**, 18 (2024).

[47] M. Stammeier, S. Garcia, T. Thiele, J. Deiglmayr, J. A. Agner, H. Schmutz, F. Merkt, and A. Wallraff, *Measuring the dispersive frequency shift of a rectangular microwave cavity induced by an ensemble of Rydberg atoms*, Phys. Rev. A **95**, 053855 (2017).

[48] S. Garcia, M. Stammeier, J. Deiglmayr, F. Merkt, and A. Wallraff, *Single-shot nondestructive detection of Rydberg-atom ensembles by transmission measurement of a microwave cavity*, Phys. Rev. Lett. **123**, 193201 (2019).

[49] J. A. Sedlacek, A. Schwettmann, H. Kübler, R. Löw, T. Pfau, and J. P. Shaffer, *Microwave electrometry with Rydberg atoms in a vapour cell using bright atomic resonances*, Nature Physics **8**, 819–824 (2012).

[50] D. Yu, L. C. Kwek, L. Amico, and R. Dumke, *Superconducting qubit-resonator-atom hybrid system*, Quantum Science and Technology **2**, 035005 (2017).

[51] F. L. Semião and M. Keller, *Cavity-assisted quantum transduction between superconducting qubits and trapped atomic particles mediated by Rydberg levels*, arXiv:2501.03201 [quant-ph] (2025).

[52] Y. Kubo, I. Diniz, A. Dewes, V. Jacques, A. Dréau, J.-F. Roch, A. Auffeves, D. Vion, D. Esteve, and P. Bertet, *Storage and retrieval of a microwave field in a spin ensemble*, Physical Review A **85**, 012333 (2012).

[53] B. Julsgaard, C. Grezes, P. Bertet, and K. Mølmer, *Quantum memory for microwave photons in an inhomogeneously broadened spin ensemble*, Physical Review Letters **110**, 250503 (2013).

[54] S. J. Bosman, V. Singh, A. Bruno, and G. A. Steele, *Broadband architecture for galvanically accessible superconducting microwave resonators*, Applied Physics Letters **107**, 192602 (2015).

[55] J. Grimmel, M. Mack, F. Karlewski, F. Jessen, M. Reinschmidt, N. Sándor, and J. Fortágh, *Measurement and numerical calculation of rubidium Rydberg Stark spectra*, New Journal of Physics **17**, 053005 (2015).

[56] D. A. Steck, *Rubidium 87 D line data*, revision 2.3.3, 2024, available online at https://steck.us/alkalidata/.

[57] J. Eschner, *Sub-wavelength resolution of optical fields probed by single trapped ions: Interference, phase modulation, and which-way information*, The European Physical Journal D **22**, 341–345 (2003).

[58] A. Wallraff, D. I. Schuster, A. Blais, L. Frunzio, R.-. S. Huang, J. Majer, S. Kumar, S. M. Girvin, and R. J. Schoelkopf, *Strong coupling of a single photon to a superconducting qubit using circuit quantum electrodynamics*, Nature **431**, 162–167 (2004).

[59] S. J. Bosman, M. F. Gely, V. Singh, D. Bothner, A. Castellanos-Gomez, and G. A. Steele, *Approaching ultrastrong coupling in transmon circuit QED using a high-impedance resonator*, Physical Review B **95**, 224515 (2017).

[60] A. Bruno, G. de Lange, S. Asaad, K. L. van der Enden, N. K. Langford, and L. DiCarlo, *Reducing intrinsic loss in superconducting resonators by surface treatment and deep etching of silicon substrates*, Applied Physics Letters **106**, 182601 (2015).

[61] F. E. Schmidt, D. Bothner, I. C. Rodrigues, M. F. Gely, M. D. Jenkins, and G. A. Steele, *Current detection using a Josephson parametric upconverter*, Physical Review Applied **14**, 024069 (2020).

[62] K. Uhl, D. Hackenbeck, D. Koelle, R. Kleiner, and D. Bothner, *Extracting the current-phase relation of a monolithic three-dimensional nanoconstriction using a dc-current-tunable superconducting microwave cavity*, Physical Review Applied **22**, 064052 (2024).

[63] D. Rieger, S. Günzler, M. Spiecker, A. Nambisan, W. Wernsdorfer, and I. M. Pop, *Fano interference in microwave resonator measurements*, Physical Review Applied **20**, 014059 (2023).

[64] M. Saffman, T. G. Walker, and K. Mølmer,
Quantum information with Rydberg atoms,
Reviews of Modern Physics **82**, 2313–2363 (2010).

[65] M. Stecker, R. Nold, L.-M. Steinert, J. Grimmel, D. Petrosyan, J. Fortágh, and A. Günther, *Controlling the dipole blockade and ionization rate of Rydberg atoms in strong electric fields*, Physical Review Letters **125**, 103602 (2020).

[66] I. Diniz, S. Portolan, R. Ferreira, J. M. Gérard, P. Bertet, and A. Auffèves,
Strongly coupling a cavity to inhomogeneous ensembles of emitters: Potential for long-lived solid-state quantum memories,
Physical Review A **84**, 063810 (2011).

[67] R. Benevides, M. Drimmer, G. Bisson, F. Adinolfi, U. v. Lüpke, H. M. Doeleman, G. Catelani, and Y. Chu, *Quasiparticle dynamics in a superconducting qubit irradiated by a localized infrared source*,
Physical Review Letters **133**, 060602 (2024).

[68] R. P. Budoyo, J. B. Hertzberg, C. J. Ballard, K. D. Voigt, Z. Kim, J. R. Anderson, C. J. Lobb, and F. C. Wellstood,
Effects of nonequilibrium quasiparticles in a thin-film superconducting microwave resonator under optical illumination,
Physical Review B **93**, 024514 (2016).

[69] N. Klein, H. Chaloupka, G. Müller, S. Orbach, H. Piel, B. Roas, L. Schultz, U. Klein, and M. Peiniger,
The effective microwave surface impedance of high T_c thin films,
Journal of Applied Physics **67**, 6940–6945 (1990).

[70] A. I. Gubin, K. S. Il'in, S. A. Vitusevich, M. Siegel, and N. Klein,
Dependence of magnetic penetration depth on the thickness of superconducting Nb thin films, Physical Review B **72**, 064503 (2005).

[71] R. Garg, I. Bahl, and M. Bozzi, *Microstrip lines and slotlines*, 3rd ed. (Artech House, 2013).

[72] K. Watanabe, K. Yoshida, T. Aoki, and S. Kohjiro,
Kinetic inductance of superconducting coplanar waveguides,
Japanese Journal of Applied Physics **33**, 5708–5712 (1994).

The following chapter is derived from a manuscript with co-authors.

author contributions

B.W. conducted the experiments, performed data processing and analysis, implemented the algorithms for numerical solutions as well as data fitting, prepared the figures, wrote the first draft of the manuscript and contributed to sample design and theory development. M. K. contributed to the experiments. T. K. designed and fabricated the device and contributed to the experimental setup. K. U. contributed to design and installation of the vector magnet and to sample fabrication. C. F. contributed to design and installation of the vector magnet. D. K. and R. K. contributed to funding acquisition and participated in scientific discussions. D. B. conceived the experiment, supervised all aspects of the project, performed funding acquisition, developed the theoretical framework and wrote the first draft of the manuscript. All authors discussed the results and conclusions, and contributed to manuscript revisions.

acknowledgments

The authors thank Markus Turad, Ronny Löffler (instrument scientists at the core facility LISA$^+$), Christoph Back and Christoph Kalkuhl for technical support. This research received funding from the Deutsche Forschungsgemeinschaft (DFG) via grant numbers 490939971 (BO 6068/1-1) and 511315638 (BO 6068/2-1) and from the Vector Stiftung via project number P2023-0201. M. K. gratefully acknowledges financial support by the Studienstiftung des Deutschen Volkes. We also acknowledge support by the COST actions NANOCOHYBRI (CA16218) and SUPERQUMAP (CA21144).

data availability

All data presented in this chapter, including raw data, and the corresponding processing scripts will be made publicly available on the repository Zenodo with the identifier 10.5281/zenodo.17093328.

4 Integrated magnetically induced Josephson nano-diodes

The content of this chapter was published as the preprint

Magnetically induced Josephson nano-diodes in field-resilient superconducting microwave circuits

Benedikt Wilde, Mohamad Kazouini, Timo Kern, Kevin Uhl, Christoph Füger, Dieter Koelle, Reinhold Kleiner and Daniel Bothner

arXiv:2511.16727 [quant-ph] (2025)

and is under review for publication

The development of nonlinear and frequency-tunable superconducting microwave circuits for operation in large magnetic fields is of high relevance for hybrid quantum systems such as spin resonance spectrometers, microwave quantum magnonics, dark matter axion detectors or flux-mediated optomechanics. With these exciting perspectives in mind, we investigate niobium-based circuits with integrated nano-constriction quantum interferometers in magnetic in-plane fields up to several hundred mT. Our experiments reveal an unexpected and pronounced field-induced asymmetry in the bias-flux response of the circuits, which is demonstrated to originate from a field-induced Josephson-diode effect within the nano-constrictions and which considerably enhances the circuit figures of merit in a magnetic field. An intuitive macroscopic Josephson-diode model attributes the effect to inhomogeneous constriction properties and provides us with the diode current-phase relation as a function of the in-plane field. Finally, we demonstrate that in the diode-state the circuit Kerr nonlinearity is bimodal in frequency, not only eliminating alternative explanations for the bias-flux-asymmetries but also being potentially useful for quantum circuit applications. Overall, our report underlines that niobium nano-constriction circuits belong to the most promising candidates for high-field hybrid quantum systems and reveals the untapped potential of combining Josephson nano-diodes with microwave quantum circuits.

4.1 Introduction

Superconducting microwave circuits with integrated nonlinear elements such as Josephson junctions or high-kinetic-inductance nanowires are the workhorse of superconducting and hybrid quantum technologies [1–3]. Lately, there has been growing demand for such circuits being compatible with large magnetic fields for use in field-resilient circuit quantum electrodynamics [4–7], field-compatible parametric amplifiers [8–10], dispersive magnetometry [11], and hybrid systems with e.g. micromechanical oscillators [12–14], spin ensembles [15–17], magnonic oscillators [18–20] or topological quantum bits [21, 22]. Some of the envisioned high-field experiments might reveal groundbreaking new insights and technologies regarding quantum gravity, axion dark matter, quantum sensing or topologically protected qubits. Since the standard material aluminum and the commonly used trilayer superconducting tunnel junctions cannot easily be combined with high magnetic fields [7, 23], other circuit materials and junction technologies are currently under intense investigation [4–6, 17, 24–27], however, with no technology proven to be superior or dominant yet.

A promising platform towards high-field Josephson microwave devices are niobium (alloy) circuits, which have been demonstrated to possess high coherence in fields up to the tesla regime [8, 28–30], integrated with nano-constrictions as nonlinear elements, either as single nanowires [8, 31–33] or as superconducting quantum interference devices (SQUIDs) [25, 34]. Various implementations of niobium nano-constrictions have been realized in the past [25, 33–39], both in direct-current (dc) and in microwave platforms, and using both two-dimensional (2D) and three-dimensional (3D) constriction types. Surprisingly, only few experiments, and all in dc, focused on their high-field characteristics [40–42], and hence little is known about their high-field microwave properties. Recently, it has been observed that niobium nano-constrictions can develop a considerable dc superconducting diode (SD) effect in an external field [43], a nonreciprocal regime with an asymmetry between forward and reverse critical currents that originates from a simultaneous breaking of space-inversion and time-reversal symmetries. After the early realizations of SDs several decades ago [44–49], they have experienced an impressive renaissance during the past few years [50–53], since they promise fascinating possibilities for superconducting electronics, spintronics and quantum technologies [53, 54]. However, reports of integrating intrinsic SDs into microwave circuits, and thus combining two potentially groundbreaking technologies, are scarce to date [55], and many aspects of their sub-critical, inductive properties, their current-phase relations as well as their potential for application in quantum circuits beyond three-wave-mixing [56, 57] remain elusive.

Here, we present the magnetic-field operation of superconducting niobium microwave circuits with integrated nano-constriction quantum interferometers. To

guarantee minimized coupling of current-source noise into the SQUIDs, we implement a setup combining a single-current-source 2D-vector-magnet with in-situ sample rotation, and characterize the microwave circuits in magnetic in-plane fields up to ∼300 mT. The properties of the circuits turn out to be very promising for applications in large magnetic fields and we observe that the circuit flux responsivity – one of the most important figures of merit for many applications – is even enhanced by the external field. At the same time, we find that with increasing in-plane field the characteristic flux-tuning arcs of usual microwave SQUID devices become considerably asymmetric, an intriguing effect which we explain with the constrictions gradually turning into field-induced Josephson diodes (JDs). From our data and a macroscopic theoretical JD model, we finally reconstruct the current-phase-relations (CPRs) of the JD-constrictions and identify spatial inhomogeneities as the origin of the diode effect. Our results shine light on the magnetic-field compatibility of niobium nano-constriction SQUID circuits, and reveal insights into the sub-critical characteristics of field-induced constriction-diodes, detected through their microwave inductance. The observations presented in this chapter are of high relevance for high-field hybrid quantum systems involving superconducting microwave electronics, for focused-ion-beam-patterned nano-devices, for the design and understanding of Josephson diodes, and for diode-enhanced quantum interference circuits.

4.2 Devices and setup

The base layout of our circuits is a superconducting lumped element LC circuit, which comprises two interdigital capacitors C_{idc} with multiple linear inductances that can formally be combined into a single inductor L_{b} (without constriction contributions), cf. Figure 4.1. The superconducting lines have a width of 2 µm and the gaps between two capacitor fingers are 4 µm wide. At the heart of the circuit is a rectangular loop with inner loop dimensions 19 µm × 8 µm and a loop self-inductance $L_{\mathrm{loop}} \approx 44$ pH including kinetic inductance, cf. Section 4.19. By means of a capacitor C_{c}, the circuits are side-coupled to a coplanar waveguide (CPW) feedline with characteristic impedance $Z_0 \approx 50\,\Omega$ for driving and readout. Without constrictions, the resonance frequency of the circuits is given by $\omega_{0\mathrm{b}} = 1/\sqrt{L_{\mathrm{b}} C_{\mathrm{tot}}}$, where $C_{\mathrm{tot}} = 2C_{\mathrm{idc}} + C_{\mathrm{c}}$.

We combine six such circuits along a single microwave CPW feedline on a 10 mm × 10 mm microchip for simultaneous characterization and readout. For a picture of the complete layout and details regarding the individual circuit components and their values, cf. Section 4.18. The individual circuit layouts differ solely by their number N_{idc} of capacitor fingers, which primarily leads to distinct capacitances, but also to slightly different L_{b}, since the capacitor fingers contribute

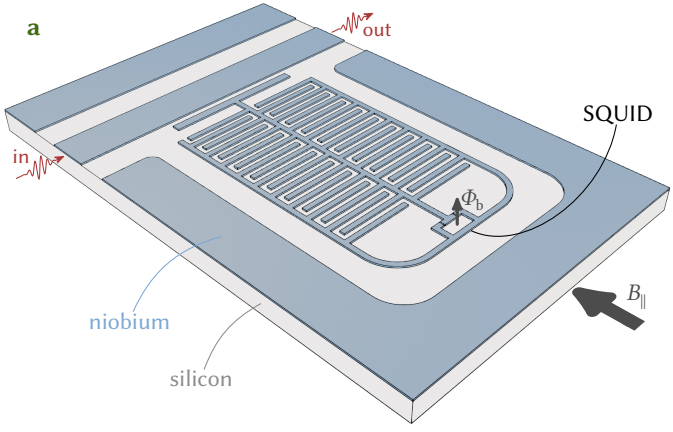
a
out
in
SQUID
Φ_b
$B_\parallel$
niobium
silicon

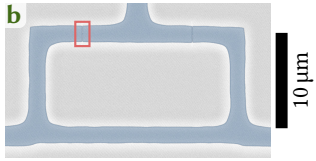
b
10 µm

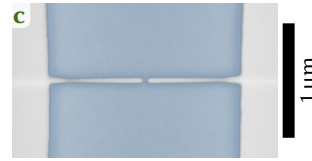
c
1 µm

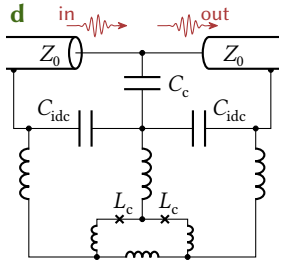
d
in
out
Z_0
Z_0
C_c
C_{idc}
C_{idc}
L_c
L_c

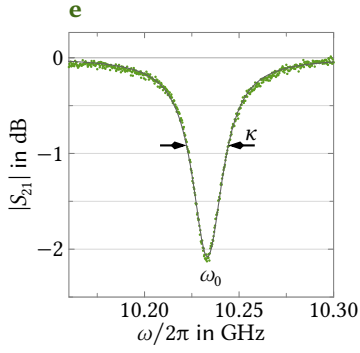
e
0
−1
−2
$|S_{21}|$ in dB
κ
ω_0
10.20
10.25
10.30
$\omega/2\pi$ in GHz

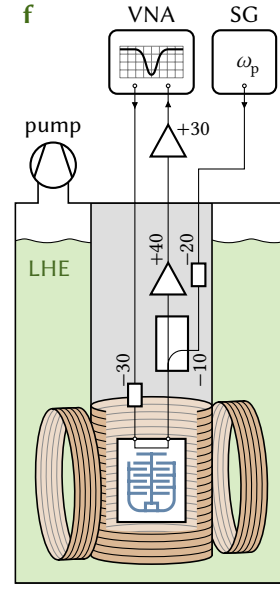
f
VNA
SG
ω_p
pump
+30
+40
−20
LHE
−30
−10

to the total inductance. The spacing of two neighboring resonance frequencies is roughly 700 MHz, and the six devices in total cover the frequency range from 8.9 GHz to 12.5 GHz. The superconducting structures on the chip are patterned from a ~100 nm thick niobium film, deposited on an intrinsic high-resistivity silicon wafer by dc-magnetron sputtering. All niobium patterning of the main circuits is performed using maskless optical lithography and SF_6 reactive ion etching. A detailed description of the complete fabrication recipe can be found in Section 4.8.

After a spectroscopic pre-characterization in liquid helium, three of the six circuits are patterned with a pair of monolithic nano-constrictions, which are placed symmetrically into their SQUID loops (cf. Figure 4.1); the other three circuits are operated as reference devices. Patterning of the constrictions is done via local

Figure 4.1: Niobium nano-constriction SQUID circuits for microwave hybrid systems in large magnetic fields. **a** Rendered schematic of a typical microwave SQUID circuit as discussed in this chapter. The circuit comprises interdigital capacitors (IDCs) connected with linear inductors and is patterned from a 100 nm thick layer of niobium (blue) on top of an intrinsic silicon substrate (gray). A rectangular-loop SQUID based on ion-beam patterned nano-constrictions is integrated at the bottom of the circuit. The circuit is capacitively side-coupled to a coplanar waveguide (CPW) feedline for driving and readout by means of the scattering matrix element $S_{21} = S_{\mathrm{out}}/S_{\mathrm{in}}$. The SQUID can be flux-biased with a perpendicular flux Φ_{b} and, independently, a large magnetic in-plane field $B_{\parallel}$ can be applied. **b** False-color scanning electron microscopy (SEM) image of a typical SQUID. The position of one of the two symmetrically placed nano-constrictions is indicated by a red rectangle. **c** Enlarged false-color SEM image of the indicated junction, rotated by 90°. **d** Equivalent circuit of the device, featuring the coupling capacitance C_{c} to the CPW feedline with characteristic impedance Z_0, the IDC capacitances C_{idc}, and the constriction inductances L_{c} (symbolized by crosses). The individual linear inductances are not labeled in this diagram for the sake of simplicity and since we will mainly use the effective composite inductance L_{b} (total circuit inductance for $L_{\mathrm{c}} = 0$). For the contributions to the total SQUID loop inductance L_{loop}, cf. Figure 4.2. **e** CPW transmission S_{21} vs probe frequency ω for $B_{\parallel} = 0$, $\Phi_{\mathrm{b}} = 0$. Dots are data, the line is a fit. From the fit, we obtain the resonance frequency $\omega_0 = 2\pi \cdot 10.233\,\mathrm{GHz}$ and the linewidth $\kappa = 2\pi \cdot 22\,\mathrm{MHz}$. **f** Simplified schematic of the experimental setup. The superconducting chip is enclosed in the vacuum compartment of a liquid helium (LHE) cryostat. The microwave input lines are attenuated by 30 dB each to equilibrate the noise of the vector network analyzer (VNA) and the signal generator (SG) as close as possible to the measurement temperature $T_{\mathrm{s}} = 2.8\,\mathrm{K}$ (achieved by pumping on the helium gas) and the output line is equipped with two high-electron-mobility-transistor (HEMT) amplifiers for maximized signal-to-noise ratio. A cylindrical superconducting coil is wrapped directly around the cup of the vacuum compartment for the application of magnetic in-plane fields $B_{\parallel}$, and an additional split-coil magnet for compensating out-of-plane components is rigidly attached to the cryostat. A small magnetic sample coil (not shown) is directly attached to the chip housing for the application of Φ_{b}.

high-precision milling using a focused neon-ion-beam (Ne-FIB), analogous to what is described in [34]. Two of the three SQUIDs have 3D constrictions (where the constrictions were milled down from the top) and one of them has 2D variants (where the constrictions have the full film height). From here on, we will focus on the 2D device, but we do provide analogous results for one of the 3D constriction circuits as well as a comparative discussion in Section 4.23. The constrictions have a length and width of $l = w = 40\,\mathrm{nm}$. After Ne-FIB patterning, the chip is mounted and wirebonded to a microwave printed circuit board (PCB) and enclosed in a radiation-tight copper housing, before it is placed in the vacuum compartment of a liquid helium cryostat.

The experimental setup combines multiple coaxial microwave input/output lines, various dc twisted-pair copper wires as well as a temperature-control unit consisting of a temperature-diode and a resistive heater for feedback-controlled temperature stability better than 1 mK, cf. Figure 4.1f for a simplified schematic and Section 4.17 for the complete one. For magnetic shielding, the entire cryostat is surrounded by a double-layer mu-metal shield at room-temperature. Two equally attenuated coaxial input lines are used to send a vector network analyzer (VNA) probe tone and an additional high-power microwave pump tone to the device, respectively, and the output line is equipped with a cryogenic high-electron-mobility-transistor (HEMT) amplifier as well as a room-temperature HEMT amplifier. We insert the pump tone into the device at the probe signal output in order to protect the amplifiers from being saturated by the pump signal. The chip with a small sample-coil attached to the copper housing for applying SQUID-bias flux Φ_b and the temperature-control components are located in an evacuated cylindrical cup, around which a high-inductance superconducting coil is wrapped for the application of an in-plane magnetic field with $B_\parallel/I_\mathrm{coil} = 250\,\mathrm{mT\,A^{-1}}$, with the coil current I_coil. Thus, the superconducting coil can be immersed directly in liquid helium, while the sample is located in vacuum with variable temperature, maintaining a rigid relative position and orientation between the two. At the bottom of the cryostat, around the position of the cylindrical sample cup, a second superconducting electromagnet, a split-coil, is installed for the application of an out-of-plane magnetic compensation field $B_\perp/I_\mathrm{coil} = 2\,\mathrm{mT\,A^{-1}}$. Finally, it is possible to pump on the helium compartment of the cryostat to reach sample temperatures T_s down to $T_\mathrm{s}^\mathrm{min} \sim 2\,\mathrm{K}$. Throughout this chapter, we operate at a temperature $T_\mathrm{s} = 2.8\,\mathrm{K}$.

4.3 Circuit characteristics without in-plane field

The first experiment we perform is the microwave characterization of the SQUID circuit as a function of bias-flux Φ_b through the SQUID, with the large magnetic coils switched off $B_\parallel = B_\perp = 0$. This will allow us to quantitatively model the

constriction-type Josephson junctions (cJJs) and to extract their characteristic parameters as a basis for the later experiments and analyses. To this end, we trace the complex frequency response of the circuit around its resonance frequency by means of the transmission S-parameter $S_{21} = S_{\text{out}}/S_{\text{in}}$ using a VNA. We operate in the linear response regime of the circuit, which we ensure by measuring its microwave input-power dependence and then staying around one order of magnitude below the probe powers required for the onset of nonlinearity. At the sweetspot $\Phi_\text{b} = 0$, the circuit has a resonance frequency $\omega_0 = 2\pi \cdot 10.233\,\text{GHz}$, a total linewidth $\kappa = 2\pi \cdot 22\,\text{MHz}$ and an external linewidth $\kappa_{\text{ext}} = 2\pi \cdot 4.7\,\text{MHz}$, cf. Figure 4.1e.

Once $\Phi_\text{b} \neq 0$, we observe a shift of the resonance frequency to lower values and an increase of the internal decay rate, cf. Figure 4.2. On a wider flux scale, the resonance frequency modulates periodically with Φ_b, and the period is given by the magnetic flux quantum $\Phi_0 = 2.068 \cdot 10^{-15}\,\text{T}\,\text{m}^2$. The origin of the frequency-shift with bias flux is an increase of the nonlinear constriction inductance L_c due to the flux in the SQUID and the resulting dc current through the cJJs. We find not only an arc-shaped periodic modulation but also observe a hysteretic flux response of ω_0; the frequencies obtained during the flux up-sweep partly differ from the ones in the down-sweep and the resonance frequency does not transition smoothly from arc to arc, but rather in discontinuous jumps, as indicated by the vertical arrows in Figure 4.2c. Adjacent arcs overlap considerably and cross at $\Phi_\text{b} = (n + 1/2)\,\Phi_0$ with $n \in \mathbb{Z}$. Such flux hysteresis originates from metastable SQUID states that occur when the effective loop inductance is not negligible [34, 58]. The jumps between the arcs occur when the screening current in the SQUID reaches a switching current $\pm I_{\text{sw}}$ and as a consequence the fluxoid number changes by ± 1. Note that I_{sw} is often considerably smaller than the junction critical current I_0, since the switching can be triggered prematurely by thermal noise, flux instabilities, phase slips or the microwave signals used to probe the resonator.

A practical way to quantitatively model the inductance of each constriction as a function of Φ_b is to separate L_c into a linear inductance L_{lin} and a flux-dependent Josephson inductance $L_\text{J} = L_{\text{J0}}/\cos\delta_\text{J}$ [33, 59]. Here, $L_{\text{J0}} = \Phi_0/2\pi I_0$ is the sweetspot Josephson inductance, I_0 is the critical constriction current and δ_J is the Josephson phase. Splitting the total cJJ inductance into a linear and a Josephson contribution is equivalent to splitting the total constriction phase drop δ_c as

$$\delta_\text{c} = \delta_\text{J} + \delta_{\text{lin}} \tag{4.1}$$

where $\delta_{\text{lin}} = 2\pi L_{\text{lin}} I/\Phi_0$ is the phase drop across the linear inductance. Using this total phase and the first Josephson relation $I = I_0 \sin\delta_\text{J}$, with the constriction current I, the cJJ current-phase relation can be expressed as the implicit function

$$I(\delta_\text{c}) = I_0 \sin\Big(\delta_\text{c} - 2\pi \frac{L_{\text{lin}} I(\delta_\text{c})}{\Phi_0}\Big). \tag{4.2}$$

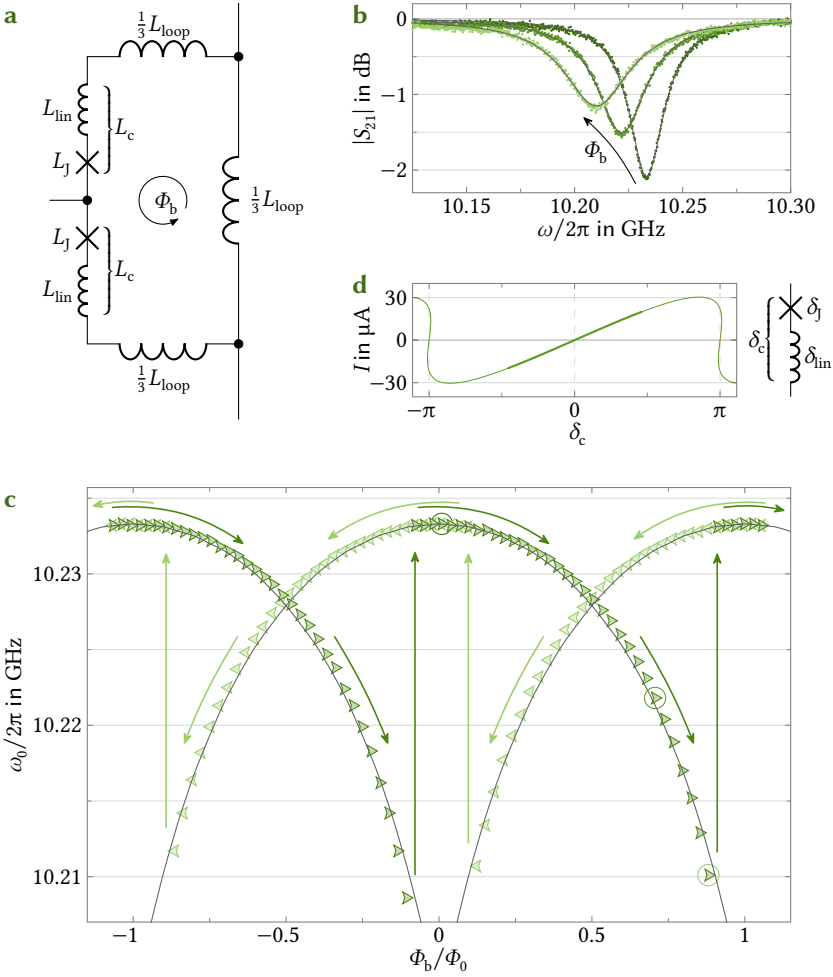
a
$\frac{1}{3}L_{\mathrm{loop}}$
L_{lin}
L_{c}
L_{J}
Φ_{b}
$\frac{1}{3}L_{\mathrm{loop}}$
L_{J}
L_{c}
L_{lin}
$\frac{1}{3}L_{\mathrm{loop}}$
b
$|S_{21}|$ in dB
0
−1
−2
Φ_{b}
10.15
10.20
10.25
10.30
$\omega/2\pi$ in GHz
d
I in µA
30
0
−30
−π
0
π
δ_{c}
δ_{J}
δ_{c}
δ_{lin}
c
$\omega_0/2\pi$ in GHz
10.23
10.22
10.21
−1
−0.5
0
0.5
1
Φ_{b}/Φ_0

The total flux Φ in the SQUID (without constriction contributions) on the other hand is related to δ_c via $\Phi/\Phi_0 = \delta_c/\pi$ and to the bias flux via

$$\Phi = \Phi_b - L_{loop} I(\pi\Phi/\Phi_0). \tag{4.3}$$

Here, we chose the signs such that a small positive bias flux Φ_b leads to a positive ring current I through the junctions, and assumed the two constrictions in the SQUID to be identical.

The numerical solution of (4.2) and (4.3) provides us with δ_c as a function of Φ_b, which in turn allows us to calculate the constriction inductance for a given Φ_b according to

$$L_c(\delta_c) = \frac{\Phi_0}{2\pi}\left(\frac{dI}{d\delta_c}\right)^{-1} \tag{4.4}$$

and to finally fit the flux-tuning of the resonance frequency using

$$\omega_0(\Phi_b) = \frac{\omega_{0b}}{\sqrt{1 + L_c(\Phi_b)/2L_b}}. \tag{4.5}$$

Here, $\omega_{0b} = 2\pi \cdot 10.380\,\text{GHz}$ is the fixed circuit resonance frequency before the cJJ patterning and we use the sweetspot resonance frequency $\omega_{00} = \omega_0(0)$ to fix the

Figure 4.2: Hysteretic flux response and constriction current-phase relation without magnetic in-plane field. a Circuit schematic of the SQUID. The total loop inductance is split into three equal contributions, each carrying $L_{loop}/3$. The total constriction inductance L_c is described by a series combination of a linear inductance L_{lin} and an ideal Josephson inductance L_J. The Josephson part L_J can be tuned by applying a bias flux Φ_b through the SQUID. **b** Transmission S_{21} through the circuit for three different bias fluxes $\Phi_b/\Phi_0 \in \{0, 0.71, 0.88\}$. With increasing Φ_b (arrow), the resonance shifts to lower frequencies. From fits (lines) to the data (dots), we obtain ω_0 as a function of the bias flux. The shift of ω_0 is due to an increase of L_J with Φ_b. **c** Resonance frequency ω_0 vs Φ_b/Φ_0 as obtained from the S_{21} fit curves for a larger range of flux values; the presented dataset combines a flux up-sweep (dark kites pointing right) and a flux down-sweep (light kites pointing left), arrows indicate the sweep direction. The three encircled data points on the central arc correspond to the resonances shown in panel b. The resonance frequency modulates with a period of Φ_0, and the modulation is hysteretic with discontinuous jumps from one flux arc to the neighboring ones at $\Phi_b/\Phi_0 \sim (n \pm 0.9)\,\Phi_0$ where $n \in \mathbb{Z}$. Jumps are always upwards in frequency and indicated by long vertical arrows. Lines are fit curves, from which we obtain the linear inductance $L_{lin} = 12\,\text{pH}$ and the sweetspot Josephson inductance $L_{J0} = 11\,\text{pH}$. **d** Inferred current-phase relation of the constriction. The total phase δ_c is the sum of a linear phase δ_{lin} and a Josephson phase δ_j. The critical currents are identical in both current directions and given by $I_0^{\pm} = \pm 30\,\mu\text{A}$. The thick line segment for $|\delta_c| \leq 1.45$ shows the part of the CPR that corresponds to the experimentally accessible flux arc range between the jumps; the switching currents are $I_{sw}^{\pm} \approx \pm 20\,\mu\text{A}$.

sweetspot constriction inductance L_{c0}, while I_0 is a free fit parameter. For the flux response tuning curves shown in Figure 4.2c we obtain $L_{c0} = 23\,\mathrm{pH}$ and $I_0 = 30\,\mu\mathrm{A}$, which corresponds to $L_{lin} = L_{c0} - L_{J0} = 12\,\mathrm{pH}$.

The corresponding constriction CPR is shown in Figure 4.2d and is typical for niobium constrictions. Instead of a sinusoidal shape, as expected for an ideal Josephson junction, the CPR is considerably forward-skewed which reflects the presence of L_{lin}. In a small interval around $\delta_c = \pi$ it even becomes multi-valued, which indicates that $L_{lin}/L_{c0} > 1/2$. From the CPR segment that is experimentally accessible before the jump to the next arc occurs (indicated by a thick line in Figure 4.2d) we conclude that the switching indeed occurs prematurely at $\delta_c \sim \pi/2$ and $I_{sw} \approx 20\,\mu\mathrm{A}$. This is not unusual for the type of constriction we use here [33, 34], although the exact mechanism behind this discrepancy is not yet fully understood.

In summary, both the microwave circuit and the constrictions are well-behaved and quantitatively modeled at this point and the time is ripe for switching on $B_\parallel$.

4.4 Impact of the magnetic in-plane field

When investigating in-plane-field operation of superconducting circuits, it is always a challenge to align the magnetic field as parallel as possible to the circuit plane, particularly when large SQUIDs are involved. In practice, there is always a finite mounting misalignment between field and chip, e.g. due to machining inaccuracies. One way to achieve parallel alignment would be to operate the vector magnet with two independent current sources and to adjust the split-coil current such that $B_\perp$ exactly cancels the out-of-plane component of the main-coil field $B_\parallel$. The out-of-plane component and the necessary compensation factor can be determined using the SQUID itself. This standard method, however, leads to the two current sources coupling uncorrelated noise into the SQUID, which is very sensitive to this due to its large area. Additionally, independent drifts of the two current sources would pose a severe challenge for effective field alignment. In order to cancel out the source-related field-noise and avoid compensation drifts, we decided to instead operate the two magnets in series, driven by a single current source. Naturally, the out-of-plane components of the two fields do not coincidentally cancel then, and an additional measure has to be taken: We rotate the sample assembly, including the in-plane magnet, in the field of the fixed split-coil until an optimal compensation-angle is reached. This leads to a small additional misalignment between the symmetry axis of the circuits and the in-plane field (here $\sim 0.4°$), but this is on the order of the original misalignment and has negligible consequences for our experiment. A detailed description of this alignment procedure is given in Section 4.11.

Once field and sample are aligned, we apply increasing coil currents in steps of $\Delta I_{coil} = 100\,\mathrm{mA}$, which corresponds to field steps $\Delta B_\parallel = 25\,\mathrm{mT}$, and for each

in-plane field we characterize the circuit. We implement a field-cooling procedure to minimize potential noise factors and flux instabilities that can occur with critical states in zero-field-cooling situations, in particular when the alignment is not completely perfect [60–62]. To this end, we set I_{coil} to its desired value, then heat the sample in the vacuum compartment to $T \sim 12\,\mathrm{K}$ for a few seconds, and finally let it thermalize to $T_{\mathrm{s}} = 2.8\,\mathrm{K}$ again. We begin the characterization by sweeping Φ_{b} using the sample coil and measure S_{21} traces with the VNA for each SQUID flux as described above. The results are summarized in Figure 4.3.

First, we find that the sweetspot resonance frequency ω_{00} (that is, ω_0 at the flux arc maximum) decreases with $B_{\parallel}$. Partly, this effect is caused by the in-plane field increasing the penetration depth λ_{L} and correspondingly the kinetic inductance of the superconducting film, i.e. by an increase of L_{b} with $B_{\parallel}$. From simultaneous reference measurements of the cJJ-less circuits on the same chip, however, we find that this effect is not sufficient to explain the magnitude of the shift, cf. Section 4.19. Hence, the cJJs themselves are impacted considerably and their inductance increases even stronger than that of the remaining circuit; roughly two thirds of the total sweetspot frequency shift can be attributed to the constrictions and only one third to the remaining film. Similarly, the sweetspot linewidth κ_0 increases with $B_{\parallel}$, indicating increased thermal quasiparticles due to a field-induced suppression of the superconducting energy gap. Again, the increase of κ_0 is stronger in the circuits with cJJs than in those without cJJs; almost the complete additional loss can be attributed to the constrictions.

A second and quite surprising effect of $B_{\parallel}$ is that the shape of the flux arcs is strongly modified. Most strikingly, they become narrower and more and more skewed with increasing $B_{\parallel}$, i.e. asymmetric with respect to their sweetspots. For the highest fields, neighboring arcs do not even cross anymore. In conjunction with the skewing, one of the arc branches (the right one for each arc in Figure 4.3a) gets extended while the opposite branch (the left ones in Figure 4.3a) becomes shorter. For $B_{\parallel} = 200\,\mathrm{mT}$ this lengthening/shortening has reached a level where one of the discontinuous transitions between arcs more than doubled in frequency range while the other nearly vanished. For still larger $B_{\parallel}$, the shortening of the left branch is so strong that the corresponding frequency jump is downwards, meaning that the metastable branch has a higher resonance frequency than the stable one. Before we explain and model this unusual shape of the flux response, we discuss how the characteristics of the circuit are impacted by $B_{\parallel}$ and the arc skewing with respect to possible applications.

Regarding the circuit figures of merit, we find that $B_{\parallel}$ enhances – especially on the right, longer arc branch – both the total frequency tuning range $\omega_{0,\mathrm{max}} - \omega_{0,\mathrm{min}}$ and the tuning range between sweetspot and transition to the metastable part of each arc. These enhancements are potentially very useful for sensing and hybrid systems, where tuning range and the flux responsivity $\mathcal{F} = \partial\omega_0/\partial\Phi_{\mathrm{b}}$ are

Figure 4.3: Skewed flux-response and enhanced flux-responsivity in large magnetic in-plane fields. a Bias flux response $\omega_0(\Phi_b)$ of the circuit for five different magnetic in-plane fields between 0 mT and 300 mT; labels next to the datasets denote $B_\parallel$. Data combine flux up-sweep (dark kites pointing right) and flux down-sweep (light kites pointing left); lines are fits, cf. main text. With increasing $B_\parallel$, sweetspot resonance frequency and flux hysteresis decrease and a tilt of the arcs emerges, an asymmetry with respect to the field-shifting sweetspot flux. The arc skewing also impacts the discontinuous transitions from one arc to the next, indicated by vertical arrows for $B_\parallel \in \{0, 200, 300\}$ mT. For $B_\parallel = 0$, these jumps from the metastable to the stable branch always occur upwards in frequency and are symmetric around the arc crossing points (ACPs). At 200 mT, the jumps occurring in the up-sweep are larger compared to the $B_\parallel = 0$ case, which correlates with an increase of the total tuning range $\omega_{0,\mathrm{max}} - \omega_{0,\mathrm{min}}$. The jumps in the down-sweep, on the other hand, are significantly diminished in size. Still, both jumps are upwards in frequency. For the two largest fields, the ACPs disappear and the jumps in the down-sweep are downwards in frequency, meaning that the metastable branch has a higher frequency than the stable one. **b**, **c** Sweetspot resonance frequency ω_{00} and linewidth κ_0 as a function of $B_\parallel$. The in-plane field reduces the energy gap in the Nb film and the cJJs, increasing the kinetic inductance and the number of thermal quasiparticles, resulting in ω_{00} decreasing and κ_0 increasing, respectively. Symbols are data extracted from the flux arcs, colors denote the value of $B_\parallel$, as in all panels. The dashed lines show the expected behavior in the absence of the constrictions as inferred from reference circuits. Hence, about two thirds of the ω_{00} decrease and almost all of the κ_0 increase can be attributed to the constrictions. **d** Flux responsivity $\mathcal{F} = \partial\omega_0/\partial\Phi_b$ for various $B_\parallel$ and plotted vs ω_0 as a figure of merit for sensing and parametric coupling applications. Large symbols correspond to values on stable branches, small symbols to those on metastable branches,* lines are derivatives of the arc fits. The stable operation regime is considerably and asymmetrically magnified by $B_\parallel$.

*We assume the transition to the metastable state on a flux arc branch to be located in the center between the two jumps (arrows in panel a) to and from that branch, which at $B_\parallel = 0$ corresponds to the arc crossing point but shifts right of it for larger fields. While we believe that this is the most reasonable value to use, our conclusions would not be changed much if the transition were in fact located somewhere else between the jumps.

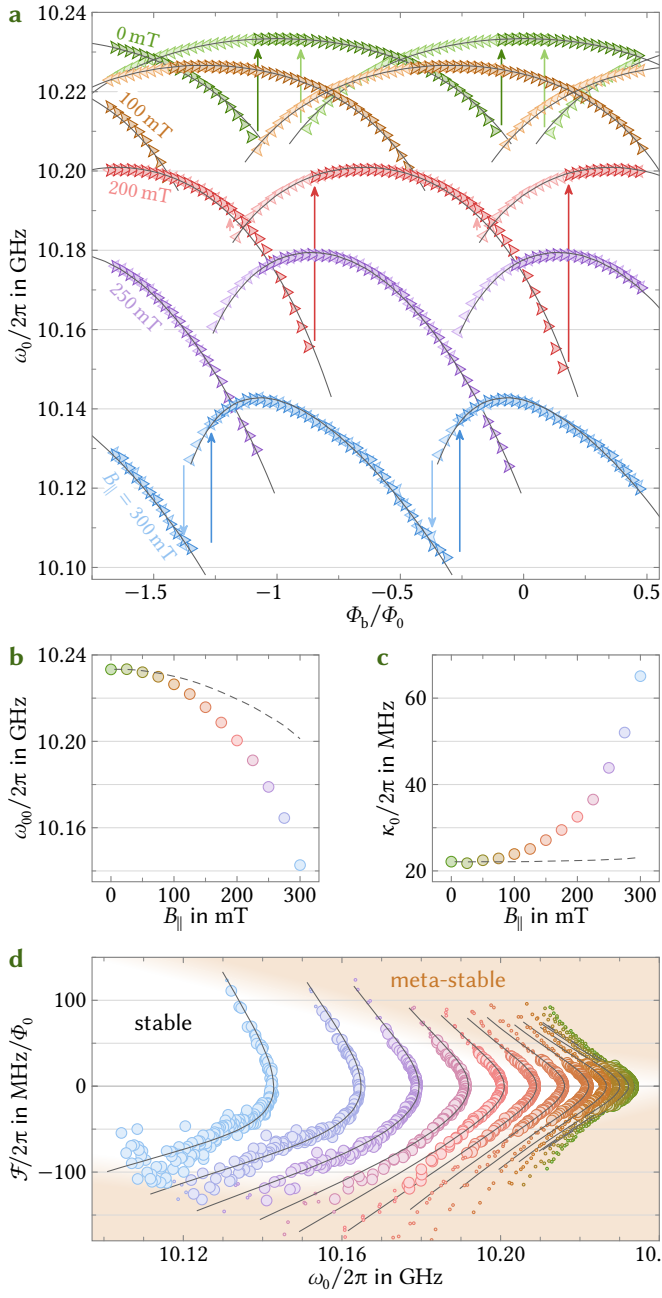
a
0 mT
100 mT
200 mT
250 mT
$B_\parallel$ = 300 mT
$\omega_0/2\pi$ in GHz
Φ_b/Φ_0
b
$\omega_{00}/2\pi$ in GHz
$B_\parallel$ in mT
c
$\kappa_0/2\pi$ in MHz
$B_\parallel$ in mT
d
stable
meta-stable
$\mathcal{F}/2\pi$ in MHz/Φ_0
$\omega_0/2\pi$ in GHz

critical parameters that need to be maximized [12, 63], particularly in the stable operation regime. As can be seen in Figure 4.3d, the in-plane field increases the highest stable $|\mathcal{F}|/2\pi$ by a factor of more than 5 from $\sim 25\,\mathrm{MHz}/\Phi_0$ at $B_\parallel = 0$ to $\sim 130\,\mathrm{MHz}/\Phi_0$ at high fields. Due to the asymmetry, the maximized $|\mathcal{F}|$ can even be reached at different in-plane fields, depending on which side of the skewed arc is chosen for operation. This provides another degree of freedom to pick the most desired $B_\parallel$ without sacrificing a large flux responsivity. In several of the potential target systems, such as SQUID optomechanics [12–14], the most crucial figure of merit is the cooperativity $\mathcal{C} \propto \mathcal{F}^2/\kappa$, which might suffer from an increased κ. However, the enhancement of $\mathcal{F}$ is sufficiently large here to more than compensate for the increase of κ due to $B_\parallel$ in this ratio (cf. also Section 4.20), and thus $B_\parallel$ is actually able to boost $\mathcal{C}$. When operating the device in the mK temperature regime, we expect the impact on κ to be much smaller, since even the field-reduced superconducting energy gap in the cJJs will not lead to a substantial thermal quasiparticle population, while the enhancement of $\mathcal{F}$ likely persists.

Now we finally address the most pressing question: What is the cause of this unexpected arc skewing? Various candidates may initially spring to mind, such as SQUID asymmetries or slight flux-dependent sample tilts/rotations in the large in-plane fields. These first explanations, however, can be ruled out upon further reflection. Differences in junction properties and SQUID loop asymmetries do not lead to asymmetric arcs, but to symmetric arc modifications and to odd circuit nonlinearities [56, 57]. Furthermore, we find that the tilt direction of the arcs does not depend on the direction of Φ_b in the experiment; it does, however, invert when $B_\parallel$ is reversed, cf. Section 4.24. Lastly, the arcs of one of the three SQUID circuits we characterized always tilt opposite to the arcs of the other two. This third circuit is rotated by 180° on the chip (cf. Section 4.18), which in principle is equivalent to reversing the direction of $B_\parallel$ but in combination with the other circuits demonstrates that the effect is intrinsic to the devices and not related to the chip alignment. A presentation of the corresponding experimental data can be found in Section 4.23. Overall, the observations indicate a simultaneous symmetry breaking in both cJJs of the SQUID, induced by $B_\parallel$, that causes a dependence of the cJJ inductances (shape of the arc) and the switching currents (jumps between arcs) on the direction of the screening current in the SQUID loop. In other words, the results suggest that the constrictions are turned into intrinsic superconducting nano-diodes by $B_\parallel$, with asymmetric CPRs and asymmetric critical currents.

We emphasize that this is not the same as the SQUID as a whole turning into a diode with respect to a transport current flowing across it, which can indeed be caused by SQUID or cJJ asymmetries [44, 46, 47, 49, 56, 57]. The individual-constriction diode-model discussed in the next section will further clarify this important aspect.

4.5 Field-induced Josephson-diode effect

To quantitatively demonstrate that such a superconducting diode effect causes the flux response to tilt, the corresponding CPRs are of central relevance. Once the CPRs are known, the constriction inductance and the circuit resonance frequency as a function of Φ_b can be calculated using (4.2) to (4.5). More precisely, once a model for the CPRs is available, the model parameters can be adjusted to resemble the experimental flux arcs using a fitting routine. In contrast to earlier reports of diodes in constrictions [43, 64], we formulate a simple macroscopic model in terms of only phase, flux and inductances, which does not require sophisticated microscopic details and can be applied to other types of Josephson diodes as well.

In the presence of a magnetic in-plane field, the whole nano-constriction will be penetrated by the field due to the cJJ dimensions all being smaller than the penetration depth of the Nb film $\lambda_L \sim 130\,\mathrm{nm}$. Most likely, the constriction itself has an even larger penetration depth due to its significantly reduced transition temperature and electron mean free path as compared to the un-milled film [33]. Now, the penetrating field $B_\parallel$ determines the phase gradient across the constriction in z-direction, cf. Figure 4.4, and the total phase drop is

$$\delta(z) = \delta_0 + \frac{2\pi}{\Phi_0} B_\parallel l_{\mathrm{eff}} z \tag{4.6}$$

with δ_0 the phase drop at $z = 0$ and $l_{\mathrm{eff}} \gtrsim l$ the effective length of the cJJ in current direction. The current density is then described by the local first Josephson relation

$$j(z, \delta_0) = j_0 \sin\Big(\delta_0 + \frac{2\pi}{\Phi_0} B_\parallel l_{\mathrm{eff}} z - \frac{2\pi}{\Phi_0} \ell_{\mathrm{lin}} j(z, \delta_0)\Big) \tag{4.7}$$

with the critical current density j_0 and the specific linear inductance contribution ℓ_{lin}. The total current-phase relation can be obtained from $j(z, \delta_0)$ by integration over the cJJ cross-section as

$$I(\delta_0) = w \int_{-a/2}^{a/2} j(z, \delta_0)\, \mathrm{d}z \tag{4.8}$$

where w is the width of the cJJ. However, this is not sufficient to generate a diode CPR, since the spatial symmetry remains unbroken.

To get the constrictions to turn into nano-diodes, we need their intrinsic properties to be a function of z, i.e. we need an inhomogeneous constriction. Conveniently, this is very likely the experimental situation due to the fabrication using Ne-FIB milling, a process that is known to damage the material in close proximity to the milled parts. Partly, this is due to the Gaussian profile of the ion beam, leading to slight milling and/or ion implantation also next to the main cuts [37, 65], and partly

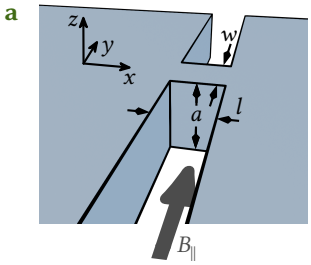
a
z
y
x
w
a
l
$B_\parallel$

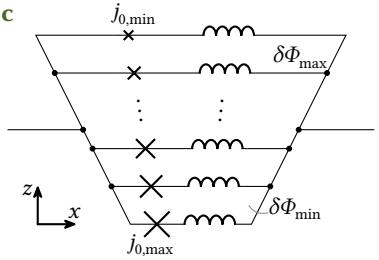
c
$j_{0,\min}$
$\delta\Phi_{\max}$
$\delta\Phi_{\min}$
$j_{0,\max}$
z
x

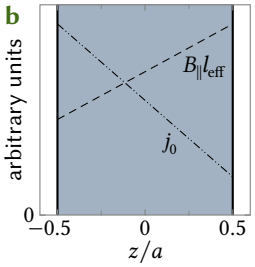
b
arbitrary units
$B_\parallel l_{\text{eff}}$
j_0
0
−0.5
0
0.5
z/a

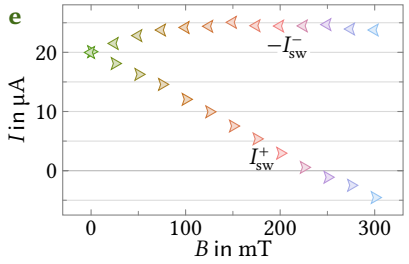
e
I in µA
20
10
0
$-I_{\text{sw}}^-$
I_{sw}^+
0
100
200
300
B in mT

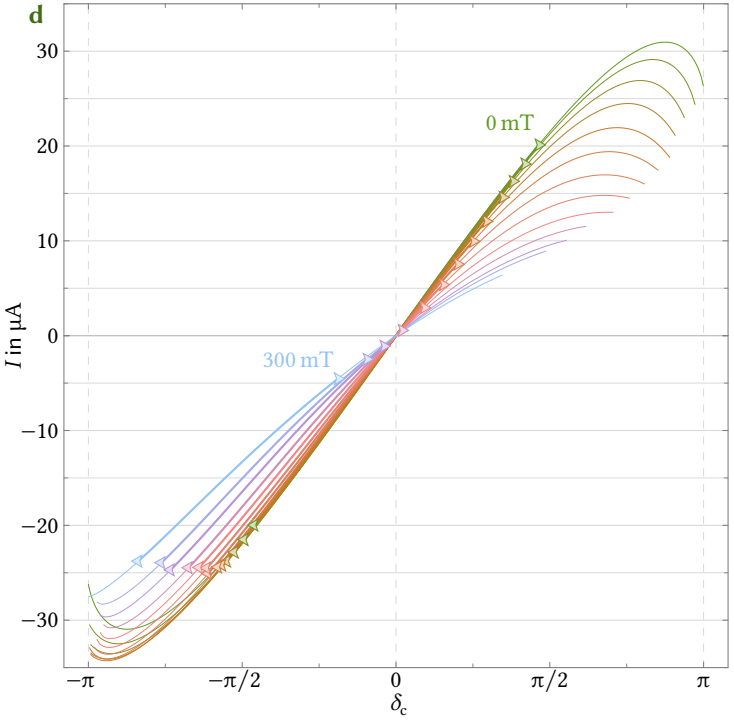
d
I in µA
30
20
10
0
−10
−20
−30
0 mT
300 mT
−π
−π/2
0
π/2
π
δ_c

due to re-deposition of the milled material onto the adjacent structures, e.g. the constriction. It is plausible to assume that the surface of the constriction receives more damage from this process than the lower parts, which are somewhat shielded by the surface layer, and that a damage-gradient is formed.

We do not know the exact details of the constriction inhomogeneity; in principle all of the quantities j_0, $B_\parallel$, l_{eff} and ℓ_{lin} could be a complicated function of z (and even y). For simplicity, we take into account only a linear decrease of the critical current density and a linear increase of the flux per length

$$j_0(z) = \left(1 - \frac{2\epsilon}{a}\, z\right) j_0(0) \tag{4.9}$$

$$B_\parallel l_{\mathrm{eff}}(z) = \left(1 + \frac{b}{a}\, z\right) B_\parallel l_{\mathrm{eff}}(0) \tag{4.10}$$

Figure 4.4: Inhomogeneous nano-constrictions are Josephson-diodes in large magnetic fields. **a** Schematic of a 2D nano-constriction defining its width w, length l and height a as well as the direction of $B_\parallel$. For our device $a = 100\,\mathrm{nm}$ and $l = w = 40\,\mathrm{nm}$. **b** To model the skewed flux response, we assume the critical current density j_0 to linearly decrease from the bottom of the constriction at $z = -a/2$ to the top at $z = +a/2$. This is consistent with e.g. surface damage by the Ne-FIB process. Such a quality gradient is also associated with more magnetic flux per height $\delta\Phi = B_\parallel l_{\mathrm{eff}}$ entering the junction at the top than at the bottom, and we model it as increasing linearly in z-direction. **c** Circuit equivalent of the Josephson-diode model consisting of a multi-loop parallel arrangement of infinitesimal constrictions whose inductive Josephson contribution grows with z due to a decreasing critical current density. At the same time, the flux per height $\delta\Phi$ between the paths increases with z, here illustrated by an increasing loop length $l_{\mathrm{eff}}(z)$. **d** Constriction CPR $I(\delta_c)$ as a function of $B_\parallel$ obtained from fits to the flux arc data (lines in Figure 4.3a). Thin lines show the full range for which our numerical algorithm yields a result, thick line segments show the parts that correspond to the experimental flux arcs in between the discontinuous jumps, symbols mark the corresponding switching currents/phases (i.e. the ends of the thick line segments). With increasing $B_\parallel$, the CPRs become increasingly asymmetric, both in slope and in critical current (points of vanishing slope). Negative critical currents initially increase in magnitude with $B_\parallel$ and then slightly decrease for the higher fields, positive critical currents decrease quickly and monotonically. Switching currents are $\sim 10\,\mu\mathrm{A}$ lower than critical currents. As before as well as in the next panel, colors encode $B_\parallel$. **e** Switching currents I_{sw}^+ and $-I_{\mathrm{sw}}^-$ as derived from the flux arc discontinuities and the CPR model. For $B_\parallel = 0$, positive and negative switching currents are equal in magnitude, but with increasing $B_\parallel$ the difference between the two values grows, indicating an increasing diode effect. Negative switching currents stay larger in magnitude than the initial value for all $B_\parallel > 0$, positive switching currents decrease nearly linearly. For the largest fields $B_\parallel \geq 250\,\mathrm{mT}$ both switches happen at the same current polarity ($I_{\mathrm{sw}}^+ < 0$), confirming that the switching current does not match the theoretical critical current I_0^+.

with $\epsilon, b \in [0, 1]$ and no gradient in y-direction. Note that either one of them alone would be sufficient to obtain a diode, but the effect is stronger and resembles our experiment much more closely if both are included. For consistency, also the linear contribution ℓ_{lin} could be considered a function of z, which would most likely enhance the diode effect even further; however, we have not implemented it here for the sake of simplicity, since it is not required to reproduce the experimental data. Due to the z-inhomogeneity of the junction, the phase δ_0 in the center of the junction is not necessarily zero when $I = 0$ in the presence of an in-plane field. Since we are in principle free to choose any $\delta_c := \delta(z_0)$ to describe the CPR (rather than δ_0, i.e. $z_0 = 0$) and the SQUID loop current should be zero when no external flux is applied, we choose z_0 to be the position where the phase vanishes when no net current flows through the junction, such that for $\delta_c = 0$ we have $I = 0$ as well as $\Phi = \Phi_b = 0$, cf. (4.3) as well as Section 4.12.

The numerical solution of this model, fitting the model parameters to all experimental flux arcs simultaneously, reveals compelling agreement between theory and measurement, both qualitatively and quantitatively, cf. the lines in Figure 4.3a. In the fit we vary the model parameters $j_0(0)$, ϵ, $l_{\mathrm{eff}}(0)$, b as well as, separately for each in-plane field, $\ell_{\mathrm{lin}}(B_\parallel)$; cf. Section 4.13 for a detailed description of the fit routine and Section 4.25 for the resulting fit parameters. The circuit characteristics $\omega_{0b}(B_\parallel)$, $L_b(B_\parallel)$ and $L_{\mathrm{loop}}(B_\parallel)$ are inferred from their $B_\parallel = 0$ values and the corresponding field-dependence of the reference circuits, cf. Section 4.19. Figure 4.4d finally shows the numerically determined current-phase relations belonging to the flux-arc fits, which clearly reveal the field-induced diode effect, both in the corresponding Josephson inductance (inverse CPR slope) and in the critical currents.

The slope of the straight part of the CPRs decreases with $B_\parallel$, reflecting the increased sweetspot inductance (the flux sweetspot corresponds to the point of maximum slope on the CPR). Notably, the point of maximum slope is not at $\delta_c = 0$ anymore for $B_\parallel \neq 0$, but shifts to negative phases and currents, which is also visible in the sweetspot not being located at $\Phi_b = n\Phi_0$ for $B_\parallel > 0$ in Figure 4.3a. Furthermore, a clear asymmetry between the critical currents in positive and negative direction develops with increasing $B_\parallel$. The magnitude of the negative critical current I_0^- increases at first, before it starts to gently decline again to a value slightly smaller than the one at $B_\parallel = 0$. The positive critical current I_0^+ on the other hand immediately and monotonically decreases with the application of $B_\parallel$, and so does the critical phase. At the highest fields, we get $|I_0^-/I_0^+| \sim 3$; the exact values are hard to determine, since our numerical algorithm is not able to provide the CPR for all phases, cf. Sections 4.12 and 4.21.

The experimental switching currents are consistently smaller than $I_0^\pm$, as has been observed in Nb constrictions before [33], which – as mentioned above – could have multiple reasons including phase slips, phase diffusion, flux noise or thermal noise. Nevertheless, $I_{\mathrm{sw}}^\pm$ has the same trend as $I_0^\pm$, just with a nearly constant

current offset, which leads to the interesting situation that for the highest $B_{\parallel}$ both switching currents have the same polarity; the circulating screening current in the SQUID never changes direction, only magnitude. Still, the ensemble of positive and negative switching currents resembles the shape of the main bulge of a skewed Fraunhofer interference pattern, which is typical for superconducting Josephson diodes, cf. e.g. [66]. This also allows us to perform a sanity check on the behavior. Typically, in Josephson junctions, the critical current in a magnetic field reaches zero at the field B_0 at which one flux quantum is coupled into the junction. From the data in Figure 4.4e this seems to happen roughly at around 350 mT to 400 mT considering the trend of I_{sw}^{-} and a 10 µA to 15 µA offset to I_0^{-}. However, due to the presence of the j_0-gradient, a complete disappearance of the critical current is no longer expected (cf. Section 4.21) and the value $B_0 = \Phi_0/l_{\mathrm{eff}}(0)a$ we find from the fits is only 305 mT. The effective area A_{eff} of the cJJ should then correspond to $A_{\mathrm{eff}} = \Phi_0/B_0 = 6.8 \cdot 10^{-15}\,\mathrm{m}^2$, a reasonable value that for homogeneous field penetration and $a = 100$ nm corresponds to an effective length $l_{\mathrm{eff}}(0) = 68$ nm. For the smaller 3D constriction of a second device with $a = 75$ nm, cf. Section 4.23, analogous considerations yield a slightly larger $B_0 = 361$ mT, which is consistent with our interpretation and estimate. See Section 4.25 for a more complete discussion of all parameters resulting from the fits.

The presented diode CPR model also has an intuitive and useful circuit representation, cf. Figure 4.4c, which can be interpreted as a continuous generalization of the diode SQUID-models discussed in [67–69]. It is equivalent to a parallel multi-loop combination of (infinitesimal) constrictions, each being a series arrangement of an ideal Josephson junction and a linear inductance. With increasing z, the critical currents of the Josephson elements decrease, while the loops between two neighboring constrictions gradually increase in size. One can imagine to design constriction arrays patterned into a single wire following this circuit arrangement that show a tailored diode effect at much lower magnetic fields, requiring neither fabrication-based, uncontrolled material inhomogeneities nor more space than a single constriction. In fact, this approach would not be limited to constrictions, but (with larger footprints) could also be implemented with more standard tunnel junctions, and the necessary linear inductance contribution could be added e.g. by high kinetic-inductance wiring.

Finally, these considerations provide us with a strategy to evade the diode effect and the arc skewing when operating inhomogeneous-constriction circuits in large magnetic fields, if this is desired. All one needs to do is to align the junctions in a way that the constriction current direction and the in-plane field are parallel to each other, here e.g. by placing the constrictions in the short SQUID loop sides, which are parallel to both the circuit symmetry axis and $B_{\parallel}$ (cf. Figure 4.1). On the other hand, it is possible to utilize the diode effect in the constrictions for three-wave mixing circuits while avoiding the arc skewing by either using a single constriction or by

orienting them perpendicular to the external field but with opposite dc current flow, e.g. by again placing them in the short SQUID arms but applying the in-plane field in y-direction instead of in z-direction.

4.6 Analyzing the CPR derivatives using the Kerr anharmonicity

The next part of this chapter is dedicated to discussing the Kerr anharmonicity $\mathcal{K}$ of the circuit, which is both an extremely important design parameter for different applications [70–73] and a sensitive probe for the device nonlinearity. Its origin are third and fourth order corrections to the total circuit potential energy [33, 70], which can originate from a nonlinear kinetic inductance of the superconducting film or from the nonlinear inductance of integrated Josephson elements. Here, it stems from the nonlinearity of the constrictions. Large Kerr anharmonicities (hundreds of MHz) are useful for realizing superconducting qubits, while medium to small anharmonicities (kHz to MHz) are desired for high-dynamic-range applications like parametric amplifiers, radiation-pressure systems or magnetometry.

For the current experiment, the main relevance of $\mathcal{K}$ arises from it being a sensitive probe for the circuit nonlinearities. In fact, it is a function of the first three CPR derivatives; for the device considered here it can be calculated as (cf. Section 4.14)

$$\mathcal{K} = -\frac{e^2}{2\hbar C_{\mathrm{tot}}}\left(\frac{L_{\mathrm{arm}} + L_{\mathrm{c}}}{2L}\right)^3 \frac{3g_2^2 - g_3(1+g_1)}{g_1(1+g_1)^4} \tag{4.11}$$

with the elementary charge e, the reduced Planck constant $\hbar$, $L_{\mathrm{arm}} = L_{\mathrm{loop}}/3$, $L = L_{\mathrm{b}} + L_{\mathrm{c}}/2$ and the dimensionless CPR derivatives

$$g_k = \frac{2\pi}{\Phi_0} L_{\mathrm{arm}}\, \partial_{\delta_{\mathrm{c}}}^k I(\delta_{\mathrm{c}}), \qquad k \in \{1,2,3\}. \tag{4.12}$$

Thus, the Kerr anharmonicity is able to provide an independent probe of the subcritical superconducting diode effect. While the resonance frequency and the flux arc both probe only the constriction inductance, i.e. the first derivative of the CPR, as well as the switching current, $\mathcal{K}$ depends on L_{c} together with the second and third CPR derivatives in a nontrivial way. For two points on a point-symmetric (i.e. non-diode) CPR, one will find all derivatives to agree if the first one does (except for a sign reversal in the even derivatives); not so on a diode CPR, where even for identical slopes the magnitudes of curvature and higher order derivatives can differ by a large amount, cf. as an intuitive example the positive and negative points of $\partial I/\partial\delta_{\mathrm{c}} = 0$ in Figure 4.4d for non-zero $B_{\parallel}$. Hence, if the Kerr anharmonicities differ at identical resonance frequencies on the two sides of a skewed flux arc, it eliminates

alternative interpretations of the arc skewing, like chip rotation in the magnetic field or bias-flux lag due to screening currents, and confirms an intrinsic origin. Such an effect could also be of practical interest, since it would allow one to choose between one of two anharmonicities for one and the same resonance frequency and vice versa, depending on the needs of a specific experimental configuration.

Experimentally, it is straightforward to determine the Kerr anharmonicity, and we apply a well-established two-tone pump-and-probe scheme for it. The pump is a strong microwave tone from a signal generator with frequency ω_p and on-chip power P_p. For each in-plane field we pick multiple values on each flux arc, spaced to cover the complete arc range, and then send in the pump tone slightly blue-detuned from the circuit resonance at $\omega_p \approx \omega_0 + \kappa$. Again using a weak VNA probe tone, we scan the pumped cavity resonance at various pump powers P_p and subsequently determine the pump-induced resonance frequency shift (ac Stark shift)

$$\delta\omega_0 = \omega_{0p} - \omega_0 \tag{4.13}$$

as a function of P_p, where ω_{0p} is the resonance frequency at pump power P_p. Combined with the intracircuit pump photon number n_c, which we obtain by analytical calculation in combination with a fit estimate for the pump line attenuation, cf. Sections 4.15 and 4.16, the pump-induced frequency shift can be modeled by

$$\delta\omega_0 = \Delta_p - \sqrt{(\Delta_p - \mathcal{K}n_c)(\Delta_p - 3\mathcal{K}n_c) - (\kappa_p - \kappa)^2/16} \tag{4.14}$$

with $\Delta_p = \omega_p - \omega_0$ and the pump-broadened linewidth κ_p, cf. Figure 4.5a and c. The result of determining $\mathcal{K}$ via this procedure is shown and discussed in Figure 4.5d, additional fit parameters are given in Section 4.25.

The Kerr anharmonicity is clearly bimodal. For large $B_\parallel$ – the regime of the strongest diode effect in the CPR and the strongest flux response skewing – the experimental values for $\mathcal{K}$ at a single resonance frequency (i.e. identical L_c) differ by a factor up to $\gtrsim 4$, depending on the side of the arc or correspondingly of the CPR. For lower fields the difference is smaller but still significant with a factor ~ 1.5. Only for $B_\parallel = 0$ the bimodality disappears completely, which is also very much expected. In absolute terms, we find $\mathcal{K}$-values between ~ 70 Hz and ~ 4 kHz, i.e. we are deep in the low-anharmonicity regime $\mathcal{K}/\kappa \sim (10^{-5} - 10^{-7})$, which is ideal for most of our envisioned target devices like SQUID optomechanics and magnetometry, even if at lower temperatures κ will decrease by one to two orders of magnitude.

Finally, we can also confirm that the experimental values for $\mathcal{K}$ are not just revealing a diode effect, but are also qualitatively and quantitatively consistent with the independently obtained current-phase relations in Figure 4.4. Since tiny changes of the CPR in the experimentally accessible regime can have a strong impact on $\mathcal{K}$ through the second and third derivatives, we allow small changes $\Delta I(\delta_c)$ to

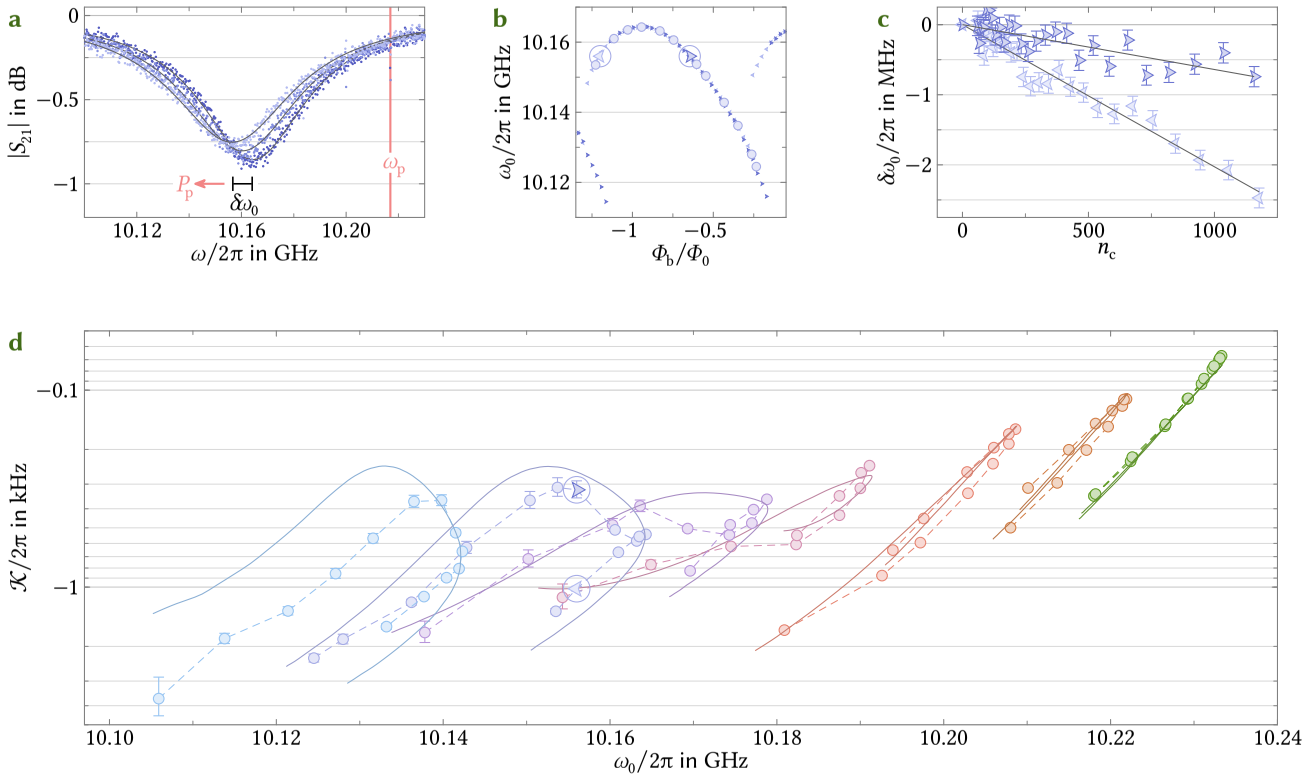
a
|S21| in dB
0
−0.5
−1
P_p
$\delta\omega_0$
ω_p
10.12
10.16
10.20
$\omega/2\pi$ in GHz
b
$\omega_0/2\pi$ in GHz
10.16
10.14
10.12
−1
−0.5
Φ_b/Φ_0
c
$\delta\omega_0/2\pi$ in MHz
0
−1
−2
0
500
1000
n_c
d
$\mathcal{K}/2\pi$ in kHz
−0.1
−1
10.10
10.12
10.14
10.16
10.18
10.20
10.22
10.24
$\omega_0/2\pi$ in GHz

Figure 4.5: Bimodal Kerr anharmonicity confirms the field-induced Josephson-diode effect and the model current-phase relations. **a** To determine the Kerr anharmonicity as a function of Φ_b and $B_\parallel$, we implement a two-tone experiment in which we send a pump tone with frequency $\omega_p \approx \omega_0 + \kappa$ from a signal generator to the circuit and probe the pumped resonance with a small VNA signal for increasing values of pump power P_p. Due to the Kerr anharmonicity of the circuit originating from the nonlinear current-phase relation, the resonance frequency shifts as a function of pump power by $\delta\omega_0 = \omega_{0p} - \omega_0$, where ω_{0p} is the pump-shifted resonance. Symbols are data, lines are fit curves, $B_\parallel = 275\,\mathrm{mT}$. **b** We conduct this two-tone scheme for multiple points on the flux arc at each $B_\parallel$, shown here for the arc at $B_\parallel = 275\,\mathrm{mT}$. Large symbols (disks and kites) show the arc points for which we performed the pump-and-probe experiment, small kites are the ω_0-values from the flux-response characterization (as shown in Figure 4.3a for other in-plane fields). Of particular relevance are points with identical ω_0 on opposite sides of the skewed arc, such as the two encircled ones marked by the left- and right-pointing kite symbols. **c** Frequency shift $\delta\omega_0$ at the two arc points shown as kite symbols in panel b vs intracircuit pump photon number n_c. Despite identical resonance frequencies ω_0, the slopes of the Stark shifts at these arc points differ by a factor $\gtrsim 3$. Lines are fits, which provide us with the Kerr anharmonicity $\mathcal{K}$. **d** Kerr anharmonicity $\mathcal{K}$ for various in-plane fields and points on the flux arc vs the corresponding un-pumped resonance frequency ω_0. Symbols are data, connected with dashed lines as guides to the eye, solid lines are fit curves based on the CPRs shown in Figure 4.4 plus a small polynomial correction, for details see main text and Section 4.16. At $B_\parallel = 0$, there is a unique relationship between ω_0 and $\mathcal{K}$, but with increasing in-plane field a bimodal distribution of the anharmonicity appears. Simultaneously, the overall values of $|\mathcal{K}|$ increase with $B_\parallel$. The bimodal distribution confirms a diode CPR and eliminates other possible mechanisms behind the skewed flux responses discussed in Figure 4.3. Field values shown are $B_\parallel \in \{0, 125, 175, 225, 250, 275, 300\}\,\mathrm{mT}$, indicated by color as before.

the CPRs in this step to better match the experimental Kerr constants. These micro-adjustments are implemented as a high-order polynomial added to the existing CPR. To guarantee a minimal deviation from the established CPR, we fit both Kerr and flux arcs simultaneously in this procedure. The resulting CPRs deviate by less than 50 nA from the original ones; a detailed discussion of the modified CPR fits can be found in Sections 4.16 and 4.22. The lines shown in Figure 4.5d are derived from these micro-modified CPRs and the agreement to the experimental values is very good, considering the amount of uncertainties such as frequency-dependent values for the pump attenuation, the external decay rate of the circuit in direction of the pump input, the gradient functions for j_0 and $B_{\parallel} l_{\mathrm{eff}}$, gradients in ℓ_{lin} and w or SQUID asymmetries due to the two constrictions not being exactly identical.

4.7 Discussion

In this chapter, we investigated niobium quantum interference microwave circuits in magnetic in-plane fields up to 300 mT, and observed a field-induced superconducting diode effect in the monolithic interferometer nano-constrictions. The diode effect leads to a strong skewing of the circuit flux response, which we were able to fully reproduce based on a simple macroscopic constriction model. The model revealed that inhomogeneities in the constriction itself are likely the origin of the diode effect. In combination with inductive sensing of the CPR-derivative, it furthermore enabled us to reveal the asymmetric constriction current-phase relation as a function of magnetic in-plane field. Finally, we were able to eliminate other possible mechanisms behind the experimental findings by measuring the Kerr anharmonicity of the circuit which showed a strong bimodal distribution as a function of circuit resonance frequency and is completely compatible with the presented diode model.

From an application-oriented perspective, the circuits show promising characteristics for hybrid quantum systems, sensing and metrology in magnetic in-plane fields up to 300 mT and possibly beyond; frequency tuning range and flux responsivity are both enhanced by the in-plane field and the resulting diode effect, making Nb constriction devices a highly competitive technology for magnetic field applications. Furthermore, the simple circuit model we developed for the constriction diodes is easily applicable for future designs of yet unexplored constriction- or barrier-junction-array diodes with small footprints but large CPR asymmetries, which could be used to study and exploit diode-based enhancements of microwave circuits even at low magnetic fields. Finally, we expect the bimodal distribution of the Kerr anharmonicity and the flux responsivity, i.e. a certain decoupling of these two quantities from the circuit resonance frequency, to have useful implications for SQUID-based radiation-pressure systems and magnetometry.

In summary, our results constitute a promising starting point for the experimental combination of superconducting microwave circuits and superconducting diodes, in particular towards enhanced quantum circuits with yet unavailable functionalities, and towards a deeper understanding of the SD effect thanks to the possibility to inductively characterize the diode CPR and its derivatives using microwave measurements. We are convinced that a wide range of research fields may benefit from the findings presented here, including SQUID optomechanics for investigating the interplay between quantum physics and gravity, photon-pressure circuits (radio-frequency up-converters) for superconducting axion dark-matter detectors, quantum-limited parametric amplifiers with tunable nonlinearities, or dispersive magnetometry for high-bandwidth SQUID microscopy.

To complete our deliberations, the remaining sections of this chapter contain more details on some of the points discussed above, including comprehensive descriptions of the device fabrication, measurement theory, the employed numerical algorithms and the field alignment procedure. Additional information on the setup and the device under testing is presented, covering the resonator linewidth, an analysis of a second resonator as well as the effect of an inverted in-plane field, and we provide a thorough analysis of the effects of the different CPR model parameters on the resulting current density and CPR.

4.8 Device fabrication and preparation

The fabrication and preparation of the superconducting chip is executed in six steps, five of which regard the actual fabrication. The steps are individually described below. Note that the fabrication is much more sophisticated than necessary for SQUID circuits, since the chip also contains micromechanical elements in some resonators, though not in the one presented above. Despite the mechanical elements thus being completely irrelevant for the experiments and results presented here, we describe the entire chip fabrication for completeness and reproducibility.

Step 1: Sacrificial layer patterning. The fabrication starts with the patterning of the sacrificial layer for mechanical beams on the chip. To this end, a 26 mm × 26 mm chip of high-resistivity ($\rho > 10\,\mathrm{k\Omega\,cm}$ at room temperature) intrinsic silicon with a nominal thickness of 525 µm is covered with the adhesion promoter AR 300-80 as well as the photo-resist ma-N 1405 by spin-coating (resist thickness ∼0.5 µm). The resist is then patterned by means of maskless photolithography ($\lambda_{\mathrm{litho}} = 365\,\mathrm{nm}$) and developed using the developer ma-D 533/S. Since the

resist making up the sacrificial layer is sensitive to the solvents usually used to clean samples between fabrication steps (acetone, isopropanol), no such cleaning can be performed from here on out.

Step 2: Niobium deposition and patterning. Before depositing the conductive niobium layer, the sample is subjected to plasma ashing in an oxygen plasma to remove possible resist and adhesion-promoter residues on the silicon surface. Next, 300 nm of niobium are deposited by dc-magnetron sputtering. Optical lithography follows as before, but with the thicker positive resist ma-P 1215 (thickness ~1.5 µm) and the developer ma-D 331/S. The pattern is etched into the Nb film using reactive ion etching with SF_6 at an angle of 40° to the chip surface in order to ensure consistent etching around the mechanical beams, in particular on the sidewalls of the sacrifical-layer patches. During etching, the chip is constantly rotated to ensure homogeneous exposure.

Step 3: Dicing and release. Before removing all resist on the chip and thus releasing the sensitive mechanical beams, the sample is diced into the final pieces of 10 mm × 10 mm. The resist is then removed using oxygen plasma etching.

Step 4: Global etching for niobium thinning. The rather thick 300 nm niobium layer helped ensure mechanical stability as well as electrical contact at the edges of the mechanical beams but for the final device we target a film thickness of only 100 nm. In this step, the film thickness is reduced to the final value, again using SF_6 reactive ion etching, this time perpendicular to the chip surface for directed etching from the top. At this point, the chip is mounted as described in Step 6 and pre-characterized before the constriction-type Josephson junctions are added in the next step.

Step 5: Constriction cutting. Each resonator contains a loop in the inductive part of the circuit where the constriction junctions are placed after pre-characterization, converting it into a SQUID (cf. Figure 4.1). This is achieved using a neon ion microscope (NIM) which is capable of high-precision milling with a focused ion beam (FIB) of nano-scale spot size. For 2D junctions, two ~40 nm wide rectangles are cut into the wire from both sides, leaving a remaining constriction of around the same width between them. For 3D junctions, the constriction is additionally milled from the top with a lower dose, leading to reduced conductor thickness. Ion acceleration voltages and ion doses can be found in Table 4.1 on page 123.

Step 6: Final mounting. After fabrication is complete, the chip is mounted into a radiation tight copper housing with a printed circuit board (PCB) surrounding the chip, where it is wire-bonded to microwave feedlines and ground. The PCB contains coplanar waveguide feedlines leading to SMP connectors, where microwave cables are attached during measurement. After mounting into the measurement setup, the characterization of the device is performed.

4.9 Single-tone circuit response

The ideal transmission-response function of a high-Q parallel RLC circuit side-coupled to a feedline with characteristic impedance Z_0 by a coupling capacitance C_c is given by

$$S_{21}^{\text{ideal}} = 1 - \frac{\kappa_{\text{ext}}}{\kappa + 2\text{i}(\omega - \omega_0)} \tag{4.15}$$

with the angular excitation frequency ω and the resonance frequency $\omega_0 = 1/\sqrt{LC_{\text{tot}}}$. The total capacitance is given by $C_{\text{tot}} = C + C_c$, L and $C = 2C_{\text{idc}}$ are inductance and capacitance of the uncoupled circuit, respectively. The internal and external decay rates (linewidths) κ_{int} and κ_{ext}, are given by

$$\kappa_{\text{int}} = \frac{1}{R(C + C_c)} \tag{4.16}$$

$$\kappa_{\text{ext}} = \frac{\omega_0^2 C_c^2 Z_0}{2(C + C_c)} \tag{4.17}$$

and the total decay rate by $\kappa = \kappa_{\text{int}} + \kappa_{\text{ext}}$. The effective resistance R accounts for all internal losses of the circuit, such as resistive, dielectric or radiative losses.

Due to the cabling and all the microwave components in between the vector network analyzer and the circuit, the ideal reflection is not what we measure, though. To take frequency-dependent attenuation, the electrical cable length and possible interferences (e.g. parasitic transmission around the chip) into account, we model the actual measurement signal as

$$S_{21}^{\text{real}} = (a_0 + a_1\omega + a_2\omega^2)\text{e}^{\text{i}(\phi_0 + \phi_1\omega)}\Big(1 - \frac{\kappa_{\text{ext}}\text{e}^{\text{i}\theta}}{\kappa + 2\text{i}(\omega - \omega_0)}\Big). \tag{4.18}$$

The factors a_0, a_1, a_2, ϕ_0, ϕ_1 and θ are real-valued fit parameters. During our automated data fitting routine we first remove the absorption resonance from the dataset (leaving a gap in the S_{21}-dataset) and fit the remaining S_{21}-response with the background function

$$S_{21}^{\text{bg}} = (a_0 + a_1\omega + a_2\omega^2)\text{e}^{\text{i}(\phi_0 + \phi_1\omega)}. \tag{4.19}$$

As a result, we obtain preliminary values for a_0, a_1, a_2, ϕ_0 and ϕ_1. Then, we calculate $S_{21}^{\text{real}}/S_{21}^{\text{bg}}$ for the complete dataset and fit the resulting data with

$$S_{21}^{\theta} = 1 - \frac{\kappa_{\text{ext}}\text{e}^{\text{i}\theta}}{\kappa + 2\text{i}(\omega - \omega_0)} \tag{4.20}$$

from which we obtain a preliminary set of values for ω_0, κ, κ_{ext} and θ. Finally, we use all the preliminary values for a_0, a_1, a_2, ϕ_1, ϕ_2, ω_0, κ, κ_{ext} and θ as starting

parameters to re-fit the original dataset using (4.18). All the S_{21}-datasets in the figures of this chapter as well as the corresponding fit curves have been completely background-corrected (cf. next section) and we have additionally removed the interference angle θ.

4.10 Two-step background-correction

In order to achieve good results with the fitting procedure described in the previous section, the background of the data must already be quite uniform, as assumed in (4.19), which is not usually the case in the experiment due to interfering resonances in the measurement setup in combination with our large resonance linewidths. Measuring the (approximate) background directly allows us to first divide each S_{21} measurement by this measured background before in a second step fitting the resulting signal as described above.

We remove the resonance signal from the measurement by heating the sample to 5 K, which leaves the measurement background largely unaffected. At this temperature, the circuit resonances are completely absent due to the reduced transition-temperature of the nano-constrictions [34], while the on-chip coplanar waveguide feedline ($T_c \approx 9$ K) remains superconducting with nearly unchanged characteristics. Then, we record S_{21} traces for each resonator frequency window with identical settings to those we use for the measurements at 2.8 K. To reduce noise in the background signal, we take 20 traces and average them point-wise. This procedure was repeated each day of the measurement series (four in total) with very consistent results, validating the stability of the measurement setup. To even further reduce noise, we use the mean of these four sets of measured backgrounds for the final evaluation.

4.11 Field alignment by rotation

In order to align the applied field with the sample plane, we employ an arrangement as shown in Figure 4.6a. The large main coil is designed to apply a strong field $B_\parallel$ parallel to the chip surface, however, due to unavoidable assembly inaccuracies, it contains a small out-of-plane component $B_\parallel^z$. For compensating this out-of-plane component, a split-coil is mounted in the cryostat in such a way that it creates a field $B_\perp$ orthogonal to $B_\parallel$. At the same current, the compensation coils generate a much smaller field at the sample location than the main coil $B_\perp/B_\parallel = 0.8\,\%$, as it only needs to account for the small out-of-plane component of $B_\parallel$. However, the actual magnitude of $B_\parallel^z$ depends on the exact alignment between the main coil and the sample and cannot be precisely controlled, so the fields of the two coils need to be coordinated such that their out-of-plane components cancel out $B_\parallel^z + B_\perp^z = 0$.

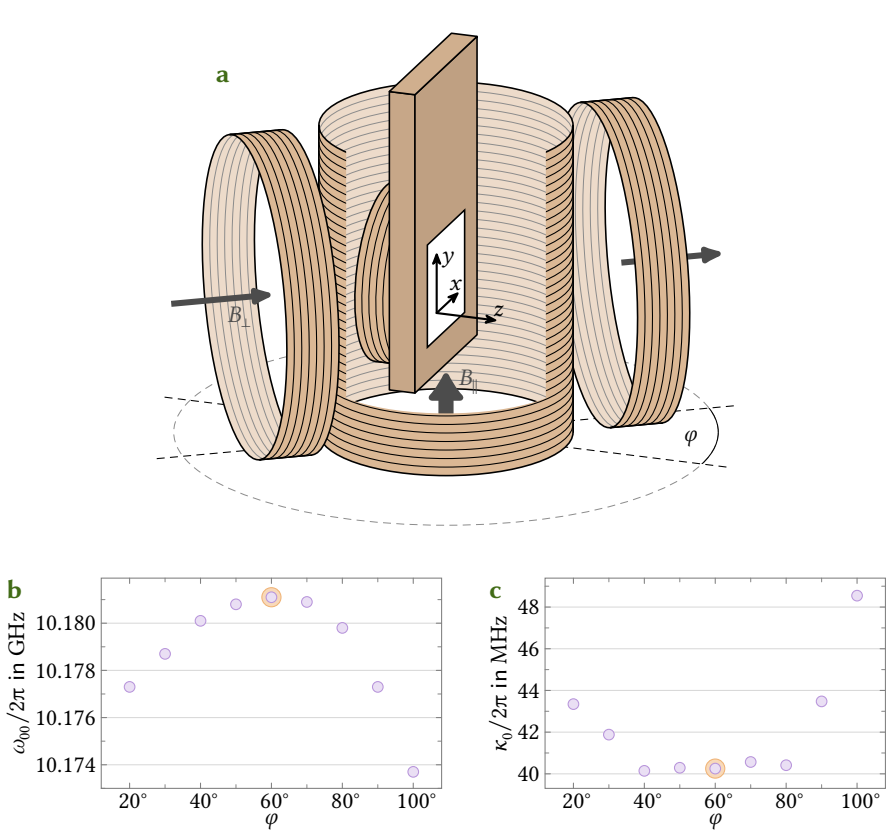

Figure 4.6: Alignment of the in-plane field by rotation. a Magnet arrangement in the cryostat. Directly attached to the chip housing is a small sample coil for applying Φ_b, which is not involved in the application of the in-plane field. A large coil generating $B_\parallel$ is wrapped on the outside of the vacuum compartment that chip and sample coil reside in. A weaker split-coil magnet applying $B_\perp$ is rigidly attached to the the cryostat, that is operated in series with the large main coil and used to compensate out-of-plane components of $B_\parallel$. To balance the compensation of the out-of-plane components of $B_\parallel$ and $B_\perp$, the vacuum compartment together with the chip assembly can be rotated inside the cryostat, adjusting their angle φ with respect to the symmetry axis of the split coil. **b** Sweetspot resonance frequencies ω_{00} vs rotation angle φ at an applied field of $B_\parallel = 250\,\mathrm{mT}$. The orange highlighted maximum at $\varphi = 60°$ marks the ideal field alignment φ_0; all experiments were performed at that angle. **c** Sweetspot linewidth κ_0 vs rotation angle φ extracted from the same resonance traces as the frequencies shown in b, again with the ideal angle φ_0 highlighted orange. Note that the sweetspot linewidth remains constant for $\varphi \in [40°, 80°]$, only increasing outside that range.

Rather than using two separate current sources for the two coils, which would entail uncorrelated current drifts as well as noise, and pose a severe challenge for effective field compensation, we operate the two coils in series, using a single in-house-built, low-noise, battery-powered current source. While this fixes the ratio $B_\perp/B_\parallel$ between the fields generated by the coils, we can control the ratio of their out-of-plane components $B_\perp^z/B_\parallel^z$ by rotating the vacuum cup with the attached sample assembly inside the cryostat and thus adjusting the angle φ between that assembly and the compensation coils. Quantitatively, $B_\parallel^z$ is constant with respect to φ while $B_\perp$ rotates around the y-axis, i.e. $B_\perp^z = B_\perp \cos\varphi$. Here, we neglect small misalignments between chip, rotational axis and split-coil, but while including inaccuracies would complicate the previous expression (and thus subsequent ones), perfect $B_\parallel^z$ compensation remains possible. We want to operate the setup with the optimal compensation angle φ_0 at which the out-of-plane components of the two fields cancel exactly $B_\perp^z + B_\parallel^z = (\cos\varphi - \cos\varphi_0)B_\perp = 0$.

In order to find φ_0, we apply a constant coil current $I_{\mathrm{coil}} = 1\,\mathrm{A}$ (i.e. $B_\parallel = 250\,\mathrm{mT}$ and $B_\perp = 2\,\mathrm{mT}$) and, for different φ, sweep the flux Φ_b through the SQUID loop using the sample coil attached directly to the sample housing, recording the flux response. The sweetspot frequencies of the resulting flux arcs are presented in Figure 4.6b. Similarly to the in-plane field, a magnetic out-of-plane field suppresses the resonance frequency ω_0 and increases the linewidth κ of the resonator, cf. Figure 4.3. Unlike the vortex-free Meissner response induced by a magnetic in-plane field, however, an out-of-plane field introduces vortices into the superconducting film as well as much larger screening currents, causing extra losses and frequency shifts at much smaller field values [74, 75], which in turn provide a sensitive probe for the magnitude of the out-of-plane field component. Comparing the sweetspot resonance frequencies $\omega_{00}(\varphi)$, we expect to find a minimum at $\varphi = 0$ (where $B_\perp^z/B_\parallel^z < -1$ is minimal), maxima at $\varphi = \pm\varphi_0$ (where $B_\perp^z/B_\parallel^z = -1$) and the global minimum at $\varphi = \pi$ (where $B_\perp^z/B_\parallel^z > 0$ is maximal). The sweetspot linewidths $\kappa_0(\varphi)$ correspondingly show opposite extrema at the same angles, but here the minimum at the optimum angle forms a plateau, with the linewidth only increasing outside some interval surrounding φ_0. This is in line with all flux being expelled from the superconducting film of the resonator below some critical field B_m, with magnetic vortices appearing and increasing the linewidth only for larger fields [76, 77]. To avoid hysteresis in the magnetic response due to Bean-like flux gradients / critical states [60, 78] and to minimize the risk of flux avalanches and flux jumps [61, 62] when microwave signals are applied, we perform field-cooling before each flux sweep and in particular for each new angle φ, heating the sample to $\sim 12\,\mathrm{K}$ and then cooling back down to 2.8 K, as described in Section 4.4.

Using this procedure, we find $\varphi_0 = 60°$, implying $|B_\parallel^z|/B_\parallel = 0.4\,\%$ and that the misalignment between the main coil field and the sample surface is $\sim 0.2°$. The additional orthogonal in-plane component $B_\perp^x$ introduced by the compensation coils

at that angle is 0.7 % of $B_{\parallel}$, corresponding to a rotation of $\sim 0.4°$, i.e. it is small, on the order of the assembly inaccuracies that are present in any case. The sweetspot linewidth remains constant at its minimum value in the interval from 40° to 80°, i.e. $\varphi_0 \pm 20°$), once more confirming the choice of compensation angle. Calculating the total out-of-plane field at these angles we estimate the threshold field for vortex penetration to be $B_{\mathrm{m}} \approx 0.7\,\mathrm{mT}$. This value is in line with the threshold fields reported in [76] for our strip width of $\sim 2\,\mu\mathrm{m}$ and serves to emphasize the quality of our field alignment.

4.12 Numerical algorithm to calculate the CPR

So as to avoid constant factors of no consequence to the numerical solution of the CPR, we introduce the normalized variables $\tilde{z} = z/a$, $\tilde{j} = j/j_0(0)$, $\delta_B = 2\pi B_{\parallel} l_{\mathrm{eff}}(0) a/\Phi_0$, $\delta_\ell = 2\pi j_0(0)\ell_{\mathrm{lin}}/\Phi_0$, $I_{00} = waj_0(0)$ and $\tilde{I} = I/I_{00}$, and rewrite (4.7) to (4.10) more concisely as

$$\tilde{j}(\tilde{z}, \delta_0) = (1 - 2\epsilon\tilde{z}) \sin\big(\delta_0 + \delta_B(1 + b\tilde{z})\tilde{z} - \delta_\ell \tilde{j}(\tilde{z}, \delta_0)\big) \tag{4.21}$$

$$\tilde{I}(\delta_0) = \int_{-1/2}^{1/2} \tilde{j}(\tilde{z}, \delta_0)\, \mathrm{d}\tilde{z}. \tag{4.22}$$

In order to find solutions to the implicit (normalized) current density equation, we treat $\tilde{j}$ as an independent variable, define

$$\mathcal{J} := (1 - 2\epsilon\tilde{z}) \sin\big(\delta_0 + \delta_B(1 + b\tilde{z})\tilde{z} - \delta_\ell \tilde{j}\big) - \tilde{j} \tag{4.23}$$

and solve $\mathcal{J}(\tilde{j}) = 0$ for a given set of model parameters $(\epsilon, b, \delta_B, \delta_\ell)$ and coordinates $(\tilde{z}, \delta_0)$ using standard root-finding algorithms. The matter is complicated by the fact that $\mathcal{J}(\tilde{j})$ may have multiple roots, and we need to find the correct one; that is, we need to find consistent roots for different $(\tilde{z}, \delta_0)$. Luckily, for $(\tilde{z}, \delta_0) = (0, 0)$ the problem is trivially solved by $\tilde{j} = 0$ and we can trace the continuously changing root from this starting value to any desired coordinates.

Naturally, doing this from scratch every time a current density needs to be computed would be very computationally expensive and inefficient, since it would trace the same values over and over again, in particular as we need to integrate over $\tilde{z}$ to obtain a CPR value, i.e. we always need the current density on the entire interval $\tilde{z} \in [-1/2, 1/2]$. Hence, instead of re-doing the calculation for each set of coordinates, we scan the relevant coordinate space $(\tilde{z}, \delta_0) \in [-1/2, 1/2] \times [-\pi, \pi]$ the first time a set of model parameters is used, overscanning it slightly to avoid edge effects, thus obtaining the complete $\tilde{j}(\tilde{z}, \delta_0)$, compute the integral $\tilde{I}(\delta_0)$ and cache the result. We then use fifth-degree splines in order to extract values of $\tilde{I}$ and

its derivatives for arbitrary δ_0 from the cached sampling of $\tilde{I}(\delta_0)$, not needing to solve $\mathcal{J} = 0$ more than once for each set of model parameters. In detail, starting from $(\tilde{z}, \delta_0) = (0, 0)$, we scan $\tilde{z}$ in both directions in steps of 0.01 and then, for all of these solutions together, scan δ_0 in both directions in steps of 0.05. The step sizes were determined by manual experimentation and allow for decent computation time without a significant reduction in accuracy.

A final wrinkle of our constriction model is that, for a given set of model parameters, the current density may not be well-defined for all sets of coordinates, particularly for large ϵ and δ_ℓ which result in regions of multiple $\mathcal{J}(\tilde{j})$ roots, similar to the multi-valued CPR of a homogeneous constriction resulting from $L_{\mathrm{lin}} > L_{\mathrm{J0}}$. In these cases, the tracked root of $\mathcal{J}(\tilde{j})$ may disappear at some $(\tilde{z}, \delta_0)$ when leaving a region of multiple roots, leaving only roots that cannot be reached from $(0, 0)$ in a continuous manner as outlined above. Our algorithm tries to detect these points by comparing the found root $\tilde{j}$ to the expected value, estimated using the gradient of $\tilde{j}(\tilde{z}, \delta_0)$, and discarding it if the discrepancy is larger than 0.01, which is why not all of the CPRs shown in Figure 4.4d fill the entire interval $\delta_0 \in [-\pi, \pi]$. This detection is not perfect, though, – especially in areas where the gradient grows very large – and, together with the unavoidable imprecision associated with numerical computations, can lead to noticeable inaccuracies at the edge of the CPR. These inaccuracies can often be alleviated by choosing different step sizes for the scanning of the coordinate space (which we do e.g. for the CPR curves presented in Figure 4.4d), but for our data evaluation they are conveniently inconsequential, as the experimentally accessible part of the CPR lies in its center, comfortably far from the numerical edge. Section 4.21 provides a detailed discussion of the effect each of the model parameters has on the current density distribution and the resulting CPR, also illustrating the appearance of the numerical edge of the solution.

As a last step in the algorithm, we numerically determine the phase $\tilde{\delta}_0$ at which $\tilde{I}(\delta_0 = \tilde{\delta}_0) = 0$ and obtain the shifted function $\tilde{I}(\delta_c)$ with the nominal constriction phase $\delta_c = \delta_0 - \tilde{\delta}_0$. This corresponds to the choice of z_0 for which $\delta_c = \delta(z_0)$ as discussed in Section 4.5.

4.13 Numerical algorithm to fit the flux arcs

We need to implement the function $\omega_0(\Phi_b)$ using the CPR $I(\delta_c) = I_{00}\,\tilde{I}(\delta_c)$ described in the previous section and fit it to the experimental data, varying the model parameters. To this end, we numerically invert (4.3) to get $\delta_c(\Phi_b)$, thus obtaining $L_c(\Phi_b)$ and finally $\omega_0(\Phi_b)$ directly from (4.4) and (4.5). However, this function only describes a single flux arc as a function of Φ_b while the experimental data consist of multiple flux arcs as a function of the bias coil current I_b. Hence,

we first need to convert this current into the bias flux

$$\frac{\Phi_\mathrm{b}}{\Phi_0} = \frac{I_\mathrm{b}}{I_\mathrm{b0}} - \frac{\Delta\Phi_\mathrm{b}}{\Phi_0} \tag{4.24}$$

with the current I_b0 coupling one flux quantum into the SQUID and a flux offset $\Delta\Phi_\mathrm{b}$, both a priori unknown. We also need to shift all flux arcs on top of each other to be able to fit them using our $\omega_0(\Phi_\mathrm{b})$.

To this end, we determine the flux arc each data point belongs to, using the discontinuous jumps to detect where the circuit jumps from one arc to the next/previous one. Due to the strong distortion of the arcs and the jumps between them at high in-plane fields, including the inversion of the jump direction, detection is more challenging there and some manual intervention is necessary to ensure a flawless separation of the data into individual flux arcs. Next, we determine the sweetspot I_b of each arc by calculating the derivative $\partial\omega_0/\partial I_\mathrm{b}$ in the vicinity of the arc maximum, fitting a linear function to it and extracting its zero. This allows us to extract I_b0 from the spacing of the sweetspot currents, and to define the shifted flux $\Phi'_\mathrm{b} = \Phi_\mathrm{b} - n\Phi_0$ with the flux arc number n, effectively shifting all arcs on top of the first one. Finally, we are able to fit $\omega_0(\Phi'_\mathrm{b})$, varying $\Delta\Phi_\mathrm{b}$ as well as the model parameters I_{00}, ϵ, b, δ_B and δ_ℓ.

However, doing this for each in-plane field separately would not lead to consistent model parameters, most of which should not depend on $B_\parallel$ or, in the case of $\delta_B \propto B_\parallel$, do so in a known manner. To account for this, we concatenate the flux arc data for all in-plane fields and fit them simultaneously, using a single set of the parameters I_{00}, ϵ, b and $\delta_B/B_\parallel$, allowing only $\Delta\Phi_\mathrm{b}$ and δ_ℓ to vary independently for each $B_\parallel$. Allowing the latter two quantities to vary with in-plane field is also physically reasonable, since the flux offset $\Delta\Phi_\mathrm{b}$ will depend on e.g. the exact alignment details between chip surface and in-plane field or single trapped flux quanta in the vicinity of the SQUID, and the specific inductance ℓ_lin is a kinetic inductance, which by nature is sensitive to magnetic fields.

In the simpler case of the CPR given by (4.2) and discussed in the context of Figure 4.2, no such concatenation is necessary, as we consider only a single field $B_\parallel = 0$. Additionally, we know the sweetspots position $\Phi'_\mathrm{b} = 0$, so we can extract $\Delta\Phi_\mathrm{b}$ directly from the sweetspot currents and need only vary I_0 in the fit.

4.14 Theory of the Kerr anharmonicity

In order to derive the Kerr anharmonicity of the system, we write its total energy as a fourth order Taylor approximation

$$U_\mathrm{tot}(\delta_\mathrm{ac}) = \sum_{k=0}^{4} \frac{c_k}{k!}\delta_\mathrm{ac}^k + \mathcal{O}(\delta_\mathrm{ac}^5) \tag{4.25}$$

in terms of some ac phase difference δ_{ac} from the equilibrium state, with the coefficients $c_k = \partial^k_{\delta_{\mathrm{ac}}} U_{\mathrm{tot}}\big|_{\delta_{\mathrm{ac}}=0}$. We are interested in the dynamics around an equilibrium state at $\delta_{\mathrm{ac}} = 0$, so we have $c_1 = 0$. Furthermore, we choose $c_0 = 0$ without loss of generality. The Kerr anharmonicity is then given by [70]

$$\mathcal{K} = \frac{e^2}{2\hbar C_{\mathrm{tot}}} \frac{c_4}{c_2}. \tag{4.26}$$

Thus, we need to determine the SQUID resonator potential as a function of the total resonator phase δ_{tot}, find the equilibrium phase and calculate the relevant derivatives.

We consider a simplified circuit model as shown in Figure 4.7, where all relevant quantities for the calculation are defined. Compared with the circuit shown in Figure 4.1d, we use a more basic representation of the LC-resonator, and we neglect the inductive effect of the bottom arm in Figure 4.2a, using $L_{\mathrm{arm}} = L_{\mathrm{loop}}/3$ and $L_{\mathrm{r}} = L_{\mathrm{b}} - L_{\mathrm{arm}}/2$. We assume the junctions to behave identically with respect to current flowing along the SQUID ring, i.e. $I_1 = I(\delta_{\mathrm{c1}})$ and $I_2 = I(\delta_{\mathrm{c2}})$ with the same CPR $I(\delta)$. The total circuit energy is

$$U_{\mathrm{tot}} = E_{\mathrm{c}}(\delta_{\mathrm{c1}}) + E_{\mathrm{c}}(\delta_{\mathrm{c2}}) + \frac{E_{\mathrm{arm}}}{2}(\delta_{L1}^2 + \delta_{L2}^2) + \frac{E_{\mathrm{r}}}{2}\delta_{\mathrm{r}}^2 \tag{4.27}$$

with the constriction energy

$$E_{\mathrm{c}}(\delta) = \frac{\Phi_0}{2\pi}\int_0^{\delta} I(\delta')\,\mathrm{d}\delta' \tag{4.28}$$

and the inductive energies

$$E_{\mathrm{arm}} = \left(\frac{\Phi_0}{2\pi}\right)^2 \frac{1}{L_{\mathrm{arm}}} \qquad E_{\mathrm{r}} = \left(\frac{\Phi_0}{2\pi}\right)^2 \frac{1}{L_{\mathrm{r}}}. \tag{4.29}$$

Current conservation dictates (cf. Figure 4.7)

$$\delta_{L1} = \frac{\Phi_0}{2\pi}\frac{I(\delta_{\mathrm{c1}})}{E_{\mathrm{arm}}} \qquad \delta_{L2} = \frac{\Phi_0}{2\pi}\frac{I(\delta_{\mathrm{c2}})}{E_{\mathrm{arm}}} \tag{4.30}$$

$$\delta_{\mathrm{r}} = \frac{L_{\mathrm{r}}}{L_{\mathrm{arm}}}(\delta_{L1} - \delta_{L2}) \tag{4.31}$$

and additionally the total SQUID flux, comprising the contributions δ_1 and δ_2 of the two SQUID arms, must compensate the externally applied flux δ_{ext}

$$\delta_1 + \delta_2 + \delta_{\mathrm{ext}} = 0. \tag{4.32}$$

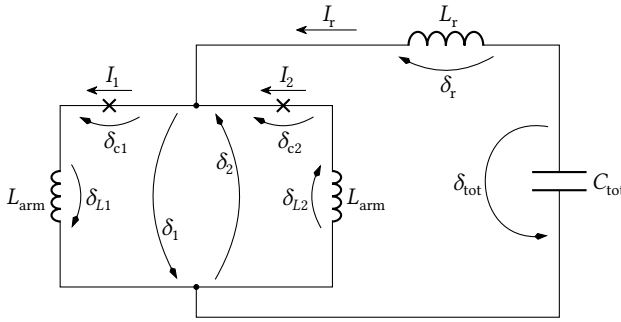

Figure 4.7: Parameters of a SQUID resonator circuit. Quantities characterizing the components, including the phase differences across them, are indicated in the diagram. Note that the orientation of the currents and phase differences in the SQUID arms is chosen such that a ring current in the SQUID contributes equally to both arms while a bias current through it contributes with opposite signs.

This means that of the five phases in (4.27) only one is actually free, or in other words, we can write all of them as a function of the free total phase δ_{tot}, and the energy as $U_{\text{tot}}(\delta_{\text{tot}})$.

Now what remains to be done is to calculate the first four derivatives $\partial^k_{\delta_{\text{tot}}} U_{\text{tot}}$ and evaluate them in the equilibrium state, where no current flows through the resonator inductance, i.e. only a ring current in the SQUID is present. This implies $\delta_r = 0$, $I_1 = I_2$ and thus $\delta_{c1} = \delta_{c2} =: \delta_c$. Using the dimensionless CPR derivatives

$$g_k = \frac{\mathrm{d}^k \mathfrak{F}_{L1}}{\mathrm{d}\delta_{c1}^k}\bigg|_{\delta_{c1}=\delta_c} = \frac{\mathrm{d}^k \mathfrak{F}_{L2}}{\mathrm{d}\delta_{c2}^k}\bigg|_{\delta_{c2}=\delta_c} = \frac{\Phi_0}{2\pi}\frac{1}{E_{\text{arm}}}\frac{\mathrm{d}^k I}{\mathrm{d}\delta^k}(\delta_c) \tag{4.33}$$

(also given in (4.12) in an alternative form) and the inductance participation ratio

$$p = \left(1 + \frac{2E_{\text{arm}}}{E_r}\frac{g_1}{1+g_1}\right)^{-1} = \frac{(L_{\text{arm}} + L_c)/2}{L_r + (L_{\text{arm}} + L_c)/2} \tag{4.34}$$

we find, after some algebra,

$$c_2 = 2pE_{\text{arm}}\frac{g_1}{1+g_1} = \left(\frac{\Phi_0}{2\pi}\right)^2 \frac{1}{L_r + (L_{\text{arm}} + L_c)/2} \tag{4.35}$$

$$c_4 = -2p^4 E_{\text{arm}}\frac{3g_2^2 - g_3(1+g_1)}{(1+g_1)^5} \tag{4.36}$$

as well as $c_3 = 0$ due to symmetry. Finally, plugging these results into (4.26), we obtain $\mathcal{K}$ as given in (4.11).

4.15 Two-tone circuit response

General considerations. We model the classical intracavity field $\alpha(t)$ of the SQUID circuits with Kerr nonlinearity and nonlinear damping using the equation of motion [27, 34]

$$\dot{\alpha} = \left(\mathrm{i}(\omega_0 + \mathcal{K}|\alpha|^2) - \frac{\kappa + \kappa_{\mathrm{nl}}|\alpha|^2}{2}\right)\alpha + \mathrm{i}\sqrt{\frac{\kappa_{\mathrm{ext}}}{2}}S_{\mathrm{in}}. \tag{4.37}$$

Here, ω_0 is the cavity resonance frequency, $\mathcal{K}$ is the Kerr nonlinearity (frequency shift per photon), κ is the bare total linewidth, κ_{nl} is the nonlinear damping constant, κ_{ext} is the external linewidth and S_{in} is the input field. The intracavity field is normalized such that $|\alpha|^2$ corresponds to the intra-cavity photon number and $|S_{\mathrm{in}}|^2$ to the input photon flux on the coplanar waveguide feedline.

The solution of this equation of motion significantly depends on the pump power and on the number of tones sent to the cavity. However, given this solution α, the circuit output field will always be given by [79, 80]

$$S_{\mathrm{out}} = S_{\mathrm{in}} + \mathrm{i}\sqrt{\frac{\kappa_{\mathrm{ext}}}{2}}\,\alpha \tag{4.38}$$

and the ideal transmission response function thus by

$$S_{21}^{\mathrm{ideal}} = 1 + \mathrm{i}\sqrt{\frac{\kappa_{\mathrm{ext}}}{2}}\frac{\alpha}{S_{\mathrm{in}}}. \tag{4.39}$$

The nonlinear single-tone regime. We start by setting the input field to a single pump-tone $S_{\mathrm{in,st}} = S_{\mathrm{p}}\mathrm{e}^{\mathrm{i}\omega_{\mathrm{p}}t}$ with the frequency ω_{p} and a complex-valued amplitude S_{p}. For the intracavity field, we make the ansatz $\alpha = \alpha_{\mathrm{p}}\mathrm{e}^{\mathrm{i}\omega_{\mathrm{p}}t}$ with real-valued α_{p}; the phase delay between input and response is encoded in $\arg(S_{\mathrm{p}})$. The equation of motion now reads

$$\mathrm{i}\omega_{\mathrm{p}}\alpha_{\mathrm{p}} = \left(\mathrm{i}(\omega_0 + \mathcal{K}\alpha_{\mathrm{p}}^2) - \frac{\kappa + \kappa_{\mathrm{nl}}\alpha_{\mathrm{p}}^2}{2}\right)\alpha_{\mathrm{p}} + \mathrm{i}\sqrt{\frac{\kappa_{\mathrm{ext}}}{2}}S_{\mathrm{p}}. \tag{4.40}$$

Introducing the intracircuit pump photon number $n_{\mathrm{c}} = \alpha_{\mathrm{p}}^2$, the pump photon flux $n_{\mathrm{p}} = |S_{\mathrm{p}}|^2 = P_{\mathrm{p}}/\hbar\omega_{\mathrm{p}}$ and the detuning $\Delta_{\mathrm{p}} = \omega_{\mathrm{p}} - \omega_0$ between the pump and the bare cavity resonance, we obtain

$$\left(\Delta_{\mathrm{p}} - \mathcal{K}n_{\mathrm{c}} - \mathrm{i}\frac{\kappa + \kappa_{\mathrm{nl}}n_{\mathrm{c}}}{2}\right)\alpha_{\mathrm{p}} = \sqrt{\frac{\kappa_{\mathrm{ext}}}{2}}S_{\mathrm{p}} \tag{4.41}$$

or, taking the absolute square on both sides,

$$\left((\Delta_{\mathrm{p}} - \mathcal{K}n_{\mathrm{c}})^2 + \left(\frac{\kappa + \kappa_{\mathrm{nl}}n_{\mathrm{c}}}{2}\right)^2\right)n_{\mathrm{c}} = \frac{\kappa_{\mathrm{ext}}}{2}n_{\mathrm{p}}. \tag{4.42}$$

Finding the real-valued roots of this characteristic third-degree polynomial yields the physical solutions for the amplitude α_p; in the case of three real-valued roots the highest and lowest amplitudes are the stable states, though there is only one such root for our $\mathcal{K} < 0$ and $\Delta_\mathrm{p} > 0$. The phase delay between input and response can be read from (4.41) and is

$$\arg(S_\mathrm{p}) = \mathrm{atan2}\Big(-\frac{\kappa + \kappa_\mathrm{nl} n_\mathrm{c}}{2}, \Delta_\mathrm{p} - \mathcal{K} n_\mathrm{c}\Big). \tag{4.43}$$

Having determined the complete complex field solution, we can calculate the transmission

$$S_{21,\mathrm{st}}^{\mathrm{ideal}} = 1 + \mathrm{i}\sqrt{\frac{\kappa_\mathrm{ext}}{2}}\frac{\alpha_\mathrm{p}}{S_\mathrm{p}}, \tag{4.44}$$

which for low pump powers (using $\mathcal{K} = \kappa_\mathrm{nl} = 0$) corresponds to (4.15). Note that we do not use these equations for any data analysis in this chapter, but we include them as a prerequisite for the calculation concerning the two-tone regime.

The linearized two-tone regime. In addition to the strong pump-tone at frequency ω_p with fixed power $P_\mathrm{p} = n_\mathrm{p}\hbar\omega_\mathrm{p}$, we now insert a weak probe signal at the scanning frequency ω_s. We write the total input as $S_\mathrm{in,tt} = S_\mathrm{p}\mathrm{e}^{\mathrm{i}\omega_\mathrm{p}t} + S_\mathrm{s}\mathrm{e}^{\mathrm{i}\omega_\mathrm{s}t}$ with another complex field amplitude S_s. For the intracavity field, we use the ansatz $\alpha = \big(\alpha_\mathrm{p} + \alpha_\mathrm{s}(t)\big)\mathrm{e}^{\mathrm{i}\omega_\mathrm{p}t}$ with a complex and time-dependent $\alpha_\mathrm{s}(t)$ and obtain the equation of motion

$$\begin{aligned}
&\mathrm{i}\omega_\mathrm{p}(\alpha_\mathrm{p} + \alpha_\mathrm{s}) + \dot{\alpha}_\mathrm{s} \\
&\quad = \mathrm{i}\Big(\omega_0 + \mathcal{K}\big(\alpha_\mathrm{p}^2 + \alpha_\mathrm{p}(\alpha_\mathrm{s} + \alpha_\mathrm{s}^*) + |\alpha_\mathrm{s}|^2\big)\Big)(\alpha_\mathrm{p} + \alpha_\mathrm{s}) \\
&\qquad - \Big(\frac{\kappa}{2} + \frac{\kappa_\mathrm{nl}}{2}\big(\alpha_\mathrm{p}^2 + \alpha_\mathrm{p}(\alpha_\mathrm{s} + \alpha_\mathrm{s}^*) + |\alpha_\mathrm{s}|^2\big)\Big)(\alpha_\mathrm{p} + \alpha_\mathrm{s}) \\
&\qquad + \mathrm{i}\sqrt{\frac{\kappa_\mathrm{ext}}{2}}(S_\mathrm{p} + S_\mathrm{s}\mathrm{e}^{\mathrm{i}\Omega_\mathrm{s}t})
\end{aligned} \tag{4.45}$$

where we introduced the probe frequency with respect to the pump $\Omega_\mathrm{s} = \omega_\mathrm{s} - \omega_\mathrm{p}$.

We now perform the linearization by dropping all terms not linear or constant in the small quantity α_s and get

$$\begin{aligned}
&\mathrm{i}\omega_\mathrm{p}(\alpha_\mathrm{p} + \alpha_\mathrm{s}) + \dot{\alpha}_\mathrm{s} \\
&\quad = \Big(\mathrm{i}(\omega_0 + \mathcal{K}\alpha_\mathrm{p}^2) - \frac{\kappa + \kappa_\mathrm{nl}\alpha_\mathrm{p}^2}{2}\Big)(\alpha_\mathrm{p} + \alpha_\mathrm{s}) \\
&\qquad + \Big(\mathrm{i}\mathcal{K} - \frac{\kappa_\mathrm{nl}}{2}\Big)(\alpha_\mathrm{s} + \alpha_\mathrm{s}^*)\alpha_\mathrm{p}^2 \\
&\qquad + \mathrm{i}\sqrt{\frac{\kappa_\mathrm{ext}}{2}}(S_\mathrm{p} + S_\mathrm{s}\mathrm{e}^{\mathrm{i}\Omega_\mathrm{s}t}).
\end{aligned} \tag{4.46}$$

The time-independent terms are identical to (4.40) of the single-tone case and allow us to determine α_p and n_c as before. Fourier transforming the remaining terms with the transform variable Ω (frequency relative to the pump frequency) yields

$$\frac{\hat{\alpha}_\mathrm{s}}{\chi_\alpha} = \left(\mathrm{i}\mathcal{K} - \frac{\kappa_\mathrm{nl}}{2}\right) n_\mathrm{c} \hat{\alpha}_\mathrm{s}^\star + \mathrm{i}\sqrt{\frac{\kappa_\mathrm{ext}}{2}}\hat{S}_\mathrm{s} \tag{4.47}$$

where $\hat{\alpha}_\mathrm{s}(\Omega)$ is the Fourier transform of $\alpha_\mathrm{s}(t)$, $\hat{S}_\mathrm{s}(\Omega)$ is a Dirac peak at $\Omega = \Omega_\mathrm{s}$ and we introduced the counter-rotating complex conjugate $\hat{\alpha}_\mathrm{s}^\star(\Omega) = \hat{\alpha}_\mathrm{s}^*(-\Omega)$, such that $\hat{\alpha}_\mathrm{s}^\star(\Omega)$ is the Fourier transform of $\alpha_\mathrm{s}^*(t)$. Furthermore, we defined

$$\chi_\alpha(\Omega) = \left(\mathrm{i}(\Delta_\mathrm{p} - 2\mathcal{K}n_\mathrm{c} + \Omega) + \frac{\kappa + 2\kappa_\mathrm{nl} n_\mathrm{c}}{2}\right)^{-1}. \tag{4.48}$$

Substituting the equivalent relation for $\hat{\alpha}_\mathrm{s}^\star$, we find

$$\hat{\alpha}_\mathrm{s} = \mathrm{i}\chi_\mathrm{s}\sqrt{\frac{\kappa_\mathrm{ext}}{2}}\left(\hat{S}_\mathrm{s} - \left(\mathrm{i}\mathcal{K} - \frac{\kappa_\mathrm{nl}}{2}\right) n_\mathrm{c} \chi_\alpha^\star \hat{S}_\mathrm{s}^\star\right) \tag{4.49}$$

with

$$\chi_\mathrm{s} = \frac{\chi_\alpha}{1 - (\mathcal{K}^2 + \kappa_\mathrm{nl}^2/4) n_\mathrm{c}^2 \chi_\alpha \chi_\alpha^\star}. \tag{4.50}$$

The VNA measures only the circuit response at $\Omega = \Omega_\mathrm{s}$, so we need not consider the second, counter-rotating term in (4.49) and finally find the transmission response at the probe frequency

$$S_{21,\mathrm{tt}}^\mathrm{ideal} = 1 - \frac{\kappa_\mathrm{ext}}{2}\chi_\mathrm{s}. \tag{4.51}$$

The pumped Kerr modes. To find the resonance frequencies of the susceptibility χ_s, we determine the complex frequencies $\tilde{\Omega}_{0\mathrm{p}}$ for which $1/\chi_\mathrm{s} = 0$. The real part of such a solution is the resonance frequency $\Omega_{0\mathrm{p}} = \mathrm{Re}(\tilde{\Omega}_{0\mathrm{p}}) = \omega_{0\mathrm{p}} - \omega_\mathrm{p}$ while the imaginary part corresponds to half the mode linewidth $\kappa_\mathrm{p} = 2\,\mathrm{Im}(\tilde{\Omega}_{0\mathrm{p}})$. Setting the denominator from (4.50) to zero leads to

$$\tilde{\Omega}_{0\mathrm{p}}^\pm = \mathrm{i}\frac{\kappa + 2\kappa_\mathrm{nl} n_\mathrm{c}}{2} \pm \sqrt{(\Delta_\mathrm{p} - \mathcal{K}n_\mathrm{c})(\Delta_\mathrm{p} - 3\mathcal{K}n_\mathrm{c}) - \frac{\kappa_\mathrm{nl}^2 n_\mathrm{c}^2}{4}}. \tag{4.52}$$

The radicand is always positive for our experimental parameters, so the system has two resonances

$$\omega_{0\mathrm{p}}^\pm = \omega_\mathrm{p} \pm \sqrt{(\Delta_\mathrm{p} - \mathcal{K}n_\mathrm{c})(\Delta_\mathrm{p} - 3\mathcal{K}n_\mathrm{c}) - \frac{\kappa_\mathrm{nl}^2 n_\mathrm{c}^2}{4}} \tag{4.53}$$

split symmetrically around the pump frequency, though we observe only $\omega_{0\mathrm{p}} = \omega_{0\mathrm{p}}^-$ due to our experimental parameters.

In the experiment, we measure the shift of this mode with respect to the unpumped resonance frequency $\delta\omega_0 = \omega_{0\mathrm{p}} - \omega_0$ which is given by

$$\delta\omega_0 = \Delta_\mathrm{p} - \sqrt{(\Delta_\mathrm{p} - \mathcal{K}n_\mathrm{c})(\Delta_\mathrm{p} - 3\mathcal{K}n_\mathrm{c}) - \frac{\kappa_\mathrm{nl}^2 n_\mathrm{c}^2}{4}}. \tag{4.54}$$

Besides the shifted resonance frequency, we also extract the pumped linewidth from the transmission data

$$\kappa_\mathrm{p} = \kappa + 2\kappa_\mathrm{nl} n_\mathrm{c} \tag{4.55}$$

and so the only unknown value remaining in (4.54) is the product $\mathcal{K}n_\mathrm{c}$. Given n_c, we can thus determine $\mathcal{K}$ by fitting that relation to the experimental data.

Calculating the photon number. We now solve (4.54) for $\Delta_\mathrm{p} - \mathcal{K}n_\mathrm{c}$, recalling that $\Omega_{0\mathrm{p}} = \omega_{0\mathrm{p}} - \omega_\mathrm{p} = \delta\omega_0 - \Delta_\mathrm{p}$, and get

$$\Delta_\mathrm{p} - \mathcal{K}n_\mathrm{c} = \frac{1}{3}\left(\Delta_\mathrm{p} \pm \sqrt{\Delta_\mathrm{p}^2 + 3\left(\frac{\kappa_\mathrm{nl}^2 n_\mathrm{c}^2}{4} + \Omega_{0\mathrm{p}}^2\right)}\right). \tag{4.56}$$

Note that only the positive solution is relevant for our purposes. In the experiment, we measure or set all of the values on the right-hand side of this equation, i.e. we have direct experimental access to $\tilde{\Delta} \coloneqq \Delta_\mathrm{p} - \mathcal{K}n_\mathrm{c}$. The characteristic polynomial (4.42) contains the same quantity and so we can extract n_c from it using

$$n_\mathrm{c} = \frac{2P_\mathrm{p}}{\hbar\omega_\mathrm{p}} \frac{\kappa_\mathrm{ext}}{(\kappa + \kappa_\mathrm{nl} n_\mathrm{c})^2 + \tilde{\Delta}^2}. \tag{4.57}$$

Again, all values on the right-hand side are directly accessible in the experiment, except that the pump power P_SG is set at the signal generator and reaches the chip attenuated by some unknown factor $P_\mathrm{p} = \zeta P_\mathrm{SG}$. We can, however, determine the ratio n_c/ζ from the experimental data and, since only the product $\mathcal{K}n_\mathrm{c}$ appears in (4.54), use that value to find $\zeta\mathcal{K}$ from a fit to the experimental $\delta\omega_0$ data. By comparing the result with the $\mathcal{K}$-values predicted by the CPR model we can later extract a value for ζ.

4.16 Numerical algorithm to fit $\mathcal{K}$ with modified CPRs

In a first step, we determine $\zeta\mathcal{K}$ for each two-tone measurement as outlined above by extracting $\delta\omega_0$ and n_c/ζ from the measurement data for each power and then fitting the function $\delta\omega_0(n_\mathrm{c}/\zeta)$ given by (4.54) to those data under variation of $\zeta\mathcal{K}$. From the CPRs resulting from the flux arc fits, we calculate the theoretically predicted

$\mathcal{K}_{\text{theo}}$ and by dividing the two values obtain $\zeta \sim 4 \cdot 10^{-5}$, corresponding to 44 dB of attenuation, consistent with the expected attenuation in our setup (30 dB of explicit attenuation, cf. Figure 4.1f or 4.8, and ∼14 dB from cables and connectors).

Since the Kerr anharmonicity depends on the second- and third-order derivatives of the CPR, it is extremely sensitive to small errors in the theoretical CPR and indeed the experimental data match the model prediction only roughly, cf. Section 4.22. As a consequence, we do not get a constant ζ for all flux bias points and magnetic in-plane fields, though the qualitative features of the Kerr response to bias flux response are reproduced nicely by the model. Possible reasons include imperfections in the model (e.g. due to the assumed linear gradients of j_0 and $B_{\parallel} l_{\text{eff}}$ in the junction) as well as as possible pump-frequency dependence of the attenuation ζ. To account for these unknowns and demonstrate that a good match between theory and data can be achieved using imperceptible changes to the CPR, we modify the CPR to $I(\delta_c) + \Delta I(\delta_c)$ using a small polynomial correction

$$\Delta I = J(q_1 \tilde{\delta}_c + q_3 \tilde{\delta}_c^3 + q_8 \tilde{\delta}_c^8 + q_9 \tilde{\delta}_c^9) \tag{4.58}$$

where the factor $J = \max(\partial_{\delta_c} I) = \partial_{\delta_c} I(\delta_{c0})$ is the maximum slope of the original CPR (corresponding to the flux arc sweetspot) and $\tilde{\delta}_c = \delta_c - \delta_{c0}$ is the constriction phase relative to that point. The inclusion of J serves to keep the free parameters in an intermediate value range and to thus avoid possible numerical problems when varying them in a fitting routine, and it also eases interpretation of the q_k by making them encode the relative change to the junction inductance, rather than an absolute CPR offset. Additionally, we consider a ζ that is linear in pump frequency

$$\zeta(\omega_p) = \zeta_0\big(1 + \zeta_1 (\omega_p - \omega_p^{\text{ref}})\big) \tag{4.59}$$

with a constant $\omega_p^{\text{ref}} = 2\pi \cdot 10.25\,\text{GHz}$ which is chosen near the pump frequency used at the zero-field arc sweetspot, such that ζ_0 is approximately the attenuation at that point. This is useful both for an intuitive interpretation of the fit parameters and for the fit routine itself, as changes in ζ_1 do not cause large changes in the absolute value of ζ in the relevant ω_p region, only changing its slope.

Now, we fit the theoretical values to the measured Kerr anharmonicity and to the flux arcs simultaneously, varying ζ_0 and ζ_1 (affecting the experimental $\mathcal{K}(\Phi_b)$) as well as, individually for each field, q_1, q_3, q_8 and q_9 (affecting $\mathcal{K}_{\text{theo}}(\Phi_b)$ and, to a lesser extent, the flux-arc fits $\omega_0(\Phi_b)$). Since there are many more flux-arc points than two-tone measurements, and their numerical value is several orders of magnitude larger, we need to weight the flux arc residuals in the fit such that they do not overwhelm the Kerr data (or vice versa). We find that a relative weight of 10^{-4} strikes a nice balance between the two datasets, except for the highest fields, where we use slightly larger weights ($2.5 \cdot 10^{-4}$ at 275 mT and $5 \cdot 10^{-4}$ at 300 mT).

The discrepancy between the measured and the predicted Kerr response is largest near the edge of the flux arc, where the uncertainty of the experimental values is also greatest, cf. the error bars in Figure 4.5d or 4.14c. We take this fact into account by weighting the Kerr residuals in the fit with the factor $(\sigma_{\mathcal{K}}^{\min}/\sigma_{\mathcal{K}})^{1/3}$, where $\sigma_{\mathcal{K}}$ is the fit uncertainty reported by the $\zeta\mathcal{K}$ fit used to determine the value in question and $\sigma_{\mathcal{K}}^{\min}$ is its minimum value at the same in-plane field. The exponent 1/3 was again determined by experimentation and found to strike a good balance, reducing the impact of the uncertain points without neglecting them completely.

Varying all of the fit parameters at the same time does not result in good fit convergence, so we employ a multi-step process. In a first step, we set $\zeta_1 = 0$ and vary the other parameters (including ζ_0) individually for each $B_{\parallel}$. Using starting values for ζ_0 and ζ_1 that result in $\zeta(\omega_{\mathrm{p}})$ on the order of those just found, we vary only those two parameters in a second fit for all fields simultaneously, keeping the polynomial coefficients q_k constant at the values from the first fit. Finally, in the third step, we vary the coefficients q_k once more, at each field individually, keeping ζ_0 and ζ_1 constant at the values from the previous fit.

4.17 Complete experimental setup

A schematic of the complete experimental setup is shown in Figure 4.8 and described there. We use in-house-built, low-noise, battery-powered dc current sources to drive the different magnetic coils in the setup. Driving the compensation coils in series with the main coil ensures that any current drifts or noise contributions from the current source are present equally in all of them, thus not affecting the compensation, i.e. the orientation of the total field. To minimize the coupling of external fields as well as wire cross-talk, all dc wires inside the vacuum compartment are installed as twisted pairs and those outside the cryostat are shielded.

The microwave cables in the cryostat dipstick are coaxial stainless steel cables for low thermal conductivity. At our measurement frequencies of ~10 GHz we expect ~8 dB of attenuation from the ~1.5 m stainless-steel cable and ~3 dB from the 2 m room-temperature cable in each input/output line. Additionally attenuating the input signals by 30 dB at cryogenic temperatures ensures that room-temperature noise from the vector network analyzer (VNA) and the signal generator (SG) is reduced to a level close to that of the sample temperature $T_{\mathrm{s}} = 2.8\,\mathrm{K}$.

Since the temperature-sensing diode used to control T_{s} is placed directly on the copper sample box for optimal thermal contact, it is also exposed to the strong magnetic field $B_{\parallel}$ applied to the sample, affecting its temperature response and thus the temperature measured by the T controller. Even though the orientation of the diode in the field is chosen to minimize this effect, it is still considerable, reducing the temperature reading at the measurement temperature by more than 0.5 K at

$B_{\parallel} = 300\,\mathrm{mT}$ compared to the zero-field value. In order to keep the temperature constant despite this shift, we set the temperature to 2.8 K at zero field and interrupt the PID feedback temperature control while ramping the coil current I_{coil}, instead keeping the power supplied to the heating resistor constant. After the target current has been reached, we use the shifted temperature reading as the new temperature set-point and resume the PID control. We verify the integrity of this process using a second temperature diode placed outside the large $B_{\parallel}$ coil in the sample assembly, which does not experience as high fields and is thus less affected, as well as by checking the set-point that results from it after ramping the field back to zero. Typically, the discrepancy from the original set-point after a full measurement day comprising several field-ramps is only a few mK, mostly driven by the fact that the heating power of the T controller cannot be set with the same precision as that used by the device during PID control.

Figure 4.8: Schematic of the experimental setup. The superconducting chip is mounted inside a radiation-tight copper sample holder, which in turn is placed inside the vacuum compartment of a liquid helium (LHE) cryostat. A temperature-sensing diode mounted directly on the copper sample box, in combination with a resistive heater placed close by in the dipstick assembly, allows temperature control with a stability $\Delta T_{\mathrm{s}} < 1\,\mathrm{mK}$ using PID feedback control provided by a temperature controller. Pumping on the helium gas allows setting the measurement temperature to $T_{\mathrm{s}} = 2.8\,\mathrm{K}$. Coaxial microwave cables connect the vector network analyzer (VNA) as well as, via a directional coupler, a signal generator (SG) to the sample, with both devices sharing the 10 MHz reference-clock signal provided by the SG. The input lines both of VNA and of SG are attenuated by 30 dB at cryogenic temperatures to reduce the input noise to approximately the noise level at the measurement temperature. The output line is equipped with two high-electron-mobility-transistor (HEMT) amplifiers for maximized signal-to-noise ratio, one at cryogenic temperatures and one at room temperature. To prevent the amplifiers from saturating, the pump signal is inserted into the device at the probe signal output and an attenuator is placed at the input of the room-temperature amplifier. Another attenuator is placed at the SG output to shift its power output range, with the power P_{SG} of the pump signal with frequency ω_{p} defined as the shifted power. Numbers near the attenuators, the directional coupler and the amplifiers are given in units of dB. For the application of the magnetic in-plane field, a large cylindrical superconducting coil is wrapped directly around the cup of the vacuum compartment, connected in series with a split-coil magnet that is rigidly attached to the cryostat and used to compensate out-of-plane components of the main coil field $B_{\parallel}$. Part of the sample assembly is clipped away in the diagram to reveal the small magnetic sample coil mounted behind it. Two low-noise dc current sources provide the driving currents I_{b} for the sample coil and I_{coil} for the in-plane field coils, and I_{b} is additionally low-pass filtered at cryogenic temperatures with a cutoff frequency of $\sim 3\,\mathrm{kHz}$. The entire cryostat is surrounded by a double-layer mu-metal shield for magnetic screening.

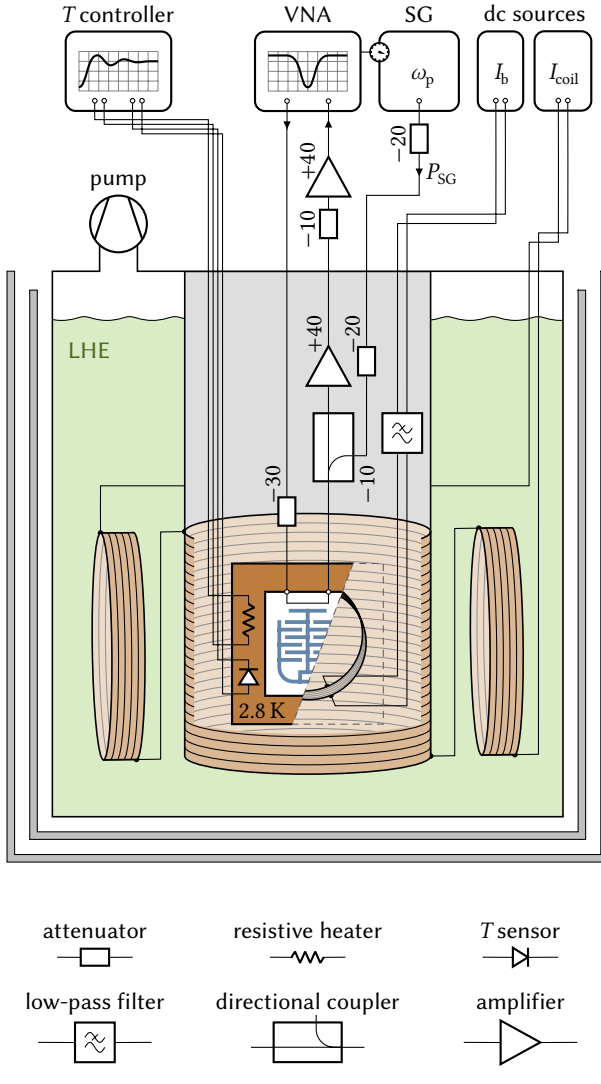
T controller
VNA
SG
dc sources
ω_p
I_b
I_{coil}
pump
+40
−10
−20
P_{SG}
LHE
+40
−20
−30
−10
2.8 K
attenuator
resistive heater
T sensor
low-pass filter
directional coupler
amplifier

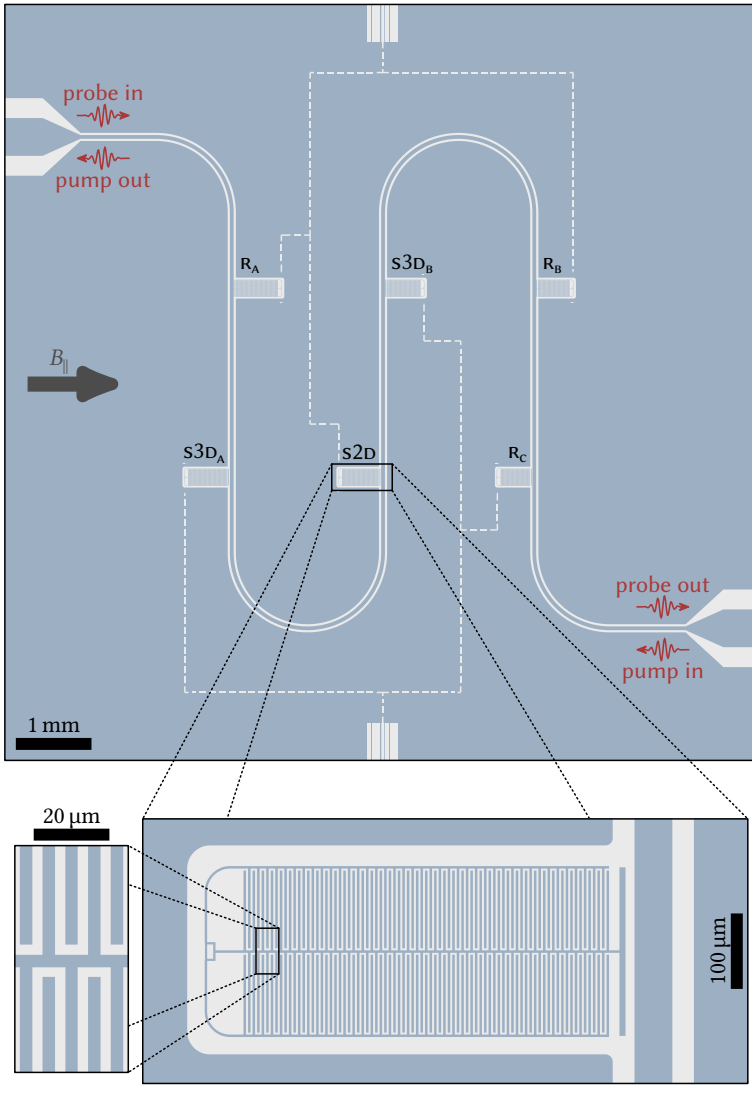
probe in
pump out
R_A
$S3D_B$
R_B
$B_\parallel$
$S3D_A$
S2D
R_C
probe out
pump in
1 mm
20 µm
100 µm

	N_{idc}	mech.	V_{acc} in kV	D_1 in ions	D_2 in nm^{-2}
R_A	94	no	–	–	–
$S3D_A$	87	yes	25	18 000	1000
S2D	81	no	25	18 000	0
$S3D_B$	75	yes	25	18 000	2000
R_B	70	no	–	–	–
R_C	65	yes	–	–	–

Table 4.1: Fabrication parameters of the resonators. We show the number N_{idc} of capacitor fingers, whether the resonator SQUID loop contains a mechanical beam, as well as the neon-ion acceleration voltage V_{acc} and beam doses D_1 for cutting the constrictions and D_2 for thinning them down.

4.18 Full chip layout

The full chip layout is depicted in Figure 4.9. The six resonator designs differ solely in the number N_{idc} of capacitor fingers in each IDC. Additional differences are introduced during fabrication, namely through cutting constriction-type Josephson junctions into the loop at the center of some resonators, turning them into SQUID resonators, as well as by integrating a mechanical beam into the long side of the loop for some resonators. The parameters used for each resonator are summarized in Table 4.1. Note that all Nb structures on the chip are ~1 µm smaller than in the layout depicted in Figure 4.9 due to over-exposure of the photo-resist during fabrication, e.g. the interdigital capacitor (IDC) lines are 2 µm wide with gaps of 4 µm between them. The true, fabricated device dimensions were extracted from scanning electron microscope (SEM) images and used in all simulations for determining device parameters.

Next, we will use the reference resonators to infer certain parameters of the SQUID resonators that we cannot access directly. Since the reference resonators R_A and R_B are closest to the SQUID resonators in resonance frequency (cf. Table 4.2), we only use those two for that purpose, not employing R_C as a reference.

Figure 4.9: Full chip layout. The microwave is guided through a meandering coplanar waveguide (CPW) alongside which six side-coupled LC-resonators are placed. Each resonator consists of a capacitive plate for coupling to the CPW, interdigital capacitors (IDCs) and inductive wires, all arranged symmetrically around the central axis. At the core of each resonator is a loop that can be turned into a SQUID acting as a flux-tunable inductance by cutting constrictions into its two arms using a neon ion microscope (NIM), cf. Figure 4.1. This is done for the resonators $S3D_A$, S2D and $S3D_B$, while R_A, R_B and R_C remain un-altered and serve as reference resonators. S2D is the resonator discussed up to now, data for $S3D_B$ are shown in Section 4.23. The dashed lines leading to the resonators from the chip edges are markers used for focusing, orientation and accurate movement in the NIM, such that unnecessary irradiation of circuit structures can be avoided.

4.19 Determination of the resonator parameters

The resonance frequency of our resonators is given by

$$\omega_0 = \frac{1}{\sqrt{C_{\mathrm{tot}} L}} \tag{4.60}$$

with the total capacitance C_{tot} and inductance L of the resonator. For the SQUID resonators, $L = L_{\mathrm{b}}$ before cutting the constrictions and $L = L_{\mathrm{b}} + L_{\mathrm{c}}/2$ after. For the reference resonators there are no constrictions, so $L = L_{\mathrm{b}}$ always.

Applying an in-plane magnetic field $B_{\parallel}$ partly suppresses the superconducting state of the resonator material, increasing its penetration depth λ_{L} and thus its kinetic inductance, causing a downwards shift in resonance frequency, as shown in Figure 4.10a for the reference resonators and in Figure 4.11a for the SQUID resonators. Assuming the resonator capacitance to remain unaffected by the applied field, we obtain the in-plane-field dependence of the resonator inductance

$$L(B_{\parallel}) = \left(\frac{\omega_0(0)}{\omega_0(B_{\parallel})}\right)^2 L(0). \tag{4.61}$$

In order to obtain the field-dependent penetration depth $\lambda_{\mathrm{L}}(B_{\parallel})$, we simulate the inductance L_{b} of each circuit geometry using the software *3D-MLSI* [81], varying the penetration depth, and, in order to remove simulation output resolution artifacts as well as for convenient interpolation, fit the results using [82]

$$L_{\mathrm{b}}(\lambda_{\mathrm{L}}) = L_{\mathrm{b}}^{\mathrm{geo}} + \lambda_{\mathrm{L}} L_{\mathrm{b}}^{*} \coth(d/\lambda_{\mathrm{L}}) \tag{4.62}$$

with the film thickness $d = 100\,\mathrm{nm}$ and fit parameters $L_{\mathrm{b}}^{\mathrm{geo}}$ and L_{b}^{*}, as shown in Figure 4.10b. Assuming a zero-field value $\lambda_{\mathrm{L}}(0) = 130\,\mathrm{nm}$ typical for our films at low temperatures $T \lesssim 4\,\mathrm{K}$, we find $L_{\mathrm{b}}(0)$ for all circuits from these simulations. For the reference circuits, we thus obtain $L_{\mathrm{b}}(B_{\parallel})$ using (4.61) and, again from the simulation data, $\lambda_{\mathrm{L}}(B_{\parallel})$. The result of this calculation is shown in Figure 4.10c. Due to the inaccuracies involved, the resulting values are not exactly identical for both resonators. We fit the expected behavior $\lambda_{\mathrm{L}}(B_{\parallel}) = \left(1+(B_{\parallel}/B^{*})^2\right)\lambda_{\mathrm{L}}(0)$ [83] to these data for $\mathtt{R_A}$ and $\mathtt{R_B}$ and use the resulting fit values for subsequent calculations. The fit parameter B^{*} introduced here can be interpreted as a characteristic magnetic field, but has no deeper meaning for the further analysis.

Now that we have obtained $\lambda_{\mathrm{L}}(B_{\parallel})$, we can calculate the field-dependent inductance $L_{\mathrm{b}}(B_{\parallel})$ of the SQUID resonators as well as their loop inductances $L_{\mathrm{loop}}(B_{\parallel})$ from the simulated $L_{\mathrm{b}}(\lambda_{\mathrm{L}})$ and $L_{\mathrm{loop}}(\lambda_{\mathrm{L}})$. The resulting field-induced change of both inductances is shown in Figure 4.11b.

For the SQUID resonators, we also need to consider the constriction inductance L_{c} that contributes to the total inductance. Indeed, comparing Figures 4.10a and 4.11a

reveals that the sweetspot resonance frequency ω_{00} of the SQUID resonators reacts considerably stronger to $B_\parallel$ than the reference resonator frequency ω_0, highlighting the additional effect of the sweetspot constriction inductance L_{c0}. Using the resonance frequency ω_{0b} of the SQUID circuits before cutting the junctions (i.e. without L_c), we find

$$\omega_{00} = \frac{1}{\sqrt{C_{tot}(L_b + L_{c0}/2)}} = \frac{\omega_{0b}}{\sqrt{1 + L_{c0}/2L_b}} \tag{4.63}$$

$$\implies \qquad L_{c0}(B_\parallel) = 2L_b(B_\parallel)\left(\left(\frac{\omega_{0b}(B_\parallel)}{\omega_{00}(B_\parallel)}\right)^2 - 1\right). \tag{4.64}$$

Before constriction cutting, the resonators were not characterized at the measurement temperature 2.8 K of the main experiment. Hence, we must infer ω_{0b} at that temperature from other data. Assuming that the capacitance C_{tot} remains unaffected by temperature and that any resonance frequency shift is due to a change in L caused by a changing λ_L (as for the field-induced shift discussed above), the ratio $\omega_{0b}/\omega_0^{R_A}$ must be constant with temperature for each SQUID resonator. Thus, using the measured ratio at 4.2 K as well as $\omega_0^{R_A}(0)$ at 2.8 K, we can calculate $\omega_{0b}(0)$. To improve accuracy, we do this both using R_A and using R_B as a reference, obtaining values differing by ~0.05 %, and use the average. Analogously to (4.61), we now

Table 4.2: Key resonator parameters. We show the resonance frequencies ω_{0b} and ω_0 before and after cutting the constrictions, respectively, the resonance linewidth κ, the inductances of the resonator before cutting the junctions L_b, of the constrictions L_c and of the SQUID loop L_{loop}, as well as the total inductance L and capacitance C_{tot} of the resonator. For the SQUID resonators, the bias-flux dependent values ω_0, κ and L_c are given at the sweetspot. The dimensions used for simulating the loop inductances L_{loop} (as well as L_b) were extracted from SEM images of the fabricated circuits, which is why their values vary slightly despite the SQUID ring layouts being identical.

	$\omega_{0b}/2\pi$ in GHz	$\omega_0/2\pi$ in GHz	$\kappa/2\pi$ in MHz	L_b in pH	L_c in pH	L_{loop} in pH	L in pH	C_{tot} in fF
R_A	8.937	8.937	8	441	–	–	441	719
$S3D_A$	9.654	9.475	28	418	32	45	433	651
S2D	10.380	10.233	22	397	23	44	409	592
$S3D_B$	10.983	10.774	44	377	29	45	392	557
R_B	11.641	11.641	11	360	–	–	360	519
R_C	12.532	12.532	10	343	–	–	343	470

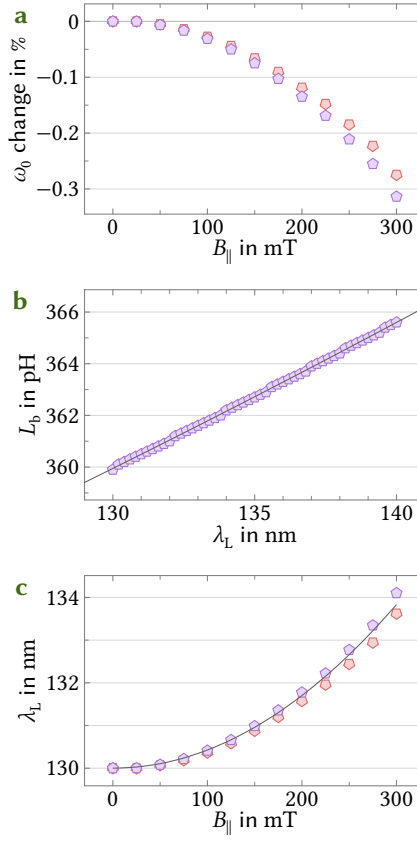

Figure 4.10: Magnetic in-plane field response of the superconductor penetration depth. Symbols are data for the two relevant reference resonators R$_A$ and R$_B$. **a** Relative change of the resonance frequency ω_0 with $B_\parallel$. **b** Simulated resonator inductance $L_b(\lambda_L)$ without constrictions, shown here for R$_B$. Symbols are simulated data points, the gray line is a fit. **c** $\lambda_L(B_\parallel)$ inferred from the simulation results together with the resonance frequency shift. The gray line is a fit to the data of both resonators.

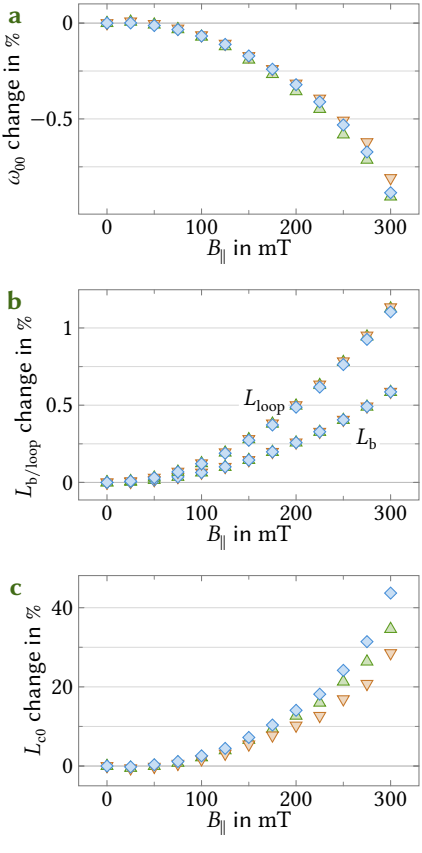

Figure 4.11: Magnetic in-plane field response of the SQUID resonator inductances. Symbols are data for the resonators △ s3D$_A$, ◇ s2D and ▽ s3D$_B$. **a** Relative change of the sweetspot resonance frequency ω_{00} with $B_\parallel$. **b** Relative change of the inductance L_b of the SQUID resonators as well as of their SQUID loop inductances L_{loop} as calculated from the simulated λ_L-dependence together with $\lambda_L(B_\parallel)$ (cf. Figure 4.10c). Since all values are calculated using the same $\lambda_L(B_\parallel)$, they are almost identical and the symbols mostly cover each other. Small visible deviations in L_{loop} are due to the simulated dimensions being extracted from SEM images of the SQUID rings, thus carrying small differences between the circuits over to the simulation. **c** Relative change of the constriction inductance L_{c0} at the flux arc sweetspot for the SQUID resonators as inferred from the resonance frequency shifts in combination with $L_b(B_\parallel)$.

obtain the field dependence of this frequency

$$\omega_{0\mathrm{b}}(B_\parallel) = \omega_{0\mathrm{b}}(0)\sqrt{\frac{L_\mathrm{b}(0)}{L_\mathrm{b}(B_\parallel)}}, \tag{4.65}$$

finally allowing us to calculate $L_{\mathrm{c}0}(B_\parallel)$. The resulting field-induced change is depicted in Figure 4.11c.

Having determined all resonator inductances, we can calculate the total capacitance of each circuit from (4.60). All of the zero-field parameter values resulting from this procedure are summarized in Table 4.2.

4.20 The resonator linewidth

For completeness, we present the linewidths of resonator S2D, which we did not discuss in detail up to now. As already mentioned above, the resonator is in the undercoupled regime, with an external linewidth $\kappa_\mathrm{ext} \sim 2\pi \cdot 5\,\mathrm{MHz}$ and a total linewidth $\kappa > 4\kappa_\mathrm{ext}$ dominated by the internal linewidth. Figure 4.12 summarizes the linewidth flux-responses $\kappa(\Phi_\mathrm{b})$ and $\kappa_\mathrm{ext}(\Phi_\mathrm{b})$ for different $B_\parallel$. Each data point was extracted from the same fit as the corresponding resonance frequency point in Figure 4.3a. As expected, the linewidth κ (panel a) reacts to both flux and field in an inverse fashion compared to the resonance frequency, increasing where ω_0 decreases, but with a similar shift and skewing present. The magnetic field suppresses the superconducting energy gap, leading to an increased number of quasiparticles and thus to higher losses, particularly in the constrictions (cf. Figure 4.3c). These losses contribute to the internal linewidth while leaving the external linewidth (panel b) largely unaffected, which only shows a small field-dependent bias-flux response (most likely caused by a frequency-dependence of κ_ext or a misattribution of κ_int-contributions to κ_ext by the fit, not by an actual field-dependence). Bias-flux induced losses (caused by the circulating current) are also present in the internal linewidth, of course, and are enhanced by the applied $B_\parallel$, with both the sweetspot linewidth and the linewidth tuning increasing by a similar value; at $B_\parallel = 300\,\mathrm{mT}$ by $\sim 50\,\mathrm{MHz}$. We note that in principle the apparent linewidth may also be broadened by flux-noise effects when the circuit is biased away from the sweetspot, but experience with similar devices leads us to expect that this is not the case here [84].

4.21 The effect of each CPR model parameter

To illustrate the effect of the different CPR model parameters on the current density distribution inside the junction as well as the resulting CPR, we will now have a look at the solution obtained using the CPR algorithm described in Section 4.12

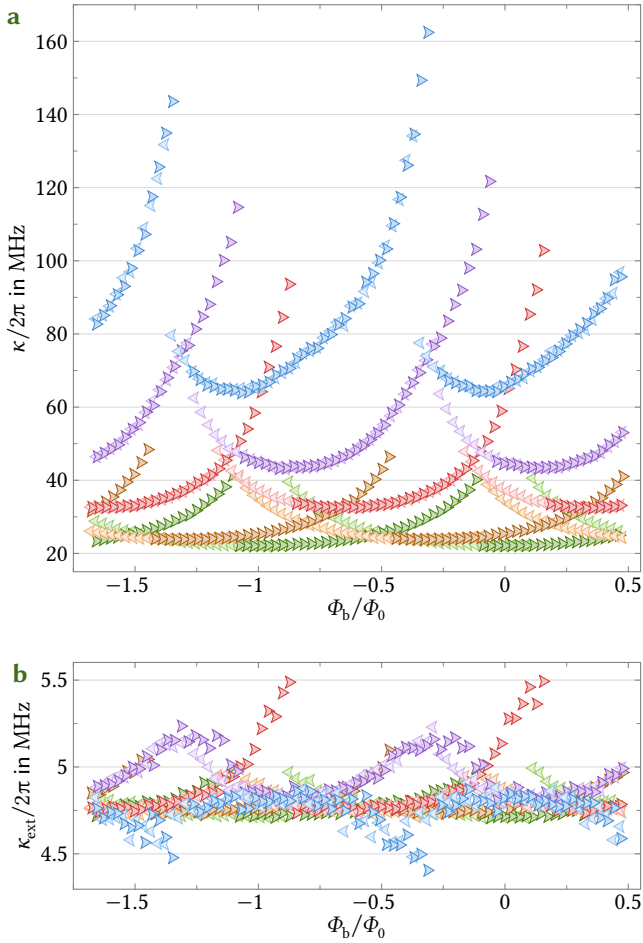

Figure 4.12: Linewidth flux-response in large magnetic in-plane fields. **a** Total linewidth $\kappa(\Phi_b)$ and **b** external linewidth $\kappa_{ext}(\Phi_b)$ corresponding to the frequency flux-response data $\omega_0(\Phi_b)$ presented in Figure 4.3a. Again, the depicted in-plane field values are $B_\parallel \in \{0, 100, 200, 250, 300\}$ mT (from green to blue) and the pointing direction of the kite symbols indicates the flux-sweep direction. We observe a linewidth behavior matching that of the resonance frequencies, with κ increasing when ω_0 decreases and a corresponding skewing of the flux arcs appearing. κ_{ext} remains largely unaffected by the field, only showing a small, field-dependent bias-flux response away from the sweetspot.

for different sets of model parameters. Throughout, we will use the normalized parameters $(\epsilon, b, \delta_B, \delta_\ell)$ and the corresponding normalized current density $\tilde{j}(\tilde{z}, \delta_0)$ and normalized CPR $\tilde{I}(\delta_0)$. Note that we consider $\tilde{j}$ and $\tilde{I}$ as functions of the phase δ_0 in the center of the junction, not of the shifted phase $\delta_c = \delta_0 - \tilde{\delta}_0$ used elsewhere. This simplifies the interpretation of the plots shown, as one fewer step is involved in the calculation, as well as revealing the value of $\tilde{\delta}_0$ as the zero of $\tilde{I}(\delta_0)$ near the CPR plot origin. For reference, let us repeat (4.21) and (4.22) from Section 4.12 here

$$\tilde{j}(\tilde{z}, \delta_0) = (1 - 2\epsilon\tilde{z}) \sin\big(\delta_0 + \delta_B(1 + b\tilde{z})\tilde{z} - \delta_\ell \tilde{j}(\tilde{z}, \delta_0)\big) \tag{4.21}$$

$$\tilde{I}(\delta_0) = \int_{-1/2}^{1/2} \tilde{j}(\tilde{z})\, \mathrm{d}\tilde{z}. \tag{4.22}$$

In Figure 4.13, both of these functions are plotted for various sets of model parameter values, with each parameter being either zero or taking its designated value $\epsilon = 0.4$, $b = 0.6$, $\delta_B = 2.2$ and $\delta_\ell = 0.9$. Each panel of the figure comprises two plots, a $j(\tilde{z}, \delta_0)$ color plot at the top and an $\tilde{I}(\delta_0)$ plot at the bottom. They share the same x-axis such that each CPR value in the bottom panel is the integral of the current density values vertically above it. The color map used for the $\tilde{j}$ plots reaches its most orange/blue color for $\tilde{j} = \pm 1$, changing towards red/violet only for $|\tilde{j}| > 1$. The trivial solutions $\tilde{j}\big(\tilde{z}, n\pi - \delta_B(1 + b\tilde{z})\tilde{z}\big) = 0$ with $n \in \mathbb{Z}$ are visible as green stripes in the color plots (when not obscured by a non-trivial solution, e.g. at low $\tilde{z}$ in panel f), with the center of the plot marking the solution $\tilde{j}(0, 0) = 0$ that is used as starting point in the algorithm, cf. Section 4.12.

In the first three panels (first column) we explore the effect of just one of the three model contributions; the magnetic field (δ_B, for now with $b = 0$), the linear inductance (δ_ℓ) and the critical current density gradient (ϵ). If all model parameters were zero (not shown), the current density would be described by a simple sine $\tilde{j} = \sin\delta_0$ independent of $\tilde{z}$, i.e. the color plot would be vertically invariant and the CPR thus identical $\tilde{I} = \tilde{j}$. The effect of δ_B (panel a) is to tilt the $\tilde{z}$-dependence of the current density, with the slope of the tilt (green stripes in the plot) given by δ_B. In the integral, this leads to a sine with a reduced amplitude $\sin(\delta_B/2)/(\delta_B/2)$ giving rise to the well-known Fraunhofer pattern of critical currents. The depicted δ_B-value corresponds to a junction with $B_\parallel/B_0 = \delta_B/2\pi = 0.35$ of a flux quantum coupled into it by the in-plane field. We already discussed the effect of a linear inductance contribution δ_ℓ (panel b) in the context of Figure 4.2; it leads to a skewed sine profile with unchanged critical currents, maintaining $\tilde{I} = \tilde{j}$. The depicted δ_ℓ-value corresponds to a linear inductance contribution $L_{\mathrm{lin}}/L_{J0} = \delta_\ell = 0.9$. Finally, the effect of ϵ (panel c) is a $\tilde{z}$-dependent scaling factor, with the amplitude of the sine profile being larger than 1 for negative $\tilde{z}$ and smaller for positive $\tilde{z}$. In the integral, this linear gradient drops out and the CPR remains unaffected.

The next three panels (second column) depict the consequence of using a combination of two of these three parameters. In the current density plots, the result is simply a combination of the individual effects of the involved parameters; a $\tilde{z}$ tilt for δ_B, skewed δ_0-dependence for δ_ℓ and a $\tilde{z}$-dependence of the amplitude for ϵ. In the CPR, on the other hand, the result is less obvious.

Including ϵ and δ_B (panel d) yields a CPR that is still a sine with reduced amplitude, but with its zero $\tilde{\delta}_0$ shifted away from $\delta_0 = 0$. This behavior applies more generally; δ_B together with a $\tilde{z}$-gradient leads to a horizontally shifted $\tilde{I}(\delta_0)$. We stress that this CPR is still completely symmetrical around its zero, the shift only indicates that $\delta_0 \neq 0$ for $\tilde{I} = 0$. Looking at the current density plot, we can now understand why the CPR does not vanish for $\delta_B = 2\pi$ (i.e. $B_\parallel = B_0$); in this case, the $\tilde{z}$ tilt reaches exactly one period over the height of the junction, i.e. the sine $\tilde{j}(\delta_0)$ is shifted half a period to the left at $\tilde{z} = 1/2$ and half a period to the right at $\tilde{z} = -1/2$. Thus, calculating $I(\delta_0)$ we integrate over all phases of the sine, but in the presence of a non-zero ϵ the amplitude is not constant for all $\tilde{z}$ and thus the integral is not zero.

In the CPR for δ_B together with δ_ℓ (panel e), we see a distorted version of the reduced-amplitude CPR caused by δ_B, but unlike before, due to the $\tilde{z}$ tilt in $\tilde{j}$, the skewing introduced by δ_ℓ affects each part of the CPR in a non-trivial way.

Finally, the combination of ϵ and δ_ℓ (panel f) produces a CPR similar to the skewed sine created by just δ_ℓ, but not quite identical. The gradient in critical current density enters into the inductive term in (4.21) and thus changes the shape of the δ_0-dependence of $\tilde{j}$ besides just its amplitude. Particularly for negative $\tilde{z}$, where the critical current density and thus the inductive contribution are amplified, $\tilde{j}(\delta_0)$ may cease being single-valued, similar as for $\delta_\ell > 1$, cf. Figure 4.2d. In this case, the root that is tracked by the CPR algorithm disappears upon exiting the region of multiple solutions. Since this happens only locally, unlike in the case without ϵ, the dynamics in the junction are no longer obvious. As mentioned in Section 4.12, the algorithm discards the $\tilde{j}$ solution in this case, which first happens here at the transition between a unique $\tilde{j}(\delta_0)$ (large $\tilde{z}$) and a multi-valued relation (small $\tilde{z}$), marked by a missing pixel in the current density plot at $(\tilde{z}, \delta_0) \approx (-0.16, \pm\pi)$. Due to the way the algorithm is implemented, it may not find solutions for any $\tilde{z}$ (or large parts of the scanning interval) once any part of the solution has been discarded, which is why $\tilde{j}(\tilde{z}, \delta_0)$ is missing for all $\tilde{z}$ after the missing pixel. As the CPR $\tilde{I}(\delta_0)$ is undefined once the current density $\tilde{j}(\tilde{z}, \delta_0)$ is undefined for any $\tilde{z}$, this is of no consequence to the final CPR solution, though, which is also illustrated by the CPR plot stopping at the last value $|\delta_0| = 3.10$ where the $\tilde{j}$ solution exists for all $\tilde{z}$.

Now, we combine all three parameters, obtaining a current density distribution featuring $\tilde{z}$ tilt, skewed δ_0-dependence as well as a $\tilde{z}$-dependent amplitude (panel g). This finally leads to new behavior in the CPR, namely to an asymmetric profile with different positive and negative critical currents $I_0^\pm$; a Josephson diode. A gray dashed curve marks the CPR mirrored about its zero, making any asymmetries

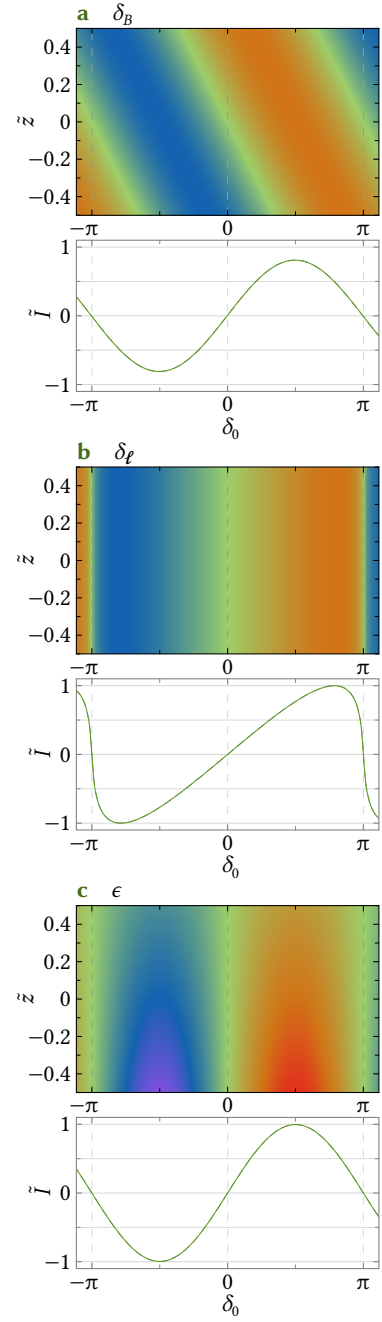

Figure 4.13: Effect of the CPR model parameters on the current density distribution and the resulting CPR. Each panel comprises a color plot of $\tilde{j}(\tilde{z}, \delta_0)$ at the top and a plot of the CPR $\tilde{I}(\delta_0)$ at the bottom, gray dashed curves correspond to the CPR mirrored about its zero. The parameters that are used (i.e. not set to zero) for each panel are mentioned at the top. When mentioned, the parameter values $\epsilon = 0.4$, $b = 0.6$, $\delta_B = 2.2$ and $\delta_\ell = 0.9$ are used. Each plot has the same axis limits and color map as other plots showing the same quantity, and both the current density and the CPR plots share the same x-axis such that each $\tilde{I}$-value corresponds to the integral of the $\tilde{j}$ values vertically above it. For a detailed description of the effect of each parameter, see Section 4.21.

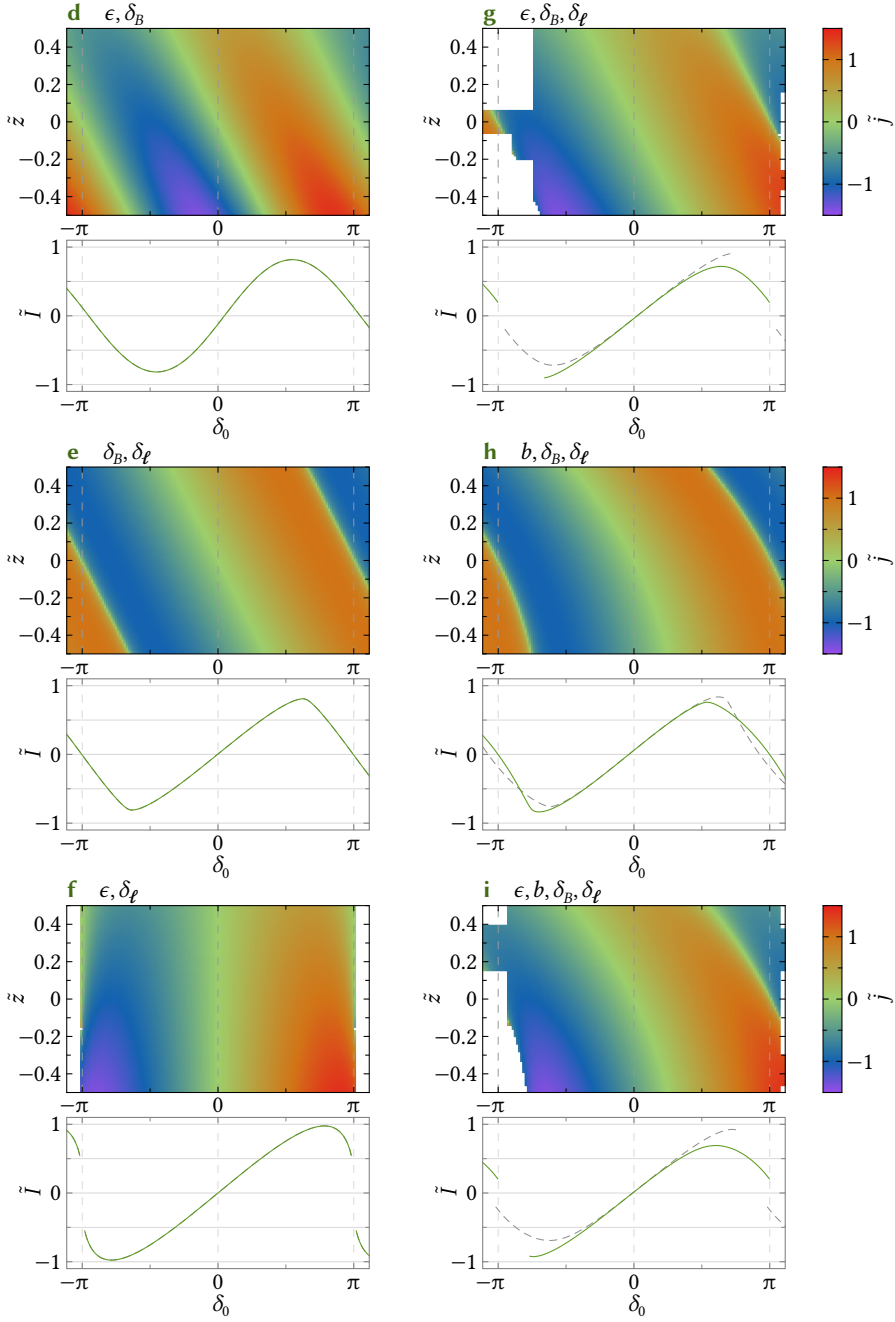
d ϵ, δ_B
g $\epsilon, \delta_B, \delta_\ell$
e δ_B, δ_ℓ
h b, δ_B, δ_ℓ
f ϵ, δ_ℓ
i $\epsilon, b, \delta_B, \delta_\ell$
$\tilde{z}$
$\tilde{j}$
$\tilde{I}$
δ_0
$-\pi$
0
π
0.4
0.2
−0.2
−0.4
1
−1

apparent. The tilt introduced by ϵ also tilts the locus of the disappearing tracked root and thus the shape of the edge of the solution found by the algorithm, as can be seen at the bottom left edge of the current density plot. For larger magnetic fields (larger δ_B), the slope of the tilt will increase and the solution will disappear closer to $\delta_0 = 0$, different model parameters, namely large $\delta_\ell > 1$, may also cause it to disappear earlier for positive δ_0. We note that the algorithm does find solutions for $\delta_0 > \pi$ in this example that could in principle be used to calculate the CPR in a small interval above $\delta_0 = (2n+1)\pi$. This is not implemented, though, as it is not relevant for the evaluation at hand, and so the CPR stops at $\delta_0 = \pi$.

Using a gradient in the magnetic contribution given by b instead of the critical current density gradient given by ϵ (panel h) also leads to an asymmetric CPR, albeit with a less pronounced asymmetry, particularly in the region of small δ_0 most relevant in the experiment. In the current density plot, b modifies the effect of δ_B from a linear tilt of the $\tilde{z}$-dependence to a parabolic one (cf. again green stripes in the $\tilde{j}$ plots). Combining both gradients, i.e. using all four model parameters (panel i), leads to a combined diode effect featuring both asymmetry contributions. Note that the shift $\tilde{\delta}_0$ of the CPR zero induced by b (in combination with δ_B) opposes that induced by ϵ, so the total shift is rather small here. This is the form of the CPR model that was used in evaluating the S2D data presented in the first sections of this chapter, obtaining the CPRs shown in Figure 4.4d. Note that a large $\delta_\ell > 1$ leads to the solution disappearing earlier for positive values of δ_c and later for negative values, which is the case for the CPRs at high fields shown there, cf. δ_ℓ-values in Figure 4.19. For the $\mathrm{S3D_B}$ data presented in Section 4.23, the magnetic contribution gradient was not used, i.e. $b = 0$ (panel g).

We note for completeness that using both gradients without the linear inductance contribution (i.e. using ϵ, b and δ_B) does not lead to a diode CPR. The resulting current density is similar to that shown in panel d but with a parabolic tilt rather than a linear one, and the resulting CPR is also alike, with the only notable difference being the additional shift to the left due to b.

4.22 Polynomial correction of the CPR

As described in Section 4.16, we modify the CPR using a small polynomial correction $\Delta I(\delta_c)$ for the fit of the Kerr anharmonicity. In Figure 4.14 we detail the magnitude of this correction and its effect on the CPR as well as the resonance frequency and Kerr response predicted by it. While the correction is several orders of magnitude smaller than the constriction critical current – and thus imperceptibly small when considering the CPR directly –, the CPR derivative, and thus the resulting resonance-frequency flux-response, is visibly affected. The effect is still small, though, and does not significantly impact the agreement with the measurement

data. Higher CPR derivatives are affected even more strongly, and thus the effect of the correction on the Kerr anharmonicity is considerable. We can greatly improve the match between modeled and observed $\mathcal{K}$ response using the correction, demonstrating that the present mismatch can be explained by minuscule CPR disparities. Such discrepancies might have a multitude of causes, like the gradients described by ϵ and b having more complicated shapes than the simple linear dependence we used in the CPR model (cf. (4.9) and (4.10)), additional gradients in other directions or parameters, non-trivial frequency dependencies of the pump attenuation $\zeta(\omega_p)$, or SQUID asymmetries due to small differences between the two constrictions. Not all of these can be addressed by the small correction $\Delta I(\delta_c)$, so some discrepancy remains, but overall agreement of the modified CPR with the experimental data is very good. All qualitative features of the asymmetric Kerr response are already present in the un-modified CPR, affirming the fundamental suitability of our model.

We note that some numerical inaccuracies are visible as wiggles at the edge of the un-corrected $\mathcal{K}$ curves (dashed gray lines) in Figure 4.14d for the highest fields, as discussed in Section 4.12. Naturally, these inaccuracies are still present with the polynomial correction, but due to the logarithmic scale of the plot axis and the much larger $|\mathcal{K}|$ values they are not visible in the corresponding curve.

4.23 Flux-tuning, current-phase relation and Kerr data of sample s3D$_B$

Besides the resonator s2D discussed up to now, we also characterized the other two SQUID resonators s3D$_A$ and s3D$_B$. Notably, the orientation of s3D$_B$ on the chip is inverted with respect to that of s2D, cf. Figure 4.9, so any in-plane field couples flux into the constrictions, relative to the SQUID loop, with opposite polarity. Figure 4.15 shows the field-dependent flux-response of s3D$_B$ and indeed the skewing occurs in the opposite direction compared to to s2D, cf. Figure 4.3. Since the junctions in s3D$_B$ are implemented as 3D constrictions, i.e. they have been thinned down from the top to ~75 nm (estimated from the NIM doses), a weaker response to $B_\parallel$ is expected, and indeed this is what we find. All qualitative features discussed before are still present, though, albeit with inverted flux orientation. We note that the other 3D constriction resonator s3D$_A$ shows a similar diode effect but with the arcs skewing in the same direction as those of s2D, confirming that the inverted skewing is indeed due to the orientation of the resonator with respect to the field rather than some effect related to the 3D constrictions. The field response of the sweetspot resonance frequency and linewidth of s3D$_B$, on the other hand, is very similar to that of s2D, with the sweetspot resonance frequency being reduced by ~10 MHz and the linewidth increasing by ~40 MHz, though its absolute value is ~20 MHz larger, probably due to a lower constriction T_c [34]. The flux responsivity, on

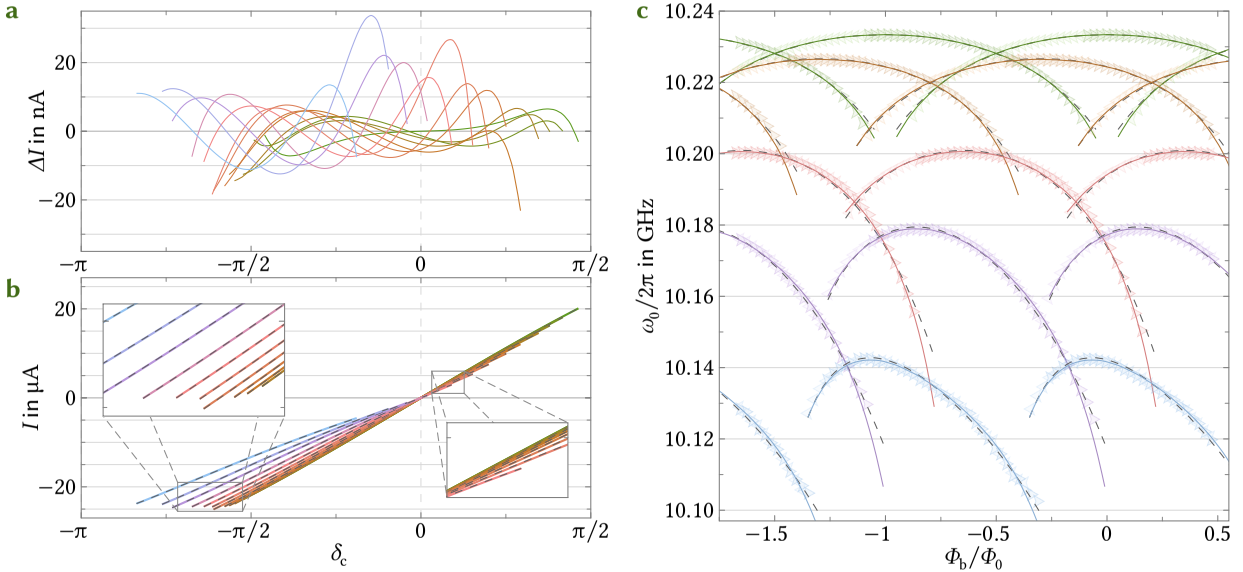

Figure 4.14: An imperceptibly small polynomial CPR correction considerably improves the Kerr fit. **a** Polynomial correction $\Delta I(\delta_c)$ used to modify the CPR for the Kerr analysis, with each curve from $B_\parallel = 0$ (green) to 300 mT (blue) corresponding to the line of the same color in Figure 4.4d, though here we only show the part corresponding to the thick segment there, i.e. the experimentally accessible part, since this is the part of the correction that participates in the fits. Inside this region, its value stays within a few tens of nA for all fields, about three orders of magnitude below the critical current (though the function diverges outside the fit range, as any polynomial fit does). **b** Corresponding current-phase relations with and without the polynomial correction; dashed gray lines correspond to the CPR model fits $I(\delta_c)$ and solid, colored lines show the modified CPRs $I(\delta_c) + \Delta I(\delta_c)$. Due to the tininess of the modifications, no difference between the curves is visible, the dashed lines seem to lie exactly on top of the colored lines; this is true even in the insets showing some enlarged plot details. **c** Flux-response fits $\omega_0(\Phi_b)$ with and without the polynomial correction. Kite

symbols in the background show the measurement data also presented in Figure 4.3a, dashed gray lines correspond to the CPR model fits (using $I(\delta_c)$) to the data that are also shown there and solid, colored lines are the fits using the modified CPR $I(\delta_c) + \Delta I(\delta_c)$. As in Figure 4.3a, we show data for $B_\parallel \in \{0, 100, 200, 250, 300\}\,\mathrm{mT}$. Unlike in a plot directly comparing the original and the modified CPR, the difference between the two functions is visible here, as the resonance frequency depends on the CPR derivative and is thus more sensitive to small changes. The fit quality, however, remains largely unchanged, with the solid line matching the data better in some places and slightly worse in others, the largest differences being located near the edge of the flux arc data, close to the divergence of the polynomial offset. **d** Kerr anharmonicity $\mathcal{K}$ with and without the polynomial correction. As before, dashed, gray lines correspond to the value derived from $I(\delta_c)$ while solid, colored lines are from $I(\delta_c) + \Delta I(\delta_c)$, data in the background are the same as presented in Figure 4.5d, comprising $B_\parallel \in \{0, 125, 175, 225, 250, 275, 300\}\,\mathrm{mT}$. Since $\mathcal{K}$ depends on still higher CPR derivatives than ω_0, it is modified much more strongly by ΔI, resulting in deviations of up to one order of magnitude. These modifications greatly improve the agreement between the theory curve and the measurement data, demonstrating that even minuscule uncertainty in the CPR is sufficient to explain the mismatch in the Kerr data, though all qualitative features of the anharmonicity response are present even before the modification.

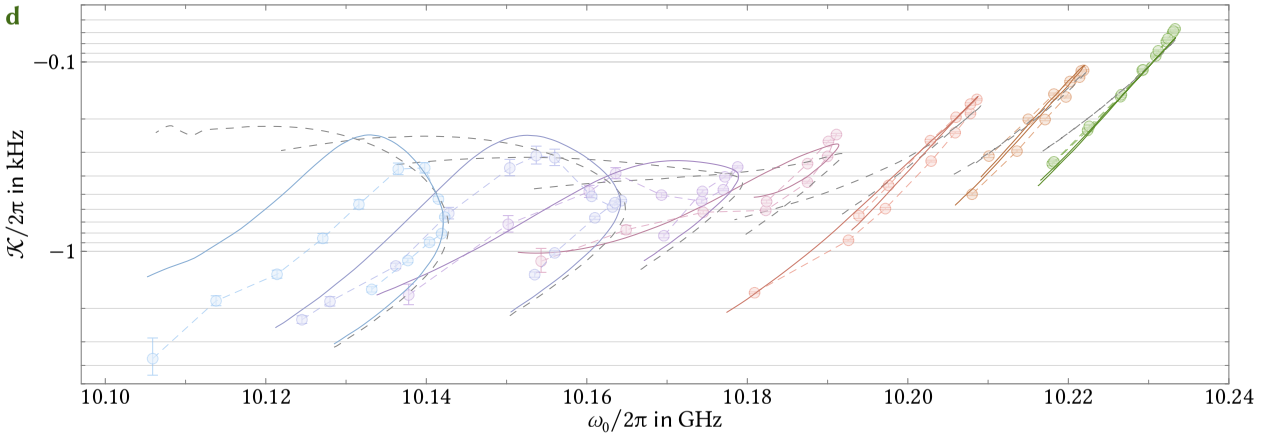

the other hand, is considerably higher than for the 2D constriction resonator, a typical result for 3D constrictions [34] due to their reduced critical current, making them better suited for sensing and parametric coupling applications. Here, the responsivity is larger by a factor of ~2 both with and without applied magnetic field, i.e. the larger responsivity is maintained even at large fields.

For s2D, we used a z-gradient of both j_0 and $B_\parallel l_{\mathrm{eff}}$ (i.e. the fit parameters ϵ and b, cf. (4.9) and (4.10)) to fit the flux arcs. Indeed, both of them were necessary to achieve good agreement with the data, though the effect of b is much weaker than that of ϵ for the parameters found. Here, we are able to fit the flux arcs without the gradient in $B_\parallel l_{\mathrm{eff}}$, i.e. we use $b = 0$. This matches the smaller constriction height, as we can expect less non-trivial parameter variation to occur in the smaller space. Figures 4.16a through c illustrate this slightly simplified model behavior and Figures 4.16d and e show the CPRs and switching currents extracted from the flux-arc fits. As expected, just like the flux arcs, the CPRs deform in the opposite direction and the reactions of the switching currents $I_{\mathrm{sw}}^{\pm}$ to $B_\parallel$ are swapped with respect to those of s2D presented in Figure 4.4. The fits yield a field $B_0 = 361\,\mathrm{mT}$ for coupling one flux quantum into the junction, corresponding to an effective area $A_{\mathrm{eff}} = 5.7 \cdot 10^{-15}\,\mathrm{m}^2$ and an effective constriction length $l_{\mathrm{eff}}(0) = 76\,\mathrm{nm}$, slightly larger than that of the s2D constrictions, which is consistent with a suppressed T_c

Figure 4.15: Skewed flux-response and enhanced flux-responsivity in large magnetic in-plane fields for resonator s3D$_B$. All data correspond to those shown in Figure 4.3 for resonator s2D. **a** Bias flux response $\omega_0(\Phi_b)$ of the circuit for five different magnetic in-plane fields between 0 mT and 300 mT; labels next to the datasets denote $B_\parallel$. Data combine flux up-sweep (dark kites pointing right) and flux down-sweep (light kites pointing left); lines are fits. Note that the flux arcs skew in the opposite direction compared to those of resonator s2D presented in Figure 4.3a, with all other features of the field response present here as well. **b**, **c** Sweetspot resonance frequency ω_{00} and linewidth κ_0 as a function of $B_\parallel$. Symbols are data extracted from the flux arcs, colors denote the value of $B_\parallel$, as in all panels, and the dashed lines show the expected behavior in the absence of the constrictions as inferred from reference circuits. Just like for resonator s2D, about two thirds of the ω_{00} decrease and almost all of the κ_0 increase can be attributed to the constrictions. **d** Flux responsivity $\mathcal{F} = \partial\omega_0/\partial\Phi_b$ for various $B_\parallel$ and plotted vs ω_0 as a figure of merit for sensing and parametric coupling applications. Large symbols correspond to values on stable branches, small symbols to those on metastable branches,* lines are derivatives of the arc fits. Typical for 3D constrictions, the responsivity here is larger than that of the 2D resonator s2D shown in Figure 4.3d, with a factor of ~2 between them both with and without a magnetic field.

*As noted in the context of Figure 4.3, we assume the transition to the metastable state on a flux arc branch to be located in the center between the two jumps (arrows in panel a) to and from that branch, which at $B_\parallel = 0$ corresponds to the arc crossing point but shifts left of it for larger fields.

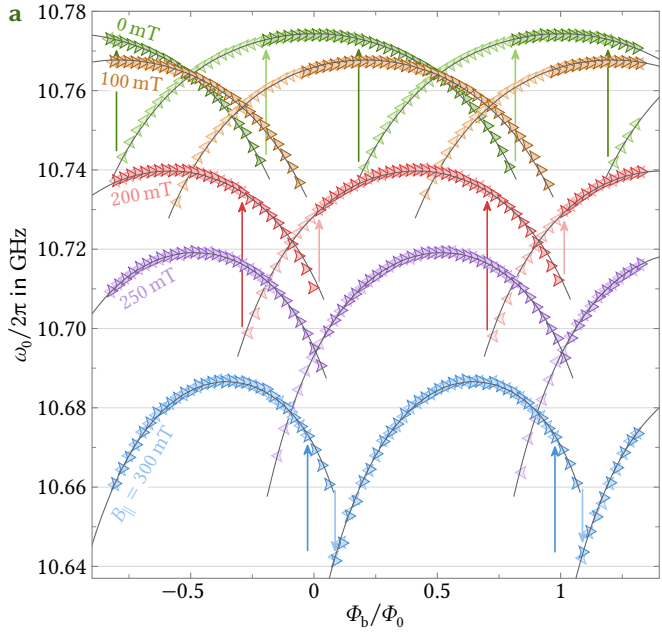
a
0 mT
100 mT
200 mT
250 mT
$B_\parallel$ = 300 mT
$\omega_0/2\pi$ in GHz
Φ_b/Φ_0

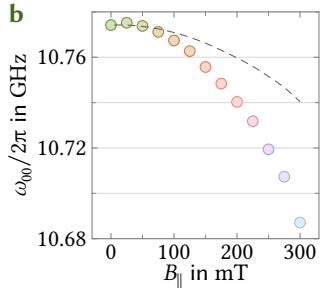
b
$\omega_{00}/2\pi$ in GHz
$B_\parallel$ in mT

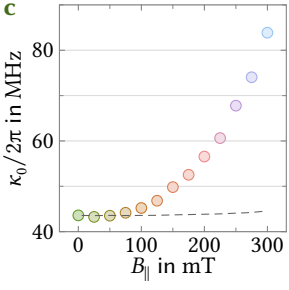
c
$\kappa_0/2\pi$ in MHz
$B_\parallel$ in mT

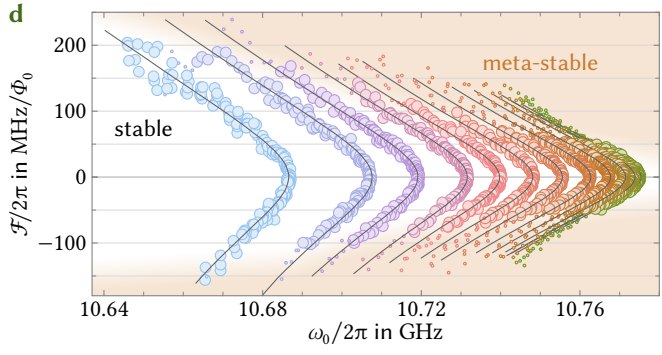
d
meta-stable
stable
$\mathcal{F}/2\pi$ in MHz/Φ_0
$\omega_0/2\pi$ in GHz

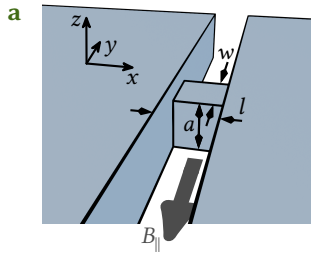
a
z
y
x
w
l
a
$B_\parallel$

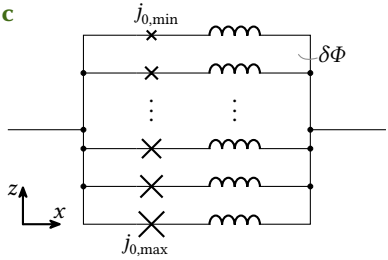
c
$j_{0,\min}$
$\delta\Phi$
z
x
$j_{0,\max}$

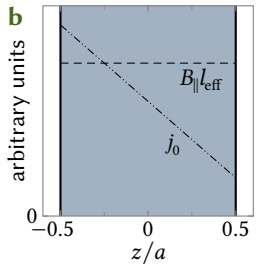
b
arbitrary units
$B_\parallel l_{\text{eff}}$
j_0
0
−0.5
0
0.5
z/a

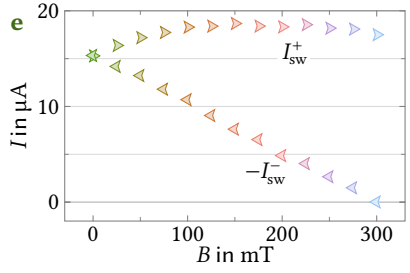
e
20
10
0
I in µA
I^+_{sw}
$-I^-_{\text{sw}}$
0
100
200
300
B in mT

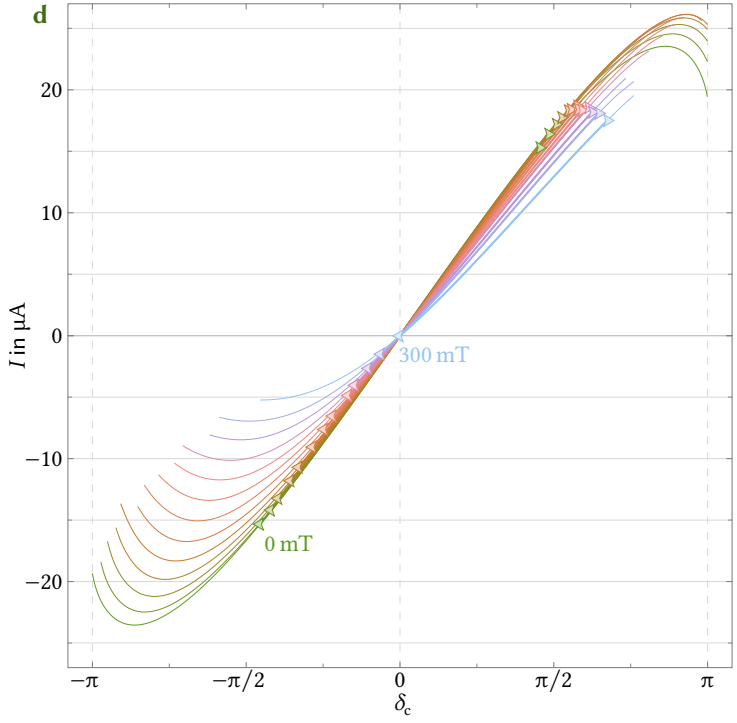
d
20
10
0
−10
−20
I in µA
300 mT
0 mT
−π
−π/2
0
π/2
π
δ_c

and a correspondingly increased λ_L in the 3D constrictions. See Section 4.25 for a discussion of all parameters resulting from the fits.

Moving on to the Kerr anharmonicity, we again find a bimodal distribution for non-zero in-plane fields that is shown in Figure 4.17, though it is significantly weaker than that of S2D presented in Figure 4.5d. For small fields, the short leg of the fit curve is at a lower value of $|\mathcal{K}|$ than the long leg, while this is inverted at the highest field. The transition occurs at around 250 mT. In the two-tone measurement data, inversion seems to be happening right at 300 mT, making the bimodality disappear at that particular field. The same transition was also present in Figure 4.5d, but at lower fields (~125 mT for the fit curves and ~250 mT for the two-tone data), making its appearance less pronounced. Quantitatively, the Kerr anharmonicity of the 3D constriction resonator is again larger than that of S2D by a factor of ~2 due to the lower critical currents, similarly to the increased flux responsivity discussed above.

Figure 4.16: Simplified Josephson-diode model for resonator S3D$_B$. All data correspond to those shown in Figure 4.4 for resonator S2D. **a** Schematic of a nano-constriction defining its width w, length l and height a as well as the direction of $B_\parallel$. Unlike with resonator S2D, here we have a 3D constriction and the magnetic field enters the junction from the opposite side (when viewed from the inside of the SQUID loop). **b** To model the skewed flux response of this resonator in accordance with the measurement data, no gradient in flux per height $\delta\Phi = B_\parallel l_{\text{eff}}$ is necessary, so we only include the j_0-gradient for the analysis here, i.e. $b = 0$. **c** Circuit equivalent of the Josephson-diode model consisting of a multi-loop parallel arrangement of infinitesimal constrictions whose inductive Josephson contribution grows with z due to a decreasing critical current density. In accordance with the constant $\delta\Phi$-value used, in contrast to the z-gradient illustrated in Figure 4.4c, here the loop length is independent of z. **d** Constriction current-phase relation $I(\delta_c)$ as a function of the applied field $B_\parallel$ obtained from fits to the flux arc data (lines in Figure 4.15a). Thin lines show the full range for which our numerical algorithm yields a result, thick line segments show the parts that correspond to the experimental flux arcs in between the discontinuous jumps, symbols mark the corresponding switching currents/phases. The magnetic-field response is much the same as that for resonator S2D presented in Figure 4.4d but with inverted polarity. Here, the positive critical currents decrease quickly while the negative ones mostly retain their magnitude. As before as well as in the next panel, colors encode $B_\parallel$. **e** Switching currents I_{sw}^+ and $-I_{sw}^-$ as derived from the flux arc discontinuities and the CPR model. For $B_\parallel = 0$, positive and negative switching currents are equal in magnitude, but with increasing $B_\parallel$ the difference between the two values grows, indicating an increasing diode effect. Positive switching currents stay larger than the initial value for all $B_\parallel > 0$, negative switching currents decrease in magnitude nearly linearly. For the largest field, the latter value reaches zero, so just as for resonator S2D, the current flows in the same direction in the SQUID ring for any applied bias flux Φ_b, though this point is reached at slightly higher fields here.

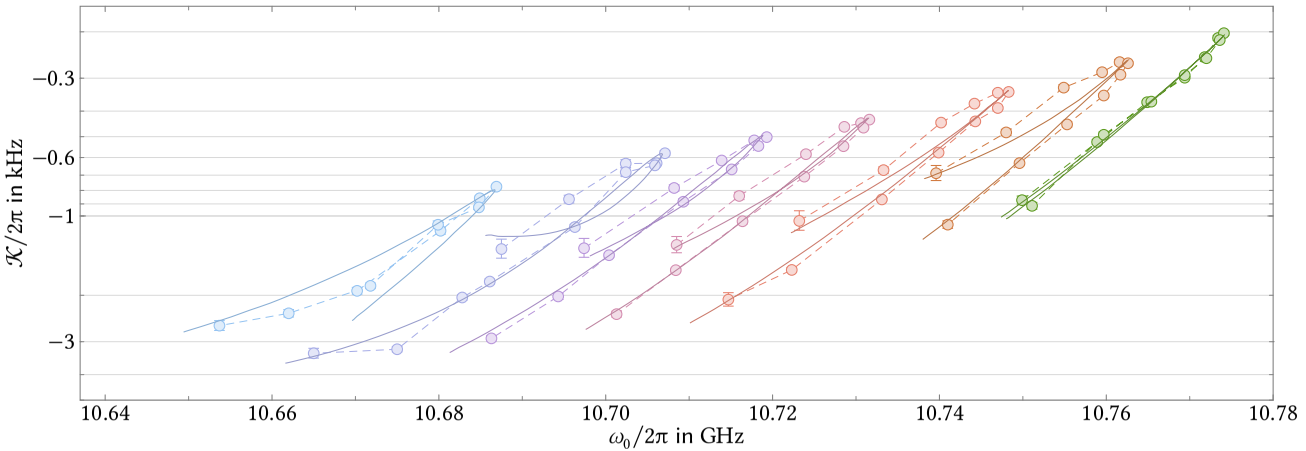

Figure 4.17: Bimodel Kerr anharmonicity for resonator s3D$_B$. The data correspond to those shown in Figure 4.5d for resonator s2D. Again, the in-plane field values shown are $B_\parallel \in \{0, 125, 175, 225, 250, 275, 300\}\,\mathrm{mT}$, indicated by color as before, symbols are data, connected with dashed lines as guides to the eye, solid lines are fit curves based on the CPRs shown in Figure 4.16 plus a small polynomial correction. The bimodality is much weaker here than for resonator s2D, but still present with all the same qualitative features, confirming the diode effect for this resonator as well.

4.24 Reversing the in-plane field

Let us compare this inversion of the circuit flux response for resonators with opposite orientation on the chip to the change of flux response of a resonator upon inverting the in-plane field. In Figure 4.18 we present resonance frequency flux arcs for the same two circuits s2D and s3D$_B$ at $|B_\parallel| = 250\,\mathrm{mT}$ for both positive and negative field orientation. Just like for the inverted resonator orientation and just as predicted by our constriction model, reversing the field orientation flips the skewing and shifting direction of the flux arcs; the arcs of s2D at positive $B_\parallel$ skew in the same way as the arcs of s3D$_B$ at negative $B_\parallel$. This result re-affirms that the diode-effect causing the distorted CPR (and thus the skewed bias-flux response) is indeed induced by the magnetic field.

The discerning reader may notice that the sweetspot frequencies of the two measurements for each resonator are not exactly identical, but differ by ~2 MHz.

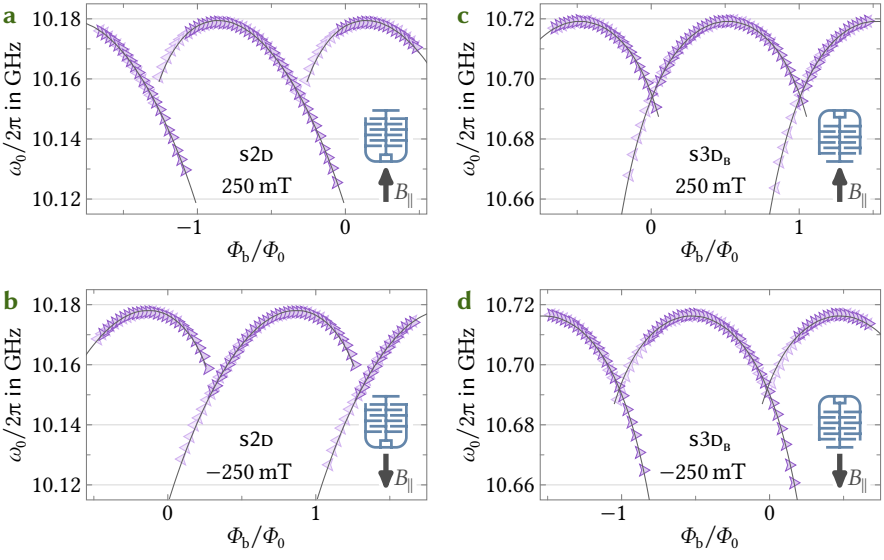

Figure 4.18: Reversing the in-plane field reverses the flux arc skewing. Bias flux response $\omega_0(\Phi_b)$ of resonators s2D and s3D$_B$ at $B_\parallel = \pm 250\,\mathrm{mT}$. The resonator as well as the $B_\parallel$ values are indicated in the panels, a small sketch additionally illustrates the orientation of resonator and field. Kite symbols are measurement data with the pointing direction indicating the flux-sweep direction, lines are fits. For the fits, the model parameters $j_0(0)$, ϵ, $l_{\mathrm{eff}}(0)$ and b are identical for both field orientations, only ℓ_{lin} being allowed to differ. Both in the data and in the fits, reversing the in-plane field also reverses the skewing of the flux arcs as well as the sweetspot-shift from $\Phi_b = 0$.

This is due to a small drift present in our setup, shifting all frequencies to slightly lower values over the course of the measurements (ca. one week). We attribute this to the pressure in the vacuum compartment slowly increasing, raising the cooling power reaching the sample assembly, which in turn causes the temperature controller to provide a higher heating power in order to keep the temperature sensor at the temperature setpoint $T_s = 2.8\,\mathrm{K}$ (cf. Figure 4.8). Since the sample diode, although directly attached to the copper housing surrounding the sample, will never have exactly the same temperature as the resonator circuits, this can cause an upwards creep of the circuit temperature, increasing its kinetic inductance and thus lowering its resonance frequency. This effect can also be observed in the sweetspot frequencies of the compensation angle measurements presented in Figure 4.6b; those were taken at a much lower pressure (before settling on the final measurement conditions) and accordingly show a noticeably higher resonance frequency at the optimum compensation angle. Here, we account for this drift in the fit curves by allowing ℓ_{lin} to vary between fits for positive and for negative field values, with small shifts in that inductance (here $\lesssim 3\,\%$) effectively shifting the resulting flux arcs without changing their shape. All other model parameters $j_0(0)$, ϵ, $l_{\mathrm{eff}}(0)$ and b are left unchanged for the negative-field fits, ensuring that the observed reversal of the skewing direction can indeed be attributed to the field reversal and not to changing parameter values.

4.25 Model parameters resulting from the fits

As described in Section 4.13, we obtain the model parameters I_{00}, ϵ, b, $\delta_B = 2\pi B_\parallel / B_0$ and $\delta_\ell(B_\parallel)$ from the flux arc fits. From this we can directly calculate the effective junction area $A_{\mathrm{eff}} = \Phi_0 / B_0$ threaded by the magnetic in-plane field. While the inductive phase $\delta_\ell(B_\parallel)$ is field dependent, at zero field we can calculate the equivalent linear inductance $L_{\mathrm{lin}} = \Phi_0 \delta_\ell(0) / 2\pi I_{00}$ of a simple constriction without gradients,

Table 4.3: Model parameters resulting from the fits and derived quantities. We show the CPR model parameters I_{00}, ϵ, b and $B_0 = 2\pi|B_\parallel/\delta_B|$ extracted from the flux arc fits as described in Section 4.13, as well as the effective constriction area A_{eff} implied by these results. The field dependent parameter δ_ℓ is depicted in plot form in Figure 4.19, here we only show the equivalent linear inductance at zero field L_{lin}. Furthermore, we state the

	I_{00} in µA	ϵ	b	B_0 in mT	A_{eff} in m^2	L_{lin} in pH
S2D	35	0.78	1	305	$6.8 \cdot 10^{-15}$	12
S3D$_B$	26	0.82	0	361	$5.7 \cdot 10^{-15}$	15

as discussed in the context of Figure 4.2. Given the constriction dimensions a and w, we can furthermore calculate the effective junction length $l_{\mathrm{eff}}(0) = A_{\mathrm{eff}}/a$ and the critical current density in the center of the junction $j_0(0) = I_{00}/wa$. All of these parameters are displayed in Table 4.3, except for the field-dependent δ_ℓ which is shown in Figure 4.19. As discussed in Section 4.24, a resonator that is rotated on the chip by 180° exhibits the same behavior when applying a positive field as one that is not rotated when applying a negative field, i.e. the fit results in a negative δ_B when not accounting for the rotation elsewhere in the formalism. We account for the rotation after the fact by removing the sign when calculating $B_0 = 2\pi|B_\parallel/\delta_B|$ for Table 4.3, leaving the fit scripts rotation-agnostic.

Overall, the values we find are quite sensible and match the typical parameter range for similar devices. Note again that, unlike in a standard junction experiencing a magnetic field, the presence of the j_0-gradient represented by ϵ has the effect that the CPR no longer vanishes when $B_\parallel = B_0$, cf. Section 4.21. Thus, despite the value $B_0 = 305\,\mathrm{mT}$ for S2D being barely above the highest measured field of 300 mT, we do not expect the critical currents to nearly disappear, and indeed our estimate of $(350 - 400)\,\mathrm{mT}$ derived from Figure 4.4e was considerably larger. The value $b = 1$ characterizing the $B_\parallel l_{\mathrm{eff}}(z)$-gradient, however, is at the very edge of its permissible parameter range $[0, 1]$. While the resulting CPRs fit the data quite well, this indicates that the model is reaching its limits here and more sophisticated dependencies than those introduced in (4.9) and (4.10) are needed for a more complete description of the circuit response, such as a nonlinear $j_0(z)$ or a z-dependent ℓ_{lin}.

The $B_\parallel$-dependence of δ_ℓ also seems reasonable for the most part. We already discussed the expected increase of kinetic inductance due to the magnetic field that should thus lead to a higher δ_ℓ-value at larger fields, which is indeed what we see. The absolute values $\delta_\ell > 1$ indicate that the current density in the center of the junction $j(0, \delta_c)$ is not unique (cf. Section 4.21), similar to $L_{\mathrm{lin}}/L_{J0} > 1$ resulting in an over-hanging CPR for the simpler case discussed in the context of Figure 4.2.

constriction dimensions a (estimated from the NIM beam dose D_2, cf. Table 4.2), w and l as well as the effective constriction length l_{eff} and the critical current density in the center of the junction $j_0(0)$ resulting from these dimensions together with the fit results. Finally, we include the parameters ω_{ref}, ζ_0 and ζ_1 obtained from the Kerr fits as described in Section 4.16 that define the pump-line damping behavior $\zeta(\omega_p)$.

a in nm	w in nm	l in nm	$l_{\mathrm{eff}}(0)$ in nm	$j_0(0)$ in $\mathrm{A\,m^{-2}}$	$\omega_{\mathrm{ref}}/2\pi$ in GHz	ζ_0	$2\pi\zeta_1$ in $\mathrm{MHz^{-1}}$
100	40	40	68	$8.7 \cdot 10^9$	10.25	$3.9 \cdot 10^{-5}$	$-7.4 \cdot 10^{-3}$
75	40	40	76	$8.8 \cdot 10^9$	10.80	$7 \cdot 10^{-5}$	$-1.9 \cdot 10^{-2}$

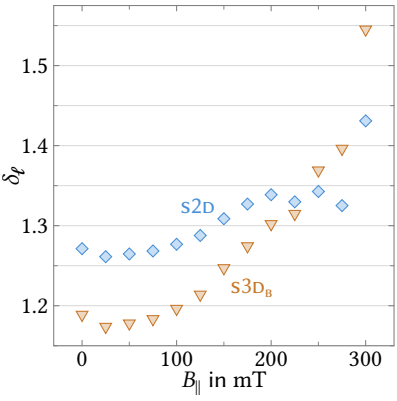

Figure 4.19: Field-dependent specific linear constriction inductance extracted from the flux-response fits. Symbols are the normalized specific linear constriction inductance $\delta_\ell(B_\parallel)$ for resonators s2D and s3D$_B$ resulting from the flux arc fits described in Section 4.13. The non-normalized value ℓ_{lin} can be obtained via multiplication with the specific Josephson inductance in the center of the constriction $\ell_{J0} = \Phi_0/2\pi j_0(0)$, which is approximately $3.8 \cdot 10^{-14}$ pH m^2 for both resonators, cf. Table 4.3.

We can gain a more intuitive comparison with this field-free, gradient-free model by considering the equivalent linear inductance L_{lin}, finding a larger value for the 3D constrictions, which makes intuitive sense. Reassuringly, the value of 12 pH we find for s2D matches the value we found using the simpler fit. Note that the zero-field value of $\delta_\ell \propto L_{\text{lin}} I_{00}$ itself is smaller for the 3D constrictions than for the 2D variants, corresponding to a less skewed CPR. While some features of $\delta_\ell(B_\parallel)$, like the large jump at $B_\parallel = 300$ mT or the plateau in the s2D-values right before it, offer no intuitive physical explanation and might simply be artifacts of model insufficiencies, the larger value at $B_\parallel = 0$ can be explained by the small value drift discussed in Section 4.24: While the other measurements were taken in order – larger fields were measured later during the measurement period – the zero-field value was measured last, so the difference between it and the next data point represents the accumulated value drift during the entire measurement process, demonstrating its smallness.

For completeness, Table 4.3 also lists the parameters ω_{ref}, ζ_0 and ζ_1 resulting from the Kerr anharmonicity fits described in Section 4.16.

References

[1] Z.-L. Xiang, S. Ashhab, J. Q. You, and F. Nori, *Hybrid quantum circuits: Superconducting circuits interacting with other quantum systems*, Reviews of Modern Physics **85**, 623–653 (2013).

[2] A. A. Clerk, K. W. Lehnert, P. Bertet, J. R. Petta, and Y. Nakamura, *Hybrid quantum systems with circuit quantum electrodynamics*, Nature Physics **16**, 257–267 (2020).

[3] A. Blais, A. L. Grimsmo, S. M. Girvin, and A. Wallraff, *Circuit quantum electrodynamics*, Reviews of Modern Physics **93**, 025005 (2021).

[4] N. Samkharadze, A. Bruno, P. Scarlino, G. Zheng, D. P. DiVincenzo, L. DiCarlo, and L. M. K. Vandersypen, *High-kinetic-inductance superconducting nanowire resonators for circuit QED in a magnetic field*, Physical Review Applied **5**, 044004 (2016).

[5] J. G. Kroll, W. Uilhoorn, K. L. van der Enden, D. de Jong, K. Watanabe, T. Taniguchi, S. Goswami, M. C. Cassidy, and L. P. Kouwenhoven, *Magnetic field compatible circuit quantum electrodynamics with graphene Josephson junctions*, Nature Communications **9**, 4615 (2018).

[6] A. Kringhøj, T. W. Larsen, O. Erlandsson, W. Uilhoorn, J. G. Kroll, M. Hesselberg, R. P. G. McNeil, P. Krogstrup, L. Casparis, C. M. Marcus, and K. D. Petersson, *Magnetic-field-compatible superconducting transmon qubit*, Physical Review Applied **15**, 054001 (2021).

[7] J. Krause, C. Dickel, E. Vaal, M. Vielmetter, J. Feng, R. Bounds, G. Catelani, J. M. Fink, and Y. Ando, *Magnetic field resilience of three-dimensional transmons with thin-film Al/AlO_x/Al Josephson junctions approaching* 1 T, Physical Review Applied **17**, 034032 (2022).

[8] M. Xu, R. Cheng, Y. Wu, G. Liu, and H. X. Tang, *Magnetic field-resilient quantum-limited parametric amplifier*, PRX Quantum **4**, 010322 (2023).

[9] N. Zapata, I. Takmakov, S. Günzler, S. Geisert, S. Ihssen, M. Field, A. Nambisan, D. Rieger, T. Reisinger, W. Wernsdorfer, and I. M. Pop, *Granular aluminum parametric amplifier for low-noise measurements in tesla fields*, Physical Review Letters **133**, 260604 (2024).

[10] S. Frasca, C. Roy, G. Beaulieu, and P. Scarlino, *Three-wave-mixing quantum-limited kinetic inductance parametric amplifier operating at* 6 T *near* 1 K, Physical Review Applied **21**, 024011 (2024).

[11] E. M. Levenson-Falk, N. Antler, and I. Siddiqi, *Dispersive nanoSQUID magnetometry*, Superconductor Science and Technology **29**, 113003 (2016).

[12] I. C. Rodrigues, D. Bothner, and G. A. Steele, *Coupling microwave photons to a mechanical resonator using quantum interference*, Nature Communications **10**, 5359 (2019).

[13] D. Zoepfl, M. L. Juan, C. M. F. Schneider, and G. Kirchmair, *Single-photon cooling in microwave magnetomechanics*, Physical Review Letters **125**, 023601 (2020).

[14] P. Schmidt, R. Claessen, G. Higgins, J. Hofer, J. J. Hansen, P. Asenbaum, M. Zemlicka, K. Uhl, R. Kleiner, R. Gross, H. Huebl, M. Trupke, and M. Aspelmeyer, *Remote sensing of a levitated superconductor with a flux-tunable microwave cavity*, Physical Review Applied **22**, 014078 (2024).

[15] D. I. Schuster, A. P. Sears, E. Ginossar, L. DiCarlo, L. Frunzio, J. J. L. Morton, H. Wu, G. A. D. Briggs, B. B. Buckley, D. D. Awschalom, and R. J. Schoelkopf, *High-cooperativity coupling of electron-spin ensembles to superconducting cavities*, Physical Review Letters **105**, 140501 (2010).

[16] C. W. Zollitsch, K. Mueller, D. P. Franke, S. T. B. Goennenwein, M. S. Brandt, R. Gross, and H. Huebl, *High cooperativity coupling between a phosphorus donor spin ensemble and a superconducting microwave resonator*, Applied Physics Letters **107**, 142105 (2015).

[17] A. Ghirri, C. Bonizzoni, D. Gerace, S. Sanna, A. Cassinese, and M. Affronte, *$YBa_2Cu_3O_7$ microwave resonators for strong collective coupling with spin ensembles*, Applied Physics Letters **106**, 184101 (2015).

[18] H. Huebl, C. W. Zollitsch, J. Lotze, F. Hocke, M. Greifenstein, A. Marx, R. Gross, and S. T. B. Goennenwein, *High cooperativity in coupled microwave resonator ferrimagnetic insulator hybrids*, Physical Review Letters **111**, 127003 (2013).

[19] Y. Li, T. Polakovic, Y.-L. Wang, J. Xu, S. Lendinez, Z. Zhang, J. Ding, T. Khaire, H. Saglam, R. Divan, J. Pearson, W.-K. Kwok, Z. Xiao, V. Novosad, A. Hoffmann, and W. Zhang, *Strong coupling between magnons and microwave photons in on-chip ferromagnet-superconductor thin-film devices*, Physical Review Letters **123**, 107701 (2019).

[20] M. Song, T. Polakovic, J. Lim, T. W. Cecil, J. Pearson, R. Divan, W.-K. Kwok, U. Welp, A. Hoffmann, K.-J. Kim, V. Novosad, and Y. Li, *Single-shot magnon interference in a magnon-superconducting-resonator hybrid circuit*, Nature Communications **16**, 3649 (2025).

[21] C. Nayak, S. H. Simon, A. Stern, M. Freedman, and S. Das Sarma, *Non-Abelian anyons and topological quantum computation*, Reviews of Modern Physics **80**, 1083–1159 (2008).

[22] F. Hassler, A. R. Akhmerov, C.-Y. Hou, and C. W. J. Beenakker, *Anyonic interferometry without anyons: how a flux qubit can read out a topological qubit*, New Journal of Physics **12**, 125002 (2010).

[23] A. Schneider, T. Wolz, M. Pfirrmann, M. Spiecker, H. Rotzinger, A. V. Ustinov, and M. Weides, *Transmon qubit in a magnetic field: Evolution of coherence and transition frequency*, Physical Review Research **1**, 023003 (2019).

[24] F. Luthi, T. Stavenga, O. W. Enzing, A. Bruno, C. Dickel, N. K. Langford, M. A. Rol, T. S. Jespersen, J. Nygård, P. Krogstrup, and L. DiCarlo, *Evolution of nanowire transmon qubits and their coherence in a magnetic field*, Physical Review Letters **120**, 100502 (2018).

[25] O. W. Kennedy, J. Burnett, J. C. Fenton, N. G. N. Constantino, P. A. Warburton, J. J. L. Morton, and E. Dupont-Ferrier, *Tunable Nb superconducting resonator based on a constriction nano-SQUID fabricated with a Ne focused ion beam*, Physical Review Applied **11**, 014006 (2019).

[26] K. Borisov, D. Rieger, P. Winkel, F. Henriques, F. Valenti, A. Ionita, M. Wessbecher, M. Spiecker, D. Gusenkova, I. M. Pop, and W. Wernsdorfer, *Superconducting granular aluminum resonators resilient to magnetic fields up to 1 Tesla*, Applied Physics Letters **117**, 120502 (2020).

[27] K. Uhl, D. Hackenbeck, C. Füger, R. Kleiner, D. Koelle, and D. Bothner, *A flux-tunable $YBa_2Cu_3O_7$ quantum interference microwave circuit*, Applied Physics Letters **122**, 182603 (2023).

[28] S. E. de Graaf, A. V. Danilov, A. Adamyan, T. Bauch, and S. E. Kubatkin, *Magnetic field resilient superconducting fractal resonators for coupling to free spins*, Journal of Applied Physics **112**, 123905 (2012).

[29] S. Kwon, A. Fadavi Roudsari, O. W. B. Benningshof, Y.-C. Tang, H. R. Mohebbi, I. A. J. Taminiau, D. Langenberg, S. Lee, G. Nichols, D. G. Cory, and G.-X. Miao, *Magnetic field dependent microwave losses in superconducting niobium microstrip resonators*, Journal of Applied Physics **124**, 033903 (2018).

[30] J. G. Kroll, F. Borsoi, K. L. van der Enden, W. Uilhoorn, D. de Jong, M. Quintero-Pérez, D. J. van Woerkom, A. Bruno, S. R. Plissard, D. Car, E. P. A. M. Bakkers, M. C. Cassidy, and L. P. Kouwenhoven, *Magnetic-field-resilient superconducting coplanar-waveguide resonators for hybrid circuit quantum electrodynamics experiments*, Physical Review Applied **11**, 064053 (2019).

[31] E. A. Tholén, A. Ergül, K. Stannigel, C. Hutter, and D. B. Haviland, *Parametric amplification with weak-link nonlinearity in superconducting microresonators*, Physica Scripta **2009**, 014019 (2009).

[32] J. Burnett, J. Sagar, O. W. Kennedy, P. A. Warburton, and J. C. Fenton, *Low-loss superconducting nanowire circuits using a neon focused ion beam*, Physical Review Applied **8**, 014039 (2017).

[33] K. Uhl, D. Hackenbeck, D. Koelle, R. Kleiner, and D. Bothner, *Extracting the current-phase relation of a monolithic three-dimensional nanoconstriction using a dc-current-tunable superconducting microwave cavity*, Physical Review Applied **22**, 064052 (2024).

[34] K. Uhl, D. Hackenbeck, J. Peter, R. Kleiner, D. Koelle, and D. Bothner, *Niobium quantum interference microwave circuits with monolithic three-dimensional nanobridge junctions*, Physical Review Applied **21**, 024051 (2024).

[35] M. Jamet, W. Wernsdorfer, C. Thirion, D. Mailly, V. Dupuis, P. Mélinon, and A. Pérez, *Magnetic anisotropy of a single cobalt nanocluster*, Physical Review Letters **86**, 4676–4679 (2001).

[36] K. Hasselbach, D. Mailly, and J. R. Kirtley, *Micro-superconducting quantum interference device characteristics*, Journal of Applied Physics **91**, 4432–4437 (2002).

[37] A. G. P. Troeman, H. Derking, B. Borger, J. Pleikies, D. Veldhuis, and H. Hilgenkamp, *NanoSQUIDs based on niobium constrictions*, Nano Letters **7**, 2152–2156 (2007).

[38] L. Chen, H. Wang, X. Liu, L. Wu, and Z. Wang, *A high-performance Nb nano-superconducting quantum interference device with a three-dimensional structure*, Nano Letters **16**, 7726–7730 (2016).

[39] T. Weber, D. Jetter, J. Ullmann, S. A. Koch, S. F. Pfander, K. Kress, A. Vervelaki, B. Gross, O. Kieler, U. Drechsler, P. R. Baral, A. Magrez, R. Kleiner, A. W. Knoll, M. Poggio, and D. Koelle, *Advanced SQUID-on-lever scanning probe for high-sensitivity magnetic microscopy with sub-100-nm spatial resolution*, Physical Review Applied **24**, 054041 (2025).

[40] L. Chen, W. Wernsdorfer, C. Lampropoulos, G. Christou, and I. Chiorescu, *On-chip SQUID measurements in the presence of high magnetic fields*, Nanotechnology **21**, 405504 (2010).

[41] E. J. Romans, S. Rozhko, L. Young, A. Blois, L. Hao, D. Cox, and J. C. Gallop, *Noise performance of niobium nano-SQUIDs in applied magnetic fields*, IEEE Transactions on Applied Superconductivity **21**, 404–407 (2011).

[42] S. K. H. Lam, J. R. Clem, and W. Yang, *A nanoscale SQUID operating at high magnetic fields*, Nanotechnology **22**, 455501 (2011).

[43] D. Margineda, A. Crippa, E. Strambini, Y. Fukaya, M. T. Mercaldo, M. Cuoco, and F. Giazotto,
Sign reversal diode effect in superconducting Dayem nanobridges,
Communications Physics **6**, 343 (2023).

[44] I. Zapata, R. Bartussek, F. Sols, and P. Hänggi,
Voltage rectification by a SQUID ratchet,
Physical Review Letters **77**, 2292–2295 (1996).

[45] V. M. Krasnov, V. A. Oboznov, and N. F. Pedersen,
Fluxon dynamics in long Josephson junctions in the presence of a temperature gradient or spatial nonuniformity,
Physical Review B **55**, 14486–14498 (1997).

[46] S. Weiss, D. Koelle, J. Müller, R. Gross, and K. Barthel,
Ratchet effect in dc SQUIDs, Europhysics Letters **51**, 499 (2000).

[47] A. Sterck, S. Weiss, and D. Koelle, *SQUID ratchets: basics and experiments*,
Applied Physics A **75**, 253–262 (2002).

[48] J. E. Villegas, S. Savel'ev, F. Nori, E. M. Gonzalez, J. V. Anguita, R. García, and J. L. Vicent, *A superconducting reversible rectifier that controls the motion of magnetic flux quanta*, Science **302**, 1188–1191 (2003).

[49] A. Sterck, R. Kleiner, and D. Koelle, *Three-junction SQUID rocking ratchet*,
Physical Review Letters **95**, 177006 (2005).

[50] F. Ando, Y. Miyasaka, T. Li, J. Ishizuka, T. Arakawa, Y. Shiota, T. Moriyama, Y. Yanase, and T. Ono, *Observation of superconducting diode effect*,
Nature **584**, 373–376 (2020).

[51] H. Wu, Y. Wang, Y. Xu, P. K. Sivakumar, C. Pasco, U. Filippozzi, S. S. P. Parkin, Y.-J. Zeng, T. McQueen, and M. N. Ali,
The field-free Josephson diode in a van der Waals heterostructure,
Nature **604**, 653–656 (2022).

[52] M. Davydova, S. Prembabu, and L. Fu, *Universal Josephson diode effect*,
Science Advances **8**, eabo0309 (2022).

[53] M. Nadeem, M. S. Fuhrer, and X. Wang, *The superconducting diode effect*,
Nature Reviews Physics **5**, 558–577 (2023).

[54] J. Ingla-Aynés, Y. Hou, S. Wang, E.-D. Chu, O. A. Mukhanov, P. Wei, and J. S. Moodera,
Efficient superconducting diodes and rectifiers for quantum circuitry,
Nature Electronics **8**, 411–416 (2025).

[55] C. Baumgartner, L. Fuchs, A. Costa, S. Reinhardt, S. Gronin, G. C. Gardner, T. Lindemann, M. J. Manfra, P. E. Faria Junior, D. Kochan, J. Fabian, N. Paradiso, and C. Strunk, *Supercurrent rectification and magnetochiral effects in symmetric Josephson junctions*, Nature Nanotechnology **17**, 39–44 (2022).

[56] A. B. Zorin, *Josephson traveling-wave parametric amplifier with three-wave mixing*, Physical Review Applied **6**, 034006 (2016).

[57] N. E. Frattini, U. Vool, S. Shankar, A. Narla, K. M. Sliwa, and M. H. Devoret, *3-wave mixing Josephson dipole element*, Applied Physics Letters **110**, 222603 (2017).

[58] S. Pogorzalek, K. G. Fedorov, L. Zhong, J. Goetz, F. Wulschner, M. Fischer, P. Eder, E. Xie, K. Inomata, T. Yamamoto, Y. Nakamura, A. Marx, F. Deppe, and R. Gross, *Hysteretic flux response and nondegenerate gain of flux-driven Josephson parametric amplifiers*, Physical Review Applied **8**, 024012 (2017).

[59] K. K. Likharev, *Superconducting weak links*, Reviews of Modern Physics **51**, 101–159 (1979).

[60] E. H. Brandt and M. Indenbom, *Type-II-superconductor strip with current in a perpendicular magnetic field*, Physical Review B **48**, 12893–12906 (1993).

[61] G. Ghigo, F. Laviano, L. Gozzelino, R. Gerbaldo, E. Mezzetti, E. Monticone, and C. Portesi, *Evidence of rf-driven dendritic vortex avalanches in MgB_2 microwave resonators*, Journal of Applied Physics **102**, 113901 (2007).

[62] L. Nulens, N. Lejeune, J. Caeyers, S. Marinković, I. Cools, H. Dausy, S. Basov, B. Raes, M. J. Van Bael, A. Geresdi, A. V. Silhanek, and J. Van de Vondel, *Catastrophic magnetic flux avalanches in NbTiN superconducting resonators*, Communications Physics **6**, 267 (2023).

[63] D. Bothner, I. C. Rodrigues, and G. A. Steele, *Photon-pressure strong coupling between two superconducting circuits*, Nature Physics **17**, 85–91 (2021).

[64] Y. Zhang, Y. Gu, P. Li, J. Hu, and K. Jiang, *General theory of Josephson diodes*, Physical Review X **12**, 041013 (2022).

[65] J. A. Potter, L. Meti, G. Chapman, E. Romans, J. Gallop, and L. Hao, *Millikelvin Nb nanoSQUID-embedded tunable resonator fabricated with a neon focused-ion-beam*, Applied Physics Letters **126**, 012601 (2025).

[66] C. Schmid, A. Jozani, R. Kleiner, D. Koelle, and E. Goldobin, *$YBa_2Cu_3O_7$ Josephson diode fabricated by focused-helium-ion-beam irradiation*, Physical Review Applied **24**, 014041 (2025).

[67] Y. V. Fominov and D. S. Mikhailov,
Asymmetric higher-harmonic SQUID as a Josephson diode,
Physical Review B **106**, 134514 (2022).

[68] R. S. Souto, M. Leijnse, and C. Schrade,
Josephson diode effect in supercurrent interferometers,
Physical Review Letters **129**, 267702 (2022).

[69] A. Greco, Q. Pichard, and F. Giazotto, *Josephson diode effect in monolithic dc-SQUIDs based on 3D Dayem nanobridges*,
Applied Physics Letters **123**, 092601 (2023).

[70] N. E. Frattini, V. V. Sivak, A. Lingenfelter, S. Shankar, and M. H. Devoret,
Optimizing the nonlinearity and dissipation of a SNAIL parametric amplifier for dynamic range, Physical Review Applied **10**, 054020 (2018).

[71] D. Bothner, I. C. Rodrigues, and G. A. Steele,
Four-wave-cooling to the single phonon level in Kerr optomechanics,
Communications Physics **5**, 33 (2022).

[72] I. C. Rodrigues, G. A. Steele, and D. Bothner,
Parametrically enhanced interactions and nonreciprocal bath dynamics in a photon-pressure Kerr amplifier, Science Advances **8**, eabq1690 (2022).

[73] D. Zoepfl, M. L. Juan, N. Diaz-Naufal, C. M. F. Schneider, L. F. Deeg, A. Sharafiev, A. Metelmann, and G. Kirchmair,
Kerr enhanced backaction cooling in magnetomechanics,
Physical Review Letters **130**, 033601 (2023).

[74] D. Bothner, T. Gaber, M. Kemmler, D. Koelle, and R. Kleiner, *Improving the performance of superconducting microwave resonators in magnetic fields*,
Applied Physics Letters **98**, 102504 (2011).

[75] D. Bothner, C. Clauss, E. Koroknay, M. Kemmler, T. Gaber, M. Jetter, M. Scheffler, P. Michler, M. Dressel, D. Koelle, and R. Kleiner,
Reducing vortex losses in superconducting microwave resonators with microsphere patterned antidot arrays,
Applied Physics Letters **100**, 012601 (2012).

[76] G. Stan, S. B. Field, and J. M. Martinis,
Critical field for complete vortex expulsion from narrow superconducting strips,
Physical Review Letters **92**, 097003 (2004).

[77] C. Song, M. P. DeFeo, K. Yu, and B. L. T. Plourde,
Reducing microwave loss in superconducting resonators due to trapped vortices,
Applied Physics Letters **95**, 232501 (2009).

[78] D. Bothner, T. Gaber, M. Kemmler, D. Koelle, R. Kleiner, S. Wünsch, and M. Siegel,
Magnetic hysteresis effects in superconducting coplanar microwave resonators, Physical Review B **86**, 014517 (2012).

[79] C. W. Gardiner and M. J. Collett, *Input and output in damped quantum systems: Quantum stochastic differential equations and the master equation*, Physical Review A **31**, 3761–3774 (1985).

[80] Q.-M. Chen, M. Partanen, F. Fesquet, K. E. Honasoge, F. Kronowetter, Y. Nojiri, M. Renger, K. G. Fedorov, A. Marx, F. Deppe, and R. Gross, *Scattering coefficients of superconducting microwave resonators. II. System-bath approach*, Physical Review B **106**, 214506 (2022).

[81] M. M. Khapaev, A. Y. Kidiyarova-Shevchenko, P. Magnelind, and M. Y. Kupriyanov, *3D-MLSI: Software package for inductance calculation in multilayer superconducting integrated circuits*, IEEE Transactions on Applied Superconductivity **11**, 1090–1093 (2001).

[82] A. I. Gubin, K. S. Il'in, S. A. Vitusevich, M. Siegel, and N. Klein, *Dependence of magnetic penetration depth on the thickness of superconducting Nb thin films*, Physical Review B **72**, 064503 (2005).

[83] J. E. Healey, T. Lindström, M. S. Colclough, C. M. Muirhead, and A. Y. Tzalenchuk, *Magnetic field tuning of coplanar waveguide resonators*, Applied Physics Letters **93**, 043513 (2008).

[84] M. Kazouini, J. Peter, Z. E. Guo, B. Wilde, K. Uhl, D. Koelle, R. Kleiner, and D. Bothner, *Tunable and nonlinearity-enhanced dispersive-plus-dissipative coupling in photon-pressure circuits*, arXiv:2511.22571 [quant-ph] (2025).

5 Concluding remarks

In the preceding chapters, we have explored two superconducting resonator designs intended for use in hybrid quantum systems with a particular focus on the requirements and constraints imposed on them by their intended use. We have presented a thorough design and optimization procedure for a microwave chip capable of tunable coupling to an ensemble of ultra-cold Rydberg atoms and we have demonstrated the analysis and modeling of Josephson nano-diodes emerging in large magnetic fields in resonators designed with optomechanical experiments in mind. In both cases, we have performed a thorough characterization of the microwave properties of the superconducting circuits, verifying their suitability for use in the targeted hybrid systems and exploring their limitations, but leaving the realization of the full hybrid system for future efforts. Besides this original objective, which is now within reach, a number of interesting adjacent research directions may be pursued given our results.

The chip for superconductor-atom coupling presented in Chapter 3 is currently mounted in a dilution refrigerator set up for the preparation and manipulation of ultra-cold Rydberg atoms. While the superconducting resonator side of the hybrid system has been implemented with the efforts presented here, the quantum optical aspects – including the preparation, transport and manipulation of atoms using magnetic traps as well as lasers – are technically complex challenges that have yet to be completed; work that is presently underway. Already during this process, the mounted chip may be a useful resource for understanding and controlling particular aspects of the unique, specialized setup. For example, characterizing the impact of incident lasers on the resonator is of course useful for understanding the constraints

within which the superconducting device remains functional, but once known, it may also serve as a sensitive probe for laser alignment and possibly as a source of feedback for monitoring or compensation of setup vibrations originating from the pulse tube cooling the fridge. Similarly, once the transport of Rydberg atoms to a dipole trap near the chip has been achieved and the two components can be made to interact with each other, either of them may be used as a sensor for investigating the other in novel ways. For instance, the dispersive shift caused by the interacting Rydberg atoms in the superconducting resonator could be utilized to count the number and lifetime of atoms in the Rydberg state. On the other hand, the atoms may be used as a probe of local electric dc and microwave fields in the vicinity of the resonator, enabling one to scan the three-dimensional structure of the fields emitted by the circuit and to thus measure its radiative properties with microscopic resolution. In addition to their intrinsic appeal, investigations such as these can serve to verify the simulations and calculations performed during the resonator design and inform adaptations for future iterations improving on its remaining shortcomings. Together with the considerations presented here, including the proposed flip chip design for optimized field homogeneity, explorations such as these should be able to highlight a clear path to the eventual attainment of strong coupling between ultra-cold Rydberg atoms and superconducting circuits.

Moving on, the Nb SQUID resonators discussed in Chapter 4 have been demonstrated to perform nicely even at substantial magnetic in-plane fields – particularly in conjunction with our effective and practical field alignment scheme – and to thus be suitable for use in optomechanical devices. This should already help achieve significant improvements over the state-of-the-art Al devices commonly used in similar systems. However, the nano-diodes we were able to observe and characterize as well as the CPR model developed for them may be of interest in much broader contexts. For any application relying on frequency tuning of a SQUID resonator, the diodes offer the possibility to enhance both its flux responsivity and the frequency tuning range, and to eliminate metastable states in the relevant operation regimes. As these are important figures of merit for several applications in hybrid systems as well as sensing devices, the employment of diodes may offer possible advancements for several related fields; an insight that extends beyond the NIM-constriction diodes discussed here to any other diode implementation. However, the interest in superconducting diodes is not restricted to applications relying on microwave measurements, and a compact, tunable Josephson diode like the nano-constrictions discussed here might be an attractive alternative to existing designs for any purpose. Particularly the possibility to tailor-make diodes that behave as desired even at low fields by following the circuit structure outlined through our diode model has the potential to prove useful for the exploitation of diode-based improvements in any number of experimental settings. Finally, the demonstrated method of investigating the sub-critical properties of a supercon-

ducting diode by integrating it into a SQUID resonator and probing its inductive properties in microwave measurements – that is, studying the diode CPR rather than relying exclusively on its critical currents as is routinely done – may prove a valuable technique in the research into superconducting diodes more generally.

Notwithstanding the merit of these proposed lines of inquiry, one lesson from looking back at the history of scientific progress, as we did briefly at the start of this thesis, is that things seldom proceed as one predicts. In retrospect, it is tempting to imagine oneself at the end point of a seemingly clear, albeit long and convoluted, path and to perceive the immediate future as the ostensibly logical extension of that path, when in truth each of us invariably inhabits the perpetual middle of history. In the spirit of that perspective, let us hope that some of the work presented here may prove useful to others in ways outside those imagined above; that it may become a node in the tangled web of roads that is history, rather than one of its many dead ends.

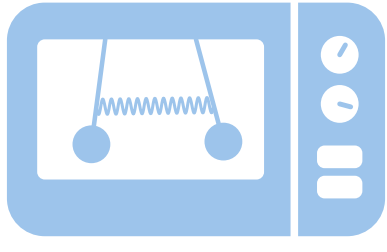

Es war ein langer Weg zur Vollendung dieser Arbeit. Viele Menschen haben mich darauf zumindest ein Stück begleitet und sicherlich habe ich nicht jedem Gefährten die gebührende Wertschätzung in Worten bezeugt. Wenngleich ich das auch hier nicht in aller Ausführlichkeit tun kann, möchte ich die Gelegenheit nutzen um noch einmal ganz explizit Danke zu sagen. Für kollegiales Zuarbeiten und gemeinsame Pausen, für gute Diskussionen, wertvolle Rückmeldungen und immer wieder neue Impulse, für Perspektive und für eine Marschrichtung, so sie mir abhanden kamen, für kompetentes Zur-Seite-Stehen, selbst wenn Freitagabend unweigerlich etwas kaputt ging, für zügige Verwaltungsprozesse und für das Erfüllen auch vielleicht etwas zu ambitionierter Werkstattaufträge, für die Initiative, mal etwas ganz anderes zusammen zu machen, für das gemeinsame Feierabend-Spaßgetränk, für ausgelassene Stunden und gediegene Abende, für offenen Austausch und für gute Gespräche, die langen wie die kurzen, für den gehaltenen Kontakt und den herzlichen Besuch, für das Bemühen, für mich da zu sein, auch wenn das nicht immer geht, für Zeit, die man sich ja bekanntlich nehmen muss, für den sicheren Rückzugsort, für auch mal mahnende Worte und für das Vertrauen, dass ich schon mein Ding machen werde. Danke.